Effects of Liquefaction-Induced Lateral Spreading
on Pile Foundations

by

John C. Horne

A dissertation submitted in partial fulfillment
of the requirements for the degree of

Doctor of Philosophy

University of Washington

1996

Approved by ______________________
Chairperson of Supervisory Committee

Program Authorized
to Offer Degree Civil Engineering

Date 10/26/96

UMI Number: 9716853

In presenting this dissertation in partial fulfillment of the requirements for the Doctoral degree at the University of Washington, I agree that the Library shall make its copies freely available for inspection. I further agree that extensive copying of this dissertation is allowable only for scholarly purposes, consistent with "fair use" as prescribed in the U.S. Copyright Law. Requests for copying or reproduction of this dissertation may be referred to University Microfilms, 1490 Eisenhower Place, P.O. Box 975, Ann Arbor, MI 48106, to whom the author has granted "the right to reproduce and sell (a) copies of the manuscript in microform and/or (b) printed copies of the manuscript made from microform."

Signature John Charles Horn

Date 10-25-96

University of Washington

Abstract

# Effects of Liquefaction-Induced Lateral Spreading on Pile Foundations

by John C. Horne

Chairperson of Supervisory Committee: Professor Steven L. Kramer
Civil Engineering Department

Earthquakes cause structural damage in many ways. A particularly devastating combination occurs when pile foundations are situated in loose, saturated soil deposits that are prone to liquefaction. If such a deposit is situated on a shallow slope or near a river channel, a state of nonzero initial shear stress exists which may induce significant lateral movements within the liquefied soil. Piles that extend through these deposits may also move laterally and sustain extensive flexural damage.

A two-step methodology was developed to analyze the structural demands placed on pile foundations due to lateral spreading. The first step involved the development of a one dimensional, time domain ground response model that computes the displacement of an arbitrary soil deposit during and after strong shaking -- both at and below the ground surface. A high resolution Godunov scheme was used in order to capture the extreme strain gradients that may exist in lateral spread regimes. Additionally, an effective stress formulation considers the influence of excess pore pressure on the strength and stiffness of the soil.

The second step involved the development of a one dimensional pile-soil interaction model. A nonlinear rheologic model composed of separate near-field and far-field elements replicates hysteretic and radiation damping associated with pile-soil interaction. Properties of the rheologic model are updated continuously based on the effective stresses computed via the ground response model.

An extensive parametric study revealed the dominant trends of the proposed methodology. It was found that lateral spread displacement -- and hence pile response -- is very sensitive to ground surface slope and standard penetration resistance, but not very sensitive to groundwater table depth. Furthermore, it was found that pile response was also strongly dependent on flexural stiffness, but not very sensitive to pile diameter or p-y curve stiffness.

The model was then applied to well-documented case histories to assess its effectiveness. These include a direct comparison between the proposed model and an existing empirical method in addition to hind-cast analyses of two Niigata case studies. This effort verified that the model is useful to assess the effects of liquefaction-induced lateral spreading on pile foundations.

TABLE OF CONTENTS

TABLE OF CONTENTS (cont.)

LIST OF FIGURES

Number Page

LIST OF FIGURES (cont.)

LIST OF FIGURES (cont.)

LIST OF FIGURES (cont.)

Number Page

LIST OF FIGURES (cont.)

LIST OF FIGURES (cont.)

LIST OF TABLES

## ACKNOWLEDGMENTS

I would like to thank the Washington State Department of Transportation for funding this research project. Additionally, I thank Professor Steven L. Kramer of the Civil Engineering Department for providing guidance as my advisor and giving me the opportunity to conduct this research. Also, I am indebted to the assistance of Professor Randall J. LeVeque of the Applied Mathematics Department for introducing me to the numerical methods used in Chapter 4 of this dissertation. Finally, my involvement in this research would not have been possible without the tireless support and thoughtful encouragement of my loving wife, Pamela.

# Chapter 1 Introduction

Throughout history, earthquakes have left damaging impacts on the lives and livelihoods of civilizations. Earthquakes can cause damage in a number of ways, but one of the most significant is related to liquefaction of near-surface soils. Liquefaction can reduce the stiffness and strength of soils subjected to cyclic loading to the point where the soil deforms significantly. Soils most susceptible to liquefaction include loose, saturated deposits of clean sand and silty sand. Both natural deposits (alluvial, lacustrine, and marine) and man-made deposits (dumped or hydraulically placed fill) can be susceptible to liquefaction. Over the past 30 years, the interest in and research of the liquefaction phenomenon have rendered it an important part of earthquake engineering.

From a regulatory or design perspective, most building codes (e.g. ICBO, 1994) require engineers to consider earthquake hazards from two sources: ground shaking and liquefaction. The former requires the designer to account for the effect of dynamic forces caused by an earthquake. The latter requires that the potential for liquefaction be addressed, including the effect of any such behavior on the planned project. In general, structural damage may be caused by four liquefaction-induced effects:

- Amplification of the bedrock shaking due to progressive softening of the soil
- Loss of bearing capacity due to progressive softening of the soil
- Settlement caused by the dissipation of excess pore pressures
- Lateral displacements caused by weakening of soils which have non-zero initial shear stresses

From a theoretical soil mechanics perspective, liquefaction phenomena can be divided into two main categories (Kramer, 1995) – flow liquefaction and cyclic mobility. Which of these phenomena occurs at a particular site depends not only on the stress and density states of the soil deposit prior to ground shaking, but also on the stress path during and after strong ground shaking. Both, however, can cause significant soil deformations, including large lateral displacements.

Liquefiable soils subjected to in situ shear stresses greater than their residual shear strengths are susceptible to flow liquefaction failure. That is, the ultimate or residual shear strength is less than that which is needed to maintain static equilibrium. As a result, flow liquefaction is driven by static stresses and can result in massive material flows over large distances. The requisite combination of loose, saturated, and highly pre-sheared soil is relatively rare in the field. Hence, true flow liquefaction failures during earthquakes are relatively rare.

Cyclic mobility, which occurs in soils whose in situ shear stresses are less than their residual shear strengths, is far more common than flow liquefaction. Permanent displacements induced by cyclic mobility are often termed "lateral spread" displacements. Because permanent strains induced by cyclic mobility occur as a result of pore pressure-induced softening and transient exceedances of available strength, lateral spreading displacements develop incrementally and are smaller in magnitude than those produced by flow liquefaction. Lateral spread displacements can, however, be large enough to cause serious structural damage – particularly to structures situated within the soil itself.

## 1.1 IDENTIFICATION OF PROBLEM

Pile foundations are designed primarily to resist vertical loads, and are often times used at sites which, by their very nature, are prone to lateral spreading. Because they are relatively flexible in bending, however, pile foundations are especially vulnerable to lateral spread displacements. Lateral spreads can cause large soil displacements in the vicinity of piles and induce bending moments that exceed the flexural capacity of piles – leading to structural failure. The magnitude and distribution of these bending moments depend on the lateral spreading behavior of the soil – both at and below the ground surface – and on the interaction between the pile and the surrounding soil. Unfortunately, structural and geotechnical engineers currently have no rational method by which these deformations and moments can be estimated so that the requirements set forth in the building codes may be satisfied.

The research described in this dissertation serves to address this gaping need. That is, it provides the practitioner with a rational method to evaluate the effect of liquefaction-induced lateral spreading on pile foundations. It can be used to analyze a proposed design or to evaluate the vulnerability of an existing structure. The remainder of this chapter sets forth the objectives of the research, the scope of the research, and the organization of the dissertation.

## 1.2 OBJECTIVES AND SCOPE OF RESEARCH

Based on the above presentation, the need for further research in this area is evident. To this end, the research has been directed towards the following three objectives:

- Development of a practical procedure for the site-specific evaluation of permanent free-field soil movements both at and below the ground surface,
- Development of a practical procedure for the site-specific evaluation of pile response to general free-field soil movements, and
- Combination of the previous two procedures in an integrated procedure for evaluating the effects of liquefaction-induced lateral spreading on pile foundations.

The scope of the research was developed as a series of steps that would be taken to achieve the research objectives. The following five items comprise the scope:

- Clear establishment of the existing state of knowledge regarding the occurrence and analysis of lateral spreading and pile-soil interaction in liquefiable soils,
- Detailed development and verification of a nonlinear, hysteretic, effective stress-based ground response model,
- Detailed development and verification of a nonlinear, hysteretic pile-soil interaction model,

- Broad study of the sensitivity of the ground response and pile-soil interaction models to the input parameters used to apply them to practical earthquake engineering problems, and
- Detailed application of the models to case histories where pile foundations have been damaged by lateral spreading.

## 1.3 ORGANIZATION OF DISSERTATION

This dissertation contains the results of the research effort described above. The information is organized among eight chapters and three appendices. Following this chapter, Chapters 2 and 3 contain the results of an extensive literature review which establishes the current state of knowledge. Chapter 2 deals with lateral movement of liquefied soil and describes prior experimental and analytical studies. Chapter 2 also contains relevant case studies of lateral ground movements reported in the literature. Chapter 3 focuses on pile-soil interaction research, including experimental, analytical, and case studies. Both chapters conclude with critical reviews of the existing states of knowledge, which paves the way for the present research.

Chapters 4 and 5 introduce analytical methods for the lateral spreading and pile-soil interaction problems, respectively. Each chapter includes an analytical description of the model and a thorough verification of its applicability to practical problems.

Chapters 6 and 7 describe a series of analytical studies conducted with the two models. The first of these contains the results of an extensive parameter study. This study serves to establish output sensitivity to input variation, and also allows for broad conclusions to be made about the cause and effect of liquefaction-induced lateral spreading. Chapter 7 describes application of the models to observed field behavior at several sites. This serves to verify that results obtained from the model are indeed reasonable. Furthermore, it establishes the legitimacy of the method for use in predictive problems.

Chapter 8 concludes the dissertation with a summary of the major research findings, and a description of the major conclusions that can be drawn from these findings. Finally, the chapter makes recommendations for future research regarding lateral spreading and its effect on pile foundations.

Three appendices contain auxiliary information. Appendix A contains an alphabetical listing of the references cited in the first eight chapters. Appendix B contains the FORTRAN source code of the ground response model introduced in Chapter 4. Finally, Appendix C contains the FORTRAN source code for the pile-soil interaction model described in Chapter 5.

# Chapter 2 Lateral Movement of Liquefied Soil: Previous Research

## 2.1 INTRODUCTION

This chapter details available information pertaining to the lateral movement of liquefied soil and establishes the current state of understanding of this phenomenon. The chapter is organized into six sections. The first serves to introduce the subject and describe the historical framework of geotechnical earthquake engineering research. Section 2.1.2 describes the mechanics by which lateral movements of liquefiable soils take place, and Section 2.1.3 presents a series of earthquake case histories that illustrate these events. Section 2.1.4 discusses efforts to study this behavior experimentally. Subsequently, Section 2.1.5 details analytical studies – both theoretical and numerical – aimed at describing lateral movement of liquefied soil. The final section provides a critique of this existing body of research.

Much of the research and case studies cited in this chapter occurred during the past three decades. Widespread earthquake-induced soil liquefaction and lateral movement occurred during the disastrous 1964 earthquakes in Niigata, Japan and Anchorage, Alaska. This prompted a massive, worldwide research effort aimed at gaining a better understanding of this phenomenon. Much of the pioneering work was conducted by Professor Harry Seed and his colleagues at the University of California at Berkeley. Early studies comprised cyclic triaxial tests and linear ground response analyses. In more recent years, these have been supplanted by centrifuge model tests and multi-dimensional numerical analyses. Kramer (1995) presents a detailed description of this historical development. After 30 years, geotechnical earthquake engineering has developed into a recognized area of research within civil engineering. However, the preponderance of liquefaction-induced soil movement caused by the 1995 Kobe, Japan earthquake indicates there is still much to learn.

In this chapter and throughout the remainder of the dissertation, "free-field" deformations refer to lateral ground deformations not impeded by man-made structures such as building walls, foundation piles, or bridge piers. Free-field deformations would be observed, for example, in an undeveloped alluvial plain or in a developed area beyond the zone of influence of existing structures. This 'zone of influence' depends on the size and stiffness of the structure relative to the depth and stiffness of the soil deposit.

The free-field case is the most widely studied in the literature. This can probably be attributed to the relatively simple boundary conditions that exist in the free-field case. Forensic studies conducted after many recent earthquakes have documented permanent deformations caused by liquefaction. Researchers have used these studies to develop empirical and analytical methods to predict the magnitude of liquefaction-induced ground surface deformations. Additionally, experimental work with shaking table and centrifuge tests have been conducted in order to verify analytical methods or to replicate field conditions.

## 2.2 FLOW LIQUEFACTION AND CYCLIC MOBILITY

The development of lateral deformations in a liquefying soil mass can be understood in terms of basic soil mechanics. The stress path concept provides a convenient framework in which to illustrate the effective stress and pore pressure conditions that lead to the development of flow liquefaction and cyclic mobility.

### 2.2.1 Flow Liquefaction

Flow liquefaction is a relatively rare phenomenon, but when it does occur, extremely large lateral deformations can develop. A classic example is Lower San Fernando Dam, which failed by flow liquefaction during the 1971 San Fernando, California earthquake. Flow liquefaction typically occurs in loose, saturated soil deposits subjected to high static shear stresses that exceed the residual strength of the soil.

A typical effective stress path for an element of soil undergoing flow liquefaction is shown in Figure 2.1. The element of soil is initially in static equilibrium at Point (a) under a shear stress equal to the q-coordinate of that point. Upon cyclic loading, the development of positive excess pore pressures causes the effective stress path to move to the left. When it reaches the flow liquefaction surface (Kramer, 1996), at Point (b), the element becomes unstable and begins to strain rapidly as the effective stress path moves to the steady state point (Point (c)). Note that the q-coordinate of Point (c) is less than that of Point (a), indicating that the initial shear stress is greater than the residual strength.

Typical stress-strain behavior corresponding to this case is shown on Figure 2.2. Point (a) indicates the initial condition of static equilibrium, and the $\tau$-coordinate represents the initial static shear stress. Upon cyclic loading, permanent shear strains develop, and the stress-strain path moves to the right. When the strength envelope is encountered, at Point (b), strain softening behavior occurs. The sample of soil strains until static equilibrium is attained at the critical state (Point (c)). Figure 2.2 shows that the amount of strain necessary to reach the flow liquefaction surface may be quite modest, while extremely large strains may develop by the time static equilibrium is regained.

### 2.2.2 **Cyclic Mobility**

Cyclic mobility is much more common than flow liquefaction. Lateral deformations caused by cyclic mobility are often referred to as "lateral spread" deformations. Lateral spread sites – like flow liquefaction sites – are typically loose, saturated deposits. However, the initial shear stresses at lateral spread sites are less than the residual strength of the soil.

A typical effective stress path for an element of soil undergoing cyclic mobility is shown in Figure 2.3. Point (a) indicates the static initial condition. Upon cyclic loading, positive excess pore pressures develop which drives the effective stress path to the right. However, the flow liquefaction surface is never reached. If cyclic loading continues, the effective stress path moves to the left until the strength envelope is reached at Point (b). At this point, the stress path is largely confined to the strength envelope itself. That is, an increase (in absolute value) of shear stress causes dilative behavior, while a decrease (in absolute value) or shear stress causes contractive behavior.

Typical stress-strain behavior of cyclic mobility is shown in Figure 2.4. Point (a) indicates the static initial condition, which reflects an initial shear stress that is less than the critical shear strength of the soil. Upon cyclic loading, permanent shear strains develop, and the path moves to the right. In contrast to the flow liquefaction case, nowhere does the soil element encounter strain softening behavior. At all times, sufficient shear strength exists to resist the cyclic shear stresses.

### 2.2.3 **Residual Strength of Liquefied Soil**

The previous two sections distinguish between flow liquefaction and cyclic mobility with the aid of stress paths and stress-strain diagrams. They also point out that the demarcation between these two possible behaviors is the relationship between the shear stress required for static equilibrium and the residual strength of the soil. The characterization of residual strength has been the focus of much research effort, most of it aimed at developing empirical relations between residual strength and index soil properties. This section contains a description of this body of research.

Seed and Harder (1990) published a correlation between critical strength and SPT blow counts corrected for fines content and overburden. Figure 2.5 reproduces their correlation, which is based on both field and laboratory data. The figure indicates a functional dependency between residual strength and corrected SPT blow counts.

Stark and Mesri (1992) proposed that residual strength is also dependent on initial effective stress. Their empirical relationship:

$$S_r = 0.0055(N_1)_{60-cs}\sigma'_{vo} \qquad (2.1)$$

where: $S_r$ is the residual shear strength of the soil

$(N_1)_{60-cs}$ is the SPT blow count, corrected for fines content and overburden

$\sigma'_{vo}$ is the initial, vertical effective stress

reflects this dependency, and like the correlation of Seed and Harder, was based on available field and laboratory data.

For sands comprised of at least 10% silt, Baziar and Dobry (1995) reported a residual strength correlation based solely on initial vertical effective stress. Their correlation uses much of the same data cited by the previous two studies, along with triaxial test data obtained by the authors:

$$S_r = \alpha\sigma'_{vo} \qquad (2.2)$$

where: $\alpha$ ranges from 0.04 to 0.2

Both the field and laboratory data used to develop residual strength correlations exhibits considerable scatter. As a result, there exists considerable uncertainty in the residual shear strengths that these methods predict. In practice, efforts to apply any of these methods in predictive analyses must be done using careful judgment

## 2.3 CASE HISTORIES

Numerous case histories of liquefaction have been documented for earthquakes of this century. Presentation of an exhaustive compilation of these case studies is beyond the scope of this dissertation. However, this section contains several case histories which illustrate the factors thought to most directly influence liquefaction-induced ground deformation.

Liquefaction-induced lateral spreading gained prominence in civil engineering research as a result of catastrophic failures associated with the 1964 earthquakes of Niigata, Japan (M 7.5) and Anchorage, Alaska (M 8.4). The data collected in the aftermath of these two events continues to be used to gain further understanding into the liquefaction phenomena. The Niigata event was accompanied by widespread lateral spreading that damaged many structures. The Alaska event was marked by several large landslides due to very sensitive clay layers, and multiple structural failures caused by lateral spreading in loose alluvium. Since 1964, other seismic events have provided valuable case studies of liquefaction-induced lateral spreading. A number of cases for which detailed geotechnical information is available are described below.

### 2.3.1 Niigata, Japan

The June 16, 1964 Niigata earthquake caused extensive damage to buildings, bridges, ports, roadways, and other facilities. The epicenter of the quake was located at a depth of about 40 km below the Sea of Japan about 50 km west of Niigata. Large lateral spread deformations were measured in many parts of the city, notably in the vicinity of the Shinano

River. Over the years, considerable reclamation activity had altered the river's course near its mouth. Fill used in the reclamation process consisted of loose, saturated hydraulically-placed silty-sands. As a result of the earthquake, these soils liquefied and spread preferentially in a channel-ward direction. Figure 2.6 shows the magnitude of the channel closure at various points, inferred using photogrammetric techniques. As can be seen, lateral spreading constricted the Shinano River by as much as about 20 meters.

### 2.3.2 **San Fernando, California**

Liquefaction-induced lateral spreads were also a common feature of the 1971 San Fernando earthquake (M 6.5). The hypocenter was located at a depth of about 8 km, approximately 13 km north-northeast of San Fernando. Well-documented lateral spreads occurred along two sites near Upper Van Norman Reservoir, located near San Fernando's western city limits.

At the Jensen Filtration Plant, located about 0.6 km northwest of the reservoir shoreline, significant lateral spreading occurred in loose alluvial soil beneath a fill slope (Figure 2.7(a)). This lateral spreading produced the measured surface deformations are shown in Figure 2.7(b).

Lateral spreading was also observed at the Juvenile Hall and Sylmar Converter Station, situated about 1 km northeast of the reservoir. Cross-sections beneath Juvenile Hall and the Sylmar Converter Station (Figure 2.8(a)) show that both sites sloped gently and were underlain by loose, saturated alluvial soil. Lateral spreading in these soils produced the displacements shown in Figure 2.8(b).

At both sites, the loose, alluvial soil that produced lateral spreading was sloped very slightly towards the reservoir. At the Sylmar Converter Station, the ground surface sloped toward the reservoir at an average angle of about 1 degree, though the slope was locally steeper in the vicinity of a channel near the reservoir. At the Juvenile Hall site, the ground surface was even flatter at about 0.4 degrees. Despite these very flat slopes, lateral spreading produced ground surface displacements of up to about 3 m. In both cases, the deformations progressed in a downhill direction, towards the reservoir basin.

### 2.3.3 **Imperial Valley, California**

The 1979 Imperial Valley earthquake produced liquefaction-induced lateral spreading along a section of Heber Road near the town of Holtville in southern California. Lateral deformations as large as four meters were measured along an irrigation canal which ran parallel to and just south of the road. Subsequent to the earthquake, extensive data was obtained from SPT and CPT soundings. At the point of maximum lateral spreading deformation, the soil profile consisted of about 1 m of loose fill underlain by about 4 m of loose alluvial sand. This sand was in turn underlain by alternating layers of soft silty clay and medium-dense sand to the depth explored. The groundwater table depth varied from about 1.5 m to 2 m. Based on topographic information, the ground surface slopes gently downward from south edge of Heber Road to the depression crest at an inclination of about 0.7 degrees, and over a horizontal distance of about 24 m. The ground surface then steepens to about a 10 degree slope, and leads down to the bottom of the depression about 32 m south of Heber Road. The canal measures roughly 4 m in width, with its centerline located about 14 m south of Heber Road. It is believed that the loose, saturated sand layer extending from a depth of about 1.5 m to 5 m liquefied during the earthquake, and spread laterally towards the 2 m deep natural depression. Lateral spread deformations measured at the Heber Road site are shown in Figure 2.9, and are based on surveyed offsets of the canal and roadway alignments.

The 1987 Imperial Valley earthquake (Superstition Hills; M=6.5) caused lateral spreading at an instrumented site known as the Wildlife site. The Wildlife site is situated adjacent to the Alamo River in the Imperial Valley Wildfowl Management Area, about 31 km from the epicenter of the earthquake. Borehole and CPT data indicates that the site is underlain by about 2.5 m of loose silt followed by 4 m of very loose to loose silty sand and sandy silt. This soil is in turn underlain by 5.5 m of stiff to very stiff clay followed by 5.5 m of medium dense sand. Below the sand are alternating layers of silty sand, sandy silt, and clayey silt to a depth of about 26.5 m. The ground surface is essentially level; the only grade transition occurs at the steep bank of the Alamo River. The groundwater table was located at a depth of about 1 m. The site had been instrumented with six pore pressure transducers and two accelerometers prior to the Superstition Hills tremblor. Borehole and transducer data indicated that the upper 6.5 m of saturated, loose silt and silty sand liquefied during the earthquake. This triggered lateral spread deformations on the order of 0.2 m., as shown in Figure 2.10. It is noteworthy that this case history is unique because excess pore pressure ratios of 100% have not been measured at any other location.

2.3.4 **Noshiro and Akita, Japan**

The 1983 Nihonkai-Chubu earthquake (M 7.7) off the west coast of Japan, produced widespread liquefaction within the cities of Noshiro and Akita, Japan. The earthquake was located at a depth of 15 km about 100 km west-northwest of Noshiro, and about 120 km northwest of Akita.

Within Noshiro, lateral spreads were well-documented at two sites. Maeyama Hill was a sand dune feature which gently rose from the surrounding land at a grade ranging of one to six percent with an elevation gain of about ten meters. The near surface soils consisted primarily of loose, saturated sand. Figure 2.11(a) shows a typical soil profile of the hillside inferred from exploratory soundings. As can be seen, the site may be characterized as having significant zones of loose, saturated granular soils. The estimated areas of liquefied sands is indicated by the gray shading in Figure 2.11(a). Figure 2.11(b) illustrates lateral spread displacements measured at the ground surface along this alignment. Using photogrammetric techniques, lateral spreads on the order of four meters were measured at many locations on the hill. These spreads generally moved in a downhill direction, producing the radial displacement pattern shown in Figure 2.12.

The second Noshiro site was located in the northern portion of the city. Here, the ground slopes very gently downward at a one percent grade in a north-north easterly direction towards the Yonashiro River. A typical sub-surface profile in this area is reproduced in Figure 2.13(a). As in the Maeyama Hill site, the surface is underlain by significant deposits of loose, saturated sand. The zones of suspected liquefaction are shaded gray in this figure. Figure 2.13(b) indicates lateral spread displacements measured along this section. Lateral spread displacements as great as 5m were measured in this part of Noshiro, as indicated by the vector diagram on Figure 2.14.

Within the city of Akita, Japan, most of the liquefaction-induced lateral spreading was confined to near-shore facilities at Akita Harbor. A well-documented case is Gaiko Wharf, an artificial peninsula constructed of hydraulically placed fill. Figure 2.15 shows the general site stratigraphy inferred from borehole data. The subsurface soils consisted of loose hydraulically placed fill sand extending from Elevation +2 down to Elevation -14. These soils are underlain by medium dense to dense sands to the depths explored. The groundwater table is indicated at Elevation +0.3, but probably fluctuates due to tidal changes. It has been estimated that the loose hydraulically-placed sands below the water table liquefied, and spread laterally. Surface displacements up to two meters were measured. The displacements pointed in generally a sea-ward direction, as shown in Figure 2.16.

### 2.3.5 **Dagupan City, Luzon, The Philippines**

Luzon Island experienced a magnitude 7.8 earthquake on July 16, 1990. The event triggered numerous landslides in the mountainous regions of the island, and widespread liquefaction in low-lying areas. In terms of liquefaction, one of the hardest hit regions was the city of Dagupan, located on the Gulf of Langayen about 50 km west of the fault rupture zone. Many of the liquefied areas within Dagupan occurred at sites constructed on loose fill that had been placed over former marsh lands. In particular, sites adjacent to the Pantal River exhibited large lateral spread deformations. Figure 2.17 depicts the stratigraphy inferred from exploratory soundings taken along Perez Boulevard in central Dagupan. The estimated extent of liquefaction is shaded in this figure. The ground surface is essentially level. As can be seen, lateral spread deformations caused an 11 m closure of the Pantal River channel at this location. Large deformations of this magnitude were common throughout Dagupan, as shown in Figure 2.18.

### 2.3.6 **Other Case Histories**

Liquefaction case histories for other earthquakes can be found in the references listed in Table 2.1. These case histories are not discussed further, because detailed geotechnical, seismological, or forensic data is not available.

## 2.4 EXPERIMENTAL STUDIES

Experimental studies on liquefaction flow have been based on either shaking table or centrifuge models. The primary difficulty in replicating field conditions in laboratory model tests is obtaining realistic effective stresses and volume change behavior in the sand. Other experimental difficulties such as scaling effects, boundary effects, and instrumentation error complicate the experimental study of liquefaction phenomena.

### 2.4.1 Shaking Table Studies

Shaking table tests have been conducted on rigid tables measuring up to 6 meters in length. Tests on loose, saturated soil deposits have been instrumented with pore pressure transducers, displacement and settlement transducers, and accelerometers. Additionally, colored markers or tell-tales have been installed in the sand to indicate permanent displacements. Shear stresses have been initiated by inclining the table (with a level sand surface), inclining the sand surface (with a level table), or combinations of both. Both harmonic and random vibrations have been used for the base excitation of shaking tables.

#### 2.4.1.1 Miyajima et al. (1991)

Miyajima et al. (1991) conducted a series of nine shaking table tests to investigate the influence of several parameters on liquefaction-induced lateral displacements. The shaking table measured 1.5 m long and 0.5 m wide. Sixteen targets were placed on a sloping sand layer in order to measure the induced displacements. The sand used in the experiments had the following physical properties: $G_s$=2.67, $C_u$=2.96, $e_{max}$=1.030, $e_{min}$=0.721, $D_{50}$=0.2 mm, and k=1.92e-2 cm/s. A harmonic base acceleration with frequency of 5 Hz was used to induce the liquefaction. A target table acceleration of 120 cm/s$^2$ was attained in about 5 s for each test. The duration of each test was 30 s.

The independent variables included slope angle (2, 4, and 6 %) and sand layer thickness (15, 17, and 19 cm). Dependent variables included average displacement of the ground surface and velocity of ground deformation. A statistical analysis of the measured data suggested that the average displacement of the slope correlated most strongly with the product of soil layer thickness and the ground surface slope. The correlation obtained from the nine tests is illustrated in Figure 2.19.

2.4.1.2 Sasaki et al. (1991)

Sasaki et al. (1991) conducted a series of eight large-scale shaking table tests to investigate the flow behavior of liquefied sands. The test set-ups are illustrated in Figure 2.20, and the geometries summarized below in Table 2.2. Each set-up was instrumented with pore water pressure transducers, accelerometers, displacement meters, and strain gages. In all models, the liquefiable layer consisted of sand with $G_s$=2.66, $e_{max}$=0.98, $e_{min}$=0.60, $D_{max}$=4.8 mm, $D_{50}$=0.27 mm, and $C_u$=1.4.

Each model was subjected to a sinusoidal input motion for a 20 s duration (2 Hz or 40 cycles). After 40 cycles, another series of cycles was applied, but at a higher acceleration amplitude. This process was repeated four times for each model (except for Model No. 8, which was subjected to only three series). The amplitudes ranged from 60 to 190 gals. The deformation profiles for Model No. 2 and Model No. 6, are shown in Figure 2.21 for the Step 2 loading. These profiles show that the majority of the shear strains developed near the interface between the liquefied and non-liquefied layers. For the models with sloped ground surfaces, the maximum displacements occurred near the middle of the slope. This displacement pattern produced tensile strains near the top of the slope, and compressive strains near the bottom of the slope. The lateral displacements stopped as soon as each collection of 40 acceleration cycles was completed.

2.4.2 **Centrifuge Studies**

A tremendous amount of interest and resources have been recently devoted to centrifuge studies of geotechnical engineering problems. Examples of the various types of problems which have been modeled may be found in Taylor, 1995.

2.4.2.1 The VELACS Project

The VELACS (for VErification of Liquefaction Analysis by Centrifuge Studies) study was conducted by a multi-institutional, multi-national collaboration of researchers to test the validity of the various liquefaction analysis schemes which have been formulated over the past 30 years (Arulanandan and Scott, (1994)). Nine different model geometries shown in Figure 2.22 were tested in the program. Models 1, 3, 4a, and 4b represented level ground liquefaction cases. Model 2, with its sloped surface, represented a free-field case of lateral spreading. More complex prototype geometries were also tested. These were represented by an embankment (Models 6 and 7), a rigid retaining wall (Model 11), and a soil-structure interaction problem (Model 12).

Because Model 2 so closely resembles free-field liquefaction cases, it will be described in further detail here, and used for subsequent analyses as described in Chapter 7. A schematic of Model 2 is shown in Figure 2.23. The sample was placed in a box having laminar plate side walls to allow the sample to freely deform in a shearing motion. The sample was instrumented with 8 accelerometers, 6 LVDT's, and 8 pore pressure transducers. The shear box was inclined at an angle of 2 deg as shown. In order to account for experimental scatter, identical samples were tested at three different centrifuges: Rensselaer Polytechnic Institute, California Institute of Technology, and University of California at Davis.

In order to obtain the correct effective stresses in the 10 m high prototype, the 20 cm high model was rotated at a sufficient angular velocity to induce a 50 g radial acceleration. Earthquake excitation was then applied to the base of the model. Figure 2.24 shows the target and recorded acceleration traces for Model 2. Of the horizontal acceleration records, it appears as though the Cal Tech and UC Davis centrifuges most closely matched the target. The target vertical acceleration record was not achieved in any of the centrifuges however.

Excess pore pressure time histories for transducer P5 are shown in Figure 2.25. There appears to be excellent agreement between the RPI and Cal Tech traces. Vertical deformations measured at LVDT1 are shown in Figure 2.26. Although somewhat inconsistent with data presented in Figure 2.24 and Figure 2.25, the Cal tech and UC Davis data shows the closest agreement, while the RPI displacement was less than impressive. Finally, lateral displacements measured by LVDT3 are shown in Figure 2.27. Although the

UC Davis centrifuge did not record this displacement record, the RPI and Cal Tech traces match very closely.

## 2.5 ANALYTICAL STUDIES

Information gathered after earthquakes has enabled engineers and earth scientists to postulate the mechanics of liquefaction-induced ground deformations. The ultimate goal of such studies is to predict the magnitude of such deformations at a given site before an earthquake occurs. Analytical studies performed thus far have been based on one of five methods: empirical, Newmark sliding block, variational, finite element, and finite difference. These are described more fully in the sections that follow.

### 2.5.1 Empirical Methods

Since many factors affect the susceptibility of an actual site to liquefaction-induced movements, it is difficult to analytically describe the deformations from purely a mechanics perspective. Therefore, some researchers have proposed empirical predictive methods based on actual field performance data.

#### 2.5.1.1 Youd and Perkins (1987)

Youd and Perkins (1987) presented an empirical model to predict the magnitude of liquefaction-induced lateral spreads in the western United States. They defined the Liquefaction Severity Index (LSI) as the maximum magnitude of lateral displacement in inches. To construct the model, the authors gathered lateral spread data from the West Coast earthquakes listed in Table 2.3.

The field performance data was used to develop a plot of LSI versus epicentral distance and moment magnitude, which is reproduced as Figure 2.28. Note that in this figure, the authors cut off the maximum LSI at 100 in. This was an arbitrary threshold chosen to represent an upper bound of 'acceptable' design displacements. Based on a best-fit of the data, the authors proposed the following LSI model:

$$\log(LSI) = -3.49 - 1.86 \log(R) + 0.98\, M_w \qquad (2.3)$$

where: LSI is the liquefaction severity index (in)

R is the epicentral distance (km)

$M_w$ is the earthquake moment magnitude

As a final step, the authors then coupled the LSI model with previously developed attenuation and recurrence relationships to derive LSI probability maps of Southern California.

2.5.1.2 Bartlett and Youd (1992)

As an improvement, Bartlett and Youd (1992) extended the LSI methodology to encompass a much broader array of independent variables and to use data from a larger number of earthquake sites. To this end, the authors performed a multiple linear regression (MLR) analyses using a total of 33 seismological, topographical, geological, and geotechnical variables. The statistical significance of each variable was analyzed. In the MLR method, the correlation of each independent variable to the dependent variable (in this case displacement) was evaluated. Only those variables which improved the correlation were 'retained' for the final empirical equation. The others were eliminated as being statistically insignificant relative to the retained independent variables. The independent variables investigated for the study are summarized in Table 2.4.

Data compiled from eight earthquakes in Japan and the Western United States was used in the MLR analysis. Table 2.5 lists the earthquakes and lateral spread sites which the authors used in the study.

As a result of the MLR procedure, the authors narrowed the list of 33 independent variables to seven. These included earthquake magnitude (M), epicentral distance (R), free face height (W=100*h/L, where h is the free face height and L is the length of the slope), ground slope (S), thickness of sand with N<15 ($T_{15}$), average fines content of sands with N<15 ($F_{15}$), and average grain size of sands with N<15 ($D_{5015}$). Two equations were developed by the authors - one for the case of a level ground with a free face (i.e. near a river channel), and one for an infinite, sloping ground surface. The equations are reproduced below, wherein the variables used are as described previously and $D_h$ is the ultimate displacement in meters.

For the free face case:

$$\log(D_h + 0.01) = -16.366 + 1.178*M - 0.927*\log(R) - 0.013*R + 0.657*\log(W) + 0.348*\log(T_{15}) + 4.527*\log(100\text{-}F_{15}) - 0.922*D_{5015} \quad (2.4)$$

For the infinite slope case:

$$\log(D_h + 0.01) = -15.787 + 1.178*M - 0.927*\log(R) - 0.013*R + 0.429*\log(S) + 0.348*\log(T_{15}) + 4.527*\log(100\text{-}F_{15}) - 0.922*D_{5015} \quad (2.5)$$

In the application of the MLR model, the following limits on the independent variables were placed by the authors:

| | |
|---|---|
| Moment magnitude: | $6.0 < M < 8.0$ |
| Free face ratio (%): | $1.0 < W < 20.0$ |
| Ground slope (%): | $0.1 < S < 6.0$ |
| Thickness of sands with $(N1)_{60} < 15$ (m): | $0.3 < T_{15} < 15$ |
| Average effective grain size in $T_{15}$ (mm): | $0.1 < D_{5015} < 1.0$ |

The authors added that the model yielded unrealistically high values of predicted displacement for very low R distances. As a result, the authors recommended use of the minimum epicentral distance or distance to the rupture zone, given in Table 2.6.

A comparison of measured displacements versus displacements predicted using the proposed equations is presented in Figure 2.29. The points were derived from earthquake data used in the regression analysis (Japanese and western US earthquakes), as well as earthquake data used by Ambraseys (1988) for a study of liquefaction potential as a function of moment magnitude and epicentral distance.

It can be seen that most of the data is bounded by the two dashed lines. The upper dashed line represents an underestimation of the actual displacement by 50 percent, while the lower dashed line represents an overestimation of the actual displacement by 100 percent. The authors attributed the poor prediction of the South of Market and Mission Creek data to boundary conditions at these two sites which impeded the flow. Close examination of Figure 2.29 indicates that this method may tend to under-predict the actual surface displacements.

### 2.5.2 Newmark Sliding Block Method

Newmark (1965) presented a simplified method to predict slope movements induced by earthquakes. Newmark's analysis replaced the classical slope failure mass shown in Figure 2.30(a) by an analogous inclined sliding block shown in Figure 2.30(b). The block was assumed to be of infinite length, constant thickness, and uniform density. The shear strength of the block-slope interface was also assumed to be constant. Newmark then assumed that the block could be subjected to a base acceleration which varied sinusoidally with time.

Newmark reasoned that block movement could only occur if the factor of safety against sliding reached unity. Based on equilibrium considerations of a block at incipient movement, an expression for the yield acceleration was derived:

$$a_y = \tan(\phi - \beta) \qquad (2.6)$$

where $a_y$ is the minimum horizontal base acceleration to cause movement of the block, $\phi$ is the friction angle at the block-slope interface, and $\beta$ is the slope angle.

Theoretically, the block could slide upslope or downslope depending on the magnitude and sign of the base acceleration. For example, if the mass of the block multiplied by the component of acceleration parallel to the slope and in the downhill direction was greater than the shear strength along this interface less the component of the block weight parallel to the slope, than the block would accelerate downslope. This reasoning was applied to the entire base acceleration time record, which resulted in a record of block acceleration versus time. This was then integrated twice with respect to time to obtain the desired slope displacement.

2.5.2.1 Dobry and Baziar (1991)

Dobry and Baziar (1991) extended Newmark's methodology to liquefied soils. The yield acceleration which would cause downslope movement was described using the following equation:

$$a_y = (S^*A - F)/m \qquad (2.7)$$

where: $a_y$ is the yield acceleration

S is the shear strength along the failure interface

A is the contact area of the block with the interface

F is the component of the block weight parallel to the interface

m is the mass of the block

The equation for upslope movement was similar, except that the resisting force, S*A and the body force component, F had the same sign.

By assuming the shear strength is equal to the normal stress multiplied by the tangent of the friction angle, and the ground acceleration is parallel to the slope, the authors presented the following expression for the yield acceleration (parallel to the slope):

$$a_y = (\sigma'_v / \sigma_v)[\cos(\alpha)\tan(\phi) - \sin(\alpha)] \qquad (2.8)$$

where: $a_y$ is the yield acceleration

$\sigma'_v$ is the vertical effective stress on the failure plane

$\sigma_v$ is the total vertical stress on the failure plane

$\alpha$ is the inclination of the slope

$\phi$ is the friction angle of the soil along the failure plane (-)

The analogous equation for upslope movement was similar, except that the $\sin(\alpha)$ term had a positive sign.

In order to apply the method, an appropriate value for the soil shear strength was needed. The authors assumed that liquefied soil behaves in a perfectly plastic manner, which implies a constant shear strength. The difficulty arose in trying to measure a large strain value of S, either in the laboratory or in the field. The authors used the Remolded

Discontinuously Wet Pluvial Soil Sample (RDWPSS) preparation method originally used by Vasquez-Herrera and Dobry (1989). In the RDWPSS method, a 2.0 in diameter sample was prepared by carefully depositing the soil sample into the mold through water in one to four separate lifts. Thirty minutes were allowed to transpire between each lift to allow for the majority of the soil to settle out of suspension. The water level was adjusted during preparation to maintain about 0.5 in of head above each lift. Samples so prepared were very loose, with an average void ratio of 1.4.

Several cyclic triaxial, anisotropically consolidated, undrained (CyT-CAU) and isotropically consolidated undrained (CIU) shear tests were conducted on RDWPSS samples. The CIU results, shown below in Figure 2.31, suggested that the shear strength could be related to the effective consolidation stress by the following relationship:

$$S_{us} = 0.12\, \sigma_{1c} \qquad (2.9)$$

where $S_{us}$ is the undrained steady-state shear strength and $\sigma_{1c}$ is the effective consolidation stress. Based on this, the authors interpreted $\sigma_{1c}$ in the laboratory to be equivalent to the effective overburden stress in the field, $\sigma'_v$.

To test the validity of the sliding block methodology, the authors analyzed the Wildlife site in California which experienced liquefaction-induced lateral deformations during the 1987 Superstition Hill earthquake. The simplified soil profile used in the analysis is shown in Figure 2.32. Blow count and pore pressure data taken near the location of the observed ground cracks suggested that liquefaction of the soil between depths of about 1.5 and 3.5 m caused the lateral spreading. An acceleration time history taken from a nearby recording station was used for the sliding block analysis. Two trial sliding blocks, one of which was shallower than the other, were chosen by the authors to bracket the possible failure planes. As shown in Figure 2.33, an ultimate displacement of 40.5 cm was calculated for the deep assumed failure surface. For the shallow assumed failure surface, an ultimate displacement of 0.21 cm was calculated. The actual ultimate displacement of the slope was 18 cm. The authors concluded that the fact that the trial failure planes bracketed the 'true' displacement supported the sliding block analogy, but noted that the magnitude of the predicted deformation was very sensitive to the choice of failure plane.

The authors then compared the sliding block method with the empirical liquefaction severity index (LSI) method developed by Youd and Perkins (1987). For their comparison, the authors analyzed the hypothetical slope shown below in Figure 2.34. Twenty acceleration records from seven earthquakes were used for the sliding block analyses. Moment magnitudes for the records ranged from 5.3 to 7.4, while epicentral distances ranged from 7 to 107 km. A comparison of predicted displacements obtained by the two methods is presented in Figure 2.35. This curve indicates that the two methods agree within an order of magnitude.

2.5.2.2 Baziar et al. (1992)

In order to extend the preceding analysis, Baziar, Dobry, and Elgamal (1992) modified the infinite sliding block to include end effects. To do this, the analytical model was modified to allow for the existence of an active or passive wedge at the uphill face. Similarly, the downhill face could be modeled as having an active, passive, or free-face boundary condition. Free-body diagrams of the sliding block and wedge(s) are shown in Figure 2.36 and Figure 2.37. Figure 2.36 shows the force system for the case of a free downhill face, with a downhill block movement. Figure 2.37 shows the force system for the case of a soil wedge at both the uphill and downhill faces, again with a downhill block movement. Uphill movements would result in similar force systems, except that the direction of the shear forces would reverse.

Through equilibrium consideration of the free body diagrams shown in Figure 2.36 and Figure 2.37, the authors obtained relationships for uphill and downhill yield accelerations as a function of active or passive wedge geometry. The effect of the active wedge is to reduce the yield acceleration, while the passive wedge has the opposite effect. In all cases, the effects of end conditions diminish rapidly as the ratio of slope length to depth increases (i.e. approaches an infinite slope condition). The four combinations investigated are listed in Table 2.7, and make reference to Figure 2.38 through Figure 2.41. Note that these figures are all based on a slope inclination of 2.86 deg, $S_{us} / \sigma_{1c} = 0.145$, and a ratio of buoyant to saturated unit weight of 0.5. These figures show the dependency of yield acceleration on wedge angle and block aspect ratio.

The authors then applied the yield acceleration concept to the case of harmonic loading. They showed that the cumulative displacement of a sliding block subjected to sinusoidal loading may be expressed as:

$$d = N^* a_p^* T^{2*}(1/2\,\pi)^* f(a_y/a_p) \tag{2.10}$$

where: N is the number of loading cycles

$a_p$ is the peak acceleration of the record

$a_y$ is the yield acceleration of the record

T is the period of harmonic loading

$f(a_y/a_p)$ is a shape function given by Figure 2.42

The model was then used to predict displacements from actual earthquake records. The idealized cross section shown in Figure 2.43 was analyzed using fifty eight acceleration records from nine different earthquakes. The earthquakes, all of which occurred in the western United States, are summarized in Table 2.8.

A typical result of the sliding block analysis is shown in Figure 2.44 for the 1979 Imperial Valley data. The corresponding LSI curve using the method of Youd and Perkins (1987) is also shown. In general, the trend of decreasing lateral displacement with increasing epicentral distance was preserved.

The authors then sought to extend the analysis by incorporating the results contained in Equation (2.9) and Figure 2.42. That is, they desired to develop a closed form expression, consistent with the sliding block analysis, which would eliminate the need of having to conduct a lengthy numerical integration to obtain the predicted displacement. To this end, the preceding equation was modified to yield:

$$d = N^*(v_{max}^2 / a_{max})^* f(a_y/a_{max}) \tag{2.11}$$

where: N is the equivalent number of cycles of harmonic loading

$v_{max}$ is the maximum site velocity

$a_{max}$ is the maximum site acceleration

$a_y$ is the yield site acceleration given by Equation (2.7)

$f(a_y/a_{max})$ is the shape function given by Figure 2.42

To obtain N, the authors incorporated the attenuation relationships proposed by Joyner and Boore (1982). The proposed attenuation relationships for earthquakes with 5.0 < Mw < 7.7 are:

$$\log(a_{max}) = 0.49 + 0.23*(M_w - 6) - \log(r1) - 0.0027*r1 \qquad (2.12)$$

$$\log(v_{max}) = 2.17 + 0.49*(M_w - 6) - \log(r2) - 0.0026*r2 + 0.17 \qquad (2.13)$$

where: $a_{max}$ is the maximum horizontal acceleration for both soil and rock sites (g)

$v_{max}$ is the maximum horizontal velocity (cm/s)

$r1 = (R^2 + 64)^{1/2}$ (km) and is valid for both soil and rock sites

$r2 = (R^2 + 16)^{1/2}$ (km) and is valid for soil sites only

R is the closest distance from the site to the vertical projection of the fault rupture on the earth surface (km)

$M_w$ is the moment magnitude of the earthquake.

Rearranging Equation (2.10), values of N were computed using displacements obtained from the sliding block analyses along with the Joyner and Boore data for 54 of the 58 earthquakes referenced in Table 2.8. The result of this exercise is presented in Figure 2.45 which shows the relationship between N and epicentral distance. Based on this, the authors concluded that there was no apparent trend of N with respect to epicentral distance, and therefore chose N to be equal to the arithmetic mean of the data, or 2.

Equation (2.10) was then used to develop lateral displacement curves as a function of epicentral distance, and earthquake magnitude. The authors chose a value of yield acceleration of 0.0477 g, corresponding to a slope angle of 2.86 degrees, , $S_{us} / \sigma_{1c} = 0.145$, and a horizontal water table (i.e. the same conditions used for the analysis in Figure 2.43). The resulting curves are shown in Figure 2.46, along with data from five earthquakes. For the data shown, the sliding block method appears to predict the actual displacements on a fairly consistent basis.

As a final comparison, the authors superimposed curves derived from the sliding block method onto the LSI curves proposed by Youd and Perkins. These are shown in Figure 2.47 The general trend of decreasing displacement with increasing source distance is preserved in both methods. However, the sliding block method predicts lower displacements at very low source distances than the Youd and Perkins' model.

### 2.5.3 **Variational Method**

Several analytical studies of liquefaction behavior have been based on the variational method. In this approach, an expression for the total energy of the flow regime is derived on the basis of an unknown displacement field. The energy is then minimized to determine the physically-correct displacement field. In practice, approximate methods such as the Rayleigh-Ritz or Galerkin procedures are employed to obtain a weak solution to the variational formulation. The computational burden is less for the variational method than for the finite element method, discussed in Section 2.5.4, because the former typically employs fewer equations. However, at this point, only very simple geometries and flow fields have been modeled with the variational method.

#### 2.5.3.1 Towhata et al. (1991)

Towhata et al. (1991) presented a two-dimensional variational analysis that formulated the energy of the soil stratum in a particular plane. The basic problem geometry considered is shown in Figure 2.48. Observations made in Noshiro, Japan after the 1983 Nihonkai-Chubu earthquake, along with results of two large-scale (model length = 6 m) and two small-scale (model length = 1 m) shaker table tests were used to make simplifying assumptions regarding the flow regime.

The total energy expression included contributions from four sources: 1) the strain energy due to axial deformation of a surface, non-liquefiable soil layer, 2) the potential energy due to a change in elevation of surcharge loading, 3) the potential energy due to a change in elevation of the liquefiable soil layer, and 4) the strain energy due to shear deformation of the liquefiable soil layer. The displacements in the x-z plane were assumed to consist of a function, F(x) which represented the unknown displacement at the top of the liquefied layer, and a function, G(z), which described the variation of this displacement with depth. A half-sinusoidal shape function was chosen to describe G(z). The total energy was integrated over the soil profile to yield a functional depending on F, dF/dx, and x. The variational problem therefore, involved finding the function, F, that minimized the total energy functional. The resulting equation for the displacement field was independent of time, and thus represented the ultimate displacement that the stratum would undergo.

Three sites that experienced lateral spreading deformations during past earthquakes were analyzed with the variational model. These included the Maeyama Hill site (during the 1983 Noshiro City earthquake), the Kasukabe site (during the 1923 Kanto earthquake), and the Oogata site (during the 1964 Niigata earthquake). Cross-sections for the three sites, along with the observed and calculated displacements, are shown in Figure 2.49 through Figure 2.51. In all three cases, the location and magnitude of the maximum calculated displacement agrees well with those observed in the field. However, the calculated displacements were generally greater than those actually observed at locations away from the maxima.

2.5.3.2 Towhata and Matsumoto (1992)

In a refinement of the previous methodology, Towhata and Matsumoto (1992) incorporated time dependency to the steady state solution by assuming that the horizontal and vertical displacements at any time could be expressed as a fraction of the ultimate displacements calculated above. In equation form:

$$u(x,z,t) = \lambda(t)\, U(x,z) \qquad (2.14)$$

$$w(x,z,t) = \lambda(t)\, W(x,z) \qquad (2.15)$$

where $\lambda(t)$ represents the aforementioned fraction and varies from 0 at $t=0$ to 1 at $t=\infty$. A Lagrangian equation of motion was then formulated which incorporated the time dependency of the kinetic and potential energies on $\lambda(t)$, in addition to a time-varying (sinusoidal) applied force. The equation of motion yielded a second order ordinary differential equation which could be solved explicitly for $\lambda(t)$. It was found however, that the predicted displacements developed much more rapidly than the observed shaking table displacements. Additionally, the predicted displacements oscillated about the ultimate, actual displacement.

To more closely mimic the observed rate of displacement and to eliminate the oscillatory numerical behavior, the authors developed energy dissipation terms through two mechanisms: viscosity and dilatant flow. The viscosity model was developed by assuming that the damping shear stress was proportional to the time rate of change of shear strain. In this formulation, the constant of proportionality is the viscosity of the liquefied sand. The rate of energy loss due to this type of damping was then obtained by multiplying the damping stress by the shear strain rate, and integrating the result over the volume of the liquefied soil mass. The second dissipative model was the dilatant flow model. Details of the dilatant flow model were not presented, but appears to be based on observations of shaking table data whereby the plot of base acceleration versus lateral displacement of the surface layer yielded a kind of hysteretic loop. For an undamped, linear single degree of freedom system, the acceleration is proportional to the displacement, where the constant of proportionality is equal to the negative of the squared natural frequency. It appears that the experimental departure from the s.d.o.f. relationship is attributed to damping due to dilatent behavior of the sand. The authors stated:

> "...a repeated loading and unloading is necessary, however small its magnitude may be, in order to keep the ground moving laterally. In other words, the ground can continue its flow as long as minor shaking is occurring with a low level of amplitude."

A small shaking table test was conducted in order to investigate the accuracy of the two dissipation models. A cross sectional view of the test set-up is shown in Figure 2.52. Observed and predicted results of $\lambda(t)$ are shown for the viscous and dilatent models in Figure 2.53 and Figure 2.54, respectively. As can be seen, the viscous model gave a fairly good curve fit for a critical damping ratio of 10%. However, the apparent viscosity of sand back-calculated with that value was 886 Pa-s, which was noted to be an order of magnitude greater than that of clover honey. The dilatant flow model also captured the time rate of displacement fairly well.

As a final check, the authors analyzed a hypothetical one percent slope of length 400 m in order to see if the model was sensitive to scaling. The results of the viscous model analysis is shown in Figure 2.55. The curve for a damping ratio of 10% is indicated by the solid line. It was found that the equivalent fluid viscosity was back-calculated to be 82.8 kPa-s, which is an order of magnitude less than that obtained for the shaker table model with the same damping ratio. The results of the dilatant flow analysis is shown below in Figure 2.56. The ultimate displacement was calculated to occur after approximately 3000 s had elapsed. The authors conceded that this is an unrealistically large period of time for ground shaking. The results from the hypothetical slope indicates that the analytical model is sensitive to scaling.

### 2.5.4 **Finite Element Method**

The finite element method has seen remarkable use in many problems of applied mechanics (see for example, Cook, 1981). Indeed, most analytical studies of free-field lateral spreading have been based on the finite element method. This method lends itself well to the free-field case of liquefaction flow. This is because the discretization can be varied to model different topographic and stratigraphic features, and constitutive relations can be incorporated which account for porewater pressure build-up and strain softening which occur during liquefaction. Some models have incorporated geometrically non-linear elements which allow for the large strains which have been documented in case histories of liquefaction flow failure.

#### 2.5.4.1 Zienkiewicz, et al., 1978

Zienkiewicz, et al. (1978) described one of the earliest attempts to apply the finite element method to the liquefaction problem. The authors formulated a time domain, effective stress analysis scheme which incorporated the Lagrangian strain tensor and an elasto-plastic non-associative constitutive law. The resulting expressions were then discretized using the finite element method. Several hypothetical models were constructed and subjected to both harmonic and random loading. The results of the numerical analyses indicate that the procedure was able to detect the onset of liquefaction within the discretized domain. However, the authors conceded that reasonable post-liquefaction deformations could not be computed with the relatively simple constitutive model used.

2.5.4.2 Zienkiewicz and Shiomi, (1984)

Zienkiewicz and Shiomi, 1984 were the first to implement the Biot theory (Biot, 1956, 1956a, 1956b) into a finite element formulation. The Biot theory appropriately considers the mechanical coupling between the soil skeleton and a pore fluid. The authors developed finite element schemes in which soil skeleton deformations, pore fluid deformations, and/or pore fluid pressure were cast as the unknown field variables. The formulations considered both compressible and incompressible pore fluid. Numerical results were presented for two simple hypothetical examples. These included a one-dimensional consolidation problem, and a dynamic two-dimensional soil-structure interaction problem. Unfortunately, the latter example did not illustrate the usefulness of the algorithms to predict post-liquefaction deformations.

2.5.4.3 Shiomi et al., (1987)

A two-dimensional finite element (horizontal and vertical dimensions) that incorporated two-phase governing equilibrium equations was proposed by Shiomi et al. (1987). The two-phase formulation accounted for both soil stress and porewater pressure during dynamic loading. A reflecting surface model was chosen as the constitutive relationship. This model allowed for strain hardening or softening during loading and unloading cycles. A small shaking table test was conducted to test the accuracy of the finite element formulation. The test set-up and accompanying finite element mesh is shown in Figure 2.57. The tests showed that excess porewater pressure dissipated more rapidly in the shaking table model than predicted by the finite element model, although the maximum value of excess porewater pressure for both models was in close agreement. Additionally, the settlements predicted by the FEM were about half those measured from the shaking table test. A second FEM with a refined mesh was then analyzed. The resulting displacements were within 10% of those measured experimentally.

2.5.4.4 Finn (1991)

Finn (1991) developed a two-dimensional finite element code, TARA-3FL to account for both material and geometric nonlinearities. The program was used to model the response of two sites with soils that were susceptible to liquefaction. The first was Sardis Dam in Mississippi, operated by the US Army Corps of Engineers, which was being considered for remedial design in the event of an upstream liquefaction-induced slope failure (similar to that which occurred in the Lower San Fernando Dam in 1971). The second site was located within the city of Niigata, Japan, portions of which experienced severe lateral spreading in the 1964 Niigata earthquake. Lateral displacements measured using photogrammetric methods were compared with those predicted by TARA-3FL. Although the measured and computed ground surface displacements were in general agreement, it is not known how accurately the model replicated the displacements at depth.

2.5.4.5 Famiglietti and Prevost (1991)

Famiglietti and Prevost (1991) developed a two dimensional finite element that incorporated finite strain and elasto-plastic material capabilities. Additionally, contact between elasto-plastic and rigid elements was modeled using Coulomb friction with various friction angles. Although the time rate of deformation was modeled, porewater pressure generation and dissipation was not. The model was used to predict the slump of fresh concrete as a function of time and base friction. The model mesh and deformed geometry is shown in Figure 2.58 for the axi-symmetric problem. Numerical results were compared with analytical results developed by others, and are shown in Figure 2.59. The capabilities of this element offer promise for prediction of potentially large deformations caused by liquefaction.

2.5.4.6 Orense and Towhata (1991)

Orense and Towhata (1991) proposed a three dimensional finite element to model liquefaction-induced flow. The element formulation used an elastic-perfectly plastic constitutive relation. A representative mesh and individual element are shown in Figure 2.60. Each element was comprised of a non-liquefied base overlain by a liquefiable layer. The liquefied layer was then overlain with a second non-liquefied layer and finally a surcharge load. A sinusoidal distribution was assumed for the lateral displacement as a function of depth in the liquefied layer. Neither porewater pressure generation and dissipation nor volume changes due to consolidation were accounted for in the formulation. The resulting finite element reduced the three-dimensional problem to one of two dimensions (x and y). The finite element was used to model a region of Noshiro City which sustained extensive liquefaction-induced lateral deformations as a result of the 1983 Nihonkai-Chubu earthquake. The finite element mesh and resulting vector displacement plot is shown in Figure 2.61. The model overestimated the maximum measured displacement by 28 percent. The finite element code was also used to model two shaker table tests conducted by Sasaki et al. (1991), which are described more fully in Section 2.2.3. A view of one of the models, along with a comparison of the displacements are shown in Figure 2.62. For the shaker table tests, the FEM overestimated the maximum value of lateral displacement from 7 to 19 percent.

2.5.4.7 Gu, et al., (1994)

A post-earthquake analysis of the Wildlife site was presented by Gu, et al (1994). The authors developed a two-dimensional finite element model in an attempt to recreate the response of the Wildlife site during the 1987 Superstition Hills earthquake. The analysis was conducted in three stages. During earthquake shaking, the liquefiable soils were modeled using a non-linear constitutive law based on the collapse surface concept of Sladen, et al. (1985). During this time, the reduction in effective stress was tracked until the collapse surface was reached. After a particular soil element reached the collapse surface, the authors employed a simplified undrained boundary surface model (Gu et al., 1992) to track the redistribution of stresses within the liquefied soil. Finally, a drained analysis was conducted using the Biot theory to compute the reconsolidated displacements. A comparison between measured and computed horizontal displacements is presented in Figure 2.63. Figure 2.64 depicts yield ratio contours in the soil after undrained stress distribution, and compares these with the locations of observed sand boils. The yield ratio is defined as the ratio of shear stress to available shear strength bounded by the collapse surface. Although the general trend of the computed data presented in Figure 2.63 and Figure 2.64 agrees with observed data, the model severely overestimates observed displacements near the bank of the river.

## 2.6 LIMITATIONS OF PREVIOUS RESEARCH

Previous research has gone far toward improving the geotechnical earthquake engineering profession's understanding of liquefaction and liquefaction-induced soil movements. The state of knowledge however, remains limited in several important respects. These incomplete areas of knowledge are central to the issue of the effects of liquefaction on pile foundations.

The LSI method developed by Youd and Perkins (1987) represents one of the first attempts to evaluate liquefaction effects in terms of displacements. Although very simple to apply in practice, its usefulness for general liquefaction analysis is limited. First the 100 in cutoff does not allow predictions of very large movements. Second, the model is based on data derived from only seven western United States earthquakes, so its applicability to regions with differing seismicity is questionable. Finally, because the significance of local geological, topographical, and geotechnical factors is not accounted for, the LSI model only considers two independent variables (moment magnitude and distance to source).

The multiple linear regression analysis proposed by Bartlett and Youd (1992) represents an improvement over the LSI method of Youd and Perkins (1987) in that a much broader array of independent variables and earthquakes were considered. However, the restrictions placed on the minimum epicentral distance (Table 2.6) limit the method's usefulness in many practical applications.

The sliding block method developed by Dobry and Baziar (1991) and later improved by Baziar, et al. (1992), marks an improvement over the LSI method of Youd and Perkins (1987) because the possibility for displacements in excess of 100 in is allowed. However, in the development of the method, it would have been more rational to conduct a regression analysis to develop a separate attenuation expression for ($v_{max}^2$ / $a_{max}$). This probably would result with a better correlation than having to rely on the two Joyner and Boore equations (one for $v_{max}$ and one for $a_{max}$) to compute the needed ratio.

The most important limitation common to all of the methods discussed above is that they provide no information about the variation of lateral spread displacements with respect to both depth and time. A spatial and temporal knowledge of the displacement profile is crucial for evaluation of the effects of liquefaction on pile foundations. However, these methods do allow 'ball-park' estimation of surficial displacements that are calibrated by observations of actual field performance.

The variational method by Towhata and Matsumoto (1992) may be used to obtain the displacement profile with depth. The variational method appears to hold promise in that relatively simple expressions are obtained which capture the temporal and spatial dependency on lateral spread displacements. However, the current limitations of simple geometry and sensitivity to scaling will need to be overcome before these methods can be applied to practical problems. Additionally, the methods are based on an assumed displacement field which may or may not accurately represent the true displacement field.

At first glance, two- and three- dimensional finite element codes seem to overcome the shortcomings of the methods described previously. However, multi-dimensional, non-linear time-domain analyses heavily tax the speed and storage capabilities of typical computers available today. Additionally, significant time is often required of practitioners to define a finite element mesh, develop input data, check the model, and review the output. Although pre- and post- processors are available to accomplish this on most commercially-available finite element codes, programs written for research studies often do not include this helpful software. Therefore, the usefulness of such codes to the practitioner may be greatly compromised. The main shortcoming of multi-dimensional, non-linear finite element codes is that the number of material constants needed to characterize their multi-dimensional constitutive laws is beyond the current ability of engineers to reliably determine these either from field or laboratory tests.

Shaking table tests provide some insight into the effect of varying the slope or thickness of a liquefiable layer on ultimate displacements in a laboratory setting. However, extrapolation of results to actual sites is difficult. Actual sites have irregular stratigraphies, varying gradations, and are subjected to random - not harmonic - earthquake vibrations. Since displacements are strongly linked to the rate of porewater dissipation (i.e. permeability), the clean sands tested in these laboratory environments fall short of the real world conditions. The biggest shortcoming of shaking tables is in their inability to correctly recreate the effective stresses in the field.

The centrifuge environment solves many of the inherent shortcomings of shaking table tests by correctly scaling the effective stresses in the model. For liquefaction problems, this is a huge benefit. The VELACS project represents the most sophisticated and comprehensive experimental effort to date with regard to lateral spread deformations. The VELACS case presented in Chapter 2 serves to illustrate that repeatable results are possible in centrifuge studies, and may prove invaluable for the purpose of testing analytical methods. However, it is important to recognize that unanticipated secondary effects - such as the high vertical accelerations - will probably cause the model response to deviate from the prototype response.

In summary, the state of knowledge regarding liquefaction effects on pile foundations would be greatly improved by the development of procedures that are capable of determining the variation of free-field soil displacements at and beneath the ground surface both during and after strong earthquake shaking.

Table 2.1 Other Notable Lateral Spread Case Histories

| Earthquake, Year | Reference |
|---|---|
| San Francisco, California, 1906 | O'Rourke et al. (1992) |
| Kanto, Japan, 1923 | Hamada et al. (1992) |
| Fukui, Japan, 1948 | Hamada et al. (1992) |
| Armenia, 1988 | Yegian, et al. (1994) |
| Loma Prieta, California, 1989 | O'Rourke et al. (1992) |
| Kobe, Japan, 1995 | SEAW (1995) |

Table 2.2 Shaking Table Test Geometries (after Sasaki (1991))

| Model No. | Surface Slope (%) | Base Slope (%) | Liquefied Layer Thickness (cm) | Model Length (cm) | Model Width (cm) | Liquefied Layer Unit Weight ($tf/m^3$) | Surface Layer Unit Weight ($tf/m^3$) |
|---|---|---|---|---|---|---|---|
| 1 | 5 | 0 | 70 | 600 | 80 | 1.93 | 1.49 |
| 2 | 7.5 | 0 | 35 | 600 | 80 | 1.88 | 1.37 |
| 3 | 5 | 5 | 5 to 35 | 600 | 80 | 1.93 | 1.57 |
| 4 | 5 | 0 | 35 | 600 | 80 | 1.90 | 1.49 |
| 5 | 2.5 | 0 | 35 | 600 | 80 | 2.06 | 5.71 |
| 6 | 0 to 5 | 0 | 35 | 600 | 80 | 2.00 | 1.48 |
| 7 | 0 | 5 | 35 to 65 | 600 | 80 | 1.93 | (-) |
| 8 | 15 | 0 | 25 | 400 | 200 | 1.84 | 1.36 |

Table 2.3 Earthquake Data Used for the LSI Model (after Youd and Perkins (1987))

| Year | Earthquake | Magnitude, $M_w$ | Number of Sites |
|---|---|---|---|
| 1964 | Alaska | 9.2 | 10 |
| 1983 | Idaho | 6.9 | 2 |
| 1979 | Imperial Valley, CA | 6.5 | 3 |
| 1973 | Point Mugu, CA | 5.75 | 2 |
| 1981 | Westmoreland, CA | 5.6 | 2 |
| 1978 | Santa Barbara, CA | 5.2 | 1 |
| 1906 | San Francisco, CA | 7.9-8.2 | 11 |

Table 2.4 Independent Variables Investigated (after Bartlett and Youd (1992))

| Variable | Description |
|---|---|
| M* | Earthquake moment magnitude |
| R* | Horizontal distance to nearest seismic energy source, (km) |
| A | Peak horizontal ground acceleration, (g) |
| D | Duration of strong ground motion (> 0.05 g), (s) |
| S* | Ground slope, (%) |
| L | Distance to free face from point of displacement, (m) |
| H | Height of free face, (m) |
| W* | Free face ratio (100*H/L), (%) |
| $T_L$ | Cumulative thickness of liquefied zone, (m) |
| $T_{10}$ | Thickness of saturated, cohesionless soils with $(N1)_{60} < 10$, (m) |
| $T_{15}$* | Thickness of saturated, cohesionless soils with $(N1)_{60}<15$, (m) |
| $T_{20}$ | Thickness of saturated, cohesionless soils with $(N1)_{60}<20$, (m) |
| I | Index of liquefaction potential (from Hamada, et al., 1991) |
| C | Depth to top of liquefied zone, (m) |
| B | Depth to bottom of liquefied zone, (m) |
| Z | Depth to lowest factor of safety against liquefaction, (m) |
| E | Depth to lowest SPT N value in saturated cohesionless soil, (m) |
| G | Depth to lowest $(N1)_{60}$ value in saturated cohesionless soil, (m) |
| N | Lowest SPT N value in saturated cohesionless soil |
| Ns | Lowest (N1)60 value in saturated cohesionless soil |
| J | Lowest factor of safety against liquefaction below water table |
| $(N1)_{60FS}$ | $(N1)_{60}$ value corresponding to J |
| K | Average liquefaction factor of safety in Ts |
| O | Average $(N1)_{60}$ in Ts |
| $D_{50S}$ | Average D50 in Ts, (mm) |
| $D_{50L}$ | Average $D_{50}$ in $T_L$, (mm) |
| $D_{5010}$ | Average $D_{50}$ in $T_{10}$, (mm) |
| $D_{5015}$* | Average $D_{50}$ in $T_{15}$, (mm) |
| $D_{5020}$ | Average $D_{50}$ in $T_{20}$, (mm) |
| F | Average fines content in T, (%) |
| F10 | Average fines content in $T_{10}$, (%) |
| $F_{15}$* | Average fines content in $T_{15}$, (%) |
| $F_{20}$ | Average fines content in $T_{20}$, (%) |

* denotes variables retained in the empirical model as a result of the MLR analysis

Table 2.5 Lateral Spread Sites Considered in MLR Analysis (after Bartlett and Youd (1992))

| Year | Earthquake | Site |
|---|---|---|
| 1906 | San Francisco | Coyote Creek Bridge near Milpitas |
| 1906 | San Francisco | Mission Creek Zone in San Francisco |
| 1906 | San Francisco | Salinas River Bridge near Salinas |
| 1906 | San Francisco | South of Market Street Zone in San Francisco |
| 1964 | Alaska | Matanuska River, Bridges 141.1, 147.4, 147.5, & 148.3 |
| 1964 | Alaska | Portage Creek, Bridges 63.0 & 63.5 |
| 1964 | Alaska | Placer River, Highway Bridge 629 |
| 1964 | Alaska | Snow River, Highway Bridge 605A |
| 1964 | Alaska | Resurrection River, Bridges 3.0, 3.2, 3.3 |
| 1964 | Niigata | Numerous lateral spread sites |
| 1971 | San Fernando | Jensen Filtration Plant |
| 1971 | San Fernando | Juvenile Hall |
| 1979 | Imperial Valley | Heber Road near El Centro |
| 1979 | Imperial Valley | River Park near Brawley |
| 1983 | Borah Peak | Whiskey Springs near Mackay |
| 1983 | Borah Peak | Pence Ranch near Mackay |
| 1983 | Nihonkai-Chubu | Lateral spreads in the northern sector of Noshiro |
| 1987 | Superstition Hills | Wildlife Instrument Array in Brawly |

Table 2.6 Recommended Minimum Epicentral Distance, R (km) for a Given Earthquake Moment Magnitude, $M_w$ (after Bartlett and Youd (1992))

| $M_w$ | R | $M_w$ | R | $M_w$ | R | $M_w$ | R |
|---|---|---|---|---|---|---|---|
| 6.5 | 0.25 | 7.2 | 1.4 | 7.9 | 8 | 8.6 | 28 |
| 6.6 | 0.3 | 7.3 | 1.8 | 8.0 | 9 | 8.7 | 33 |
| 6.7 | 0.4 | 7.4 | 2.4 | 8.1 | 12 | 8.8 | 38 |
| 6.8 | 0.5 | 7.5 | 3 | 8.2 | 14 | 8.9 | 43 |
| 6.9 | 0.7 | 7.6 | 4 | 8.3 | 17 | 9.0 | 50 |
| 7.0 | 0.9 | 7.7 | 5 | 8.4 | 20 | | |
| 7.1 | 1.1 | 7.8 | 6 | 8.5 | 24 | | |

Table 2.7 Effect of Wedge Geometry on Yield Acceleration (after Baziar et al. (1992))

| Block Displacement | Uphill Face Boundary Condition | Downhill Face Boundary Condition | Figure |
|---|---|---|---|
| Downhill | Active Wedge | Free | Figure 2.38 |
| Uphill | Passive Wedge | Free | Figure 2.39 |
| Downhill | Active Wedge | Passive Wedge | Figure 2.40 |
| Uphill | Passive Wedge | Active Wedge | Figure 2.41 |

Table 2.8 Earthquake Records Used by for the Sliding Block Analyses (after Baziar et al. (1992))

| Earthquake | Year | Magnitude $M_w$ | Number of Records |
|---|---|---|---|
| Hollister | 1974 | 5.2 | 2 |
| Lytle Creek | 1970 | 5.3 | 2 |
| Coyote Lake | 1979 | 5.8 | 5 |
| Parkfield | 1966 | 6.1 | 4 |
| Imperial Valley | 1979 | 6.5 | 31 |
| San Fernando | 1971 | 6.6 | 8 |
| Borrego Mountain | 1968 | 6.6 | 1 |
| Imperial Valley | 1940 | 7.0 | 1 |
| Kern County | 1952 | 7.4 | 4 |

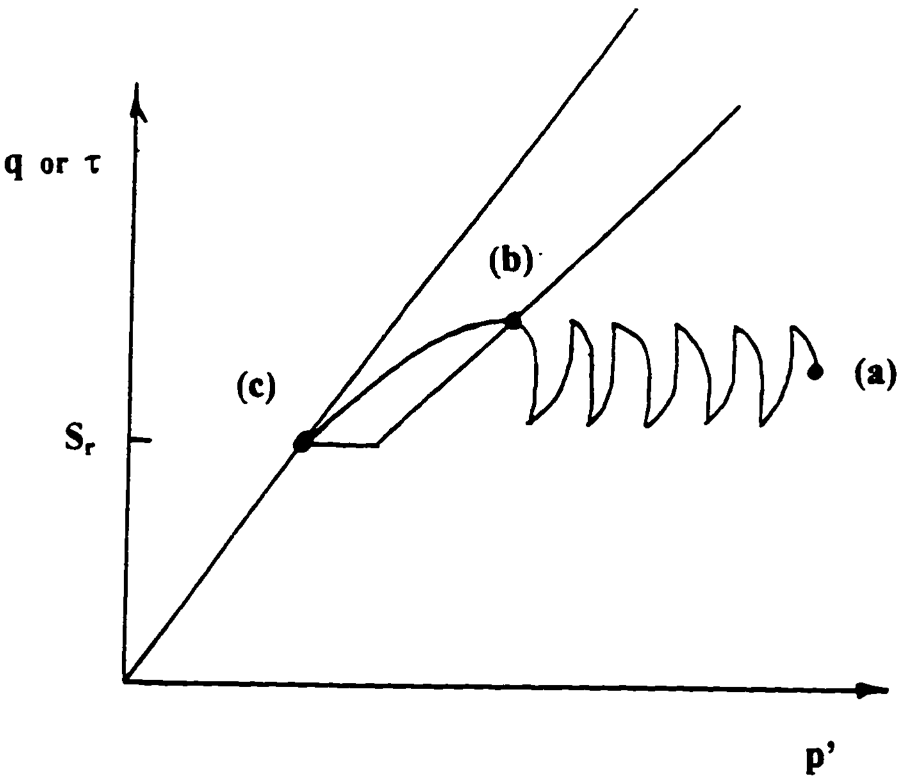


Figure 2.1 Effective Stress Path Depicting Flow Liquefaction

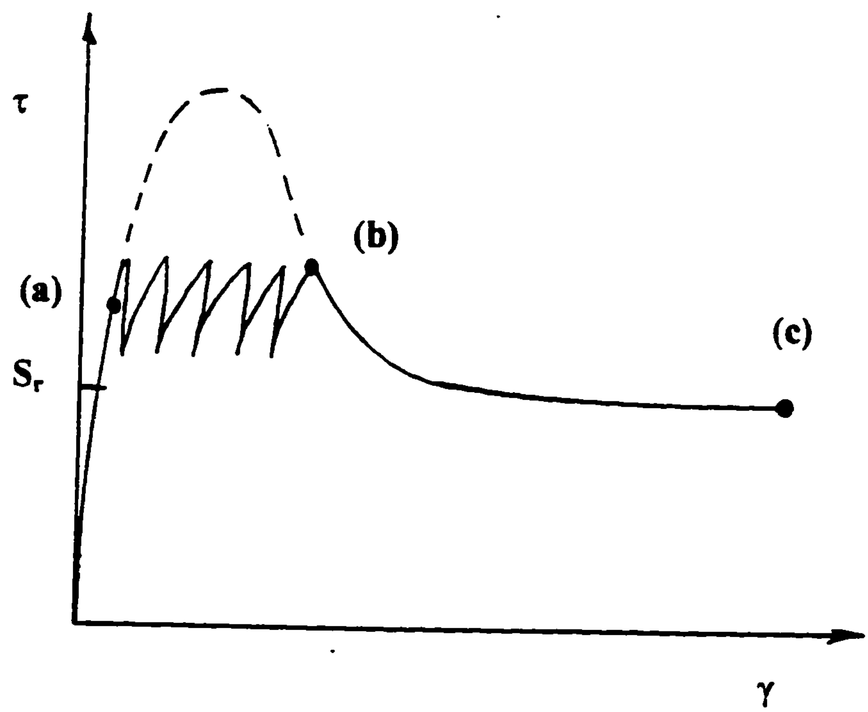


Figure 2.2 Stress-Strain Behavior of Flow Liquefaction

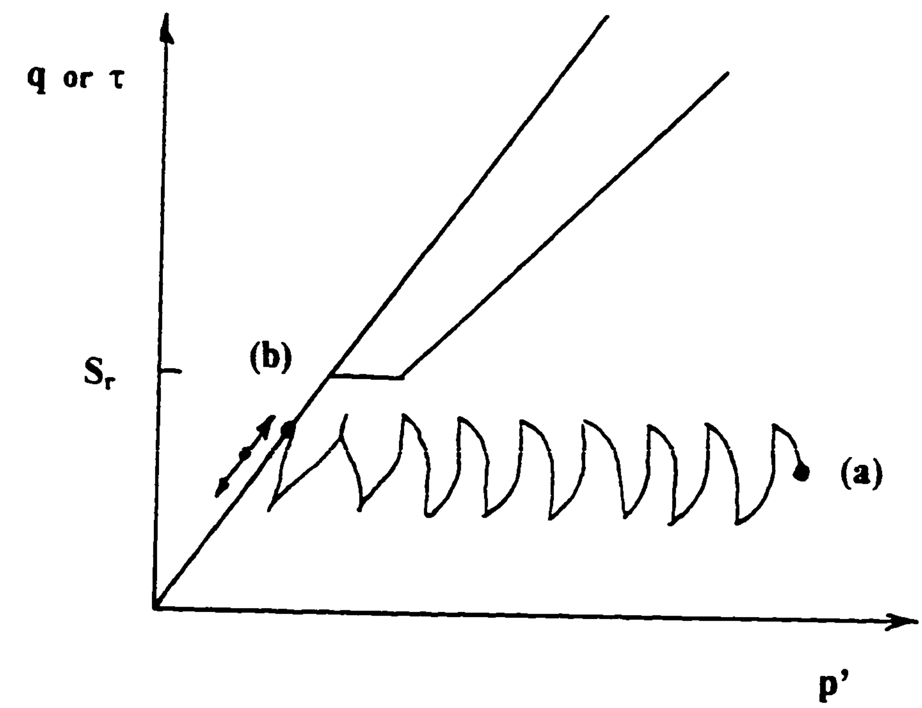


Figure 2.3 Effective Stress Path Depicting Cyclic Mobility

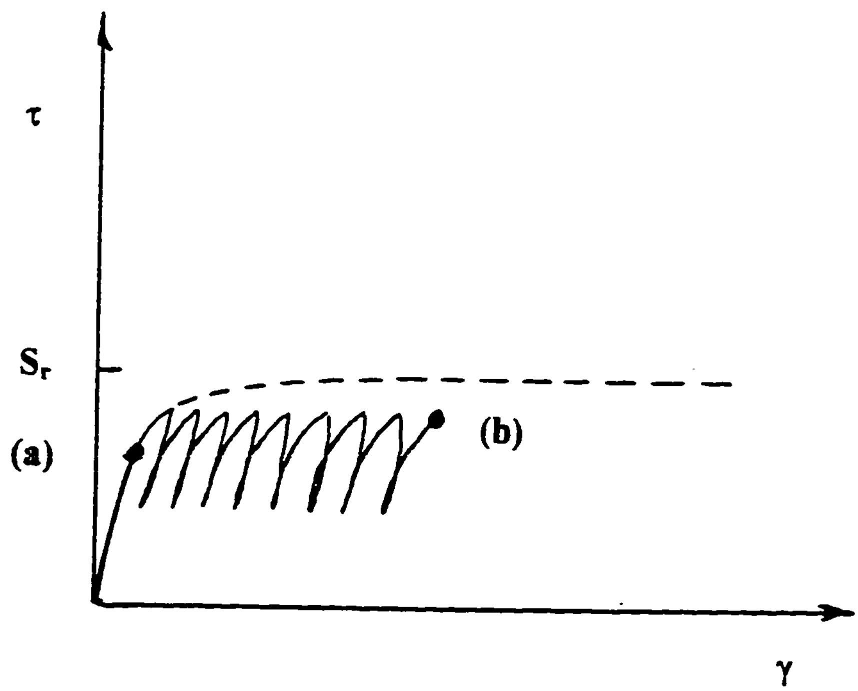


Figure 2.4 Stress-Strain Behavior of Cyclic Mobility

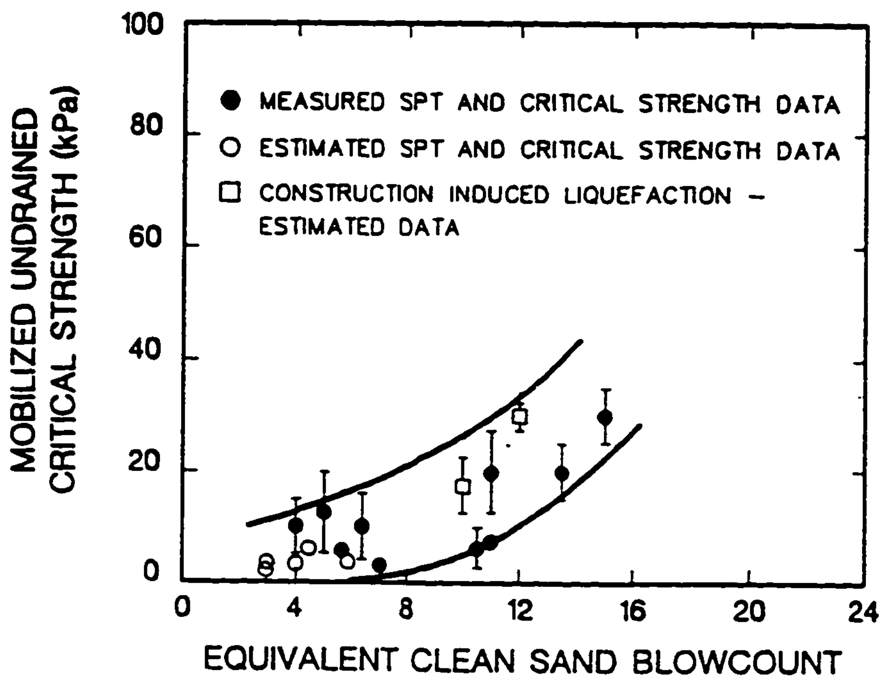


Figure 2.5 Residual Shear Strength of Liquefied Sand (after Seed and Harder (1990))

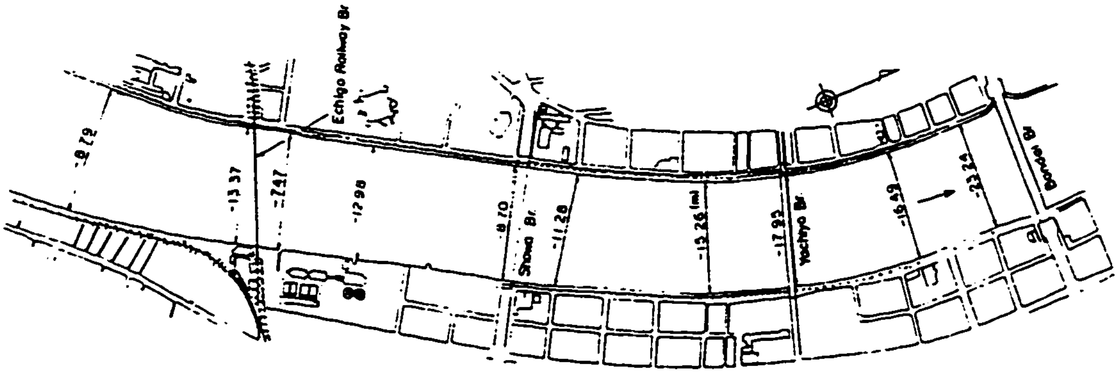


Figure 2.6 Shinano River channel closure due to the 1964 Niigata Earthquake. Width reduction in meters (after Hamada, (1992))

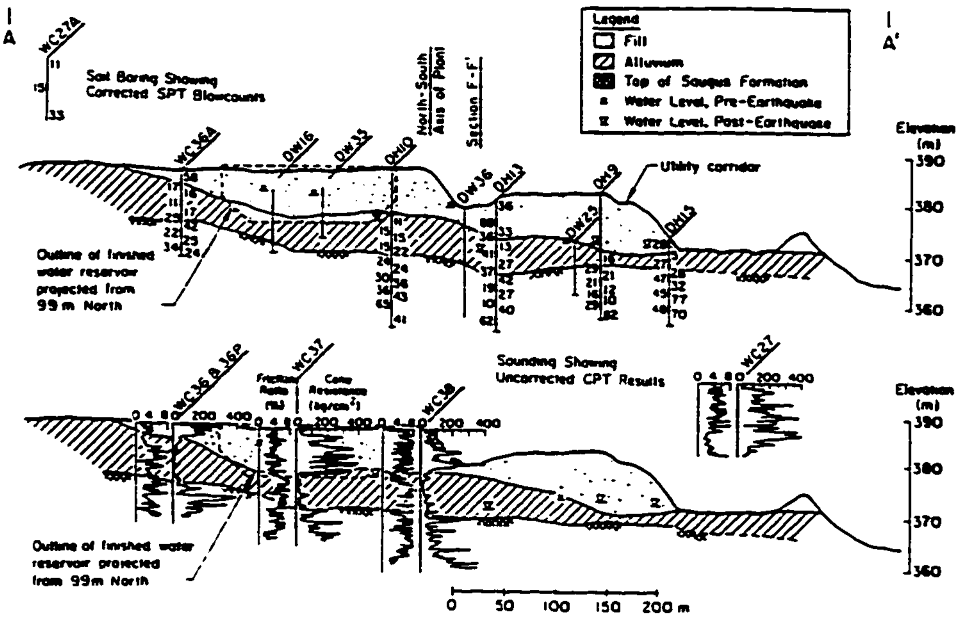


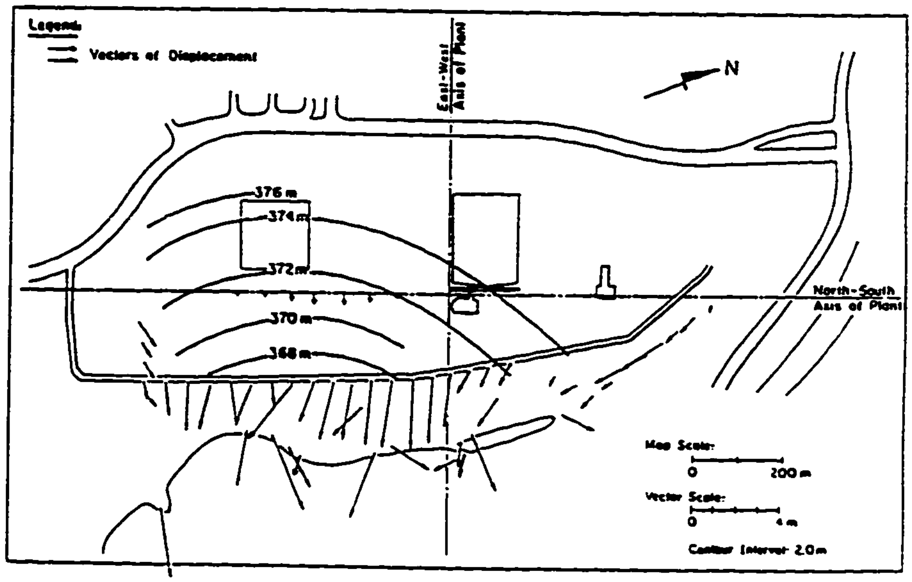


Figure 2.7 (a) Soil profile at Joseph Jensen Filtration Plant (b) Measured displacements and loose, saturated alluvium lower elevations at the Joseph Jensen Filtration Plant (after O'Rourke, et al. (1992))

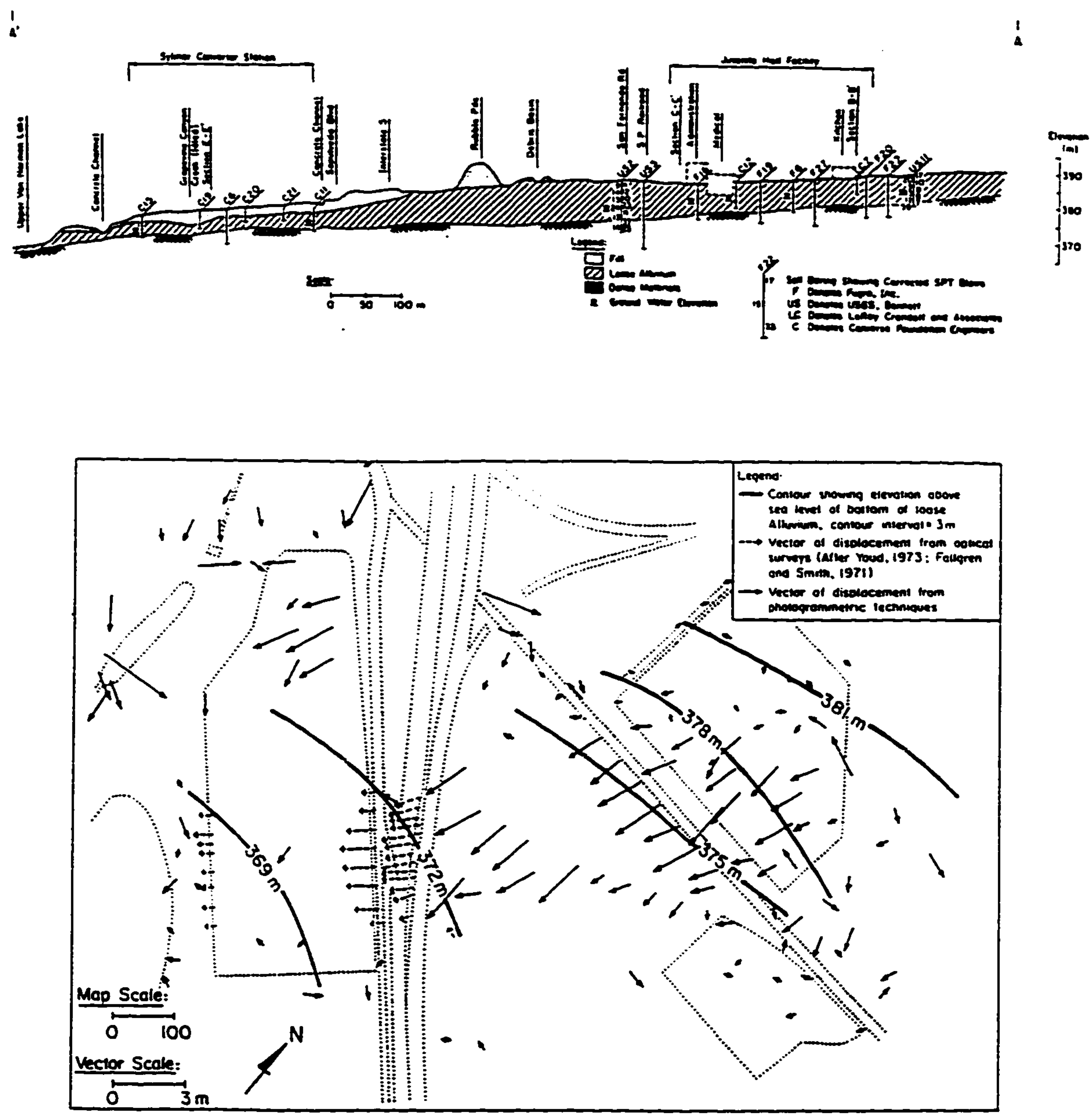


Figure 2.8 (a) Soil profile beneath Juvenile Hall and Sylmar Converter Station (b) Measured Displacements at the Sylmar Converter Station and Juvenile Hall Northeast of Upper Van Norman Reservoir (after O'Rourke et al. (1992))

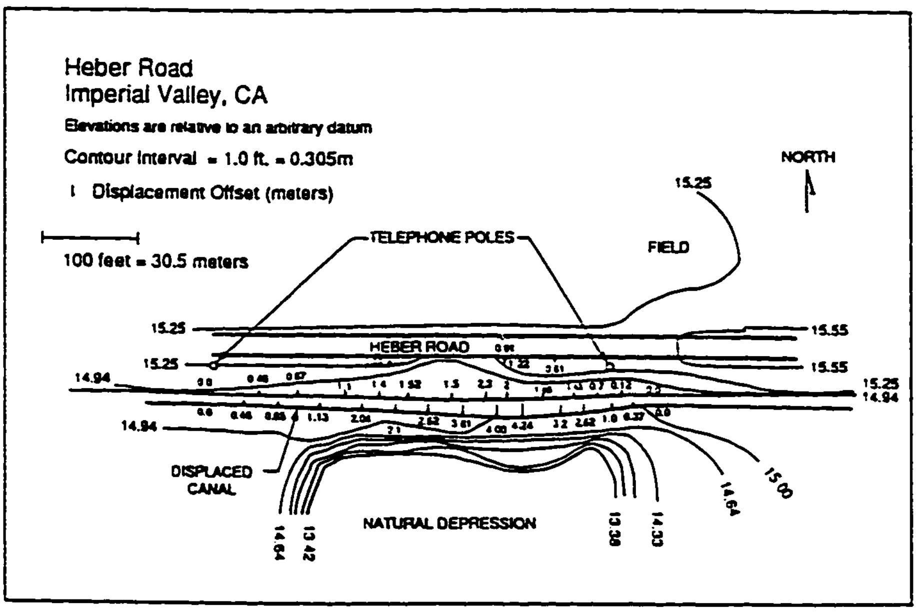


Figure 2.9 Measured deformations at the Heber Road site due to the 1979 Imperial Valley Earthquake (after Dobry et al. (1992))

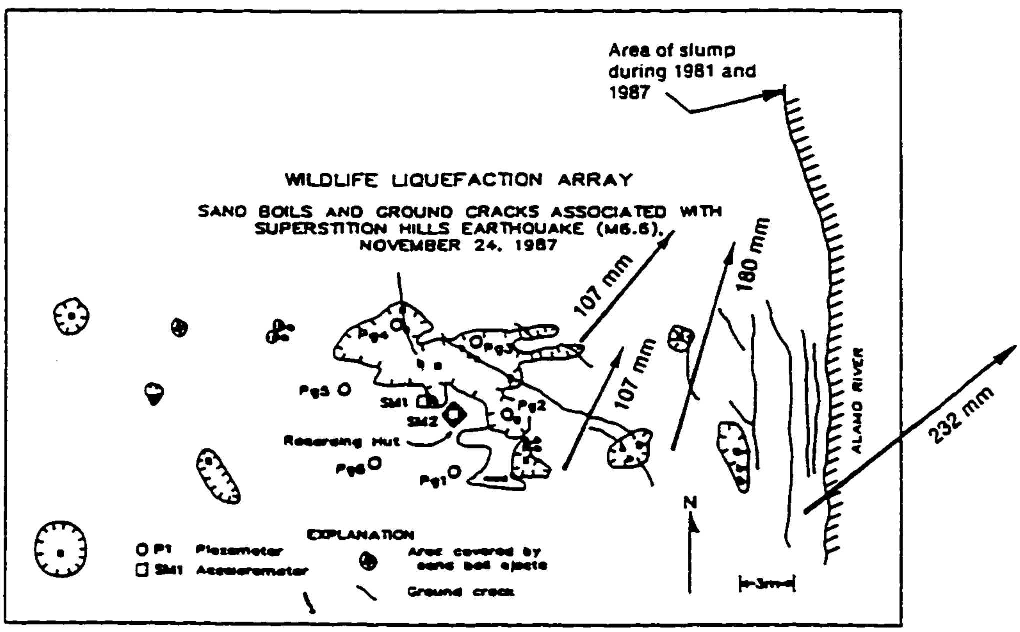


Figure 2.10 Measured deformations at the Wildlife site due to the 1987 Superstition Hills Earthquake (after Dobry et al. (1992))

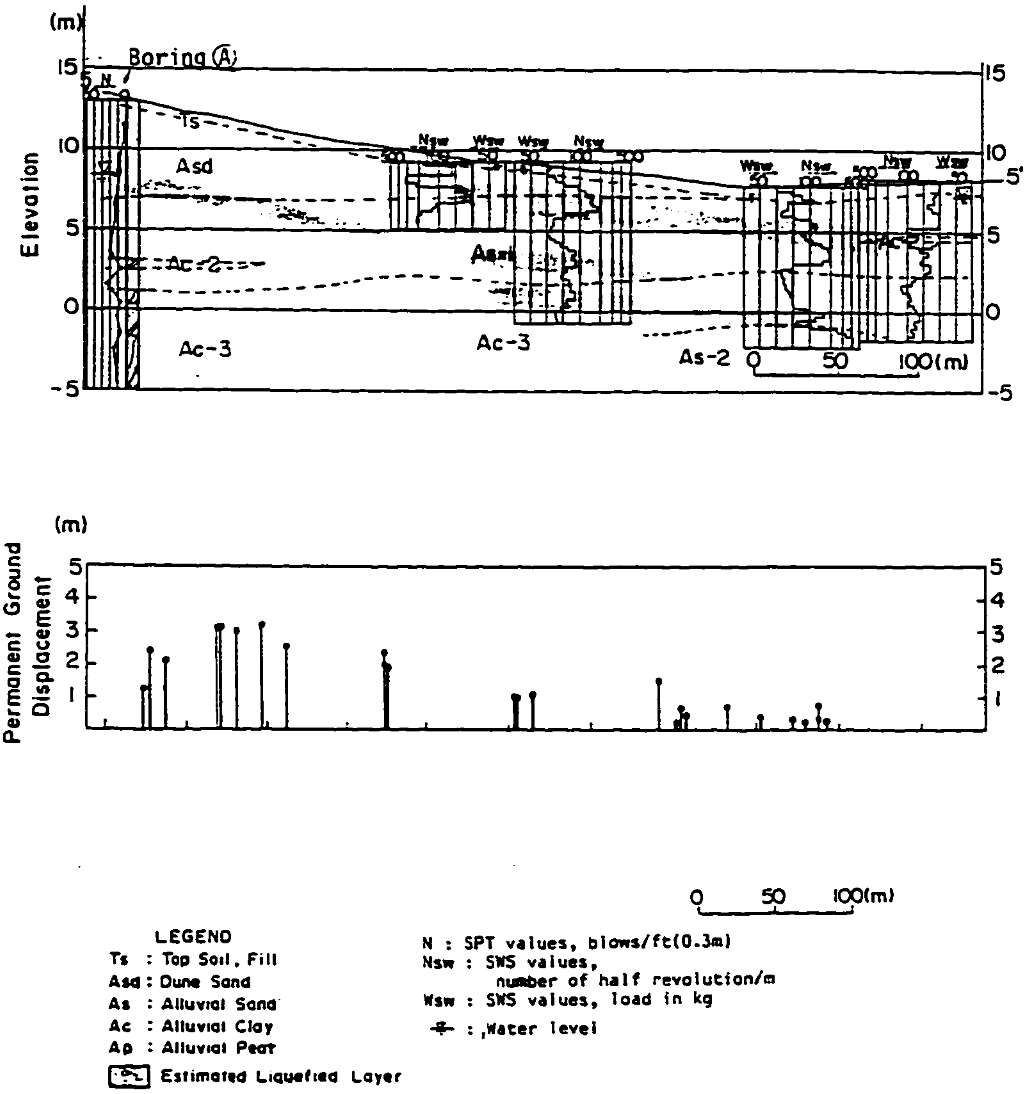


Figure 2.11 (a) Typical soil profile and (b) measured displacements on Maeyama Hill due to the 1983 Nihonkai-Chubu Earthquake (after Hamada (1992))

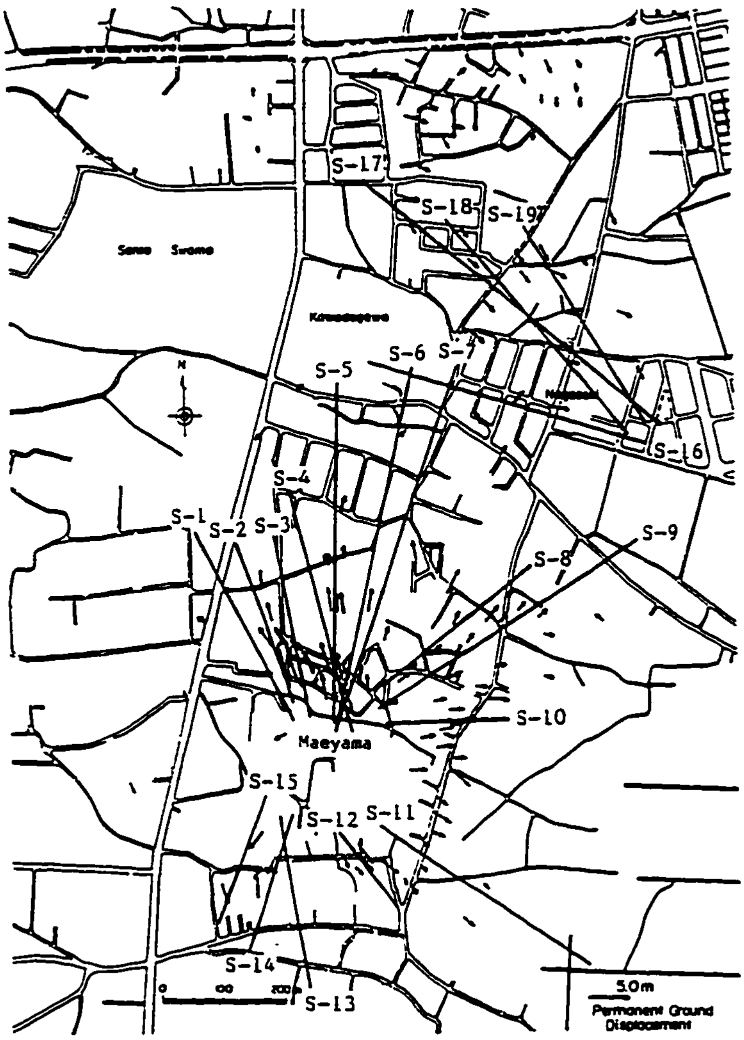


Figure 2.12 Displacement pattern around Maeyama Hill due to the 1983 Nihonkai-Chubu Earthquake (after Hamada (1992))

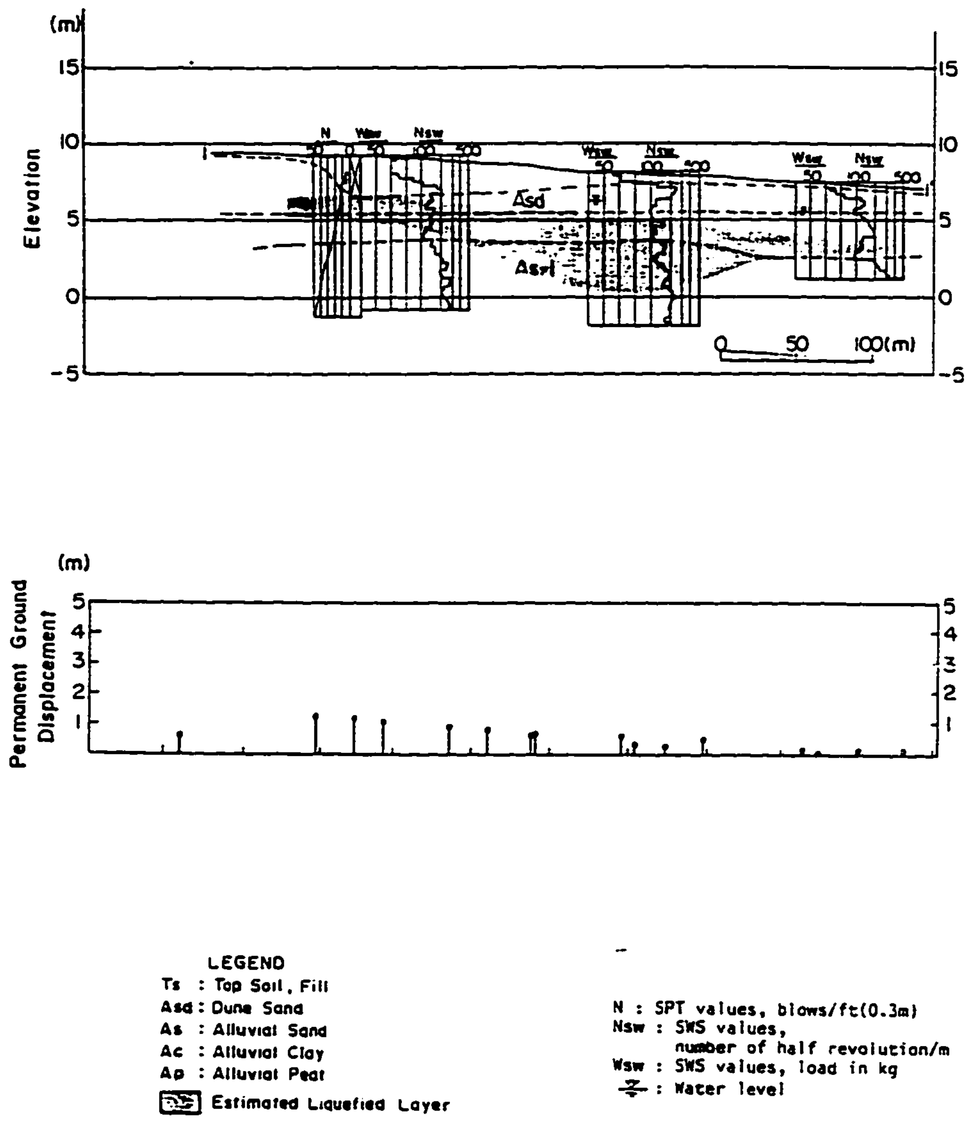


Figure 2.13 Stratigraphy, zones of suspected liquefaction, and measured displacements in north Noshiro City due to the 1983 Nihonkai-Chubu Earthquake (after Hamada (1992))

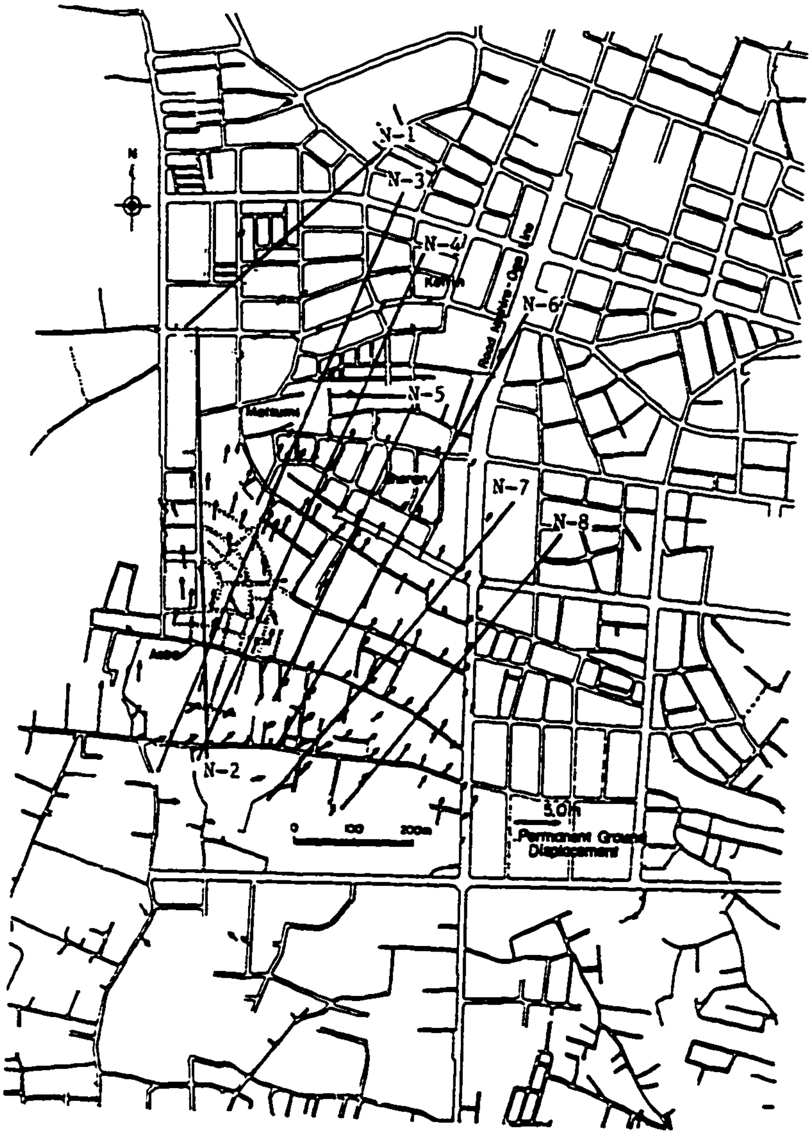


Figure 2.14 Measured lateral spread displacements, northern Noshiro City due to the 1983 Nihonkai-Chubu Earthquake (after Hamada (1992))

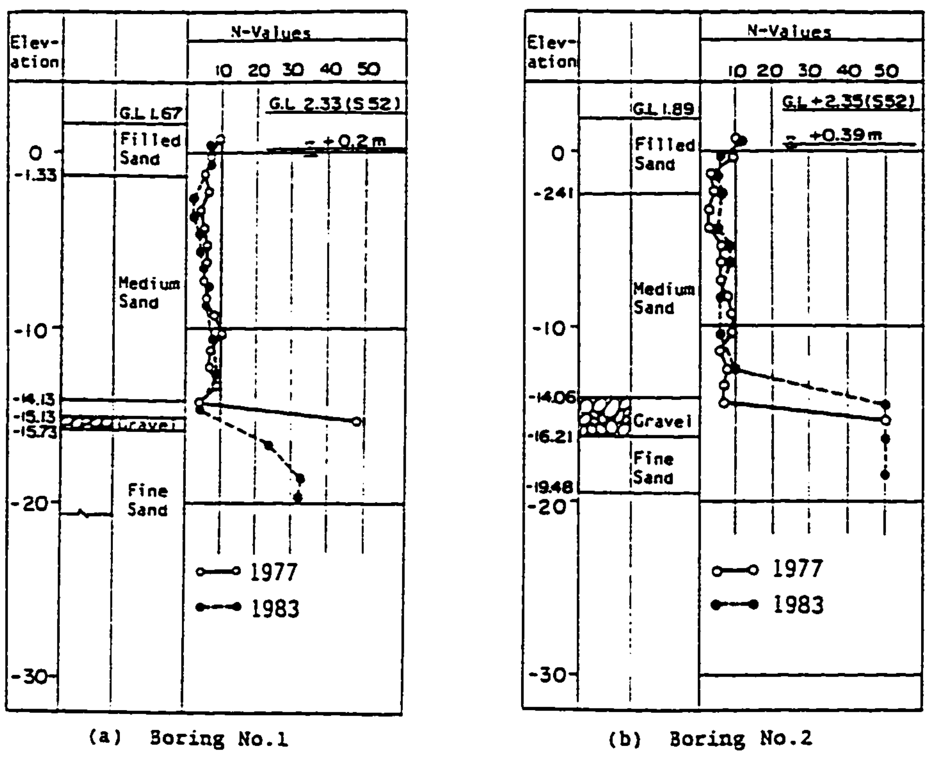


Figure 2.15 Soil conditions at Gaiko Wharf, Akita City (after Hamada (1992))

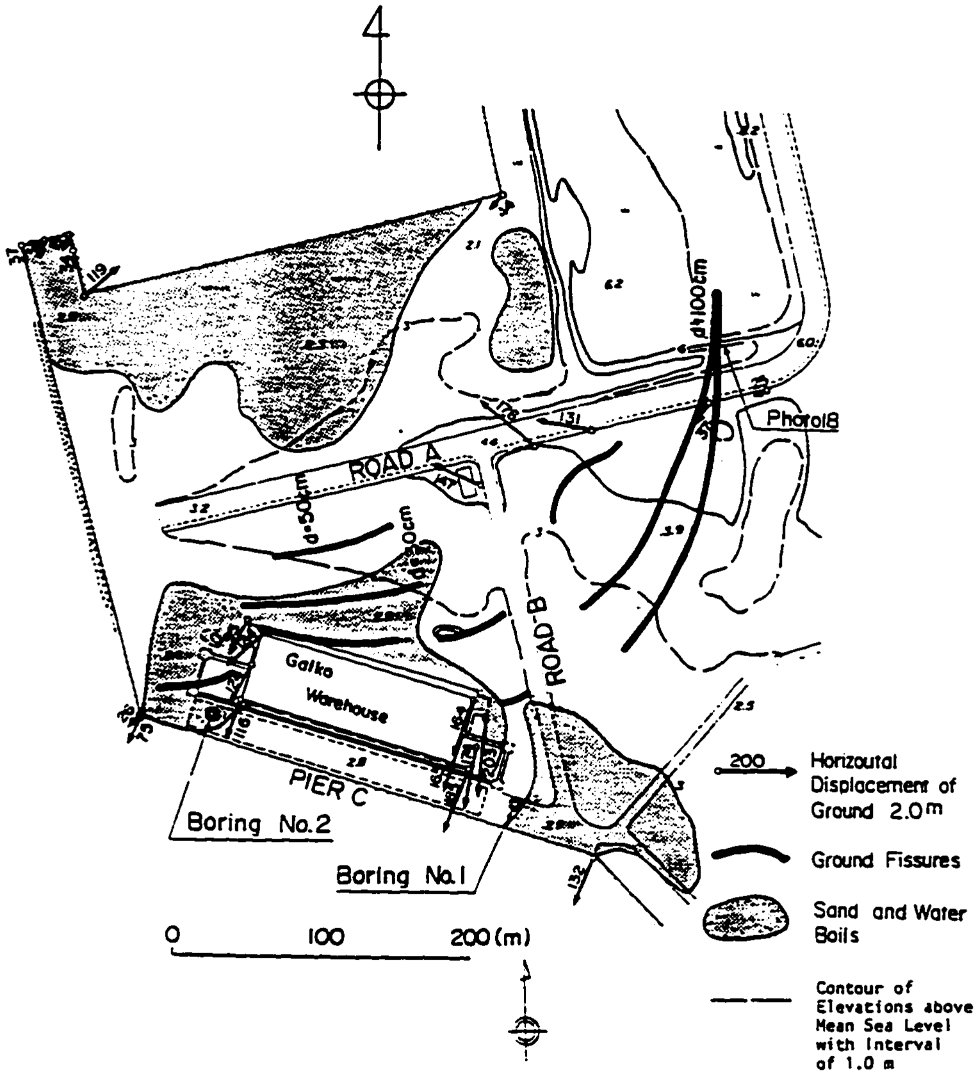


Figure 2.16 Permanent ground displacements measured at Gaiko Wharf due to the 1993 Nihonkai-Chubu Earthquake (after Hamada (1992))

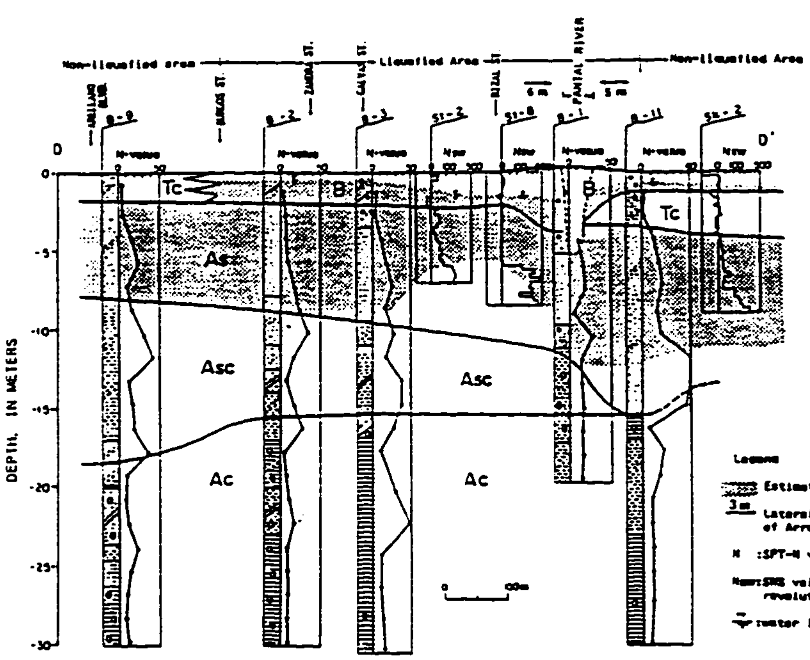

Figure 2.17 Subsurface profile along Perez Boulevard in Dagupan City, Philippines. The symbol "B" represents fill soils, and "As" represents alluvial sand deposits (after Wakamatsu et al. (1992))

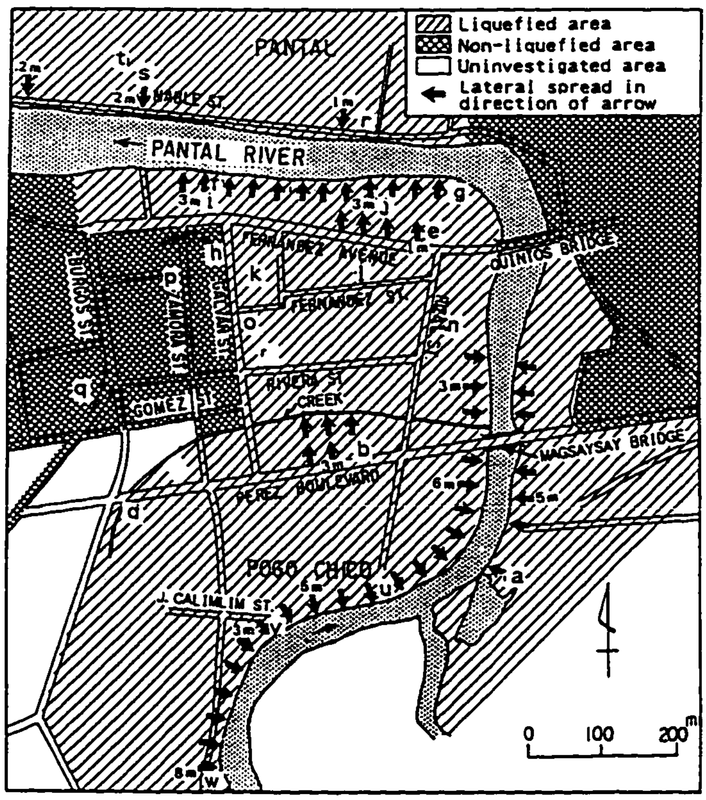


Figure 2.18 Liquefaction and associated deformations in Dagupan due to the 1990 Luzon, Philippines Earthquake (after Wakamatsu, et al. (1992))

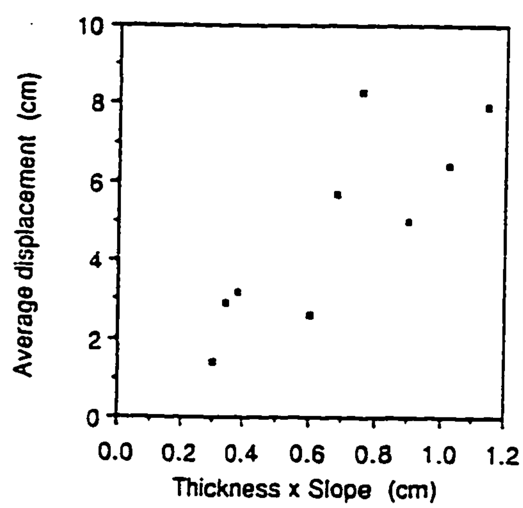


Figure 2.19 Correlation between displacement, thickness, and slope derived from shaking table tests (after Miyajima et al. (1991))

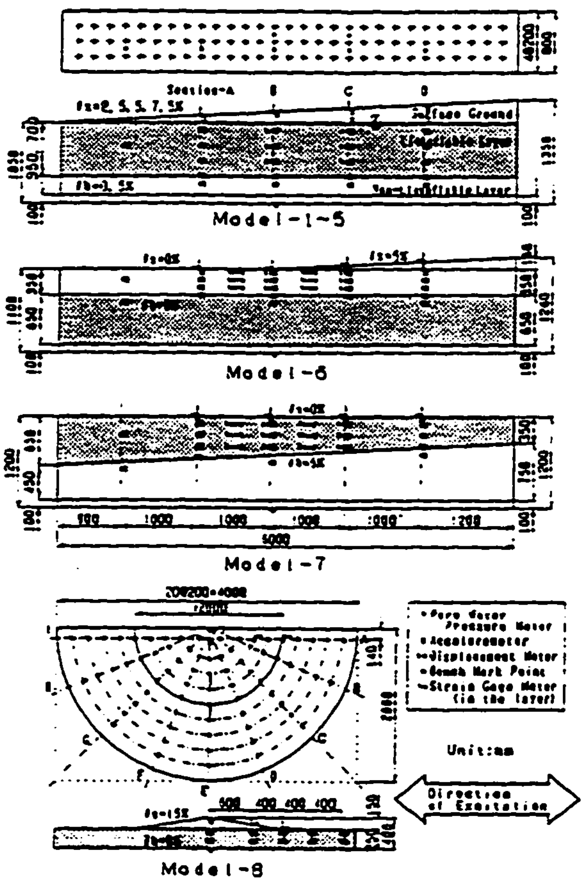


Figure 2.20 Schematics of shaking table set-ups (after Sasaki, et al. (1991))

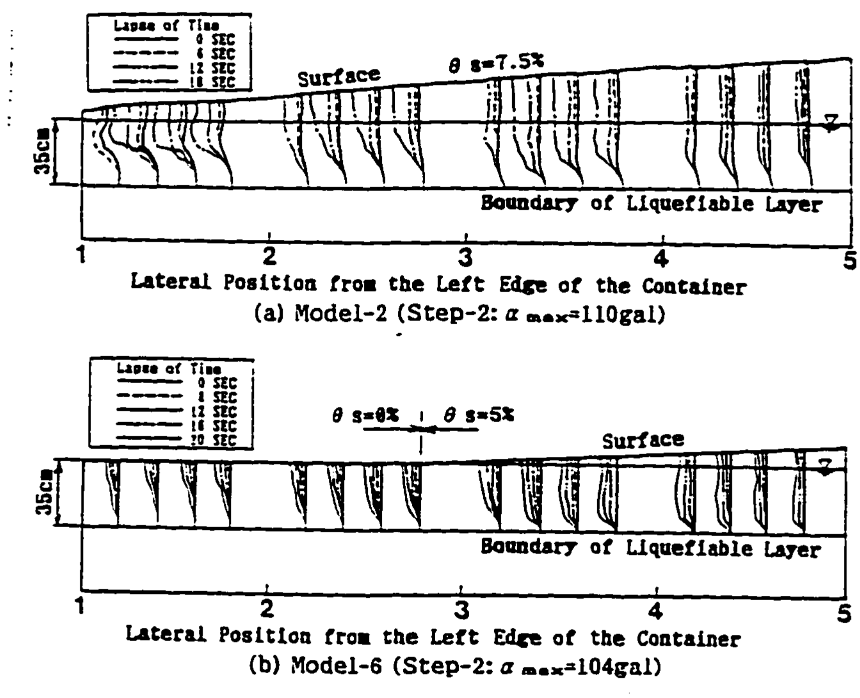


Figure 2.21 Observed displacement profiles for (a) Model 2 and (b) Model 6 (after Sasaki, et al. (1991))

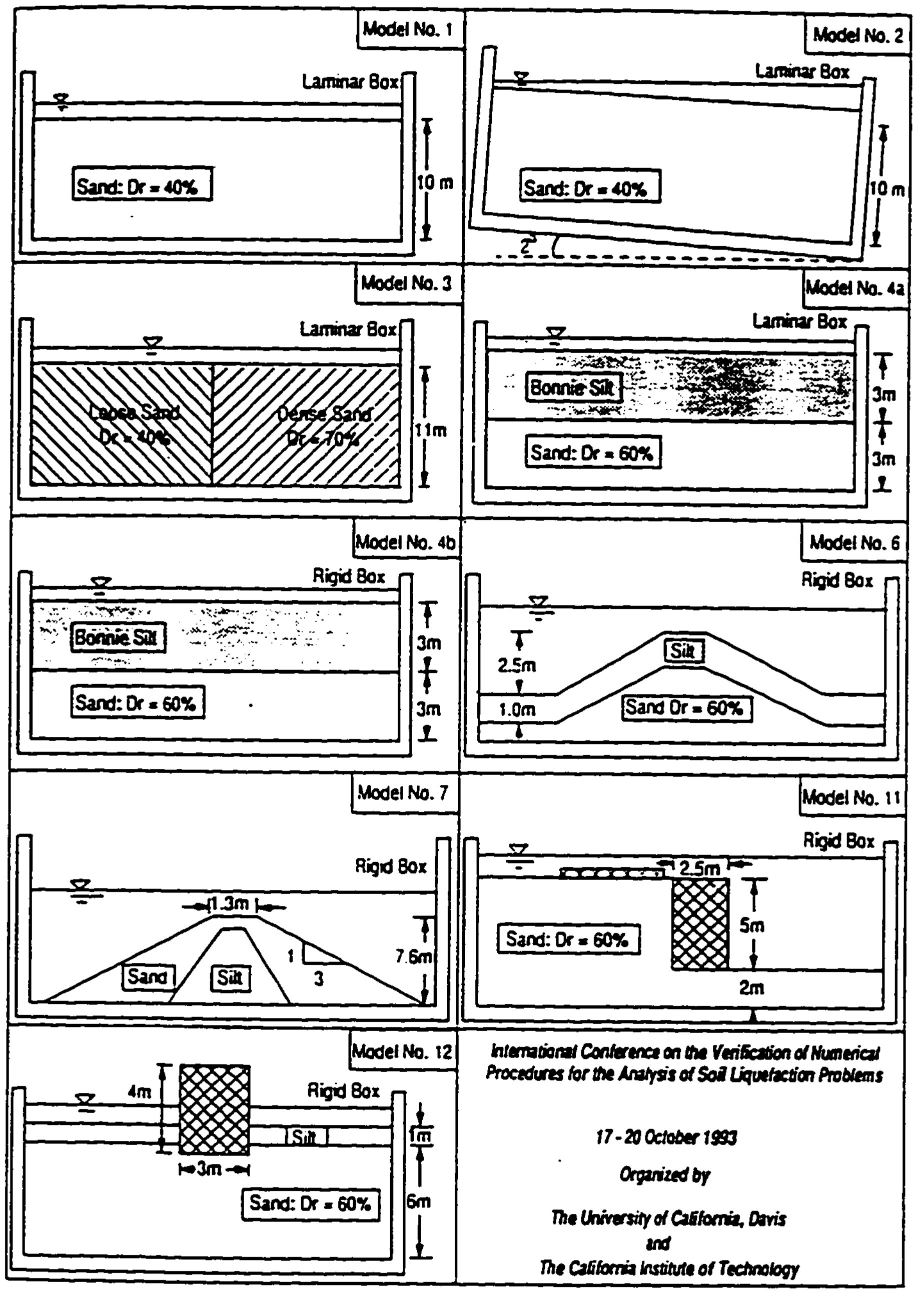


Figure 2.22 Centrifuge model configurations tested in the VELACS project (after Arulanandan and Scott (1993))

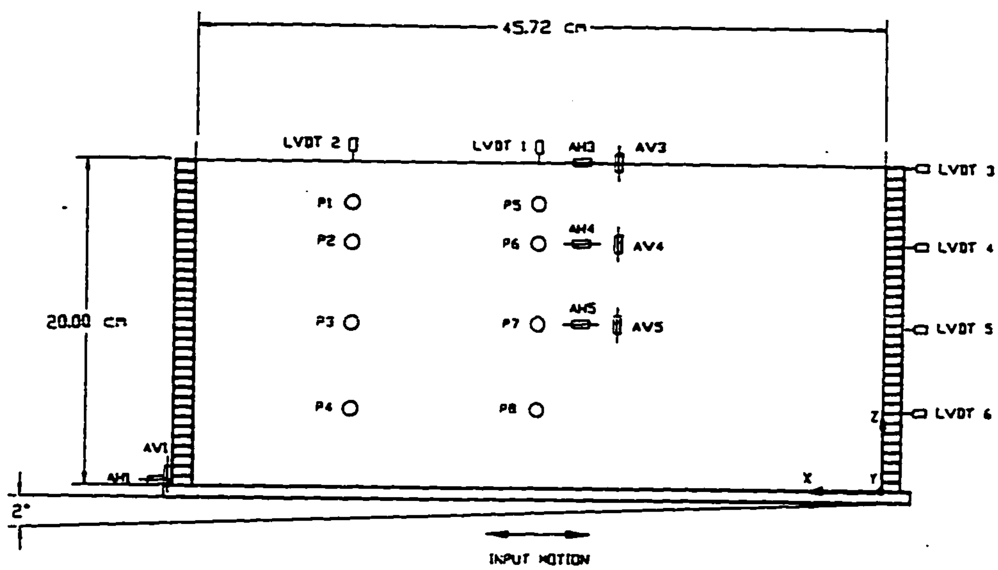


Figure 2.23 VELACS Model 2 configuration (after Arulanandan and Scott (1993))

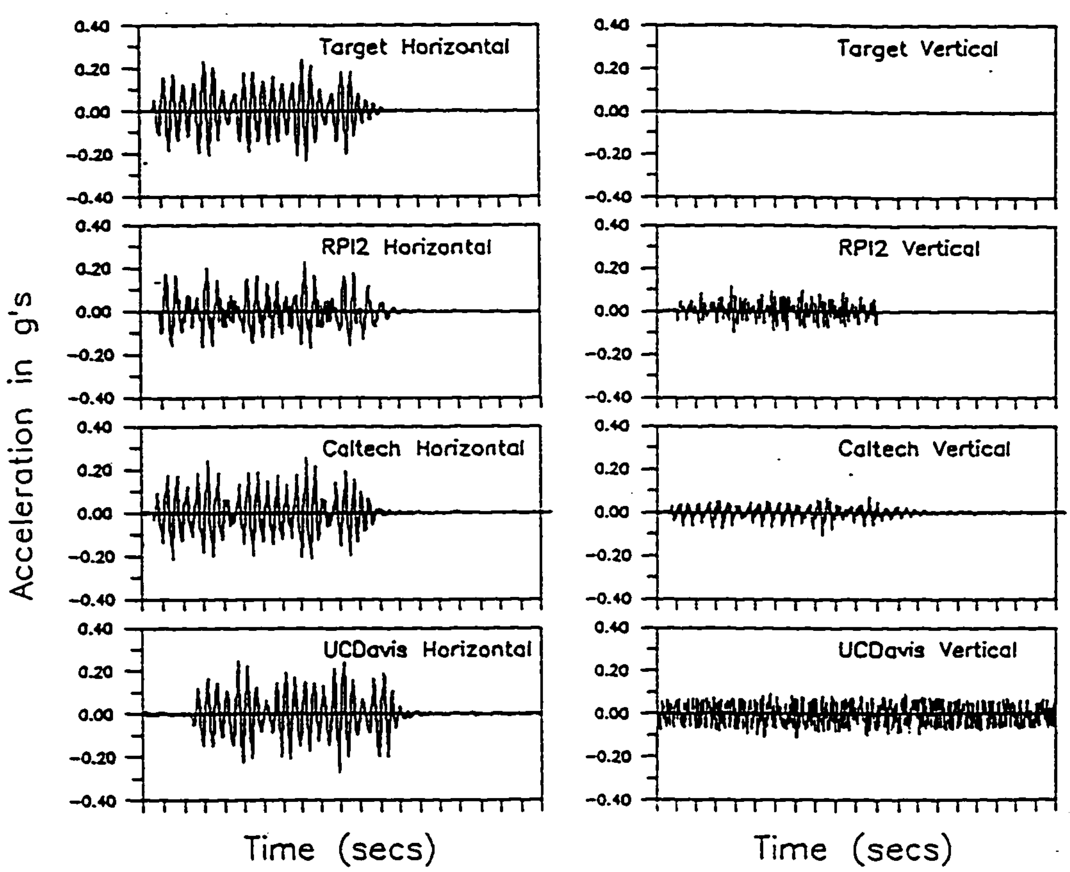


Figure 2.24 VELACS Model 2 target and measured accelerations (after Arulanandan and Scott (1993))

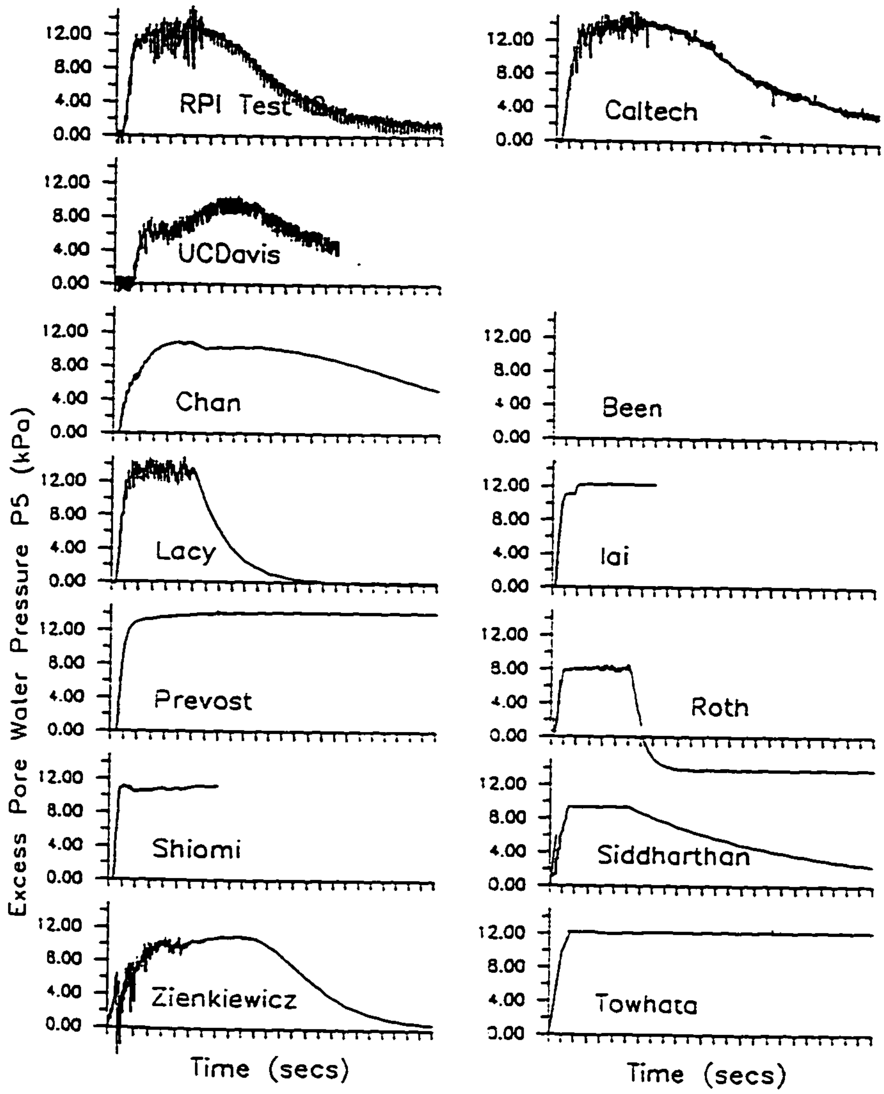


Figure 2.25 VELACS Model 2 excess pore pressure time histories (after Arulanandan and Scott (1993))

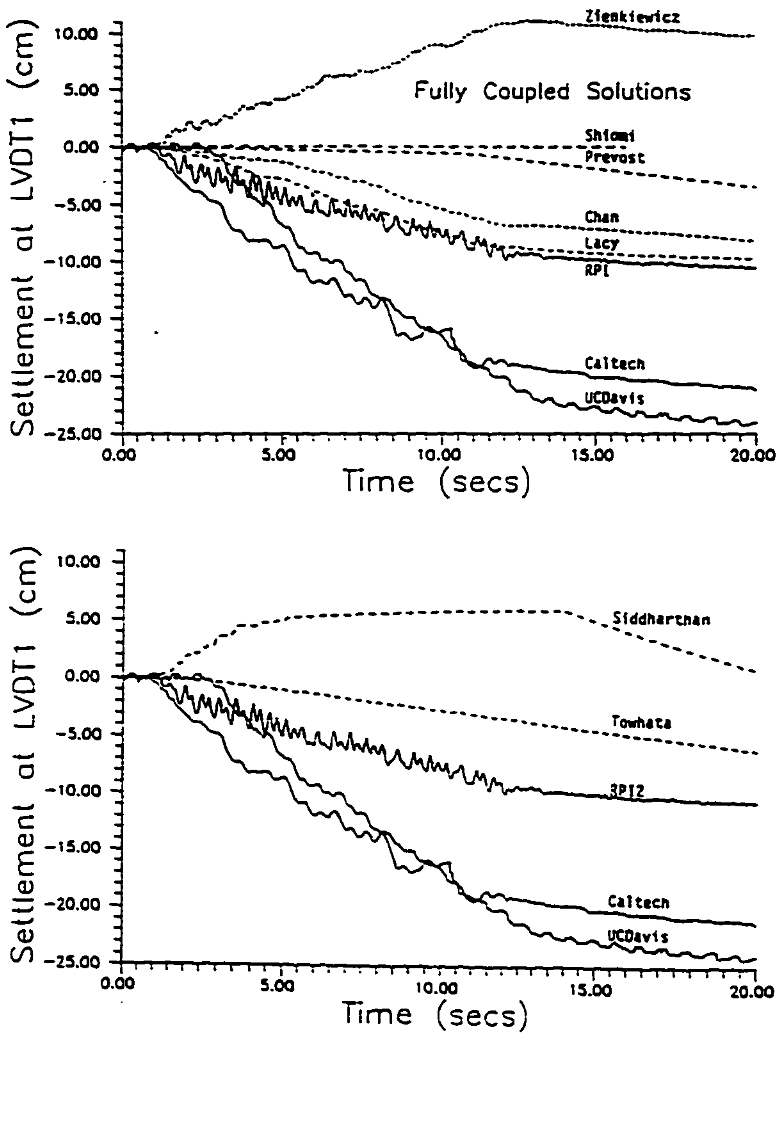


Figure 2.26 VELACS Model 2 measured vertical displacements (after Arulanandan and Scott (1993))

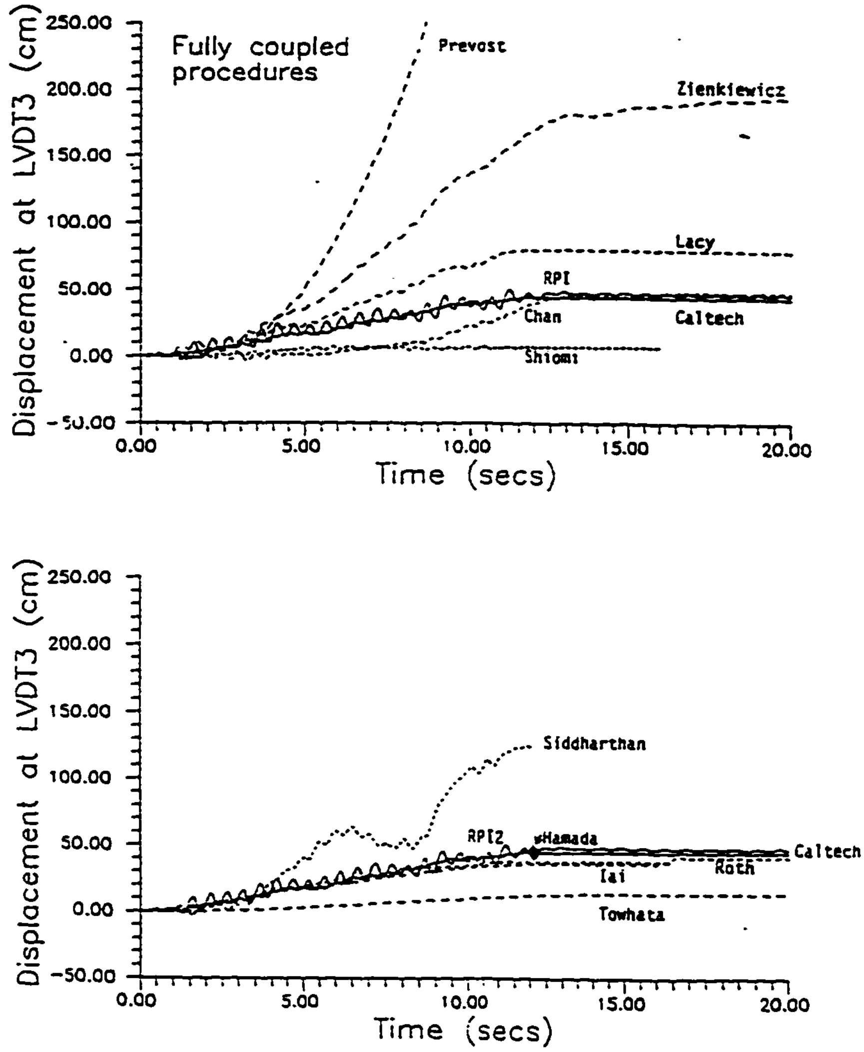


Figure 2.27 VELACS Model 2 measured lateral displacements (after Arulanandan and Scott (1993))

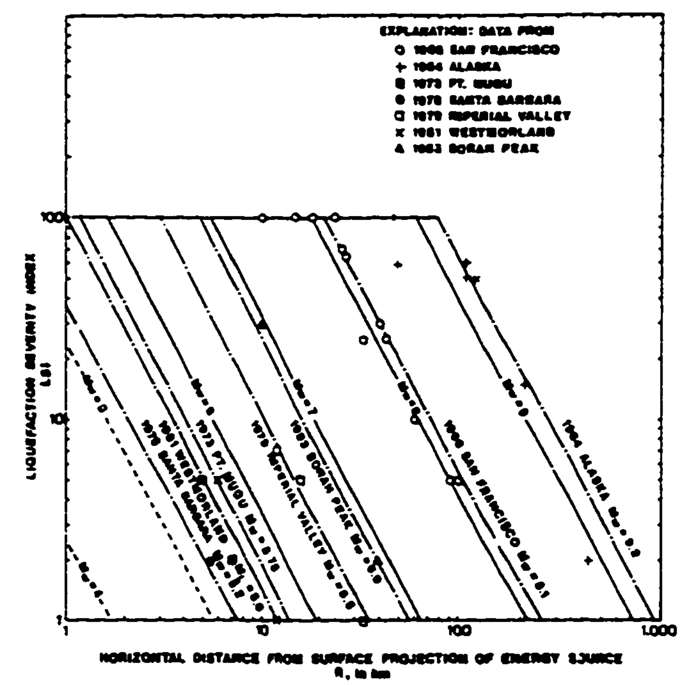


Figure 2.28 Liquefaction Severity Index versus epicentral distance and moment magnitude (after Youd and Perkins (1987))

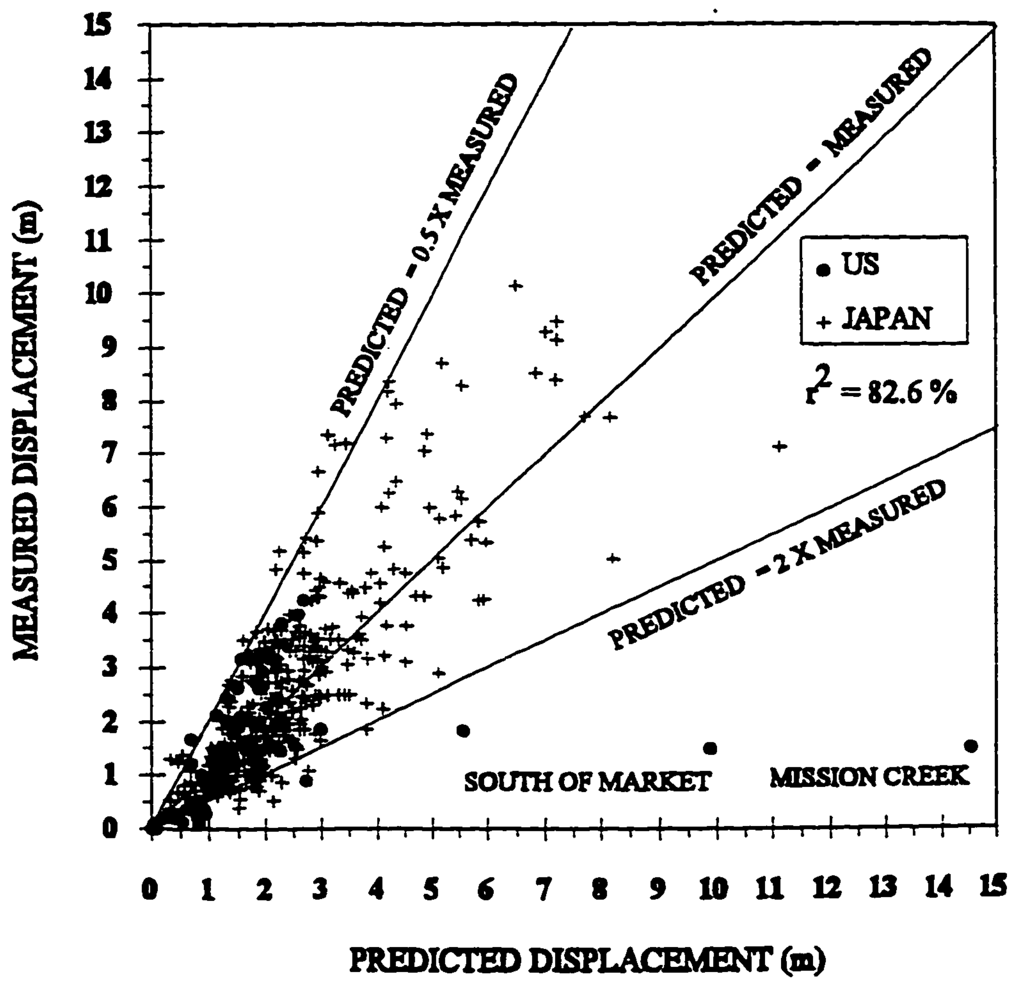


Figure 2.29 Predicted versus measured displacements using Equations (2.3) and (2.4) (after Bartlett and Youd (1992))


Figure 2.30 Illustration of analogy between potential landslide and sliding block (after Kramer (1995))

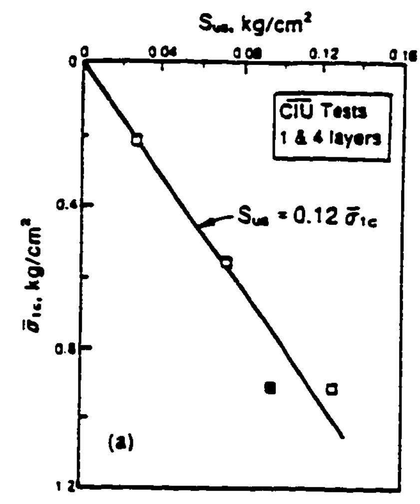


Figure 2.31 Variation of steady state strength with vertical effective consolidation pressure (after Dobry and Baziar (1991))

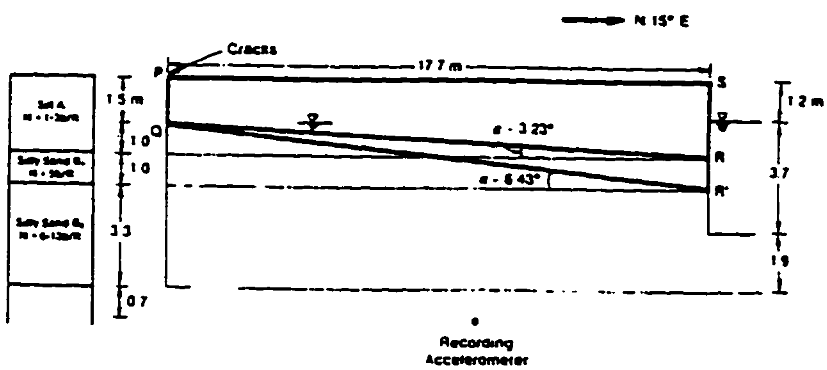


Figure 2.32 Soil profile and assumed failure planes for sliding block analysis of the Wildlife site (after Dobry and Baziar (1991))

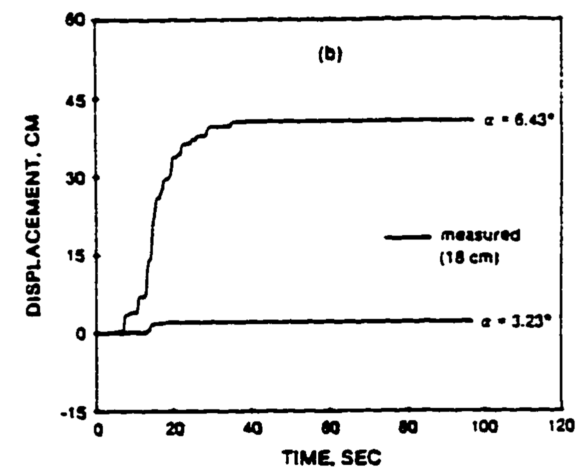


Figure 2.33 Predicted and measured lateral spread displacements at the Wildlife site (after Dobry and Baziar (1991))

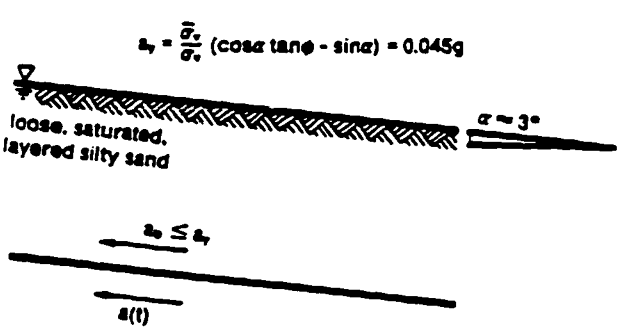


Figure 2.34 Typical site conditions used for sliding block comparison with LSI method (after Dobry and Baziar (1991))

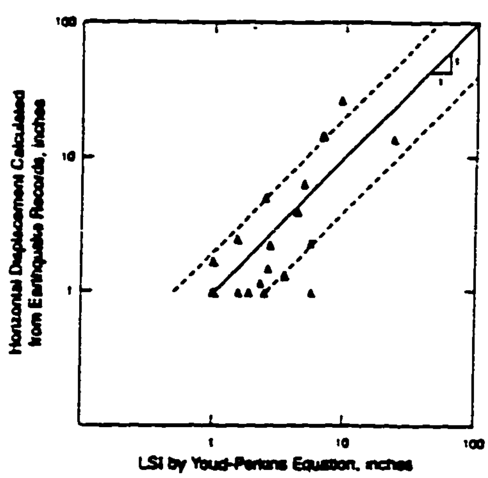


Figure 2.35 Comparison of displacements computed by the sliding block and LSI methods (after Dobry and Baziar (1991))

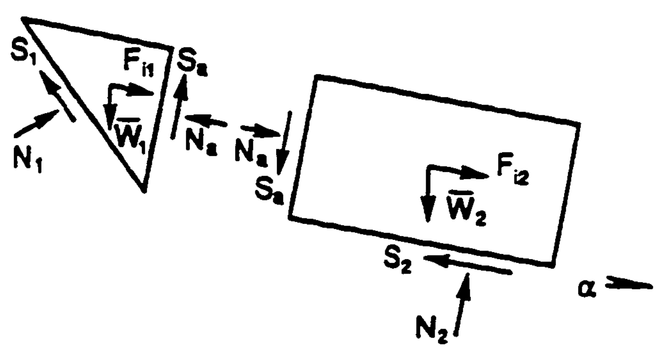


Figure 2.36 Idealized block model force system - free downhill face (after Baziar, et al. (1992))

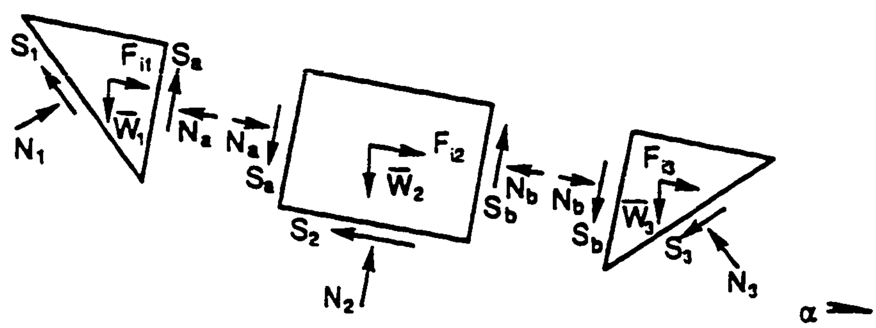


Figure 2.37 Idealized block model force system - soil wedge at both uphill and downhill faces (after Baziar, et al. (1992))

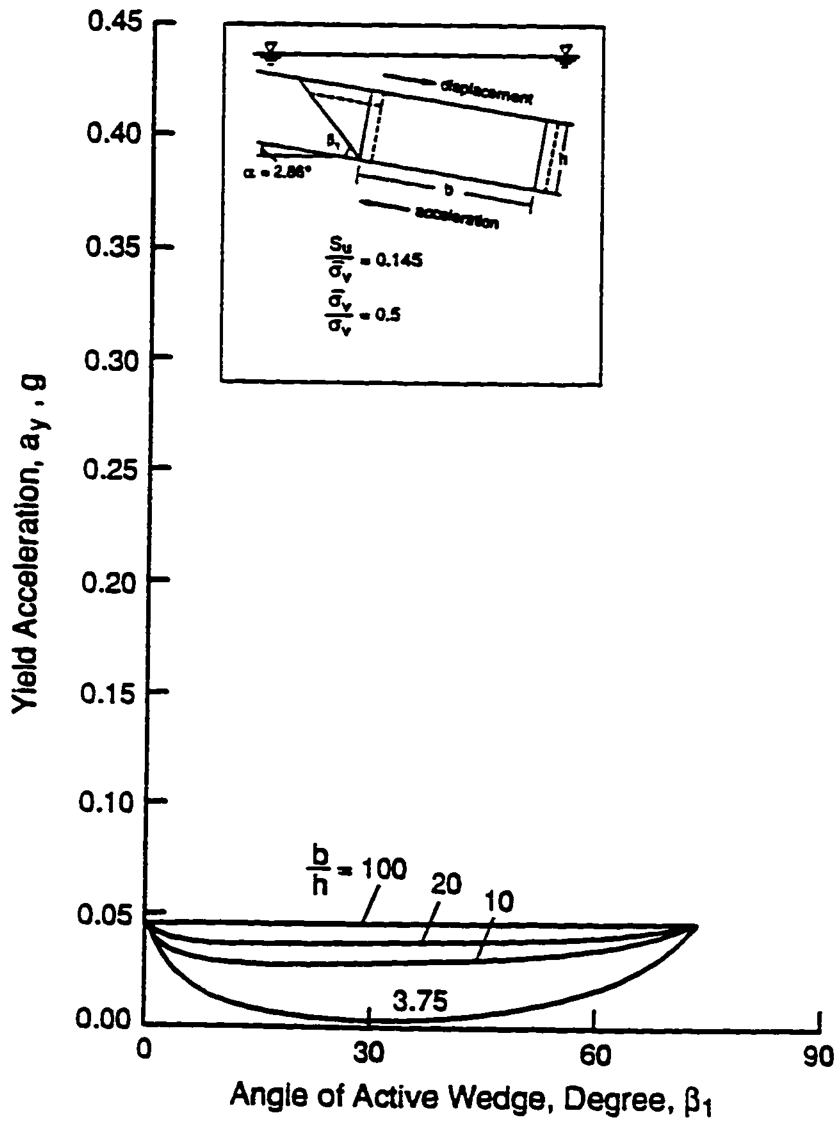


Figure 2.38 Variation of downhill yield acceleration with active wedge geometry and block aspect ratio (after Baziar, et al. (1992))

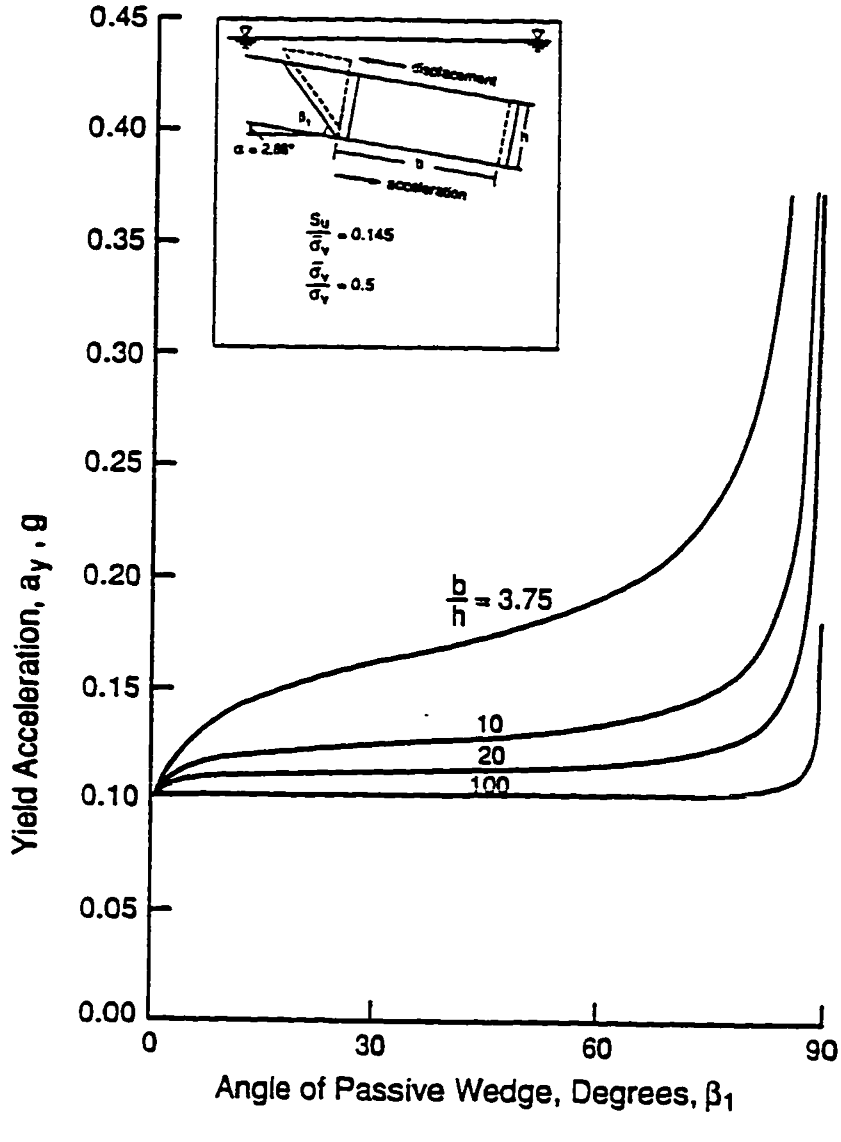


Figure 2.39 Variation of uphill yield acceleration with passive wedge geometry and block aspect ratio (after Baziar, et al. (1992))

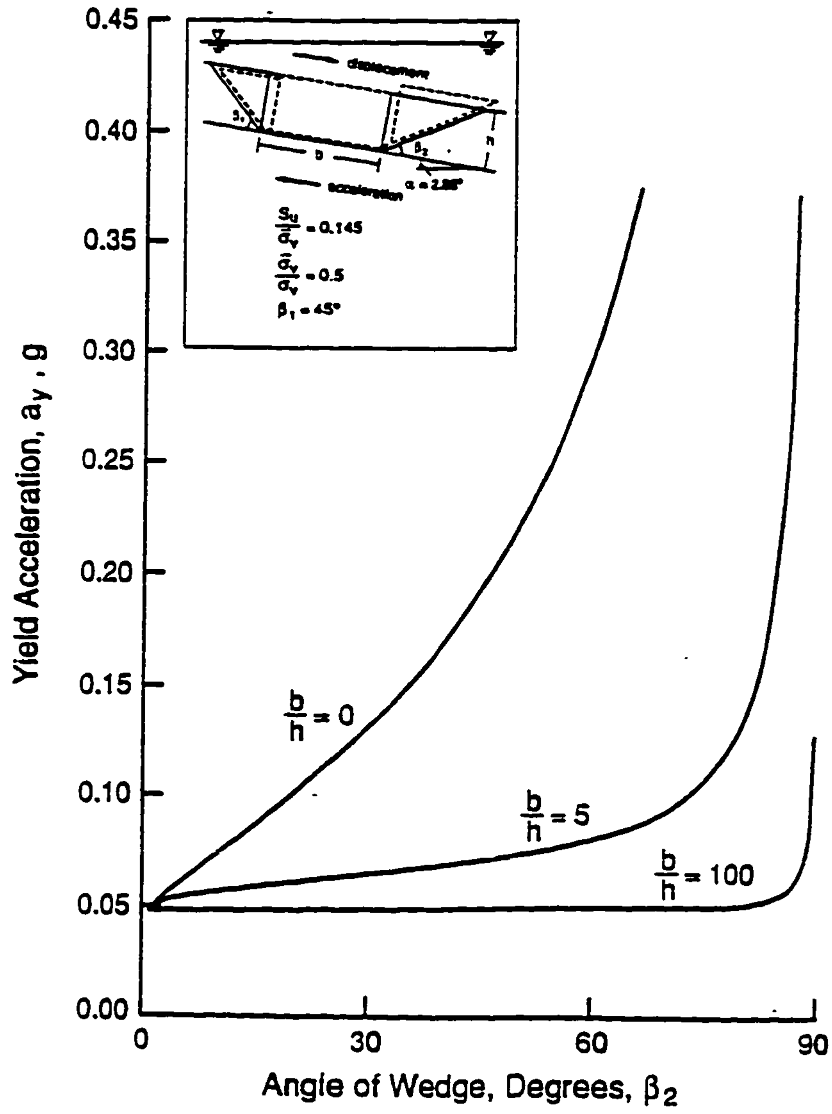


Figure 2.40 Variation of downhill yield acceleration with passive wedge geometry and block aspect ratio. Active wedge angle held constant at 45 degrees. (after Baziar, et al. (1992))

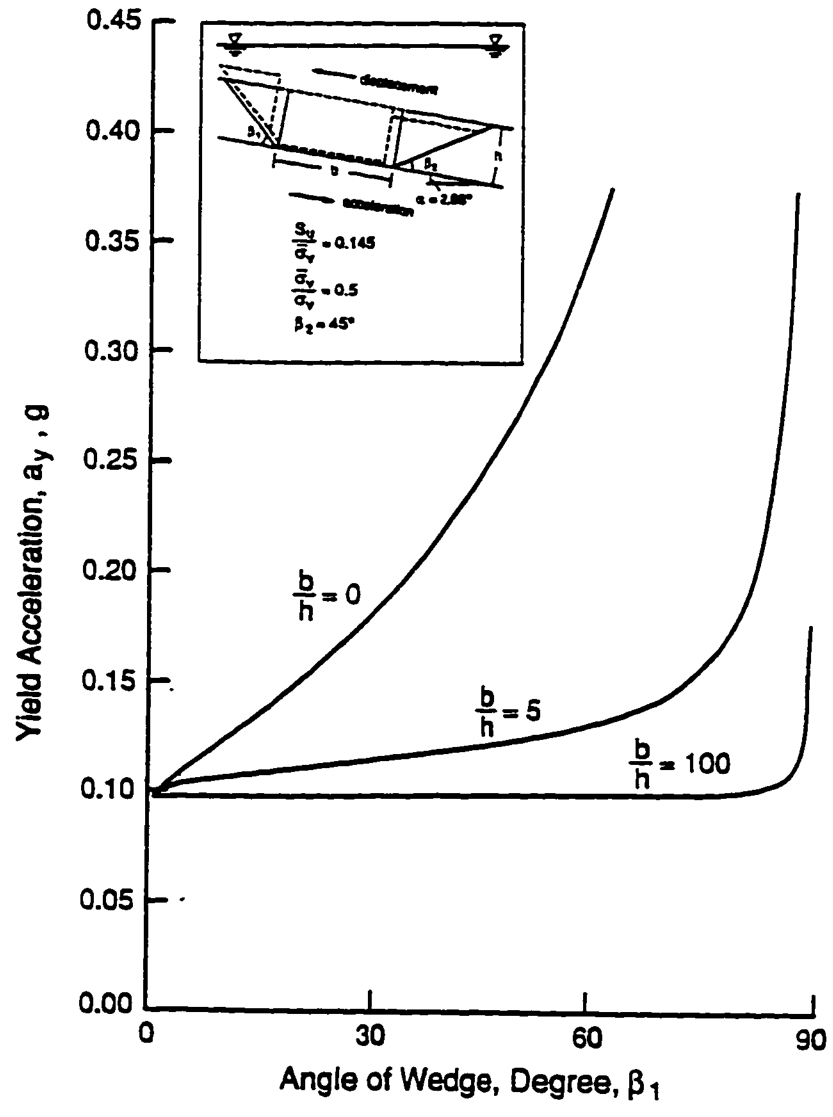


Figure 2.41 Variation of downhill yield acceleration with active wedge geometry and block aspect ratio. Active wedge angle held constant at 45 degrees. (after Baziar, et al. (1992))

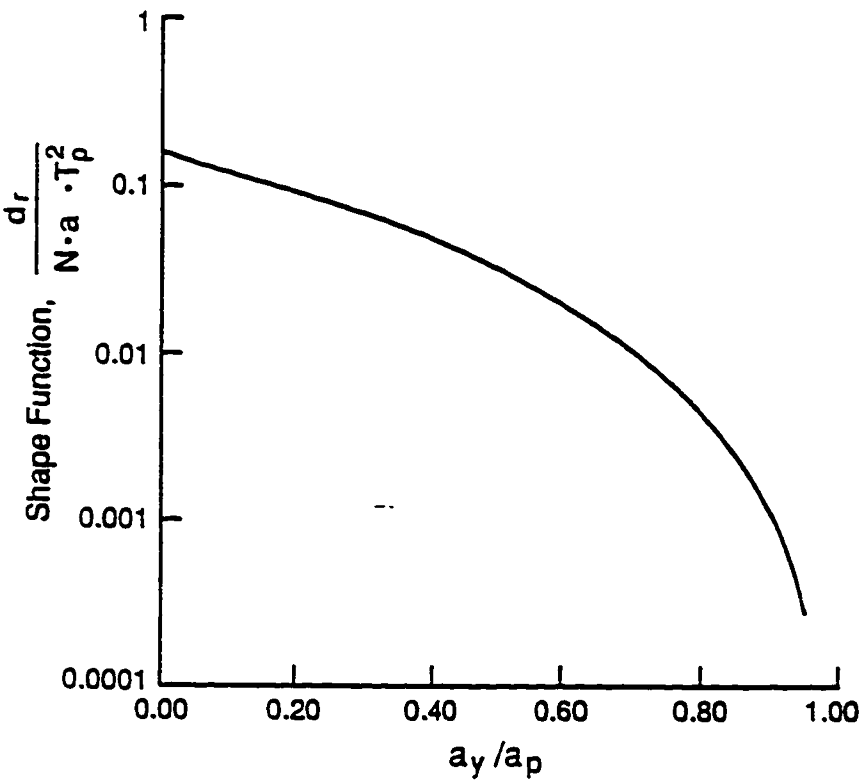


Figure 2.42 Variation of shape function in Equation (2.9) with ratio of yield to peak acceleration (after Baziar, et al. (1992))

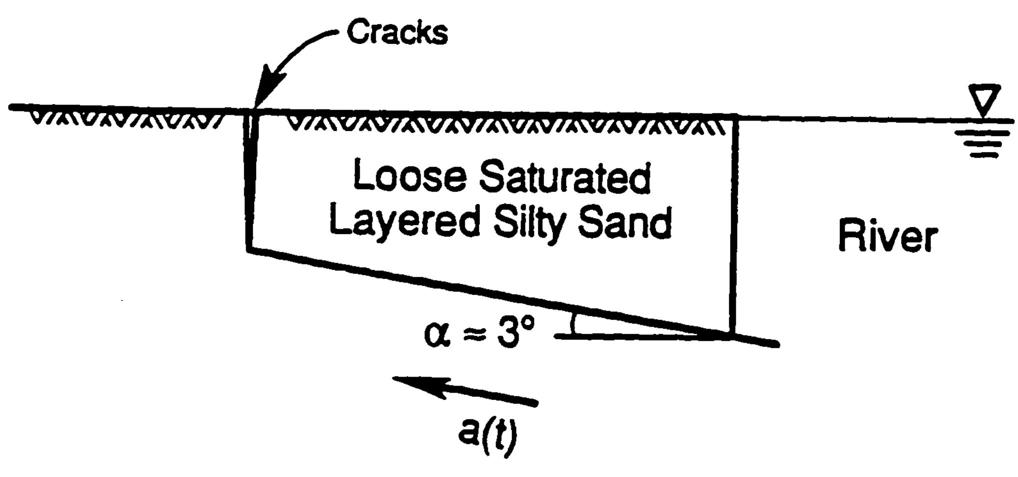


Figure 2.43 Site conditions used in conjunction with the earthquake records listed in Table 2.8 (after Baziar, et al. (1992))

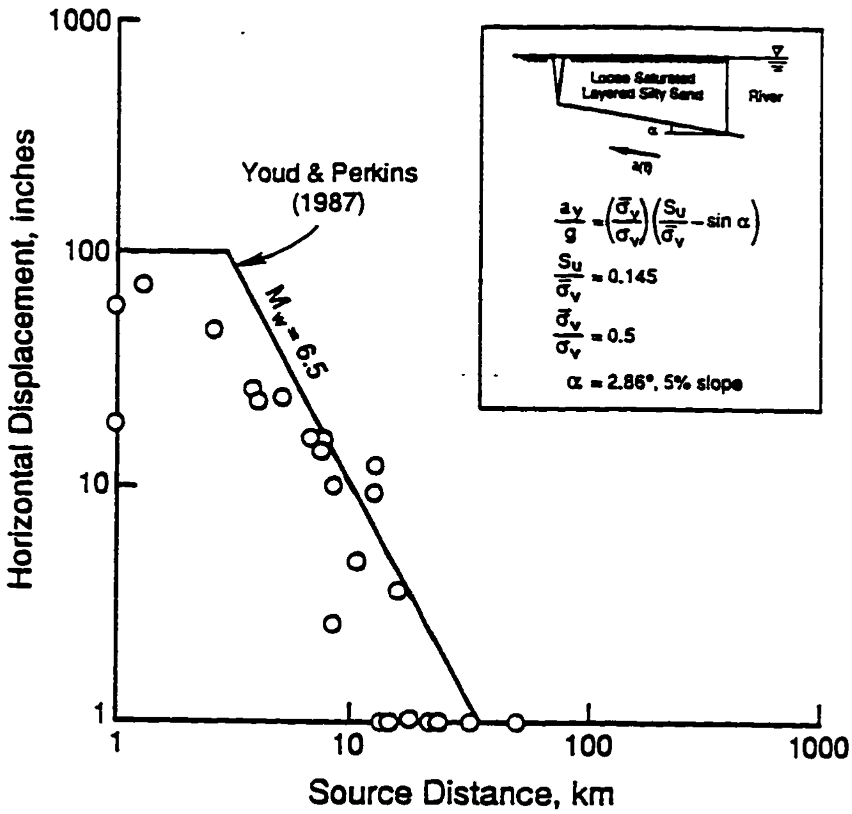


Figure 2.44 Comparison of displacements predicted using the sliding block (circles) and LSI (solid line) methodologies for the 1979 Imperial Valley earthquake data (after Baziar, et al. (1992))

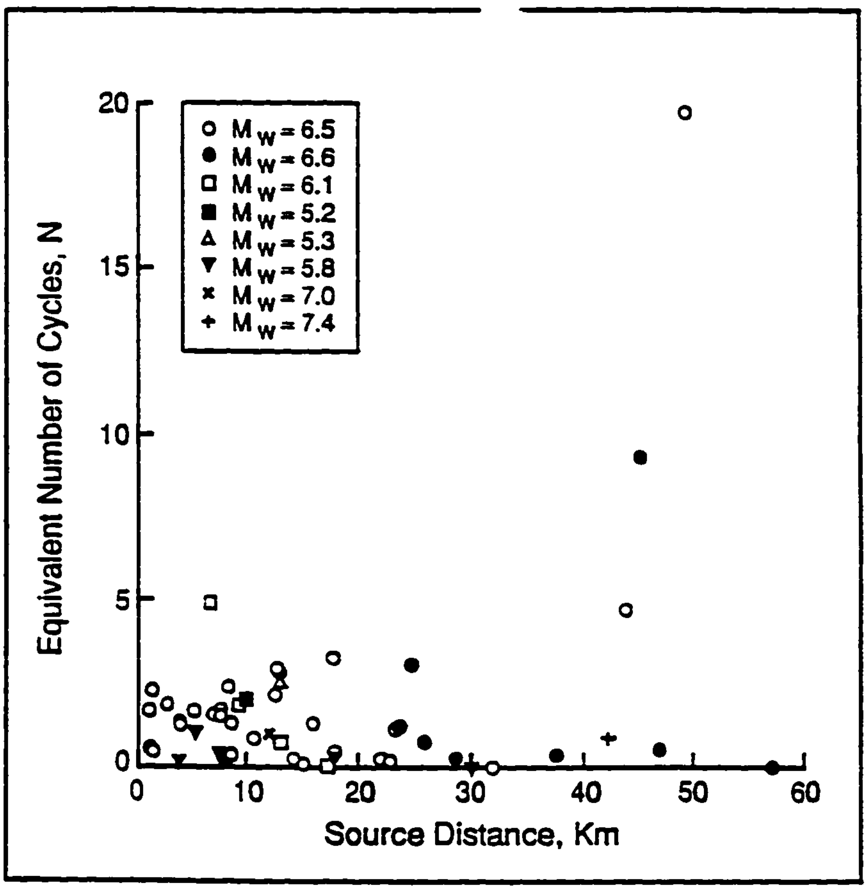


Figure 2.45 The relation between equivalent number of cycles and epicentral distance (after Baziar, et al. (1992))

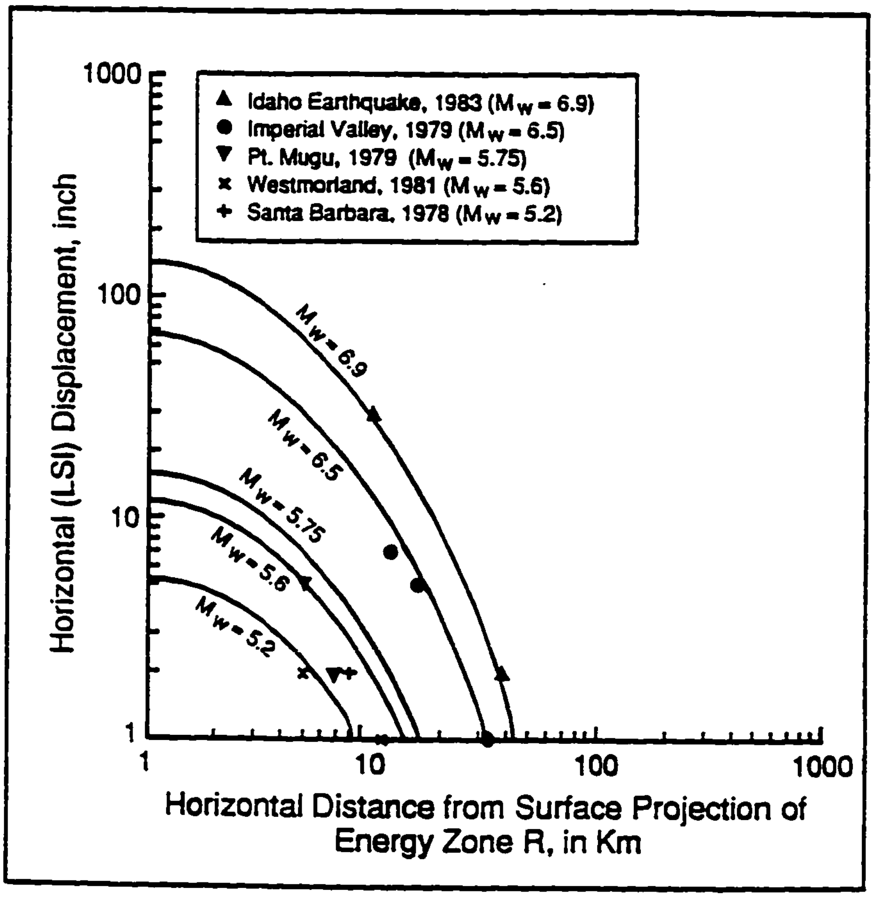


Figure 2.46 Measured displacements vs. those predicted using Equation (2.10) (after Baziar, et al. (1992))

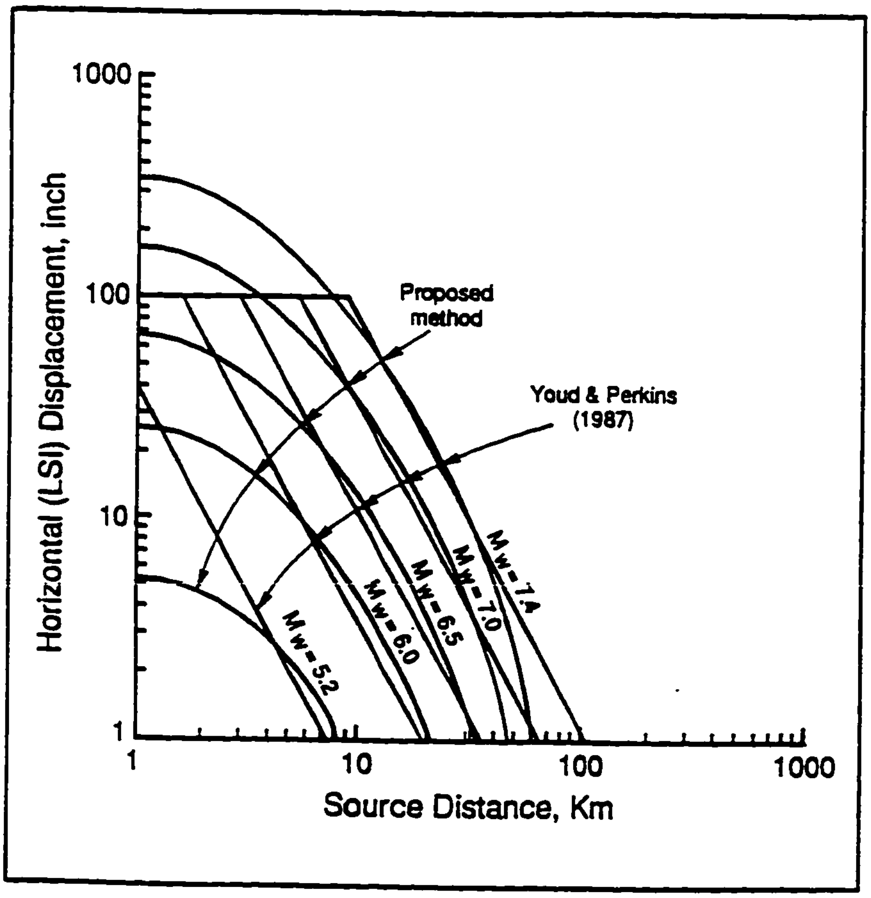


Figure 2.47 Comparison of methods proposed by Baziar, et al. (1992), and Youd and Perkins (1987) (after Baziar, et al. (1992))

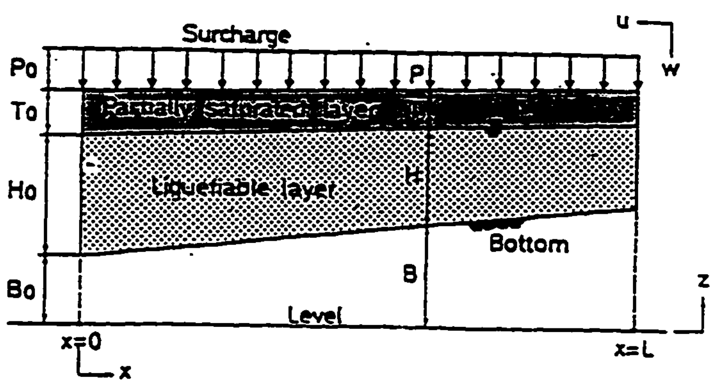


Figure 2.48 Idealized stratigraphy for use with the variational method (after Towhata, et al. (1991))

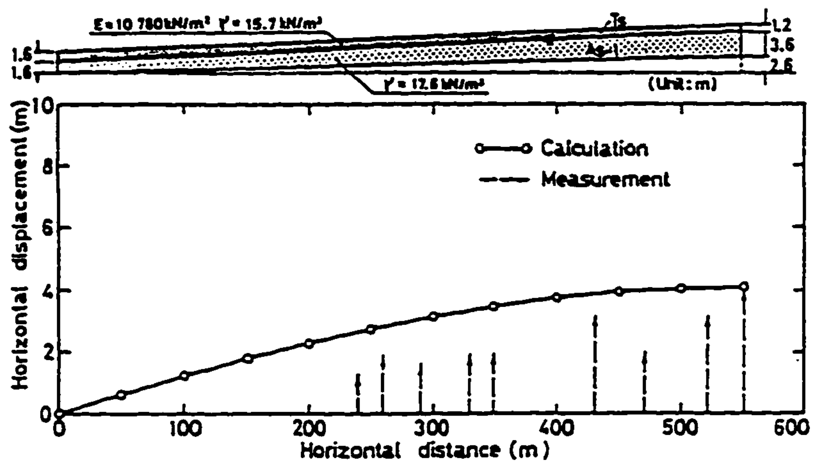


Figure 2.49 Variational method applied to the Maeyama Hill case study (Towhata, et al. (1991))

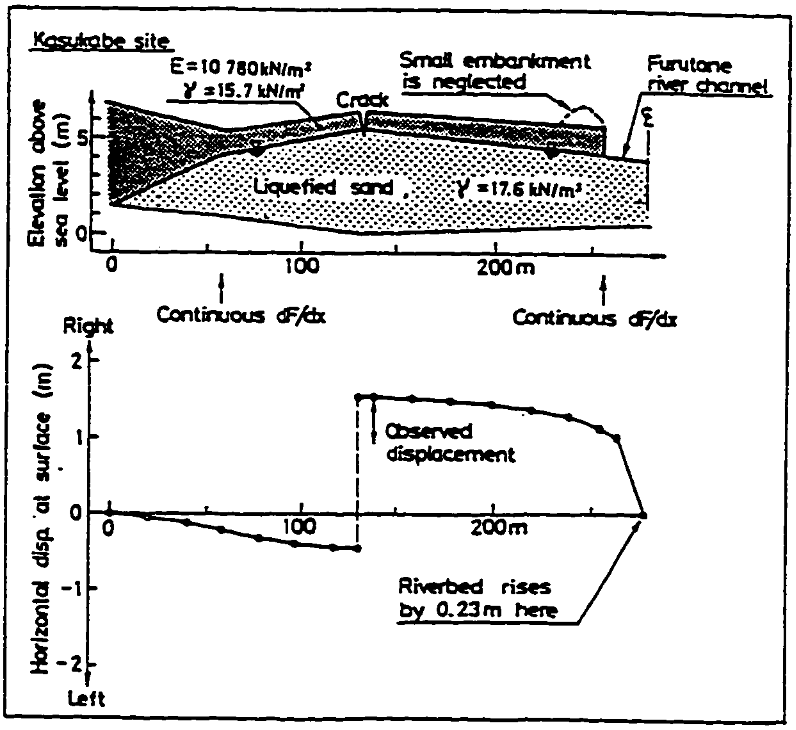


Figure 2.50 Variational method applied to the Kasukabe case study (Towhata, et al. (1991))

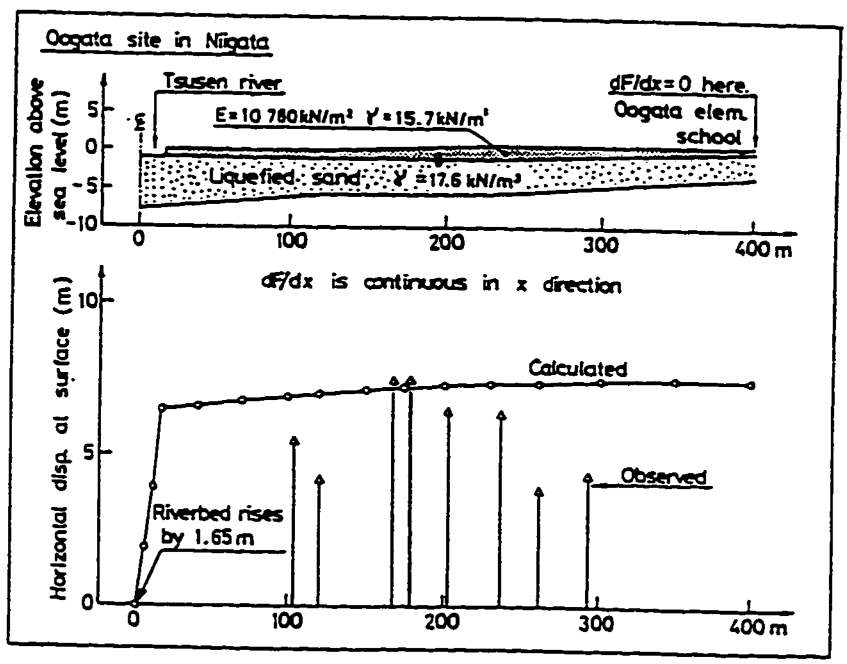


Figure 2.51 Variational method applied to the Oogata case study (Towhata, et al. (1991))

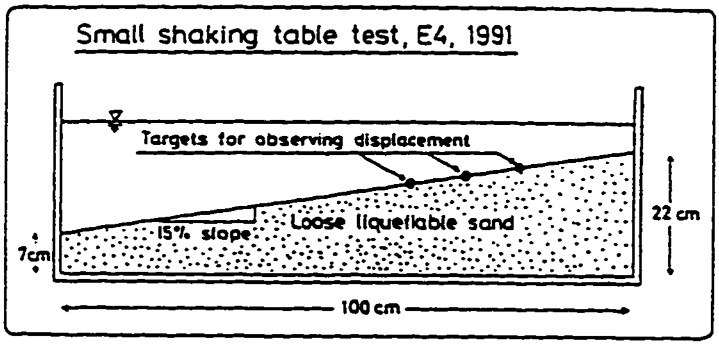


Figure 2.52 Shaking model geometry analyzed using variational method (after Towhata and Matsumoto (1992))

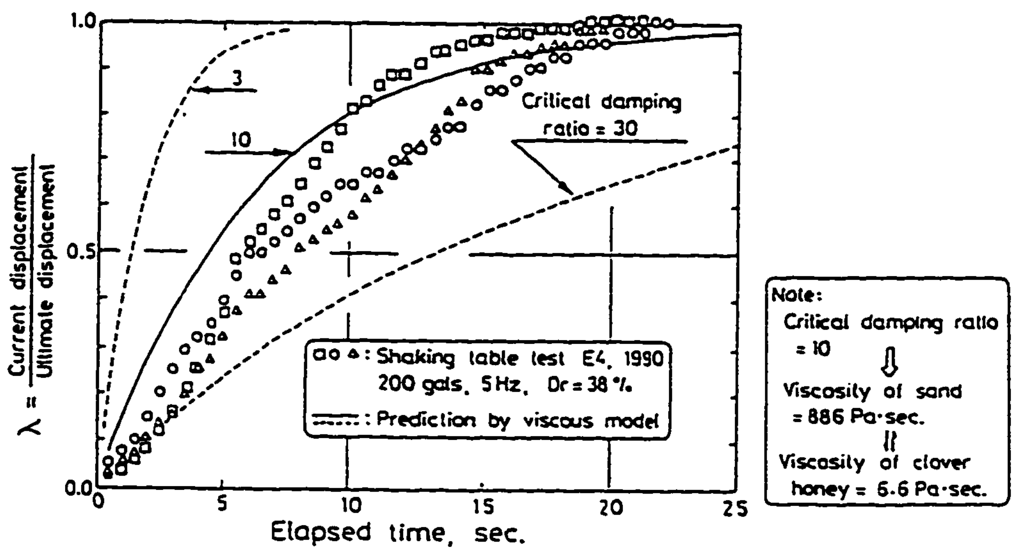


Figure 2.53 Observed and predicted development of $\lambda(t)$ in the viscous flow model (after Towhata and Matsumoto (1992))

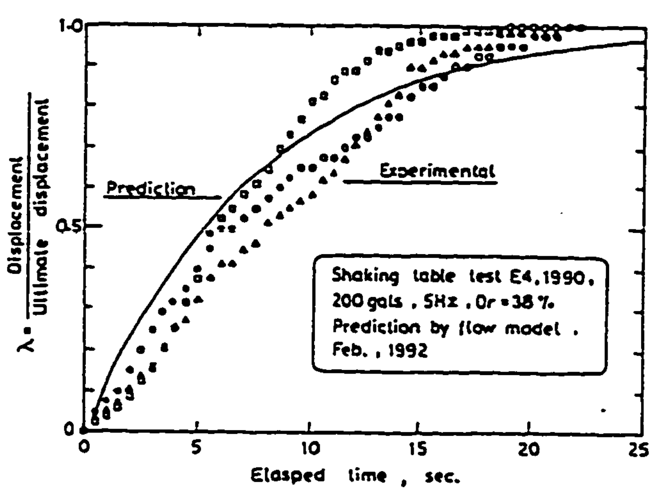


Figure 2.54 Observed and predicted development of λ(t) in the dilatent flow model (after Towhata and Matsumoto (1992))

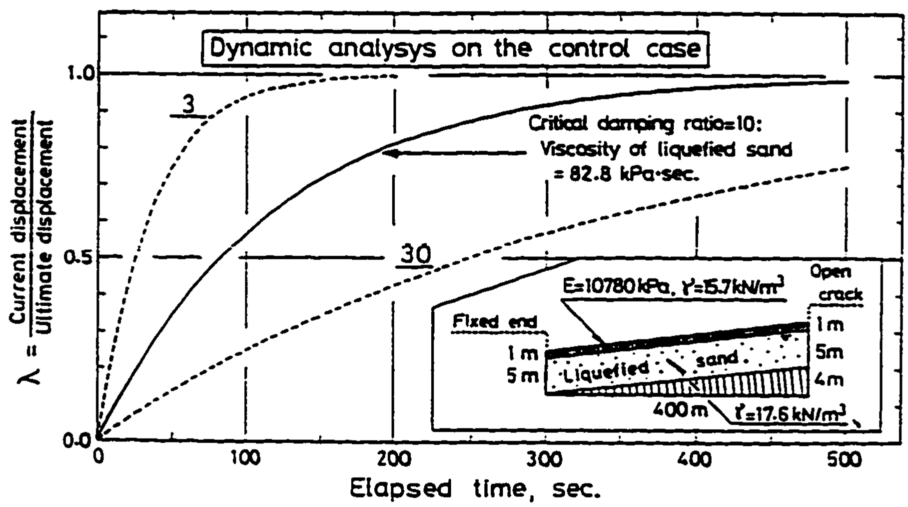


Figure 2.55 Computed displacements of hypothetical slope using the viscous model with various damping ratios (after Towhata and Matsumoto (1992))

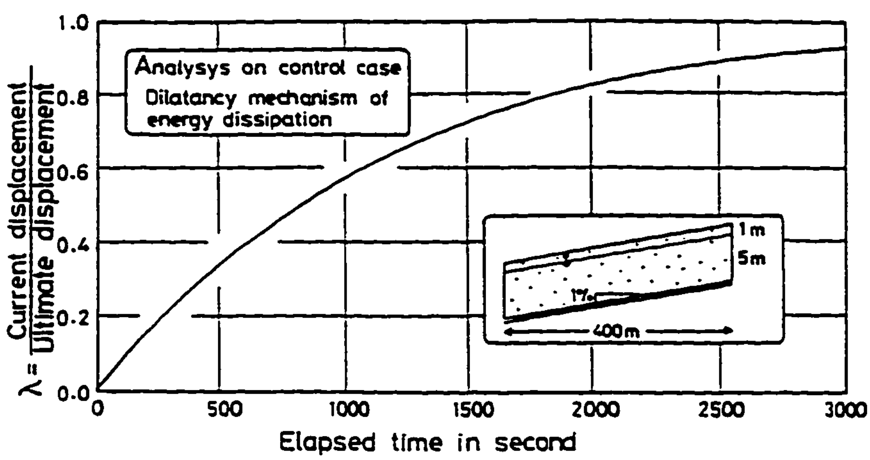


Figure 2.56 Computed displacements of hypothetical slope using the dilatent flow model (after Towhata and Matsumoto (1992))

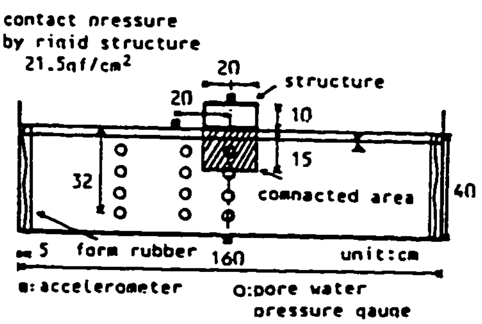


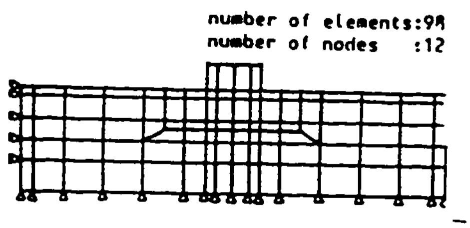


Figure 2.57 Experimental model and finite element mesh (after Shiomi et al. (1987))

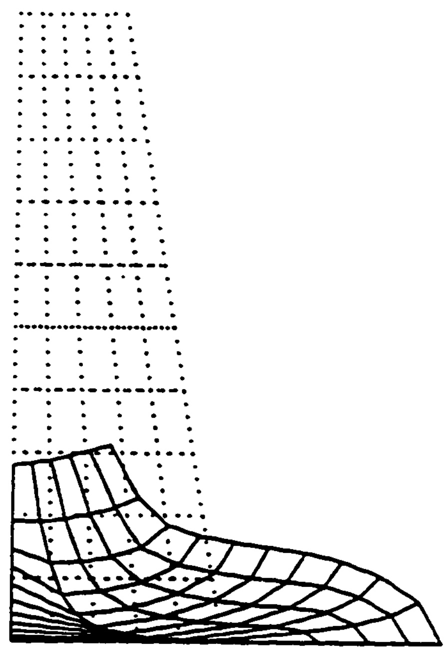

Figure 2.58 Original and deformed finite element meshes (after Famiglietti and Prevost (1991))

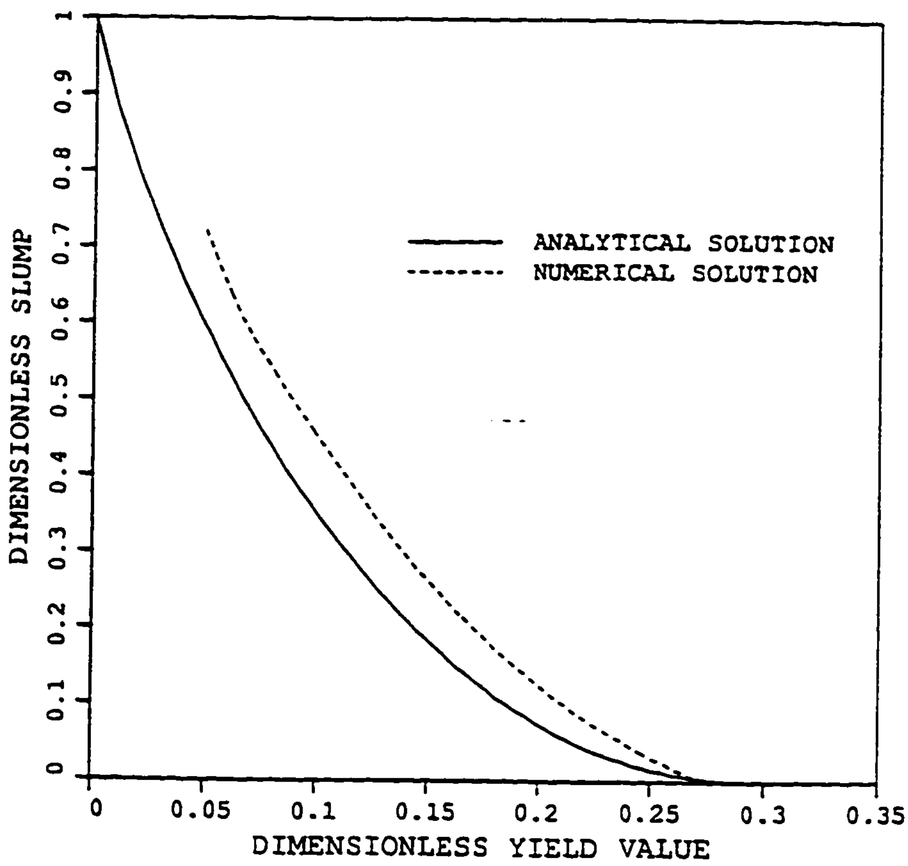


Figure 2.59 Comparison between numerical and theoretical solution for the slump test (after Famiglietti and Prevost (1991))

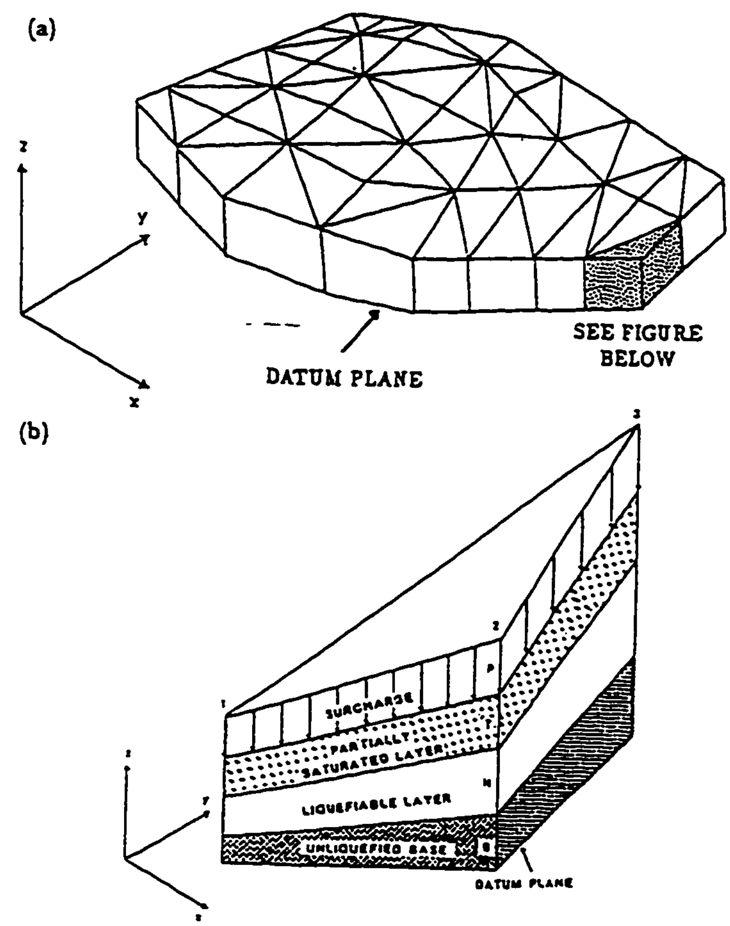


Figure 2.60 Typical (a) mesh and (b) finite element (after Orense and Towhata (1991))

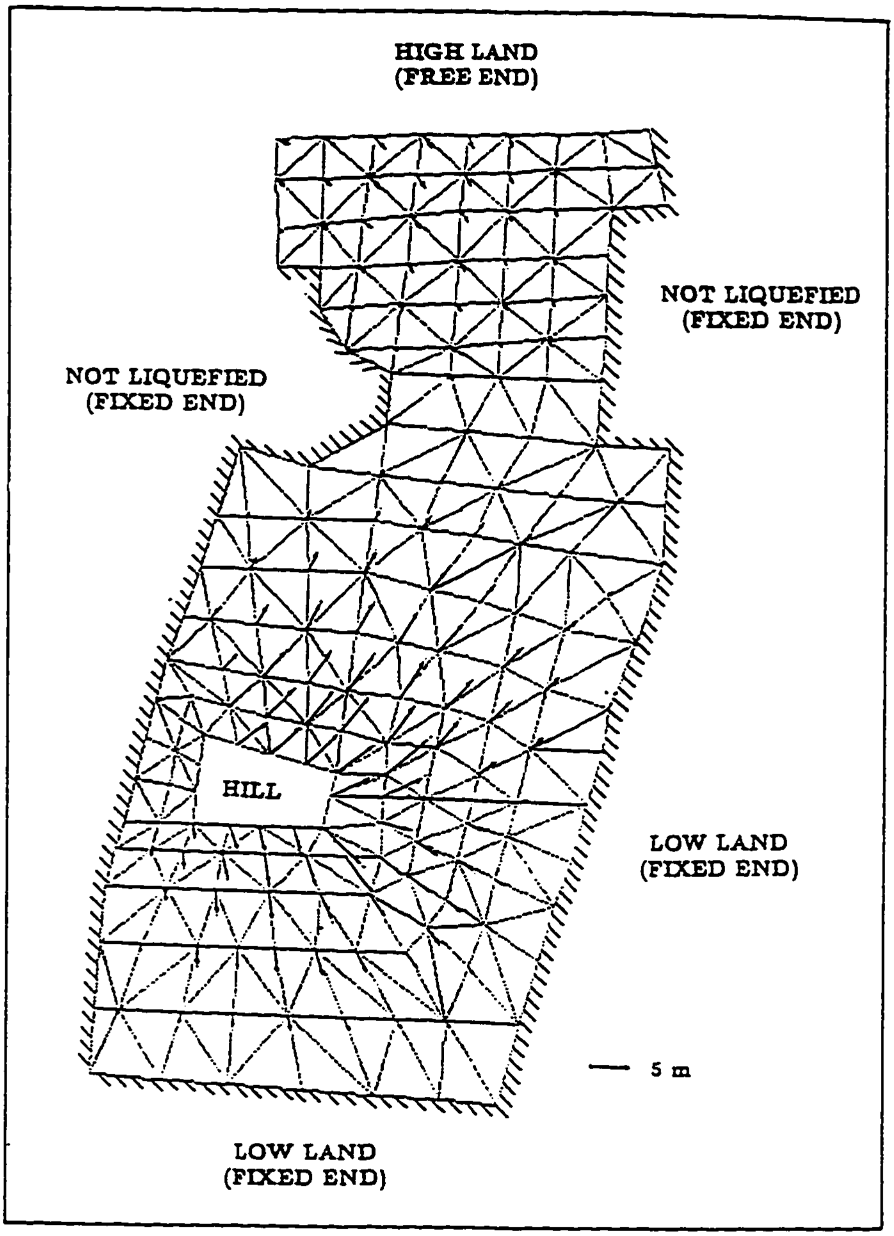


Figure 2.61 Predicted displacements at the Maeyama Hill site in Noshiro City due to the 1993 Nihonkai-Chubu earthquake (after Orense and Towhata (1991))

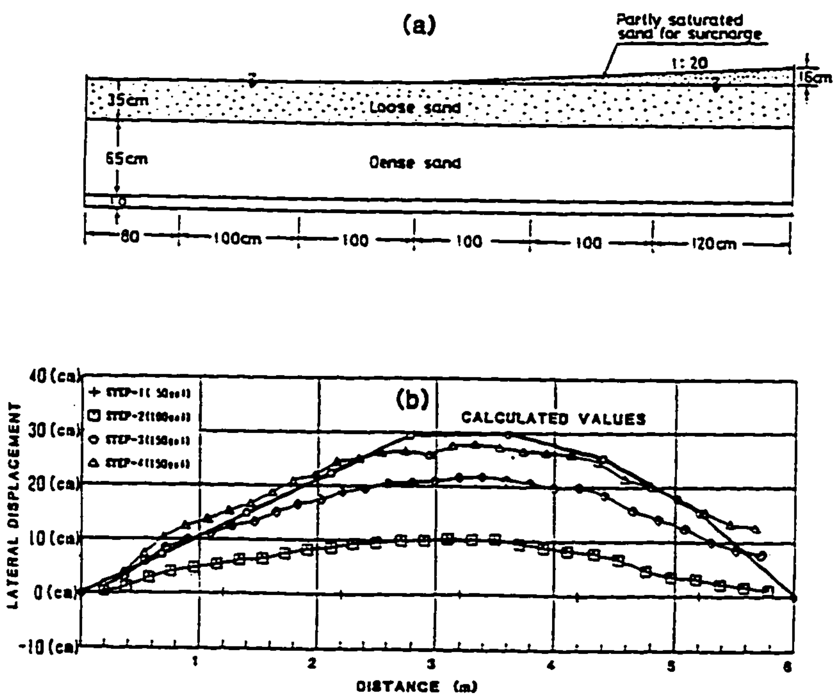


Figure 2.62 Computed and measured displacements of a sand layer tested in a large shaking table (after Orense and Towhata (1991))

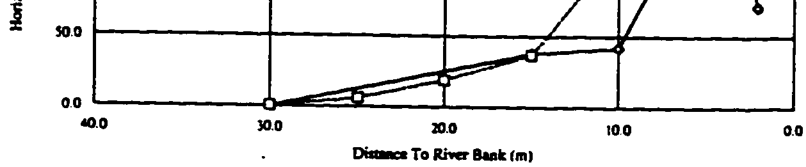


Figure 2.63 Measured and computed horizontal surface displacements at the Wildlife site during the 1987 Superstition Hills earthquake (after Gu, et al. (1994))

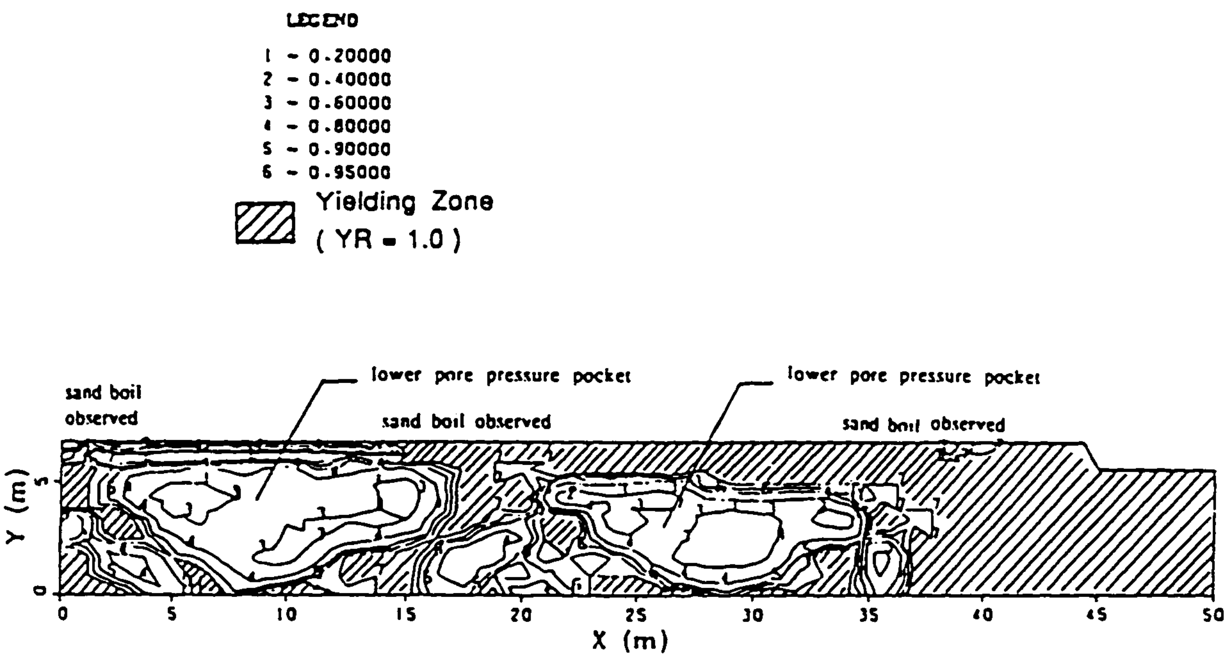


Figure 2.64 Computed yield ratio contours and observed sand boil locations at the Wildlife site during the 1987 Superstition Hills earthquake (after Gu, et al. (1994))

# Chapter 3 Pile-Soil Interaction: Previous Research

## 3.1 INTRODUCTION

Chapter 2 presented an extensive review of previous research pertaining to the lateral movement of liquefied soil. However, the ability to predict free-field deformations represents only half of the problem being addressed by this research. The second half involves prediction of the response of a pile to a general free-field motion.

This chapter reviews the previous research pertaining to pile-soil interaction. The chapter is organized into six sections. Section 3.2 discusses the basic concepts that govern the behavior of laterally loaded piles under both static and dynamic loading. Section 3.3 describes case histories which illustrate the damaging effect of lateral spreading on pile foundations. Section 3.4 reviews the relatively few experimental efforts to investigate pile-soil interaction. Previous analytical studies of pile-soil interaction are discussed in Section 3.5. Section 3.6 discusses the limitations of the research, while Section 3.7 contains conclusions based on these limitations.

## 3.2 LATERALLY LOADED PILES

As mentioned in Chapter 1, piles represent a very efficient means to resist downward-acting vertical loads such as those induced by gravity. However, their relative flexibility in bending compromises their ability to resist lateral loads. Piles may be subjected to several types of lateral loads. If loading is applied slowly so that inertial effects are negligible, then the loading may be considered "static." Section 3.2.1 contains a detailed discussion of this type of loading. Alternatively, if the loading occurs so rapidly that significant inertial forces develop, than the loading is said to be "dynamic." Section 3.2.2 discusses the dynamic case. Each section discusses two ways in which lateral loads may be applied to the pile: as either a concentrated load from the superstructure, or a distributed load along the pile length from soil movement.

### 3.2.1 Static Loading

Piles are commonly designed to resist static lateral loads. These may be actual long-term static loads or "quasi-static" design loads that represent the dynamic effect of wind or seismic events in a simplified lateral force procedure (ICBO, 1994). Figure 3.1 shows an idealized displacement profile of a pile subjected to a static lateral load at its head. The displacement is maximum at the pile head and attenuates rapidly with depth. Furthermore, the sign of the displacement varies with depth. For linearly elastic soils, the displacement profile may be described by an exponentially-decaying harmonic function. In actual soils, significant yielding occurs near the pile-soil contact, but the displacement profile is qualitatively similar. Nonlinear pile-soil interaction may be characterized with the aid of "p-y" curves (O'Neill and Murchison (1983)), illustrated in Figure 3.2. The ordinate, p represents the pile-soil interaction force per unit length of pile, while the the abscissa, y represents the pile movement relative to the free-field.

Static loading may also be applied to a pile by movement of the surrounding soil. If a pile has no flexural stiffness, then it would conform exactly to the free-field movement of the soil. Alternatively, if the pile was rigid (infinite flexural stiffness), it would translate and/or rotate, but develop no curvature in response to the free field movement. Actual piles are somewhere in-between these two extremes. Figure 3.3 shows the displaced shape of a pile with finite rigidity subjected to an arbitrary free-field motion. Obviously, the displaced shape of a pile depends on its stiffness relative to that of the surrounding soil, thus producing a static soil-structure interaction problem.

### 3.2.2 Dynamic Loading

In contrast to the previous section, certain classes of piling must be designed to resist loads that are dynamic in nature. This may include piles supporting vibrating machinery, piles designed using the dynamic force procedure of the Uniform Building Code, and piles subjected to general dynamic soil deformations. Novak (1991) presented an assessment of pile dynamics research that focused on dynamic pile-soil interaction. The displacement pattern of dynamically-excited piling is qualitatively similar to that produced by static loading. However, dynamic loading gives rise to inertial and damping forces which may have a significant effect on the pile response. It is convenient to separate dynamic pile-soil interaction into two components: the near-field and the far-field. These are discussed in greater detail below.

#### 3.2.2.1 Near-Field Behavior

The near-field consists of the region of soil adjacent to the pile that is strained inelastically as the pile moves laterally. Under dynamic loading, the near-field dissipates energy largely through hysteretic behavior. The motion of the soil within the near-field is influenced by the motion of the pile and, consequently, imparts inertial forces on the pile. Figure 3.4 illustrates idealized near-field behavior under cyclic loading.

#### 3.2.2.2 Far-Field Behavior

The far-field consists of the region of soil beyond the shearing influence of pile deformation. As a pile vibrates, it emits acoustic waves – energy that spreads out radially and does not return to the pile. The far-field represents this type of energy dissipation in what is known as "radiation damping." Figure 3.5 illustrates this idea for the case of a pile dynamically loaded at its head. Radiation damping is a geometric, frequency-dependent phenomenon.

## 3.3 CASE HISTORIES

The damaging effects of soil displacements on pile foundations is well-documented from past earthquakes. Some of this damage has been caused by the dynamic response of the pile during strong ground shaking. At sites subject to lateral spreading, however, most of the damage can be attributed to the loads applied to the piles by the lateral spreading soil.

A thorough review of available forensic data involving lateral spreading-induced pile damage was conducted. Brief desriptions of these case histories, including the earthquake, site, structure, and construction for each, are summarized in Table 3.1. Due to the paucity of data available for most of these sites, only case histories for which geotechnical, seismological, and structural data is available were studied in detail. The following sections contain additional information regarding this subset of case studies from Table 3.1.

### 3.3.1 Alaska (1964)

The Great Alaska earthquake occurred on March 27, 1964 and registered 8.3 to 8.4 on the $M_L$ scale (Bartlett and Youd, 1992). The epicenter was located in the Chugach Mountains, about 130 km east-southeast of Anchorage. The earthquake caused numerous slope failures and widespread damage to bridges and buildings. Most of the building damage was caused by extreme ground shaking. However, many of the highway and railroad bridges located in alluvial plains suffered damage due to abutment and pier movements caused in part by lateral spreading.. Ninety two highway bridges were severely damaged or destroyed (Kachadoorian, 1968), and seventy five railroad bridges were moderately to severely damaged (McCulloch and Bonilla, 1970). Figure 3.6 shows lateral spread induced deformations of a Matanuska Valley railroad bridge. This pattern was typical of many of the bridge structures which were damaged. Liquefaction-induced lateral spreads shifted flood plain deposits toward stream channels at many localities reducing channel widths by as much as 2 m. Ground fissures generally developed parallel to the river banks at lateral spread locations (up to 300 m away from riverbanks).

Table 3.1 lists 15 bridge sites in Alaska for which relatively detailed geotechnical and structural data is available. Most of the data from these sites is contained in forensic reports prepared by Kachadoorian (1968) for the highway system and by McCulloch and Bonilla (1970) for the railway system. Their reports contain information such as photographs, topographic maps, site stratigraphy, structural details, construction records, measurements of surface displacement, and damage descriptions. Geotechnical and seismological data is contained in Bartlett and Youd (1992). This report contains borehole data as well as estimates of liquefaction extent. One shortcoming of the Alaska case histories is the absence of strong motion accelerogram data.

### 3.3.2 Niigata (1964)

As described in Section 2.3.1, the epicenter of the magnitude 7.5 quake was located at a depth of about 40 km below the Sea of Japan about 50 km west of Niigata. Many pile-supported structures located in the vicinity of the Shinano River were heavily damaged during the Niigata earthquake. In all cases, the damaged structures were situated on loose, alluvial deposits or hydraulic fill. It appears that liquefaction-induced lateral spreads within these soils caused much of the observed damage.

Table 3.1 lists three bridges and five buildings which suffered extensive foundation damage and in some cases experienced total collapse. Much of the structural and geotechnical information pertaining to these cases, including photographs, detailed borehole logs, liquefaction estimates, measurements of surface displacement, structural details, and damage reports, was collected by Hamada (1992).

Two structures which experienced severe damage due to lateral spreading include the Showa Bridge and the NHK Building. The Showa bridge consisted of simply supported spans founded on 25 m long, 30 cm diameter steel pipe piles. The bridge, which suffered a major collapse because of the earthquake, is shown in Figure 3.7(a). A post earthquake survey revealed the pile deformation indicated in Figure 3.7(b). The severe translation and rotation of the piling caused the individual spans to fall from their seats into the river channel. Eyewitness accounts indicate that the collapse occurred a short time after the completion of strong ground shaking. This chronology indicates that the pile movements, and subsequent bridge collapse were most likely caused by lateral spread displacements in the surrounding soil. Ironically, the Showa Bridge was completed just five months prior to the earthquake.

The NHK Building was a four story, reinforced concrete building situated near the Shinano River. It was supported by several hundred reinforced concrete piles measuring 12 m long and 25 cm in diameter. Following the earthquake, the building was reopened and used until 1985. At this time, it was demolished in preparation for new construction at the site. During demolition however, it was discovered that many of the piles were severely damaged. Figure 3.8(a) shows pile damage typical of the 74 piles extracted from the site. All 74 piles had developed plastic hinges near their top and bottom during the 1964 event. A survey was conducted, which indicated that pile caps had translated about 1 m towards the Shinano River channel, as shown on the figure. Furthermore, the crack patterns indicate that the piling failed by monotonic deformation. A subsurface profile of the site, along with SPT data, is shown in Figure 3.8(b). The figure also indicates the likely zone of liquefaction within that profile estimated by Hamada (1992). The liquefied layer allowed for large horizontal displacement between the surficial fill soil and the medium dense alluvial soil below the piling, which ultimately failed the piles at two locations.

### 3.3.3 Imperial Valley (1979)

The Imperial Valley earthquake (Section 2.3.3) caused extensive structural damage to buildings and industrial facilities. The Highway 86 crossing of the New River was damaged from ground deformations thought to be the result of liquefaction-induced lateral spreading. Chapter 2 contains a brief description of the earthquake within the Heber Road case study. Information on the New River bridge site has been presented by Dobry et al. (1992), and contains seismic, geotechnical, and structural data. Additionally, the reconnaissance report by Brandow and Leeds (1980) contains damage descriptions, structural details, and photographs.

Figure 3.9(a) shows a profile view of the bridge, along with the presumed subsurface conditions. The bridge consisted of eight continuous reinforced concrete spans supported on pile bents with six piles per bent. Each pile consisted of a concrete-filled Raymond step-tapered shell extending about 9 m below the ground. Above the ground, octagonal cast-in-place piers connected the piles to the bridge deck. A plan view of the bridge, which indicates observed ground cracking and measured bridge displacements, is shown on Figure 3.9(b). This shows that the bridge, which crosses the river at an oblique angle, rotated counterclockwise due to the lateral spread displacements. Structural damage was limited to minor cracking and spalling of the piling/bridge deck connection at bents 2 and 8.

### 3.3.4 Nihonkai-Chubu (1983)

Liquefaction-induced lateral spreads accompanying the 1983 Nihonkai-Chubu earthquake were described in Section 2.3.4. The subsurface profile, along with the zone of suspected liquefaction is given in Figure 2.15. Figure 2.16 shows ground surface deformations mapped at the Gaiko Wharf facility in the city of Akita. The foundation piles of the warehouse shown on this figure sustained extensive damage due to these soil movements. Damage to the 18 m long, 600 mm diameter concrete pile was concentrated at two locations, as shown in Figure 3.10. Excavation of the near-surface soils revealed a crack at a depth of about 4.9 m, located on the south side of the pile. Additionally, an inclinometer placed down the center of the pile met resistance at a depth of about 14.9 m, which indicated that the pile was severely damaged at that location, which roughly coincides with the lower bound of the liquefied zone indicated on Figure 2.15. Although this pile was not extracted, the damage and deformations suggest a scenario similar to that of the NHK Building described in Section 3.3.2.

### 3.3.5 Costa Rica (1991)

The Telire-Limon, Costa Rica earthquake occurred on April 22, 1991. The epicenter of the magnitude 7.5 event was located at a depth of 16 km about 60 km south of the coastal community of Limon. The earthquake caused widespread liquefaction and lateral spreading. Much of this occurred in loose alluvium deposited by the coastal rivers which flow into the Caribbean Sea south of Limon. Lateral spreading caused the collapse of three pile supported bridges along Route 36 south of Limon (Yoshida et al., 1992). Schematic diagrams for these three bridges appear in Figure 3.11 through Figure 3.13. These figures also contain SPT blowcount data, and post-earthquake assessments of liquefaction potential. All of these bridges consisted of simple reinforced concrete spans situated on pile supported piers and abutments. The figures indicate that both vertical and batter piles were used to support the piers, and also give an indication of pile length, however, specific foundation details are not known. The surficial indication of horizontal displacement, along with the liquefaction assessment, indicates that all of these failures were caused by lateral spreading.

## 3.4 EXPERIMENTAL INVESTIGATIONS

Relatively few experimental studies have been undertaken to investigate the effect of lateral spreading on pile foundations. Experimental modeling of free-field soil behavior is difficult, but adding a pile to the experimental model complicates the instrumentation, control, and interpretation of results even further. This section describes several recent experimental programs that are divided into two parts. The first describes dynamic response models and the second details ultimate resistance models.

### 3.4.1 Dynamic Response Models

Dynamic response modeling attempt to replicate the dynamic conditions that exist in a laterally spreading soil. This has been typically accomplished through the use of shaking tables. However, recent work using the geotechnical centrifuge allows for better representation of prototype effective stress states in small models.

#### 3.4.1.1 Yasuda et al. (1992)

Yasuda et al. (1992) performed a series of 22 shaking table tests to evaluate the effect of potential countermeasures on lateral spread displacements. The test bed is shown in Figure 3.14, and measured 100 cm long, 60 cm wide, and 65 cm high. Liquefaction was constrained to a loose 20 cm thick sand layer. The slope of the liquefied layer was held constant at 3%. Thirteen of these tests studied the effect of pile foundations on lateral spread deformations. Prototype "steel" piles were modeled with 2 cm diameter PVC pipe. Both single-row and double-row configurations were tested. Pile spacings varied from 1.7 to 5.5 diameters, and the effect of drainage was investigated by drilling small holes in the piles for five of the tests. A 3 Hz harmonic base excitation was used to initiate liquefaction, and was continued for 10 s thereafter.

The tests were conducted with very little instrumentation, as only the ground surface displacements at the end of the test were measured. The test results indicated that the magnitude of lateral spread displacement could be reduced by introducing piles into the flow regime. Furthermore, by spacing the piles closer and closer, this reduction in soil displacement became more pronounced. By adding drainage holes in the piles, the displacement was further reduced in some cases.

3.4.1.2 Nomura, et al. (1991)

In this study, a shaking table was used to investigate soil-pile-structure interaction during liquefaction. A diagram of the model is shown in Figure 3.15, and consisted of a rectangular shear box shaking table which had a model pile placed in a loose, saturated sand deposit. A mass representing a structure was attached to the top of the pile. The input motion consisted of scaled earthquake records, and the model was instrumented with strain gages, LVDT's, pore pressure transducers, and accelerometers. The authors did not create a flowing or lateral spreading condition as did the previous researchers. However, the extensive instrumentation yielded enough data to make meaningful comparisons to analytical predictions made by the authors.

3.4.1.3 Liu and Dobry (1995)

Centrifuge tests conducted by Liu and Dobry (1995) may yield significant insight as to the effect of lateral spreading on pile foundations. The test set-up is shown in Figure 3.16 and involves a model pile in a liquefiable soil layer with a level surface. The centrifuge was brought to a radial acceleration of 40 g, and shaking was applied to the base in order to initiate liquefaction. The pile head was then subjected to harmonic lateral displacements, as shown in Figure 3.17(a). Figure 3.17(b) shows the increase of lateral force amplitude with time as excess pore pressures (Figure 3.17(c)) dissipated. Using the strain gage data, the authors were able to back-calculate the effect of excess pore pressure ratio on p-y behavior. This was expressed by defining a degradation coefficient, Cu as the ratio of degraded p-y strength to initial p-y strength. The values of Cu correlate very strongly with pore pressure ratio, as shown in Figure 3.18. The authors proposed to develop guidelines for degrading standard p-y curves as a function of pore pressure ratio.

### 3.4.2 Ultimate Resistance Models

Unlike dynamic response models, ultimate resistance models attempt to study pile-soil interaction in a quasi-static or steady-state fashion. This simplifies some of the scaling and instrumentation difficulties associated with fully dynamic models.

3.4.2.1 Tokida et al. (1992)

Tokida, et al. (1992) employed neither flexible piles nor harmonic base excitation to study drag induced by lateral spreading. Rather, groups of rigid piles were pulled through a loose, saturated sand deposit which had been shocked into a state of liquefaction. Figure 3.19 shows the test set-up, which included a load cell mounted on the pile cap with which to measure the group resistance as the piles as they were dragged through the sand. Pore pressures were monitored concurrently at four depths in the sand deposit. The test results for several pile group configurations are shown in Figure 3.20, which indicates that ultimate pile resistance decreased with increasing excess pore pressure and also with decreasing pile cap velocity. These results indicate that the measured drag forces acting on the piles were viscous in nature.

3.4.2.2 Hamada et al. (1992)

Hamada et al. (1992) performed a series of tests to investigate the viscous behavior of liquefied sand. Steel spheres of different diameters (3.0, 4.0 and 5.0 cm) were pulled through a liquefaction chamber at velocities ranging from about 0.5 to 9 cm/s after a state of liquefaction was initiated and maintained by harmonically shaking the chamber. The cylindrical test apparatus measured 30 cm high and 30 cm in diamter, and is shown in Figure 3.21. A total of 76 diameter/velocity combinations were investigated. The force required to maintain constant velocity was measured, and used to compute an equivalent viscosity. This equivalent viscosity was found to be strongly dependent on the diameter of the sphere. Based on these results, the authors concluded that liquefied sand can not be characterized as an ideal viscous fluid.

## 3.5 ANALYTICAL STUDIES

The response of pile foundation to dynamic loads has received considerable attention in the research community over the past two decades. Novak (1991) outlined the more recent developments, including pile group effects, material non-linearites at the pile-soil interface, and pile-soil-structure interaction. Most existing analytical methods are applicable to the dynamic response of a linear pile or piles embedded in a linear soil stratum. The lateral spread phenomenon, however, involves significant nonlinearities that introduce added complexity. A general method should be able to predict the pile response both during strong shaking (when inertial effects are greatest), and afterwards (when large free-field lateral displacements often occur). Because of the complex, nonlinear interaction between free-field deformations and the pile response, practical solutions must be obtained through the use of numerical techniques.

This section describes techniques which have been proposed to analyze dynamic pile response. The analytical topics are organized into two parts. Models which characterize the pile-soil interaction force are presented in Section 3.5.1. Section 3.5.2 describes analytical methods used to compute dynamic pile response.

### 3.5.1 Pile-Soil Interaction Models

Any analytical approach to the dynamic response of piles must be able to represent the interaction between the pile and the soil in the near-field. This involves characterization of the soil resistance to pile displacement over a broad range of pile displacements. This section describes previous research aimed at characterizing pile-soil interaction.

Matlock et al. (1978) described one of the earliest attempts to incorporate a near-field model to predict pile response to earthquake motions. The model used a nonlinear spring to represent the soil resistance. The model also allowed for a gap to form between the pile and the near-field soil. This allows for pile-soil interaction behavior as shown in Figure 3.22.

A more rigorous description of near-field behavior was proposed by Nogami and Konagai (1992). Their model (Figure 3.23) combined the hysteretic, nonlinear p-y curves with. A schematic of their model is shown in, a consistent mass matrix used to express the near-field inertial interaction.

Novak et al. (1978) presented the first analytical description of far-field behavior through the use of frequency-dependent, complex impedance functions. The stiffness and damping components of this method are shown in Figure 3.24. Unfortunately, the frequency-domain nature of Novak's procedure does not allow direct application to practical earthquake engineering problems. As an improvement, Nogami and Konagai (1988) developed a time-domain expression of far-field behavior that consisted of three Kelvin models linked in series with a lumped mass. A schematic of this model is shown in Figure 3.25. The values ascribed to the mass, springs, and dashpots depend on common physical properties of the far-field soil. Their model accurately replicates the impedance of the Novak model over a wide frequency range, as shown in Figure 3.26.

### 3.5.2 Dynamic Soil-Structure Interaction Models

Two types of numerical procedures have been successfully applied to the solution of dynamic pile response. These include the finite element method and the lumped parameter method. The finite element method reduces the governing partial differential equation to a system of ordinary differential equations through the use of assumed shape functions. The lumped parameter method involves discretizing the continuum into an assemblage of lumped masses connected by springs (Penzien et al., 1964). This section describes the application of these two methodologies to dynamic pile-soil interaction problems.

#### 3.5.2.1 Slyh and Jackura (1993)

The authors presented a finite element formulation that is currently being used by CALTRANS engineers for computing the internal forces in piles from general free-field deformations. In this method, the pile is modeled as a one-dimensional Winkler beam that is connected to the free-field by a series of nonlinear springs that follow a hysteretic Masing criteria. A schematic of the model is shown in Figure 3.27, which shows the nonlinear springs along with viscous dampers attached to the pile along its length. However, instead of being attached to the free-field, these are rigidly attached to the bottom of the pile, which implies that the viscous force acting on the pile at a given depth is proportional to the velocity of the pile at that depth relative to that at the pile base. The purpose of these dashpots is unclear. If the dashpots are intended to represent radiation damping in the far-field, they should be "connected" to the far-field. Conversely, if the dashpots are used to apply a low level of damping for numerical stability, the model then neglects far-field effects.. The authors relied on equivalent linear ground response analyses to compute the needed free-field deformations. Such analyses are incapable of modeling the pore pressure-induced softening that occurs during earthquakes, or the permanent displacements that develop as a result of lateral spreading.

Although no specific case studies were analyzed, the authors presented the results of a parametric study wherein typical values for soft, medium stiff, and stiff clays were used to define the "backbone" curves of the non-linear springs. The pile model was then subjected to several earthquake records and the results expressed as pile head acceleration response spectra. As expected, the soft site tended to amplify the input motion, resulting in higher peak spectral accelerations at the pile head. The authors did not demonstrate the applicability of the model to problems involving permanent lateral displacements of the soil.

3.5.2.2 Nomura, et al. (1991)

Nomura et al. proposed a one-dimensional lumped parameter formulation, which is schematically shown in Figure 3.28. Their procedure is more rigorous than that developed by Slyh and Jackura (1993), because the pile-soil interaction model chosen by the authors can be degraded in response to the excess pore pressures computed with the ground response portion of their model. Excess pore pressures were computed using the relatively arcane method of Martin et al. (1975). The model was used to predict the response of the shaking table test program described in Section 3.4.1.2. A comparison of computed and measured fourier amplitude spectra is presented in Figure 3.29. The numerical results showed good agreement with the experimental results.

3.5.2.3 Yasuda et al. (1991)

Yasuda et al. (1991) outlined a deformation analysis using a two-step static approach with a two-dimensional finite element model (depth and horizontal dimensions). In the first step, a static finite element analysis was performed with "pre-earthquake" soil properties to obtain the deformation of the soil under normal gravity loading. The second step involved a static analysis of the same model, but with decreased strength and stiffness properties derived from a series of 24 shaking table tests. The difference in deformation between the two models was that which the authors attributed to lateral spreading of the liquefied soil.

The methodology was used to compute displacements at a site that sustained lateral spread deformations during the 1964 Niigata earthquake. At this site, located adjacent to the Shinano River at the Showa Bridge, a sheet pile wall was thought to have partially restrained the laterally spreading sand. Unfortunately, detailed structural information regarding the wall is not known. Nevertheless, the authors ran a series of analyses to evaluate the effect of sheet pile embedment on the lateral displacements. The deformed finite element meshes for three different depths of embedment are shown in Figure 3.30. In all three cases, a degradation factor of 1/1000 (based on shaking table test results) was applied to the shear modulus of the soils within the zone of liquefaction for the second analysis step. As would be expected, the deepest embedment resulted in lowest deformation of the top of the wall.

3.5.2.4 Miura and O'Rourke (1991)

A nonlinear finite element analysis was performed by Miura and O'Rourke (1991) in an attempt to replicate the damage patterns noted in piles extracted from the NHK Building site after the 1964 Niigata earthquake (Section 3.3.2). The numerical model consisted of one dimensional, non-linear beam elements connected to the free-field by nonlinear springs, and is shown in Figure 3.31(a). The moment-curvature behavior of the pile elements was described by a tri-linear curve, and bi-linear curves (elastic-perfectly plastic) were used to describe the p-y behavior of the soil springs. Lateral spreading was simulated by incrementally applying a presumed displacement profile to the ends of the soil springs in a pseudo-static fashion. The computed bending moments are shown in Figure 3.31(b), which shows that the model predicted the formation of plastic hinges very close to the observed locations. However, it is not known if the FEM pile 'failed' at the same free-field displacement that the real pile failed.

3.5.2.5 Yoshida and Hamada (1991)

In a similar fashion to Miura and O'Rourke (1991), Yoshida and Hamada (1991) applied presumed free-field displacements to a numerical pile model. Their method, called the "seismic deformation method" was applied to case studies of failed piles which had been extracted from the A-Building and S-Building in Niigata, Japan after the 1964 earthquake. The authors employed nonlinear beam finite elements to represent the pile. A 'quad-linear' moment-curvature relation, with breaks occurring at cracking, yield, and ultimate bending moment was used to describe the pile. Soil-pile interaction was modeled with linear, non-yielding springs. Bending moments computed for two of the piles are shown in Figure 3.32, and suggest a crack pattern consistent with those of the exhumed piles. In some cases however, the computed displacement at which the ultimate moment was numerically achieved was not consistent with the displacements inferred from field observations. It is likely that this was due to the incorrect assumptions of linearity in characterization of the soil-pile interaction.

3.5.2.6 Badoni and Makris (1995)

Badoni and Makris (1995) presented a nonlinear pile response methodology based on the finite element method. The authors' formulation considered a single pile excited dynamically at its head or along its length, and is shown in Figure 3.33. Pile-soil interaction was accounted for with a single Kelvin model. The nonlinear, hysteretic behavior of the Kelvin spring was controlled by four dimensionless shape parameters. The radiation damping was controlled with the Kelvin dashpot that required the selection of a specific frequency. The authors used their formulation to replicate published pile response data taken from five field tests. In all cases, the pile was loaded statically or dynamically at the head.

The response computed with the proposed model was generally in good agreement with the experimental data.

## 3.6 LIMITATIONS OF PREVIOUS RESEARCH

The previous research is useful, but suffers from various limitations. This section discusses these limitations for each the main bodies of work presented above.

### 3.6.1 Case Histories

The literature is full of examples of damage to pile foundations caused by liquefaction-induced lateral spreading. Unfortunately, none of the written descriptions of these case histories contain enough information for detailed post-earthquake analyses. Of the case histories described in Section 3.3, the NHK Building and Showa Bridge sites of Niigata are probably the best-documented.

### 3.6.2 Experimental Investigations

Laboratory tests that study the pile response to liquefied soil introduce complexities in addition to those discussed in Section 3.4. These include such issues as scaling and instrumenting the model pile. An additional difficulty is to correctly reproduce the stress state adjacent to the pile due to installation. The shaking table tests conducted by Yasuda et al. (1992) provide valuable insight as to the effect of pile groups on the flow regime. However, because the piles themselves were not instrumented., estimates of individual p-y behavior cannot be determined.

The static liquefaction chamber tests by Tokida et al. (1992) yield insight as to the group effect of piles on the lateral spread phenomena. The fact that loads were measured makes this study especially useful, although the shock-induced liquefaction does not mimic actual site conditions.

The centrifuge work of Liu and Dobry (1995) contributes significantly to the current understanding of large strain p-y behavior in liquefied soil. The scaling problems associated with the other test regimes are eliminated in the centrifuge environment. However, the work by Liu and Dobry (1995) has the same instrumentation and secondary effects problems discussed in reference to the VELACS tests. Additionally, it may not be appropriate to study the p-y behavior - a local behavior - by modeling an entire pile. In doing so, the experimenter attempts to correctly recreate an entire boundary value problem. Unfortunately, the stress conditions on the boundary of the apparatus are not fully known at all times. Indeed, they are only known at discrete points along the boundary. This may render the task of inferring local p-y behavior impossible. Finally, because the p-y behavior was investigated while pore-pressures were dissipating, it may not be appropriate to apply the test results to problems where the pore-pressures are increasing.

### 3.6.3 Analytical Investigations

The coupled near- and far-field models of Nogami and Konagai (1988, 1992) provide a comprehensive expression of pile-soil interaction. The model combines the inertial and hysteretic effects of the near-field with the radiation damping effects of the far-field. None of the other interaction models consider the inertial effects of the near field. Most importantly, it describes the interaction force in a time-domain formulation. It is unique among the proposed interaction models in this regard. However, the Nogami and Konagai scheme has not been extended to the case of free-field excitation.

The one-dimensional methods proposed by Slyh and Jackura (1993) and Nomura et al. (1991) are promising in that non-linear soil p-y behavior can be implemented into the analysis. However, neither of these methods has been applied to the case of permanent ground displacements generated from lateral spreading. Indeed, the method of Slyh and Jackura (1993) depends upon the results of a separate analysis to determine the free-field response. The method of Nomura et al. (1991) incorporates this step within the algorithm, but their pore pressure generation scheme (Martin et al. (1975)) requires evaluating equivalent stress cycles -- an arbitrary task when confronted with earthquake loading. None of these methods properly represent radiation damping.

The two-step, two-dimensional finite element method of Yasuda et al. (1991) represents a relatively simple way of estimating post-liquefaction deformations. However, even with the knowledge of actual deformations from a real site, the authors had to iterate to determine the modulus reduction parameters which would yield reasonable displacements. Finally, it is not clear how to apply the methodology to the case of a single pile which does not obey the plane strain formulation implied by the authors.

Non-linear one-dimensional finite element methods proposed by Miura and O'Rourke (1991) and Yoshida and Hamada (1991) have merit in that they apply the lateral spread deformation in an almost quasi-static manner, with obvious computational economies. However, the crudeness of the pile-soil interaction model defeats the purpose of the sophisticated non-linear pile models that the authors used. These methods also suffer from the problematic need to know the free-field deformations a-priori.

The finite element model proposed by Badoni and Makris (1995) is severely limited due to its reliance on a specific forcing frequency to specify the radiation damping dashpot. Also, the model requires a large number of parameters to specify its nonlinear p-y stiffness, many of which have no clear physical significance.

### 3.7 CONCLUSIONS

A review of the state of knowledge regarding dynamic pile-soil interaction reveals the need for an analytical approach that accounts for nonlinear, inelastic interaction, pore pressure-induced softening, and radiation damping over a wide range of loading frequencies. The approach should ideally be flexible enough to handle any type of p-y behavior and practical boundary conditions. The development and verification of such an approach is described in Chapter 5.

Table 3.1 Pile Foundation Response - Case Study Sites

| Earthquake | Structure | Construction |
|---|---|---|
| 1964 Alaska | Railroad Bridge Milepost 146.4 Knick River crossing | Steel through girders & open timber trestle at north support. Combination of timber and steel rail piles |
| 1964 Alaska | Highway Bridge No. 1121 Knick River crossing | Under construction during earthquake Four concrete piers in place |
| 1964 Alaska | Railroad Bridge Milepost 147.1 Matanuska River crossing | Steel through trusses with steel beam approach spans |
| 1964 Alaska | Railroad Bridge Milepost 147.4 Matanuska River crossing | Steel through truss with steel beam approach spans |
| 1964 Alaska | Railroad Bridge Milepost 147.5 Matanuska River crossing | Steel girders supported by concrete piers |
| 1964 Alaska | Railroad Bridge Milepost 148.3 Matanuska River crossing | Steel girders supported by concrete piers |
| 1964 Alaska | Railroad Bridge Milepost 114.3 Ship Creek Crossing | Steel through truss with steel beam approach spans. Combination of timber and steel rail piles |
| 1964 Alaska | Railroad Bridge Milepost 64.7 Twenty-Mile River crossing | Steel trusses supported by concrete piers. Welded three-rail piles. |
| 1964 Alaska | Railroad Bridge Milepost 63.0 Portage Creek crossing | Open Timber Trestle Timber Pile Bents |
| 1964 Alaska | Railroad Bridge Milepost 63.5 Portage Creek crossing | Open Timber Trestle Timber Pile Bents |
| 1964 Alaska | Highway Bridge No. 629 Placer River crossing | Concrete girder with reinforced concrete deck. Timber pile support |
| 1964 Alaska | Highway Bridge No. 605A Snow River crossing | (under construction when earthquake occurred) Four concrete piers in place. Concrete-filled pipe piles. |
| 1964 Alaska | Railroad Bridge Milepost 3.0 Resurrection River crossing | Steel through girders with open wood trestle approaches. Three concrete piers founded on multiple rows of driven piles. |

Table 3.1 (cont.) Pile Foundation Response - Case Study Sites

| Earthquake | Structure | Construction |
|---|---|---|
| 1964 Alaska | Railroad Bridge Milepost 3.2 Resurrection River crossing | Open wood trestles |
| 1964 Alaska | Railroad Bridge at Milepost 3.3 Resurrection River crossing | Steel through girder with open wood trestle approaches |
| 1964 Niigata | East Bridge Railway Corridor Crossing | Single steel girder span Reinforced concrete piles |
| 1964 Niigata | Showa Bridge Shinano River crossing | Steel Girders Steel Pipe Piles |
| 1964 Niigata | Yachiyo Bridge Shinano River crossing | Concrete Girders Reinforced Concrete Piles |
| 1964 Niigata | S-Building: Between Showa and Yachiyo Bridges at Shinano River | Three story reinforced concrete building Circular reinforced concrete piles |
| 1964 Niigata | A-Building (Family Court House): Echigo Railway at Shinano River | Three story reinforced concrete building Circular reinforced concrete piles |
| 1964 Niigata | NHK Building: Two blocks north of Niigata Railway Station | Four story reinforced concrete building Circular reinforced concrete piles |
| 1964 Niigata | Hotel Niigata: Four blocks east of Shinano River near Bandai Bridge | (Building structure not known) Circular reinforced concrete piles |
| 1964 Niigata | Horuku Building: Two blocks north of Niigata Railway Station | Ten story reinforced concrete building with one story basement. Reinforced concrete piles |
| 1979 Imperial Valley | Highway 86 Bridge No. 58-05 New River crossing | Reinforced Concrete Girders Raymond Step Taper Piles |
| 1983 Nihonkai Chubu | Warehouse: Gaiko Wharf at Akita Harbor | (building structure not known) Hollow prestessed concrete piles |
| 1991 Costa Rica | Route 36 Bridge Viscaya River crossing | Prestressed concrete girders Pile supported piers and abutments |
| 1991 Costa Rica | Route 36 Bridge Bananito River crossing | Prestressed concrete girders Pile-supported pier and abutments |
| 1991 Costa Rica | Route 36 Bridge Negro Estuary crossing | Prestressed concrete girders Pile-supported pier and abutments |

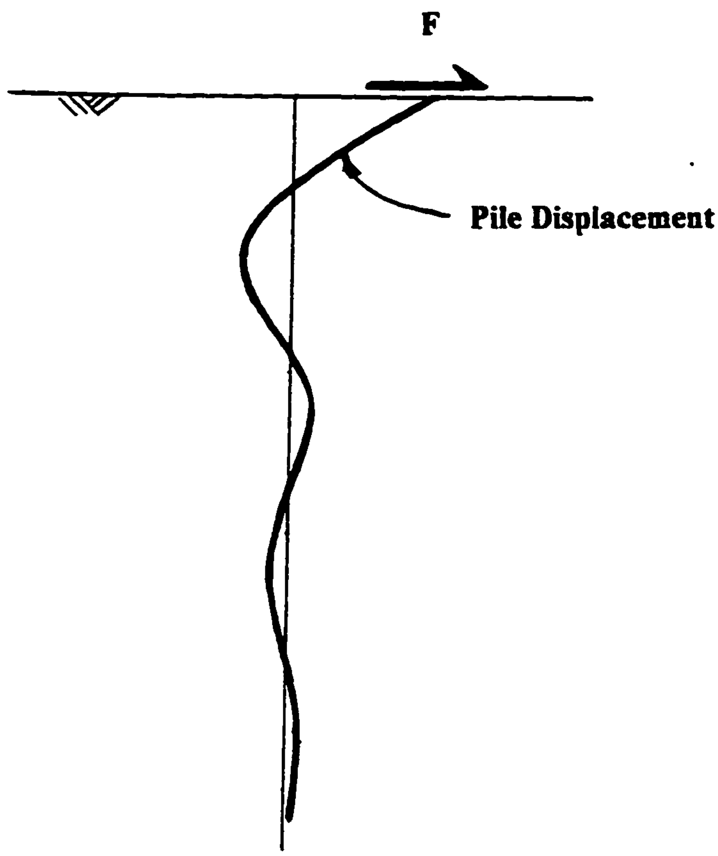


Figure 3.1 Idealized Pile Deflection Due to Static Loading at Pile Head

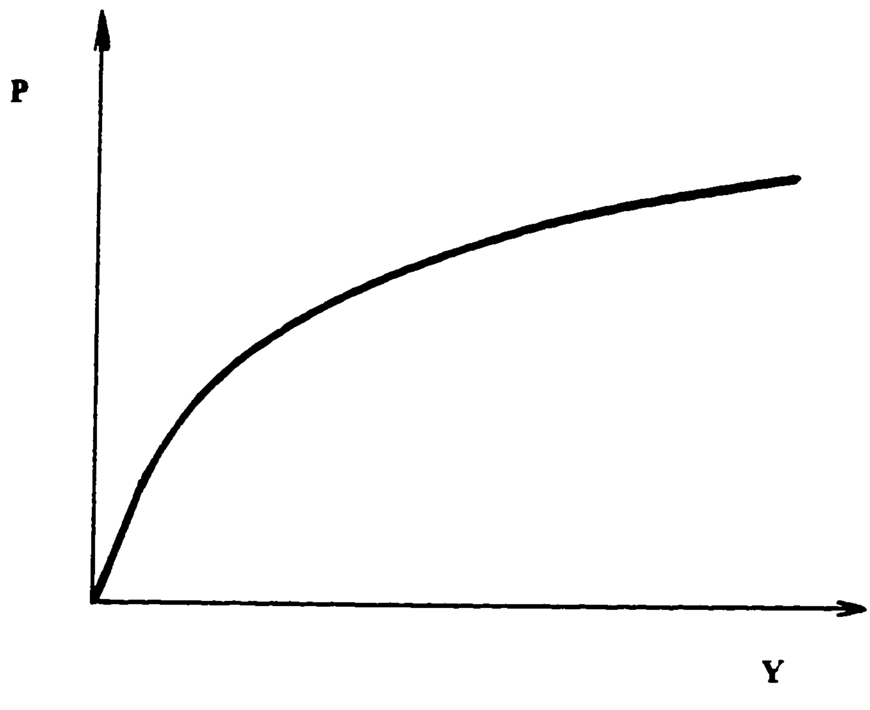


Figure 3.2 Idealized P-Y Behavior

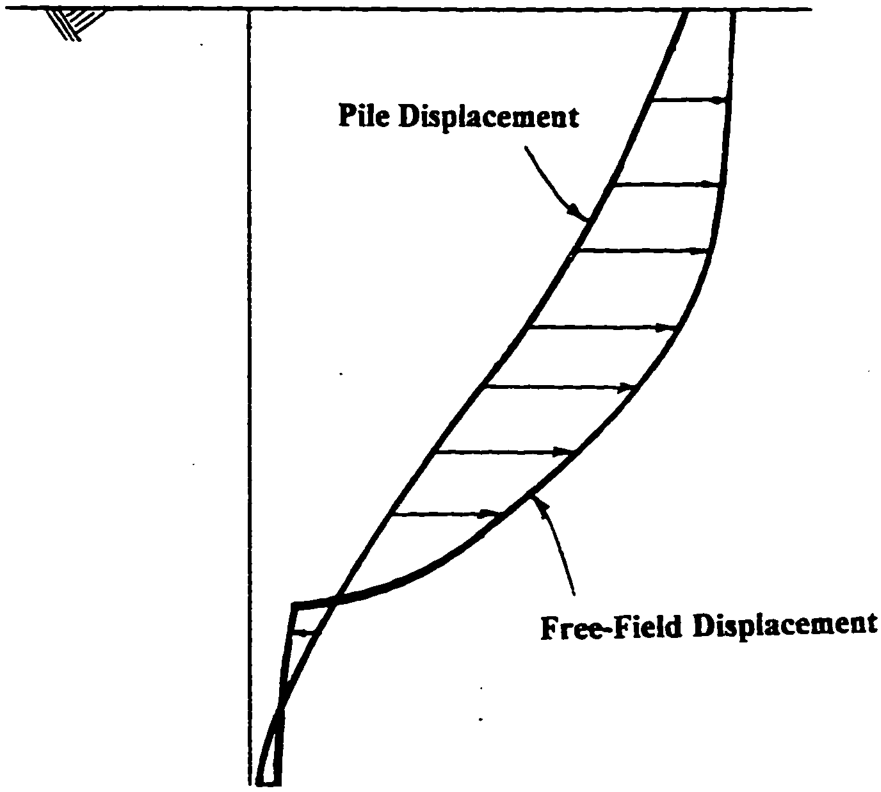


Figure 3.3 Idealized Pile Deflection Due to Static Loading From Soil Movement

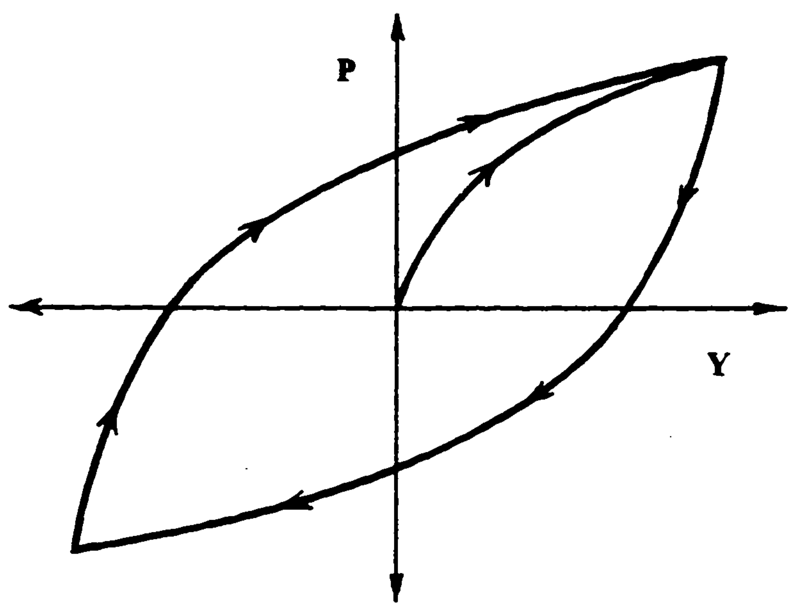


Figure 3.4 Idealized Near-Field Behavior Due to Dynamic Load

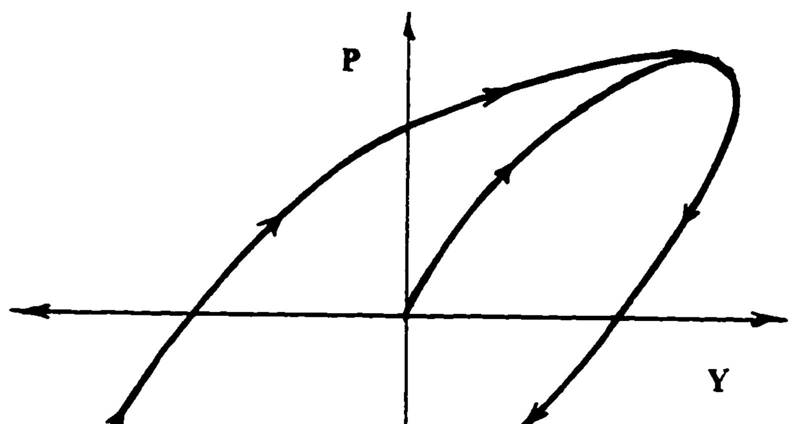


Figure 3.5 Idealized Far-Field Behavior Due to Dynamic Load

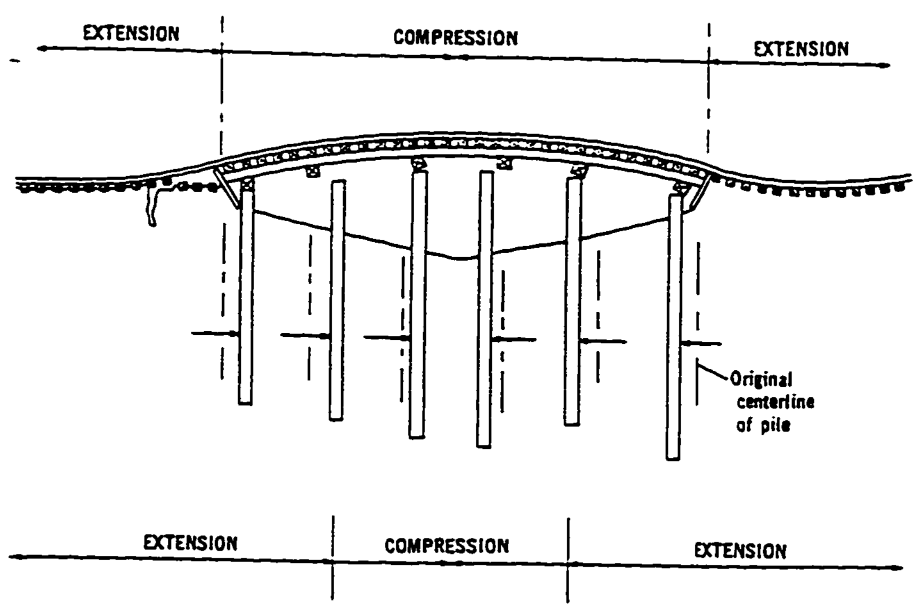


Figure 3.6 Typical Railroad bridge damage from the 1964 Alaska earthquake (after McCulloch and Bonilla, 1970)

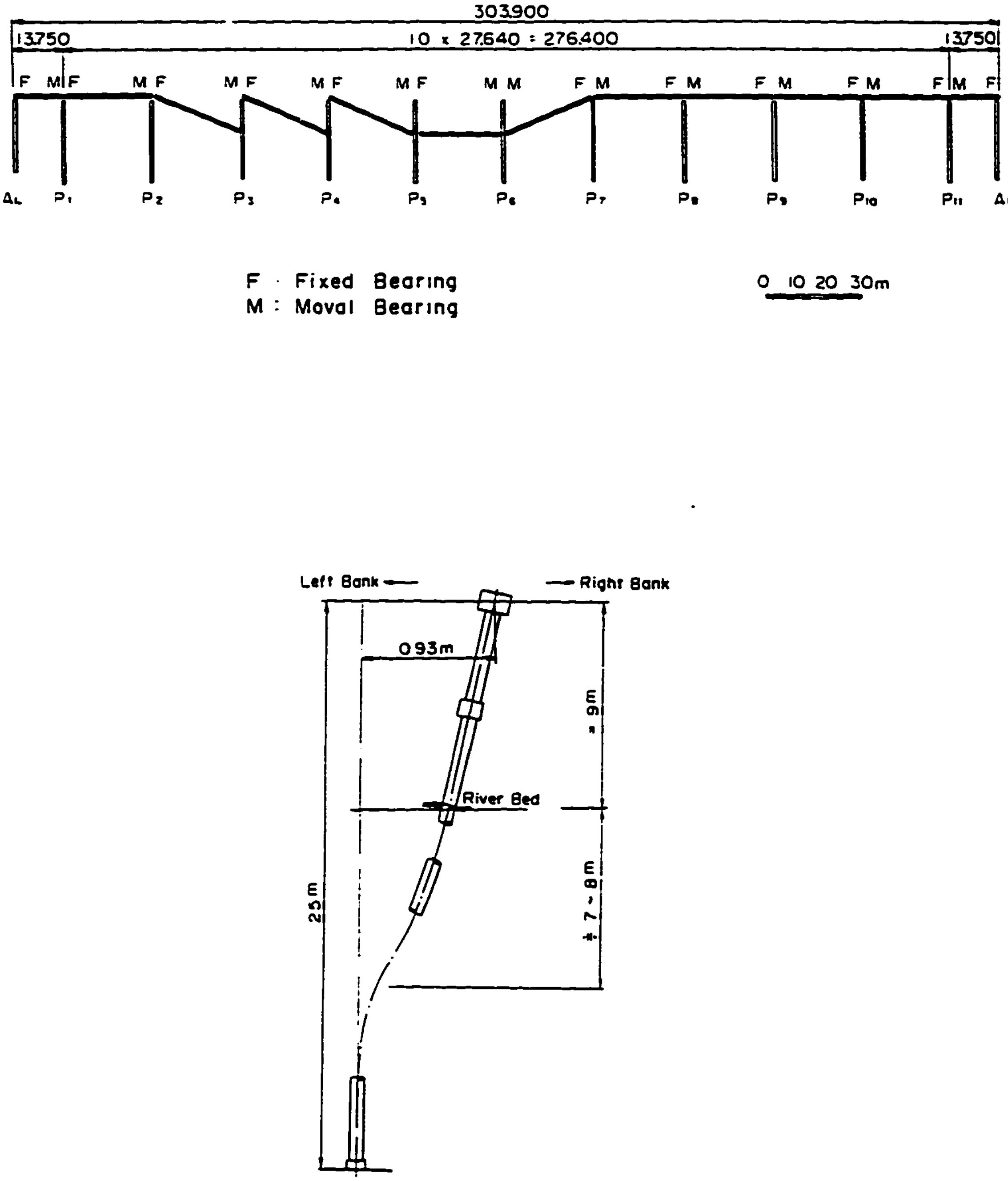


Figure 3.7 (a) Showa Bridge destroyed during the 1964 Niigata earthquake, and (b) pile displacements induced by laterally spreading soil (after Hamada, 1992)

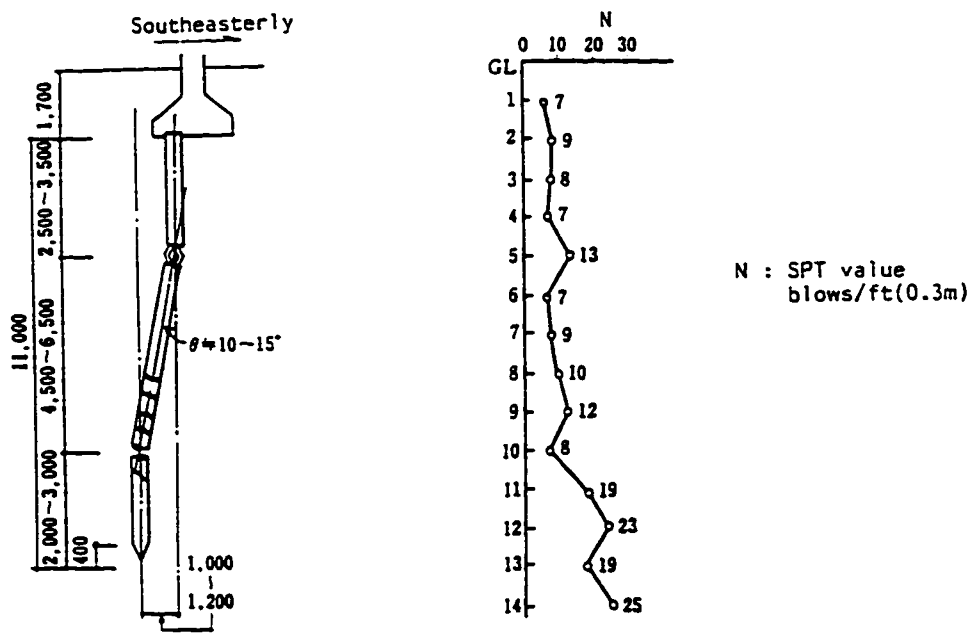


Figure 3.8 (a) Pile damage discovered in 1985 at the NHK Building that was caused by the 1964 Niigata earthquake, and (b) SPT profile at the site (after Hamada, 1992)

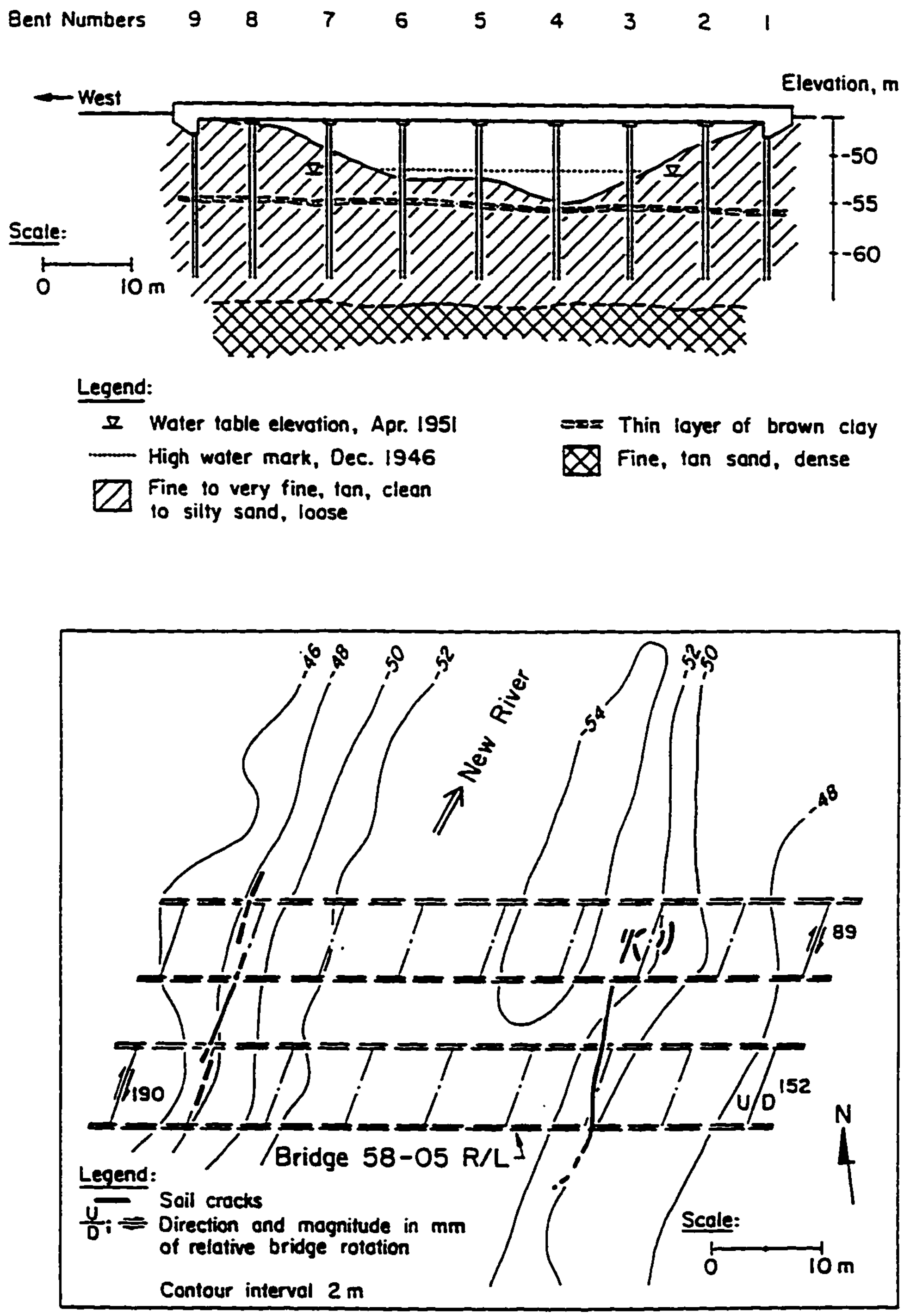


Figure 3.9 (a) Profile view of the New River Bridge, and (b) bridge displacements and ground cracking observed after the 1979 Imperial Valley earthquake (after Dobry, et al., 1992)

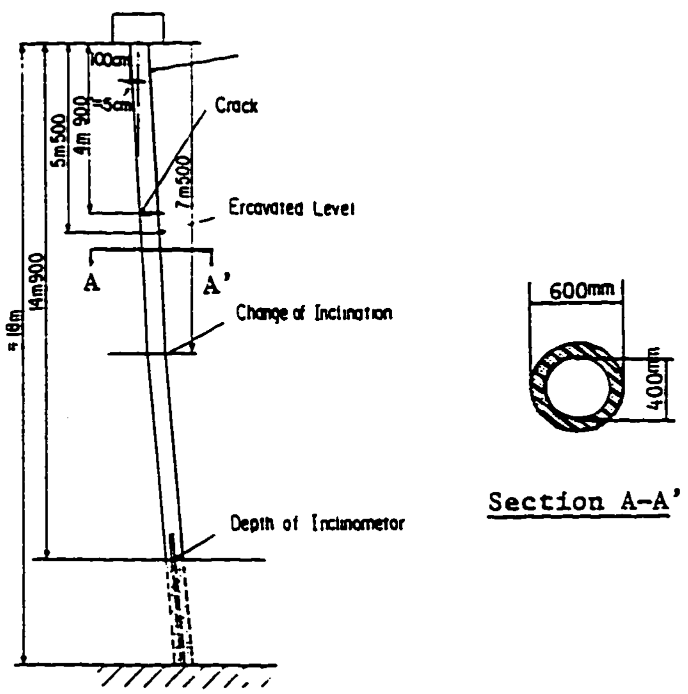


Figure 3.10 Prestressed concrete pile damage at the Gaiko Warehouse caused by the 1983 Nihonkai-Chubu earthquake (after Hamada, et al., 1992)

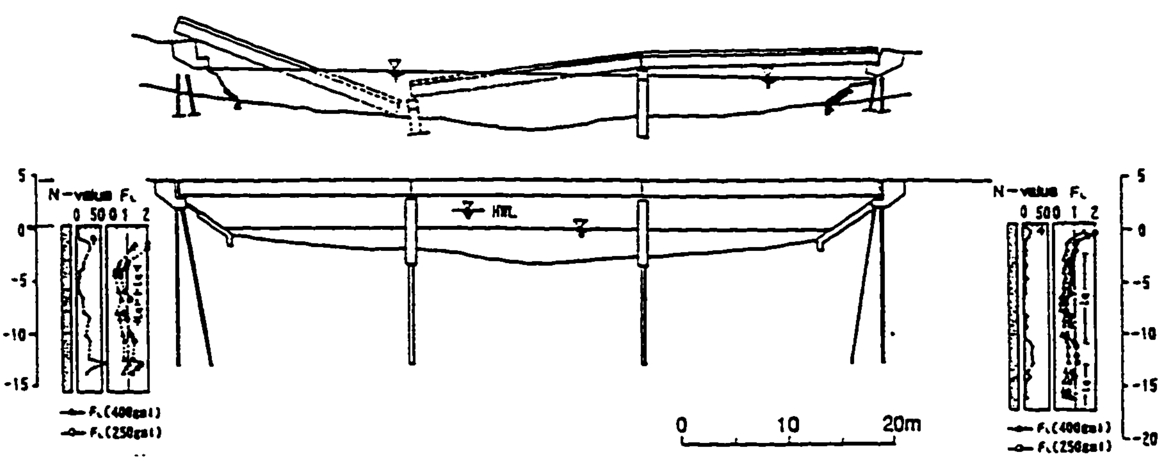


Figure 3.11 As-built and collapsed profiles of the Vizcaya River Bridge, along with STP blowcount and liquefaction assessment (after Yoshida, et al., 1992)

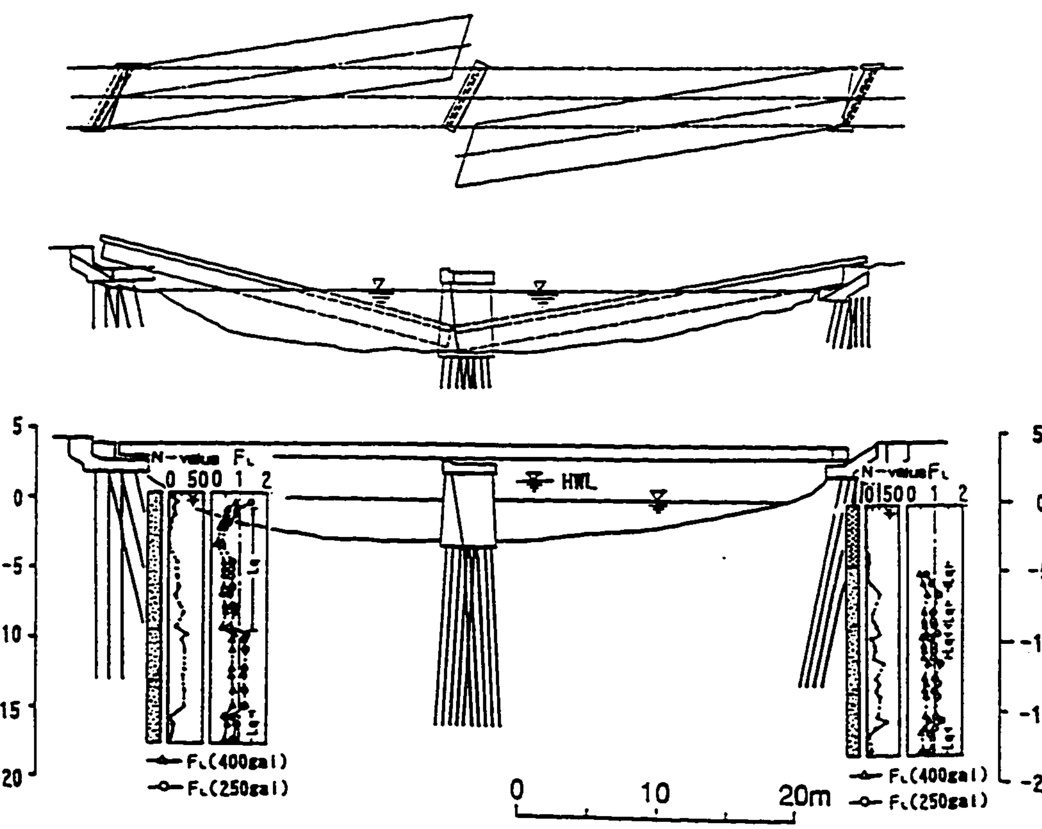


Figure 3.12 As-built profile and collapsed configuration of the Bananito River Bridge, along with STP blowcount and liquefaction assessment (after Yoshida, et al., 1992)

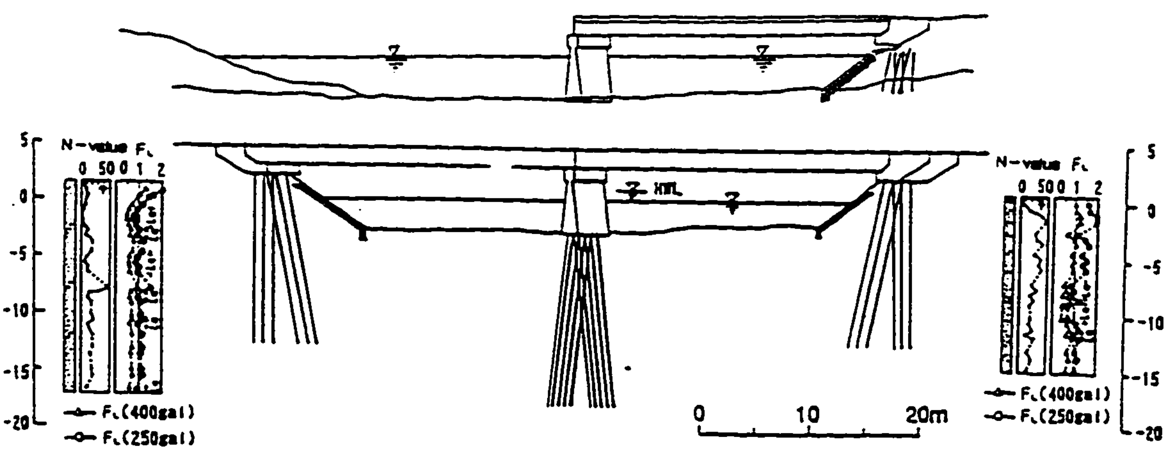


Figure 3.13 As-built and collapsed profiles of the Estero Negro River Bridge, along with STP blowcount and liquefaction assessment (after Yoshida, et al., 1992)

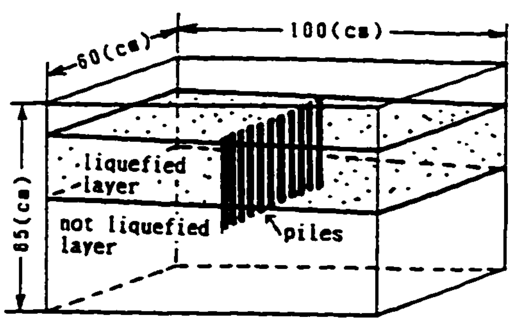


Figure 3.14 Shaking table model to investigate the effect of piles on lateral spreading (after Yasuda, et al., 1992)

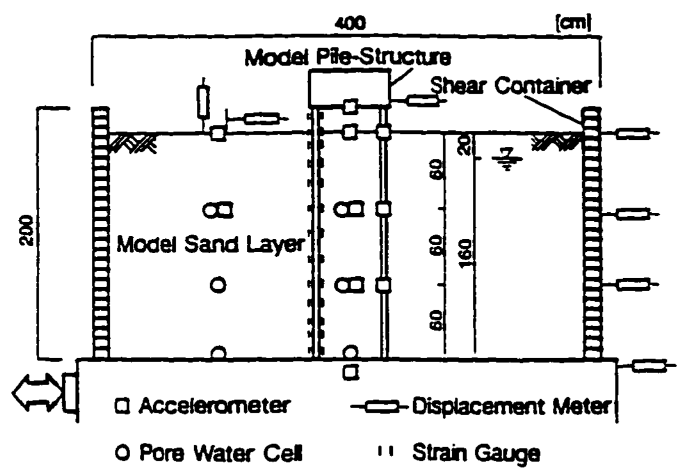


Figure 3.15 Shaking table model to investigate soil structure interaction during liquefaction (after Nomura, et al., 1991)

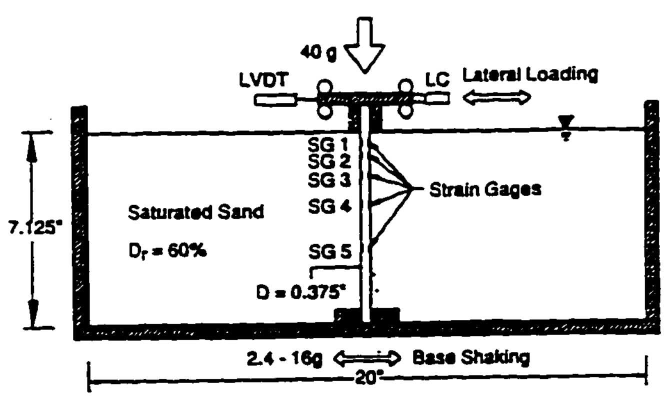


Figure 3.16 Centrifuge model to investigate p-y curve behavior in liquefied soil: (a) side view, and (b) front view (after Liu and Dobry (1995))

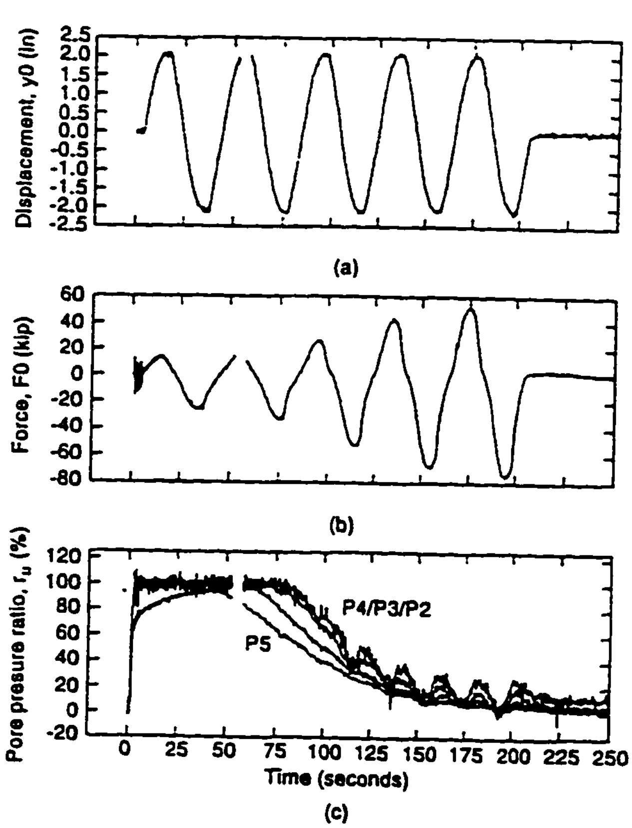


Figure 3.17 Measured time histories: (a) pile head lateral displacement, (b) pile head lateral force, and (c) pore pressure ratios of the liquefied sand (after Liu and Dobry (1995))

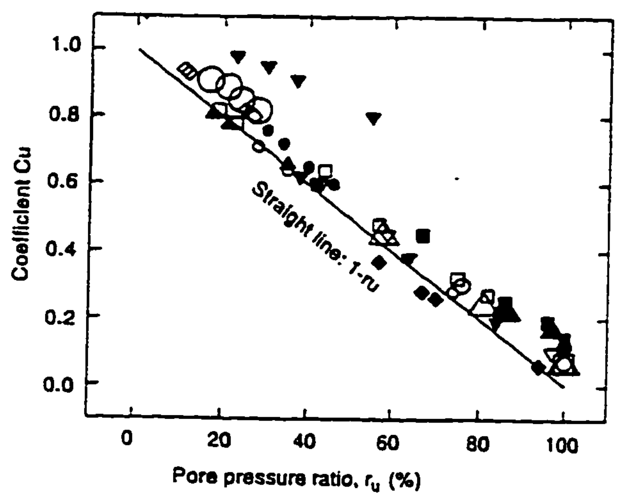


Figure 3.18 Relationship between degradation factor and pore pressure ratio inferred from centrifuge test data (after Liu and Dobry (1995))

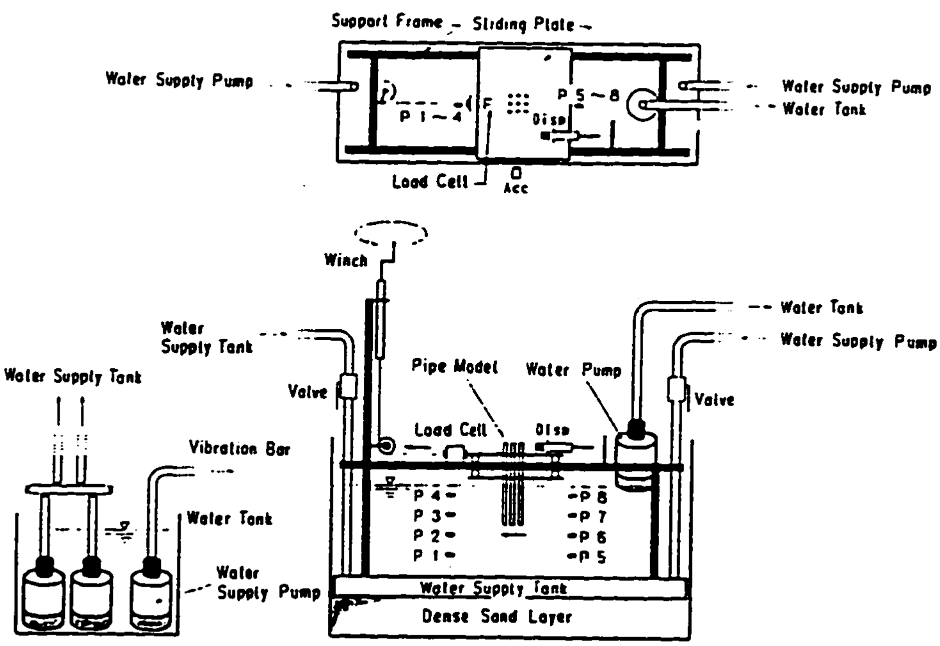


Figure 3.19 Test set up to investigate the effect of drag loads on pile groups (after Tokida et al., 1992)

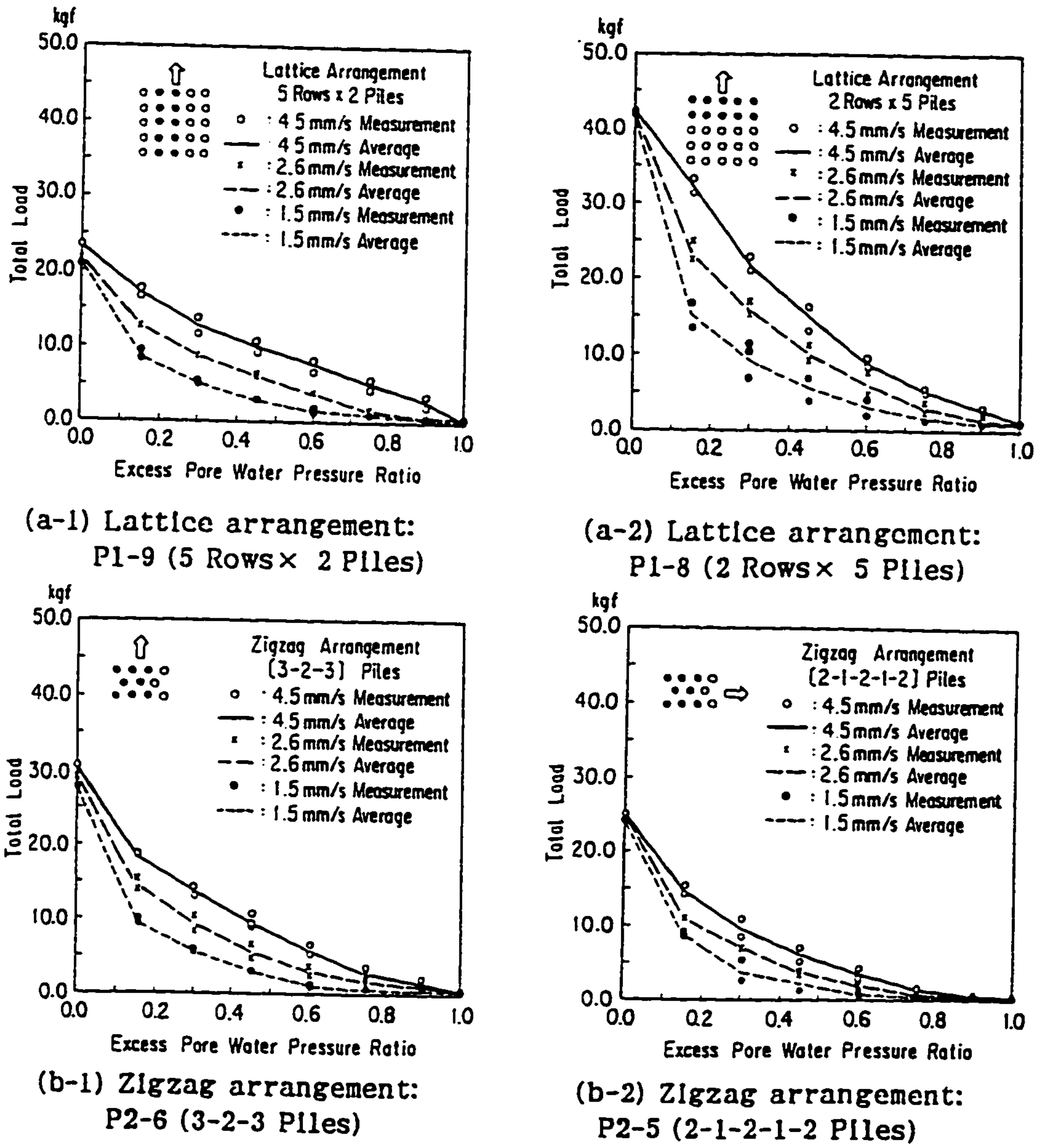


Figure 3.20 Results showing the total drag force versus excess pore pressure ratio and velocity for various pile group configurations (after Tokida et al., 1992)

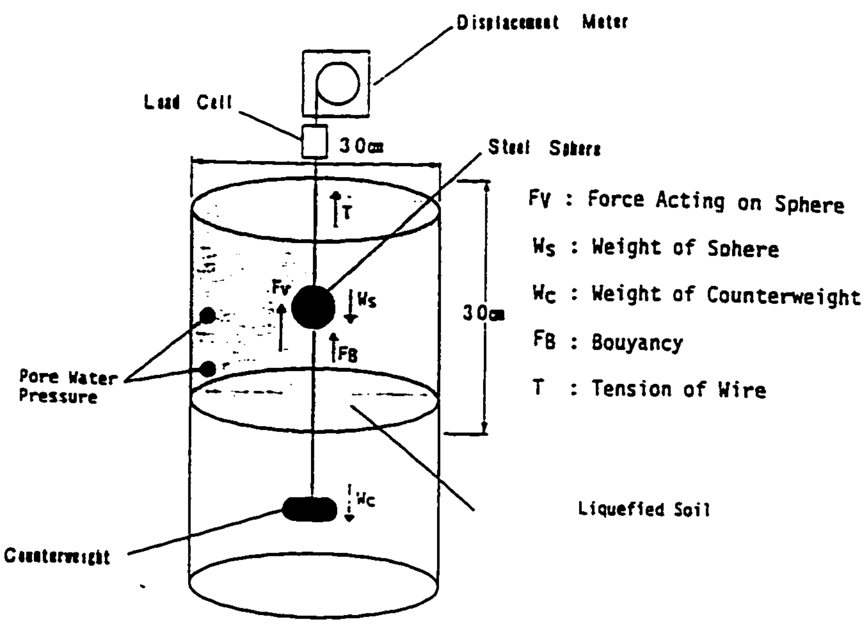


Figure 3.21 Test set-up to investigate the drag load on spheres pulled through liquefied sand (after Hamada et al., 1992)

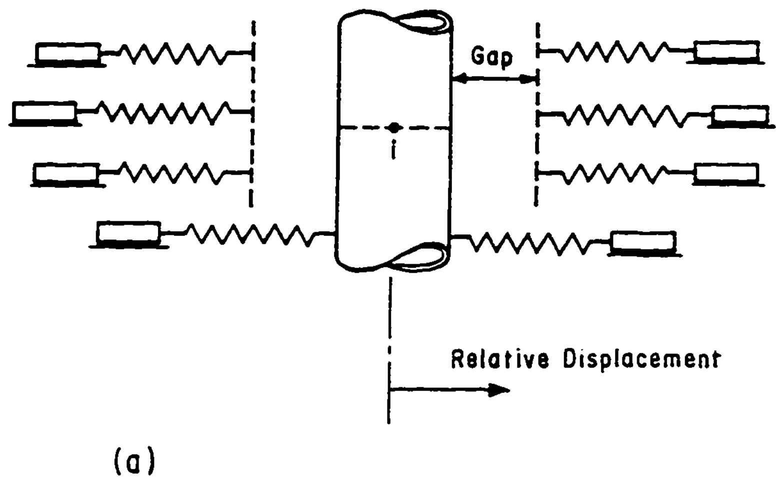


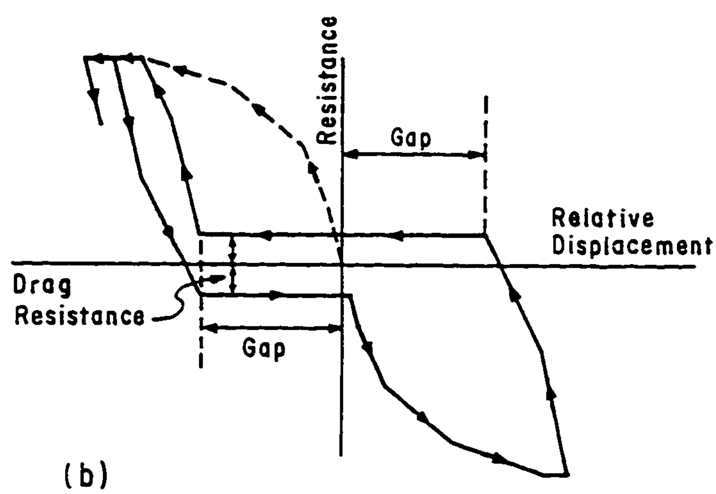


Figure 3.22 Near field pile-soil interaction behavior with gap capability (after Matlock et al., 1978)

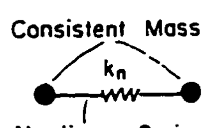


Figure 3.23 Time domain near-field pile-soil interaction model that includes inertial effects of the near-field (after Nogami and Konagai, 1992)

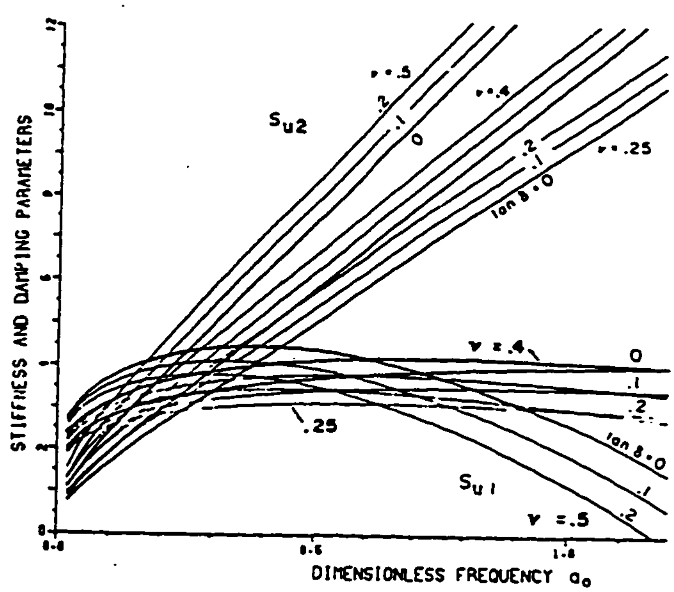


Figure 3.24 Far-field pile-soil impedances as a function of dimensionless frequency (after Novak et al., 1978)

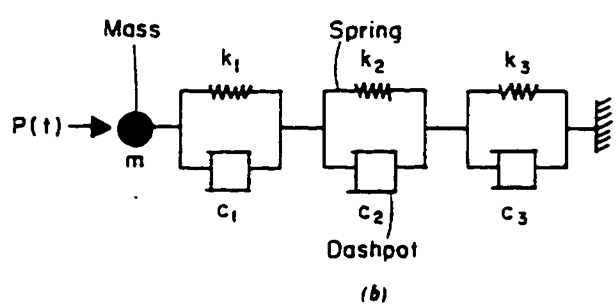


Figure 3.25 Time domain far-field pile-soil interaction model (after Nogami and Konagai, 1992)

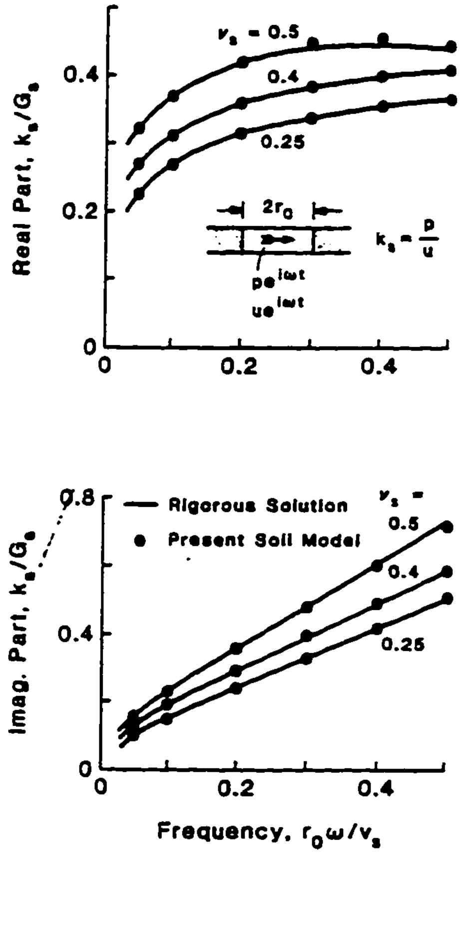


Figure 3.26 Comparison of impedance values obtained using the frequency domain and time domain methods (after Nogami and Konagai, 1988)

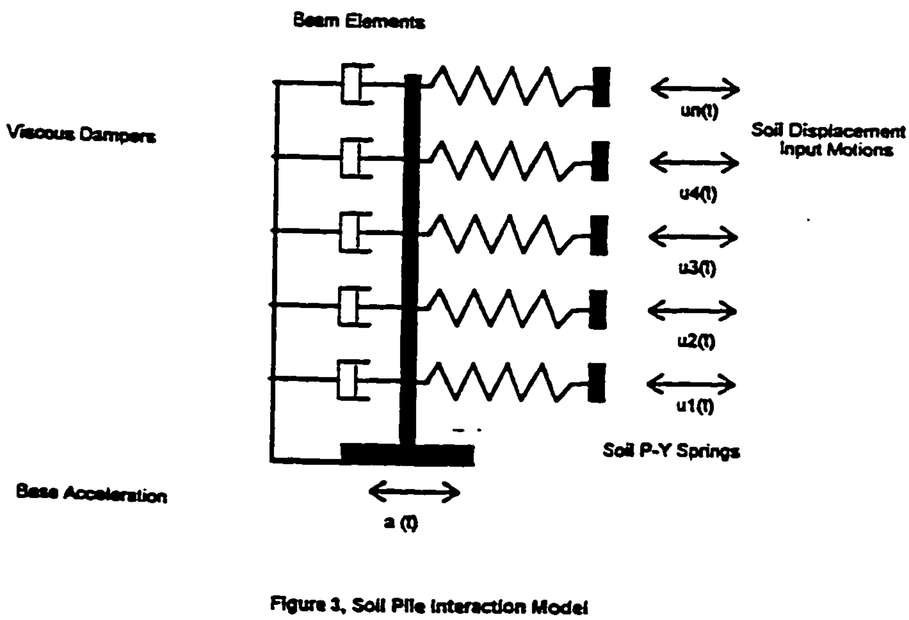


Figure 3.27 Finite element model for dynamic pile-soil interaction (after Slyh and Jackura, 1993)

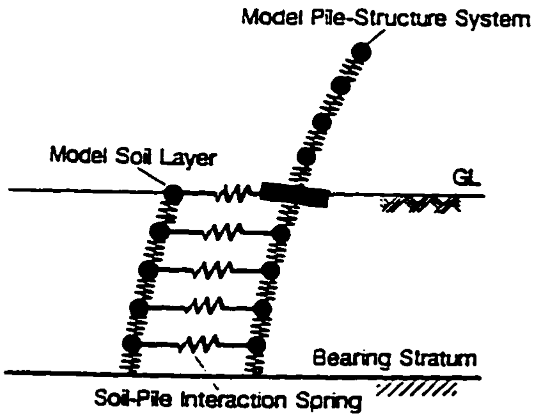


Figure 3.28 Lumped parameter model for dynamic pile-soil interaction (after Nomura, et al., 1991)

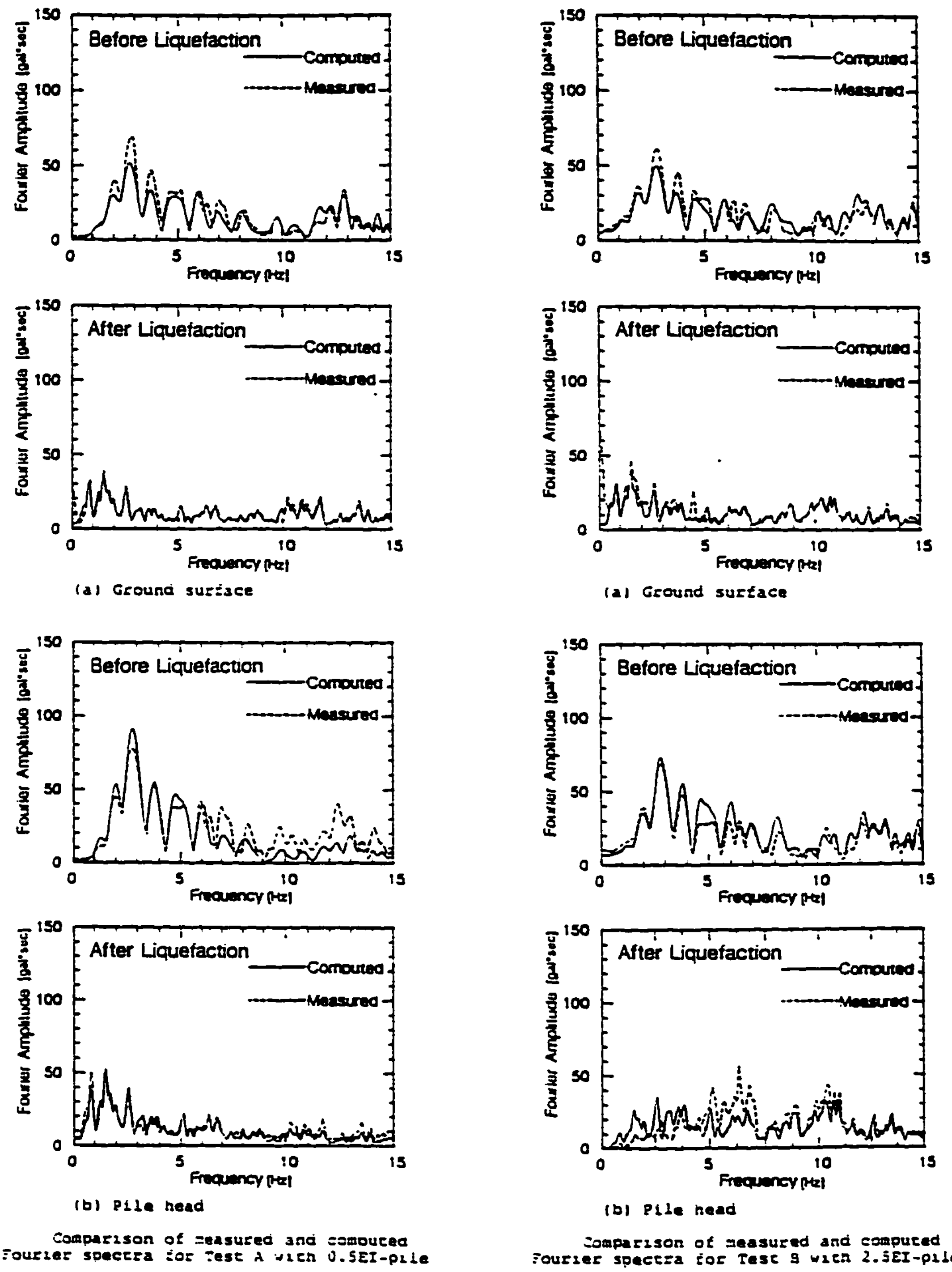


Figure 3.29 Comparison of measured and computed Fourier spectra (after Nomura, et al., 1991)

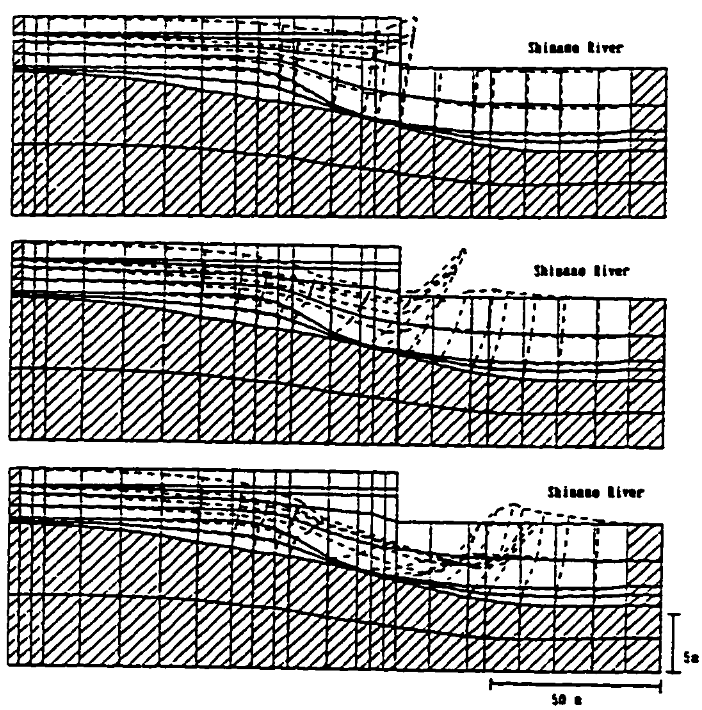


Figure 3.30 Deformed finite element meshes showing the effect of sheet pile embedment on lateral deformation (after Yasuda et al., 1991)

(a)

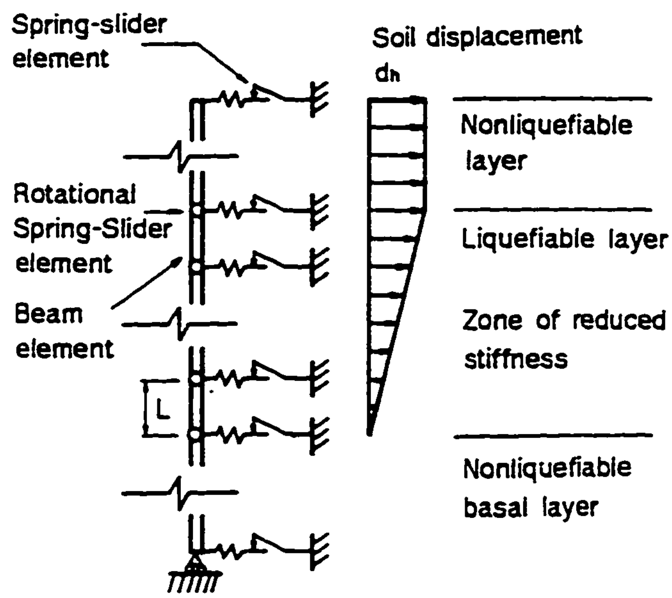


(b)

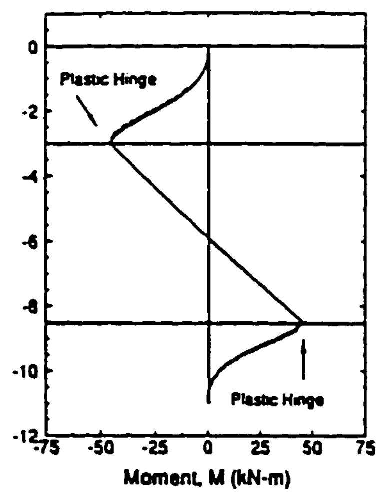


Figure 3.31 (a) Finite element model with presumed displacement field, and (b) computed bending moments (after Miura and O'Rourke, 1991, and Dobry, 1994)

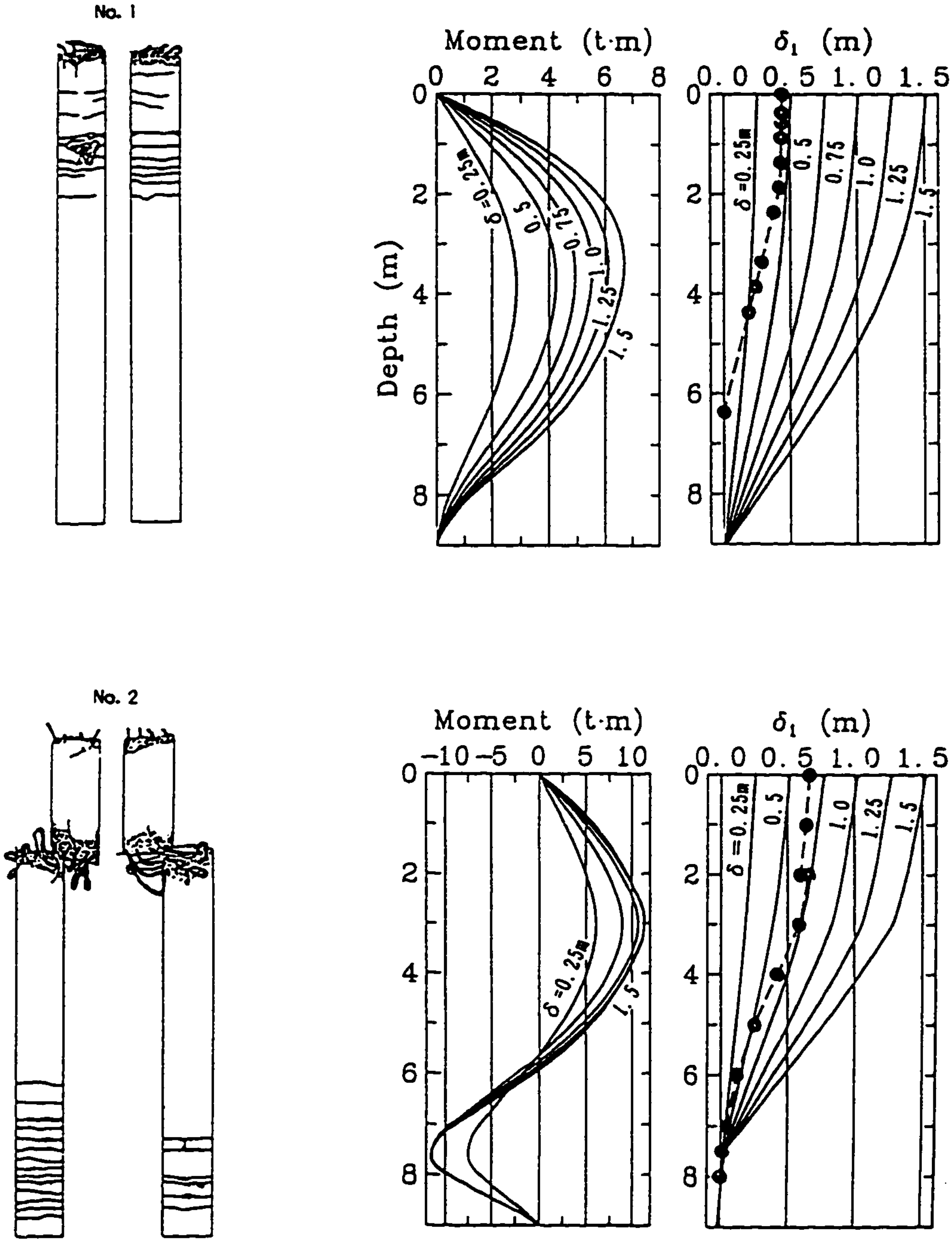


Figure 3.32 Observed pile damage, presumed displacements, and computed bending moments for two reinforced concrete piles (after Yoshida and Hamada, 1991)

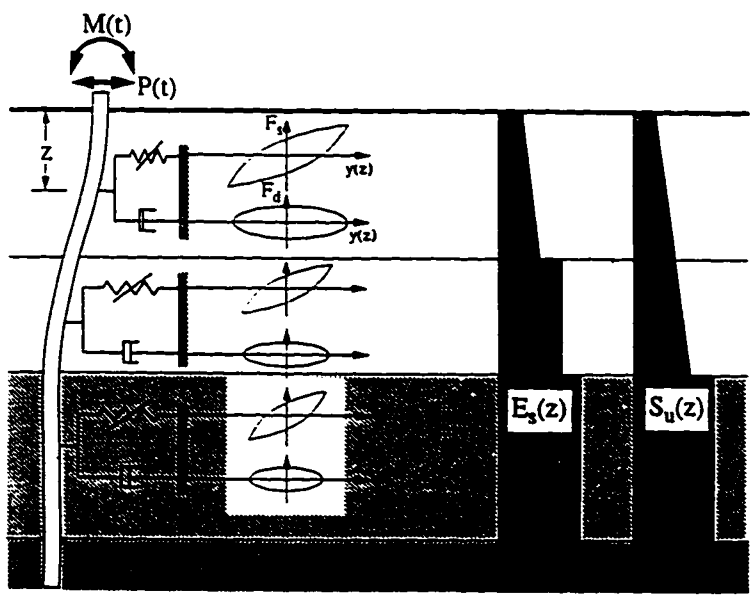


Figure 3.33 Finite element model used to compute nonlinear dynamic response (after Badoni and Makris, 1995)

# Chapter 4 Development of a Lateral Spreading Model

## 4.1 INTRODUCTION

Chapter 2 described previous research on lateral spreading, and Section 2.6 detailed the limitations of that body of work. A general procedure for analysis of lateral spreading must be able to predict the response of a soil deposit to earthquake shaking, and track the displacement, pore pressure, and stiffness fields as they evolve with depth and through time. It is these quantities -- displacement, pore pressure, and shear modulus -- that most affect the response of piles in liquefiable soils. Accurate computation of the pile response requires the successful characterization of these quantities.

This chapter introduces a new procedure for analysis of lateral spreading. The information is presented in three main sections. Section 4.2 contains the analytical and numerical description of a one-dimensional, non-linear, effective stress-based ground response model. Section 4.3 details algorithms used to model the constitutive behavior of the soil, and Section 4.4 verifies the procedure against results obtained by other methods.

## 4.2 ONE-DIMENSIONAL GROUND RESPONSE MODEL

As described in Chapter 2, various numerical procedures have been proposed for the prediction of free-field response to general earthquake loading. The level of sophistication of these codes varies from linear algorithms in one space dimension to fully non-linear codes in three space dimensions. Although the multi-dimensional codes seem attractive in terms of accurately representing the site geometry, they carry with them the troublesome burden of increased model definition time, computer storage space, and run time. More importantly, a multi-dimensional code requires a similarly defined constitutive model. For well-known engineering materials such as steel, concrete, aluminum, or plastic, it may be possible to determine necessary parameters for multi-dimensional constitutive models. Soil deposits, however, represent largely unknown continua. The enormous task of estimating the myriad of constants required to fully specify a typical multi-dimensional, non-linear constitutive model casts serious doubt as to the legitimacy of predictions based on such codes. Though many of the parameters have little apparent physical significance, the response may be very sensitive to their values.

Based on these observations, a method based on one space dimension is proposed. Despite this simplification, it is believed that an appropriately developed one-dimensional model will be useful for many sites with liquefaction hazards, including those with gently sloping ground surfaces and level sites situated near bodies of water. These conditions were present in all of the lateral spread sites described in Chapter 2, and are a necessary condition for the development of permanent lateral deformations. Additionally, material properties at most sites are empirically-derived from the results of SPT, CPT, gradation, and plasticity tests. The use of a multi-dimensional discretization is simply not consistent with the qualitative and empirical nature of these tests.

The remainder of this section describes the analytical and numerical details of the proposed ground response model. It includes development of the equation of motion, appropriate representation of boundary conditions, and the numerical solution.

### 4.2.1 Equation of Motion

The equation of motion represents the fundamental analytical description of wave propagation. Development of the equation of motion requires consideration of both equilibrium and strain-displacement relations. Two separate conditions are appropriate for exploration. The first is the level ground condition in which initial shear stresses on horizontal planes are zero. The second, more general case involves irregular or sloping ground conditions that give rise to non-zero initial shear stresses on horizontal planes -- it is this condition that produces the lateral spread displacements observed in the field.

The actual and idealized representation of a typical soil profile is shown in Figure 4.1. Figure 4.1(a) shows the actual soil system to be analyzed -- a layered half-space with groundwater table and non-zero initial shear stresses. Figure 4.1(b) shows the computed free-field displacement profile at a particular snapshot in time.

4.2.1.1 Level Ground Surface

In subsequent equations, the independent variables of depth and time appear as symbols, z and t, respectively. Subscripts z or t which appear on various terms imply spatial or temporal differentiation, respectively. For one-dimensional shear, the conservation of linear momentum (or "equilibrium" equation) reduces to:

$$\rho v_t - \tau_z = 0 \tag{4.1}$$

where: $v = v(z,t)$ = particle velocity

$\tau = \tau(z,t)$ = shear stress

$\rho = \rho(z)$ = soil density

The Lagrangian strain tensor for one-dimensional shear reduces to the following strain-displacement (or "compatibility") expression:

$$\gamma = u_z \tag{4.2}$$

where: $\gamma = \gamma(z,t)$ = shear strain

$u = u(z,t)$ = particle displacement

Temporal differentiation of (4.2) yields:

$$\gamma_t = (u_z)_t = (u_t)_z = v_z \tag{4.3}$$

By the chain rule:

$$\gamma_t = \frac{\partial \gamma}{\partial t} = \frac{\partial \gamma}{\partial \tau}\frac{\partial \tau}{\partial t} = \frac{1}{G}\frac{\partial \tau}{\partial t} = \frac{1}{G}\tau_t \tag{4.4}$$

where: $G = G(z,t)$ = shear modulus of the soil

Substitution of (4.4) into (4.3) eliminates the shear strain in the latter expression. Rearranging the resulting equation yields:

$$G\, v_z - \tau_t = 0 \tag{4.5}$$

Equations (4.1) and (4.5) form a first order, hyperbolic system of partial differential equations. This system may be expressed in matrix form as:

$$\begin{Bmatrix} \tau \\ v \end{Bmatrix}_t - \begin{bmatrix} 0 & G \\ 1/\rho & 0 \end{bmatrix} \begin{Bmatrix} \tau \\ v \end{Bmatrix}_z = \begin{Bmatrix} 0 \\ 0 \end{Bmatrix} \tag{4.6}$$

The dependent (or "field") variables contained in (4.6) are the shear stress and particle velocity of the soil deposit. The right hand side of (4.6) indicates the absence of a body force term, which is characteristic of the level ground case. The coefficient matrix of (4.6) possesses two real and distinct eigenvalues which correspond to the shear wave velocity of the material,:

$$\Lambda^{(1)} = -V_s \tag{4.7 a}$$

$$\Lambda^{(2)} = +V_s \tag{4.7 b}$$

where: $V_s = \sqrt{G/\rho}$, the shear wave velocity

The corresponding eigenvectors are given by:

$$r^{(1)} = \begin{Bmatrix} -V_s \\ -1/\rho \end{Bmatrix} \tag{4.8a}$$

$$r^{(2)} = \begin{Bmatrix} V_s \\ -1/\rho \end{Bmatrix} \tag{4.8b}$$

4.2.1.2 Sloping or Irregular Ground Surface

Figure 4.2 shows initial shear stresses which arise for sloping and irregular ground surface conditions. These represent the shear stresses required to maintain static equilibrium of the soil, and introduce a source term that was not present in Equation (4.1):

$$\rho v_t - \tau_z = \tau_z^{app} \tag{4.9}$$

where: $\tau^{app} = \tau^{app}(z)$ = initial, applied shear stress

These shear stresses are gravitational and therefore exist before, during, and after earthquake shaking. Initial shear stresses will exist in sloped soil deposits, and in predominantly level soil deposits situated adjacent to natural or cut slopes. These initial shear stresses tend to produce permanent strains in a liquefied soil stratum and result in permanent lateral deformations in the down-slope direction. For the simple case of an infinite slope, the source term may be expressed as:

$$\tau_z^{app} = \rho g \sin\theta \tag{4.10}$$

where: g = acceleration due to gravity, and

θ = angle of the slope with respect to the horizontal

Ground response analyses that include this source term assume that wave propagation is perpendicular to the ground surface. This assumption is valid for shallow slope angles, but is not accurate for steep slopes. Steep slopes result in shear waves that encounter the free surface boundary at an oblique angle, resulting in considerable scattering. This behavior is not captured in a one-dimensional formulation. The strain-displacement relation is unchanged for this case, and the resulting system of PDE's may be expressed as:

$$\begin{Bmatrix} \tau \\ v \end{Bmatrix}_t - \begin{bmatrix} 0 & G \\ 1/\rho & 0 \end{bmatrix} \begin{Bmatrix} \tau \\ v \end{Bmatrix}_z = \begin{Bmatrix} 0 \\ \tau_z^{app}/\rho \end{Bmatrix} \tag{4.11}$$

The eigenvalues and eigenvectors of the coefficient matrix appearing in (4.11) are the same as described by equations (4.7) and (4.8), respectively.

### 4.2.2 Initial and Boundary Conditions

Initial and boundary conditions must be specified in a well-posed problem. In the context of ground response analysis, the initial condition is satisfied by specifying the field variables, velocity and shear stress throughout the spatial domain at the instant analytical consideration begins. Boundary conditions are enforced by specifying values of the field variables at the boundary throughout time. These are discussed in detail in the following sections.

4.2.2.1 Initial Conditions

It is reasonable to assume that the initial velocity of a particular soil deposit is zero prior to an earthquake. Hence:

$$v(z,0) = 0 \tag{4.12}$$

However, the initial shear stress distribution depends on the configuration of the deposit. If the deposit is level, then the shear stresses are zero:

$$\tau(z,0) = 0 \tag{4.13}$$

Alternatively, for an infinite slope, the initial shear stresses can be computed as:

$$\tau(z,0) = \sigma_v \sin\theta \tag{4.14}$$

where: $\sigma_v = \sigma_v(z)$ = total vertical stress within the soil

For more general geometry, the initial shear stress distribution can be computed using elastic solutions or static finite element or finite difference codes.

4.2.2.2 Ground Surface Boundary Condition

A traction-free boundary condition is assumed to exist at the ground surface. This implies that the shear stress must vanish as a function of time:

$$\tau(0,t) = 0 \tag{4.15}$$

4.2.2.3 Bedrock Boundary Condition

Two possibilities exist at the soil-bedrock interface. For a rigid bedrock, the corresponding boundary condition is:

$$v(H,t) = v_i(t) \tag{4.16}$$

where: $v_i(t)$ = particle velocity of the incident wave

For an elastic bedrock, Joyner and Chen (1975) expressed the boundary condition as an imposed shear stress:

$$\tau(H,t) = \rho_{br} V_{sbr}[2v_i(t) - v_t(t)] \tag{4.17}$$

where: $\rho_{br}$ = bedrock density

$V_{sbr}$ = bedrock shear wave velocity

$v_t(t)$ = particle velocity of the transmitted wave

The elastic bedrock boundary condition allows a portion of downward-traveling shear waves to be transmitted through the soil-rock interface into the underlying half-space and effectively leave the domain. Because the energy of these downward-traveling waves is lost from the soil layer, this represents a form of radiation damping.

### 4.2.3 Numerical Solution

No closed-form, analytical solution exists for the partial differential equations given by (4.6) or (4.11). However, any of several numerical schemes could be employed to solve these equations approximately. The highly nonlinear behavior of liquefiable soil requires analysis of the time-domain dynamic response of a non-linear continuum to a transient loading. Using the finite element method, each time step would involve the inversion of the entire stiffness matrix of the discretized continuum to obtain the values of the field variables at the end of the time step. In contrast, an explicit finite difference formulation takes advantage of the fact that material points in a continuum are 'affected' only by neighboring points. That is, for a given material point, it is not necessary to know the solution of the field variables over the entire domain in order to compute its value at the end of a particular time step. The finite difference method was chosen in favor of the finite element method for this reason.

Many finite difference schemes have been developed to solve systems of partial differential equations (e.g., LeVeque, 1992). The available methods vary in terms of their applicability, complexity, stability, and accuracy. For the proposed ground response analysis, a high-resolution Godunov scheme was chosen. This method readily adapts to nonlinear systems of PDE's with source terms, and has the advantage of being second-order accurate in smooth regions while retaining first order accuracy near shocks. This is particularly useful for accurate resolution of liquefied zones within a soil layer. None of the currently available methods for ground response analysis have these characteristics. Details of the method may be found in LeVeque (1992), but a brief description follows.

The time-stepping algorithm is a four-part process. Within this process, "Strang splitting" is used to incorporate the source term of equation (4.11). This yields second-order accuracy for problems involving smooth solutions (LeVeque, 1995). First, the algorithm enforces boundary conditions by extending the values of field variables within the domain to auxiliary, or "ghost," cells outside of the domain. Second, a Riemann problem is solved (with second order correction) - considering just the homogeneous portion of the PDE system - over a half time-step. This yields an intermediate state of the field variables. Third, this intermediate state is used as initial data to take a full time-step on an equation which includes the source term, but neglects the flux gradient term (the second term of equation (4.11)). This yields a second intermediate state. Finally, this second intermediate state is used as initial data to solve another Riemann problem (with second order correction) - again considering just the homogeneous portion of the PDE system - over a half time step. This yields the solution to the full PDE system at the end of the time step. Relevant details regarding the Riemann solver, second order accuracy, Strang splitting, and boundary conditions, appear in the following sections. Indices i and j refer to discrete points in space and time, respectively.

4.2.3.1 Riemann Solver

As suggested above, Godunov's method involves solving individual Riemann problems forward in time at each cell interface, which is the boundary between successive grid points within the discretized domain. Consider an arbitrary cell interface within the discretized domain. This interface has an upper state $[\tau(i-1,j),v(i-1,j)]$ and a lower state $[\tau(i,j),v(i,j)]$. The change or "jump" in the shear stress and velocity across this interface gives rise to acoustic waves which, in general, will travel upward or downward away from the interface. The goal of the Riemann solver is to determine the magnitude and direction of these waves. More fundamentally, this information is used in Godunov's method to determine the values of shear stress and velocity at the end of the time step.

The Rankine-Hugoniot jump condition requires that the jump across the upward-traveling wave be an eignvector of A(i-1,j), where A(i-1,j) is the 2x2 coefficient matrix of (4.11), evaluated at the (i-1,j) cell. Conversely, the jump across the downward-traveling wave must be an eigenvectors of A(i,j). These two statements imply:

$$w^{(1)}(i,j) = \alpha^{(1)}(i,j)\, r^{(1)}(i\text{-}1,j) \qquad \text{for some scalar } \alpha^{(1)}(i,j) \tag{4.18a}$$

$$w^{(2)}(i,j) = \alpha^{(2)}(i,j)\, r^{(2)}(i,j) \qquad \text{for some scalar } \alpha^{(2)}(i,j) \tag{4.18b}$$

where $r^{(1)}(i\text{-}1,j)$ and $r^{(2)}(i,j)$ are the eigenvectors given by (4.7), evaluated using the soil properties of the (i-1,j) and (i,j) cells, respectively. The jump condition leads to the following linear system of equations:

$$w^{(1)}(i,j) + w^{(2)}(i,j) = q(i,j) - q(i\text{-}1,j) \tag{4.19}$$

The right hand side of (4.19) is a vector equal to the jump in the field variables (shear stress and velocity) across the cell interface:

$$q(i,j) - q(i-1,j) = \begin{Bmatrix} \tau(i,j) - \tau(i-1,j) \\ v(i,j) - v(i-1,j) \end{Bmatrix} \equiv \begin{Bmatrix} d\tau(i,j) \\ dv(i,j) \end{Bmatrix} \tag{4.20}$$

Substituting (4.18) and (4.20) into (4.19), and solving for the unknown values of $\alpha$:

$$\alpha^{(1)}(i,j) = \frac{-\dfrac{d\tau(i,j)}{\rho(i)} - dv(i,j)V_s(i,j)}{\dfrac{V_s(i,j)}{\rho(i-1)} + \dfrac{V_s(i-1,j)}{\rho(i)}} \tag{4.21a}$$

$$\alpha^{(2)}(i,j)= \frac{\dfrac{d\tau(i,j)}{\rho(i-1)} - dv(i,j)V_s(i-1,j)}{\dfrac{V_s(i,j)}{\rho(i-1)} + \dfrac{V_s(i-1,j)}{\rho(i)}} \qquad (4.21b)$$

The first-order Godunov update to the field variables is given by:

$$\begin{Bmatrix} \tau(i,j+1) \\ v(i,j+1) \end{Bmatrix} = \begin{Bmatrix} \tau(i,j) \\ v(i,j) \end{Bmatrix} - \frac{dt}{dx} V_s(i,j)\left[w^{(2)}(i,j) - w^{(1)}(i+1,j)\right] \qquad (4.22)$$

4.2.3.2 Second-Order Accuracy

Used alone, Godunov's method is only first order accurate. However, second-order accuracy can be attained by employing a "flux limiter" method (LeVeque (1992)). The basic idea in a flux limiting method is to make a correction to the Godunov update given above. The magnitude of this correction depends on the relative smoothness of the data. In smooth regions, the correction yields second-order accuracy. However, in the vicinity of shocks, the method reverts to a first order method which prevents spurious oscillation in the computed solution. The transition between smooth and non-smooth regions is controlled by the so-called "limiter" function. Many types of limiters have been proposed in the literature (LeVeque, 1992). For the ground response problem, the "Min-mod" limiter (Sweby, 1983) has been implemented. The Min-mod limiter results in a numerical method with two fundamental advantages: second-order accuracy and stability.

4.2.3.3 Source Term

The source term appearing in (4.11) is trivial to incorporate via Strang splitting because it does not change with respect to time. Integrating over a full time step:

$$t(i,j+1) = t(i,j) \qquad (4.23a)$$

$$v(i,j+1) = v(i,j) + \tau(i)_z^{app}\, dt / \rho(i) \qquad (4.23b)$$

4.2.3.4 Numerical Enforcement of Boundary Conditions

Section 4.2.2 detailed the boundary conditions of particular interest to the one-dimensional ground response problem. The numerical implementation of these conditions involves the use of two ghost cells at either end of the computational domain, as shown in Figure 4.3. The first ghost cell beyond the boundary maintains the boundary condition, while the second is required when flux limiters are invoked. At the top of the soil deposit (z=0), the traction free condition is maintained by setting:

$$\tau(0,j) = -\tau(1,j) \tag{4.24a}$$

$$\tau(-1,j) = -\tau(1,j) \tag{4.24b}$$

$$v(0,j) = v(1,j) \tag{4.24c}$$

$$v(-1,j) = v(1,j) \tag{4.24d}$$

Conversely, an inflow boundary condition exists at the bottom of the soil deposit (z = H). For the case of a rigid bedrock, consistent expressions for the velocity and shear stress in the ghost cells are:

$$\tau(N+1,j) = 2\tau(N,j) - \tau(N-1,j) \tag{4.25a}$$

$$\tau(N+2,j) = 3\tau(N,j) - 2\tau(N-1,j) \tag{4.25b}$$

$$v(N+1,j) = 2v_{br} - v(N,j) \tag{4.25c}$$

$$v(N+2,j) = v(N+1,j) \tag{4.25d}$$

where the index "N" refers to the total number of grid cells within the discretized domain, and $v_{br}$ refers to the specified bedrock velocity. If a compliant (elastic) bedrock exists at the lower boundary, the approach of Joyner and Chen (1975) can be implemented by replacing (4.25c) with:

$$v(N+1,j) = 2\bar{v}(j+1) - v(N,j) \tag{4.26a}$$

$$\text{where: } \tilde{v}(j+1) = \frac{\tilde{v}(j) + \dfrac{dt/dz}{\rho(N)}\left[2\rho_r V_{sr} v_{br} - \tau(N,j)\right]}{1 + \dfrac{\rho_r V_{sr} dt}{\rho(N) dz}} \qquad (4.26b)$$

$\rho_r$ = density of the elastic bedrock, and

$V_{sr}$ = shear wave velocity of the elastic bedrock

## 4.3 MATERIAL BEHAVIOR

The required material properties for solution of the one-dimensional ground response wave equation include the density and shear modulus of the soil. While the former is fairly well-known for typical soil deposits and remains constant during earthquake shaking, the latter depends on many factors, including current stress state, stress history, void ratio, degree of saturation, and gradation (Richart, et al. (1970)) . Deposits susceptible to lateral spreading consist of soils that may be both extremely weak and moderately pre-sheared. Consequently, the deposit can be near failure before an earthquake, so that any perturbation on the static stress state may induce highly nonlinear stress-strain behavior. Loose, saturated, granular soils also exhibit contractive behavior when sheared. If the loading rate is sufficiently high, the response of the soil is undrained, so the tendency for contraction results in increased pore pressure. During cyclic loading, the pore pressure tends to rise, and the effective stress drops. Because the shear modulus is strongly related to the effective stress, pore pressure changes produce highly nonlinear soil behavior. A successful lateral spread model must be able to reasonably predict the stress-strain response of the soil deposit. This includes the ability to characterize the progressive build-up of pore pressure during cyclic shearing.

The literature is rich with constitutive models aimed at characterizing liquefiable soils. These models range from simple, empirical approaches (e.g., Martin et al., 1975) to three-dimensional, non-associative plasticity models (e.g., Dafalias, 1994). This section describes a methodology which strikes a balance between the simple (yet limited) and the general (yet complex) constitutive models. It is a semi-empirical model that characterizes the stress-strain behavior with nonlinear backbone curves which obey a modified Masing criteria at load reversal. Pore pressure generation is accounted for by a simple energy-based relationship.

### 4.3.1 Stress-Strain Behavior

A "backbone curve" is used to characterize the nonlinear stress-strain behavior of the soil upon initial loading. As the soil is loaded monotonically from its initial state, the stress-strain behavior follows the backbone curve. At the point at which load reversal occurs, the inelastic behavior of soil causes the stress-strain curve to follow an unloading curve that differs from the loading curve (Figure 4.4). This requires some form of loading-unloading rule; for this model, the Cundall-Pyke hypothesis (Pyke, 1979) is used. According to the Cundall-Pyke hypothesis, a stress reversal causes unloading (or reloading) to occur on a path given by a scaled version of the original backbone curve. The origin of the scaled curve is translated to the point of reversal. The scaling factor, c, is given by:

$$c = \left| \alpha - \frac{\tau_{rev}}{\tau_{max}} \right| \tag{4.27}$$

where: $\alpha$ = -1 for unloading and +1 for reloading

$\tau_{rev}$ = the shear stress at reversal

$\tau_{max}$ = the shear strength of the material

The Cundall-Pyke hypothesis ensures that the stress never exceeds the shear strength of the soil, even under irregular, transient loading conditions. It thereby achieves the goals of the extended Masing rules, but in a much simpler manner.

A two-parameter, hyperbolic tangent function has typically been employed to define soil stress-strain backbone curves (e.g. Duncan et al., 1980). However, extensive experimental evidence on dynamic soil properties (e.g. Vucetic and Dobry, 1991) suggests that the shear modulus does not degrade as quickly as implied by the hyperbolic tangent function at low strain levels. Modulus reduction curves developed from the experimental data, are typically defined only to shear strains of about 1%. This is problematic, since lateral spreading may produce strains well beyond 1%. To overcome this limitation, the proposed model uses a hyperbolic tangent to provide a transition between the low-strain region defined by modulus reduction curves to the large-strain region at which the shear strength of the soil is mobilized. In this work, the modulus reduction curves of Vucetic and Dobry (1991) were used, and soil strengths were computed using the Mohr-Coulomb failure criterion (assuming cohesionless soil):

$$\tau_{max} = \frac{\sin\varphi}{1-\sin\varphi} K_o \sigma'_{vo} \tag{4.28}$$

where: $\varphi$ = friction angle of the sand

$K_o$ = lateral earth pressure coefficient

$\sigma'_{vo}$ = initial vertical effective stress

Using this approach, the backbone curves (Figure 4.5) capture the small strain behavior observed in dynamic soil tests yet are still bounded by the large strain strength given by the Mohr-Coulomb failure criterion.

The development of excess pore pressure reduces both the stiffness and strength of the soil; consequently the original backbone curve must be degraded as excess pore pressure accumulates. However, even at a pore pressure ratio of unity, soil strength does not reduce to zero. The dilation associated with uni-directional straining allows some residual strength to be mobilized by the soil. This is often termed the "critical," "steady-state," or "residual" strength of the soil. Empirical relationships that predict critical strength were discussed in Section 2.2.3. This model incorporates a simple parabolic relation suggested by the Seed and Harder (1990) data:

$$S_r = [0.1 + 0.0015 * N^2]\, P_{atm} \tag{4.29}$$

where: N = SPT blow count corrected for overburden and fines content

$P_{atm}$ = atmospheric pressure

Equation (4.29) is superimposed on the Seed and Harder data in Figure 4.6. In the absence of excess pore pressure generation, the shear strength is given by equation (4.28). As excess pore pressures develop, the strength will decrease from the initial value given by (4.27) to the residual value given by equation (4.28). The implementation of this process is discussed in the next section.

### 4.3.2 Pore Pressure Generation

The generation of excess pore pressure is computed using a modified version of the energy-based pore pressure scheme originally proposed by Nemat-Nasser and Shokooh (1979). Energy-based schemes relate the work done during cyclic shearing to either volume changes (for drained behavior) or pore pressure changes (for undrained behavior). Nemat-Nasser and Shokooh's model is semi-empirical, but unlike simple semi-empirical models such as Finn, et al. (1977), does not rely on counting load cycles - - a rather subjective task when confronted with dynamic loads that are random, rather than harmonic.

In the proposed model, an increment of work, dW, is computed by integrating the stress-strain path using the trapezoidal rule:

$$dW = \left\{ \frac{\left[ \tau_{t+dt} + \tau_{dt} \right]}{2} - \tau^{st} \right\} \left[ \gamma_{t+dt} - \gamma_t \right] \tag{4.30}$$

By subtracting the initial static shear stress, this equation only considers the work done by the dynamic component of shear stress. The resulting increment of pore pressure, du, is computed by the following semi-empirical expression:

$$du = \frac{\sigma'_{vo}(1+r_u)^a(1-r_u)^b(e_o - e_{min})^c}{\mu e_0} dW \tag{4.30}$$

where: $r_u$ = excess pore pressure ratio

$e_o$ = initial void ratio of the soil

$e_{min}$ = minimum void ratio of the soil a, b, c, and $\mu$ are empirical constants

The excess pore pressure is updated after each time step and used to compute a degradation factor using the following empirical expression:

$$\delta = (1-r_u)^n \tag{4.31}$$

where: $\delta$ = degradation factor

$r_u$ = excess pore pressure ratio

n = degradation exponent

Before cyclic loading commences, $r_u = 0$ and $\delta = 1$, but as u approaches 1, $\delta$ approaches 0. The factor $\delta$ is used to degrade the backbone curve between the initial strength, $\tau_{max}$ (given by (4.28)), and the residual strength, $S_r$ (given by (4.29)). It does so by multiplying the ordinate values of the backbone curve by the following factor:

$$c_b = 1-(1-\delta)\left[1-\frac{S_r}{\tau_{max}}\right] \tag{4.32}$$

which linearly varies from unity at $\delta = 1$ (or $r_u = 0$) to $S_r/\tau_{max}$ at $\delta = 0$ (or $r_u = 1$). This procedure automatically degrades both the stiffness and the strength of a soil as the excess pore pressure rises and the effective stress decreases.

## 4.4 VERIFICATION OF ONE-DIMENSIONAL GROUND RESPONSE MODEL

The previous section presented the analytical and numerical details of the proposed ground response model. However, to ensure the formulation is correct, the numerical procedure must be checked against results obtained using other analytical and numerical methods. This section presents results from a series of analyses conducted to verify the proposed numerical procedure. The analysis cases are grouped into two categories: linear elastic and nonlinear.

### 4.4.1 Linear Elastic Cases

For linear elastic cases, the complex response method was used (see for example, Kramer, 1995), which allows for comparison between the proposed procedure and an analytical method. The complex response method can compute the response of a layered visco-elastic half-space to harmonic loading. Because the proposed model does not consider viscous damping, only undamped cases were analyzed.

The following cases consider single layer and heterogeneous half-spaces, under sloped and level ground conditions, excited at the fundamental and higher modes of vibration. The comparison between theoretical and numerical response was made in the following manner. For a given case, the initial conditions (of shear stress, velocity, and displacement) were computed using the complex response method. These were then used to with the proposed numerical method to compute the steady-state response for one cycle of base loading. Because the response is steady-state, the numerical response (of shear stress, velocity, and displacement) at a end of one cycle should agree with the initial conditions. All analyses were performed using dz = 10.0 in and dt = 64/f, where f is the frequency of base excitation.

#### 4.4.1.1 Level Ground, Single Layer

Figure 4.7 shows the computed response of a single, elastic layer shaken near its fundamental frequency. For this case, a shear modulus of 1000 psi and a unit weight of 0.06 pci were assumed, with a base motion having an amplitude of 1.0 in and a frequency equal to 95% of the fundamental frequency of the deposit. The upper half of Figure 4.7 shows displacement profiles at 64 "snapshots" in time, while the lower half of the figure shows shear stress profiles corresponding to the displacement profiles. This figure shows that the traction-free boundary condition at the ground surface is maintained, and that the displacement amplitude of one inch is correctly specified at the base. The symmetry of the response indicates that the correct magnitudes of shear stress and displacement were computed throughout time and depth.

Figure 4.8 and Figure 4.9 contain the computed response to the same hypothetical soil deposit, but shaken at near its second and third natural frequencies, respectively. Again, a displacement amplitude of 1.0 in was specified at the base of the deposit, but with frequencies at 92% and 95% of the respective second and third theoretical natural frequencies. The minor perturbation shown in the third mode shear stress diagram indicates a slight deviation between the numerical and theoretical response. However, this discrepancy does not amplify through time or depth, and the behavior of the model is quite good.

4.4.1.2 Sloping Ground, Single Layer

The cases presented in the previous section demonstrate the ability of the proposed method to compute dynamic response under level ground conditions. In contrast, Figure 4.10 shows the computed response of an elastic layer that has been inclined at a 20 deg angle with respect to the horizontal. This figure illustrates several important points. First of all, the displacement and shear stress profiles in Figure 4.10 are equal to the superposition of those computed for the level ground case (Figure 4.7) and the initial static shear stress and displacement profiles that arise from the 20 deg inclination. For this particular case, the static displacement is about 6.0 in at the ground surface, and decreases in a parabolic fashion to zero at the base of the deposit. Additionally, the static shear stress is zero at the ground surface, and increases linearly to a value of about -14.0 psi at a depth of 800 in.

Secondly, Figure 4.10 suggests that under sloping ground conditions, nonlinear strains are likely to occur near the bottom of a soil deposit, but more importantly, these plastic strains would be biased (primarily negative in this example). This bias would manifest itself as permanent down-slope displacements. Figure 4.10 verifies that the proposed model can correctly interpret nonzero initial shear stresses.

4.4.1.3 Level Ground, Two Layers

Because soil deposits are inherently heterogeneous, the proposed model must be able to compute the response of a layered half-space exhibiting very high impedance contrasts. Figure 4.11 shows the computed response of a two layer stratigraphy shaken at 94% of its fundamental frequency. The hypothetical profile measures 1000 in thick with a uniform unit weight of 0.06 pci. The upper profile measures 500 in thick and possesses a shear modulus of 300 psi, while the lower profile is much softer with a shear modulus of 100 psi. The displacement response of Figure 4.11 clearly shows the strain discontinuity that exists at the contact between the upper and lower layers, and that much of the strain develops in the lower, softer layer. It also shows that the shear stresses are continuous across this boundary.

Figure 4.12 illustrates the response of a two layer deposit wherein the lower layer is nine times as stiff as the upper layer. Again the shear strains are discontinuous across the layer boundary, while the shear stresses are continuous throughout the deposit. This figure shows that much of the strains develop in the softer layer.

### 4.4.2 Nonlinear Case

Elastic analyses are valuable because analytical solutions exist which allow for direct comparison of a numerical method. Unfortunately, this is not the case for nonlinear analyses, and one must resort to other approximate methods to "verify" a proposed model. To this end, the nonlinear ground response program TESS (Taga Inc., 1993) was used to provide an alternative method against which to compare the proposed numerical method. Although TESS can be used to compute permanent displacements due to initial shear stresses, its finite difference algorithm is only first-order accurate, and there is no provision for decreasing the time step to maintain numerical stability. The user is forced to increase the depth increment, dz, so that stability is maintained, which severely limits the code's applicability to lateral spread behavior, as will be shown in Chapters 6 and 7. The details and results of this analysis effort are presented in the following section.

#### 4.4.2.1 Sloping, Nonlinear Case

The hypothetical soil deposit for this case consisted of two layers – an upper, 80 ft thick layer of yielding soil underlain by a 20 ft thick layer of elastic soil. The yielding soil was characterized with a hyperbolic stress-strain backbone curve possessing a shear modulus of 550 psi and a shear strength of 10 psi. The shear modulus of the elastic layer was held constant at 550 psi. The soil unit weight was assumed to be 0.05 pci and initial shear stresses were computed assuming the deposit was inclined at a 5 deg slope. The deposit was discretized with 20 elements (dz = 5 ft), and the 1949 Olympia earthquake record (M = 7.1, $a_{max}$ = 0.164 g) was used for the input motion. This record is approximately 90 s in duration, with a main shock that lasted until about 25 s, with a peak accelerations below 0.05 g thereafter.

The ground surface displacement time histories computed using the two methods are presented in Figure 4.13. Both methods predict a permanent displacement on the order of 16 to 18 in, with TESS predicting a somewhat larger value than the proposed method. It is interesting to note that both methods indicated that about half the permanent displacement developed after the main shock at 25 s. It is impossible to explain the observed differences between the computed displacement records, because the details surrounding the constitutive model used in TESS are not known. In spite of this, the results are in very good general agreement.

## 4.5 SUMMARY

This chapter has introduced a new method to compute lateral spread displacements. This includes a numerical procedure to solve the governing differential equations, a constitutive model to track non-linear stress-strain behavior, and a model that predicts the generation of excess pore pressures during shaking. The numerical procedure was verified through direct comparison with numerical and analytical methods. This substantiates the model's ability to predict the dynamic response of nonlinear soil deposits subjected to non-zero initial shear stresses. Chapters 6 and 7 of this dissertation describe additional analyses conducted using the proposed methodology. This includes cases using the pore pressure model described above to compute liquefaction-induced lateral spread displacements.

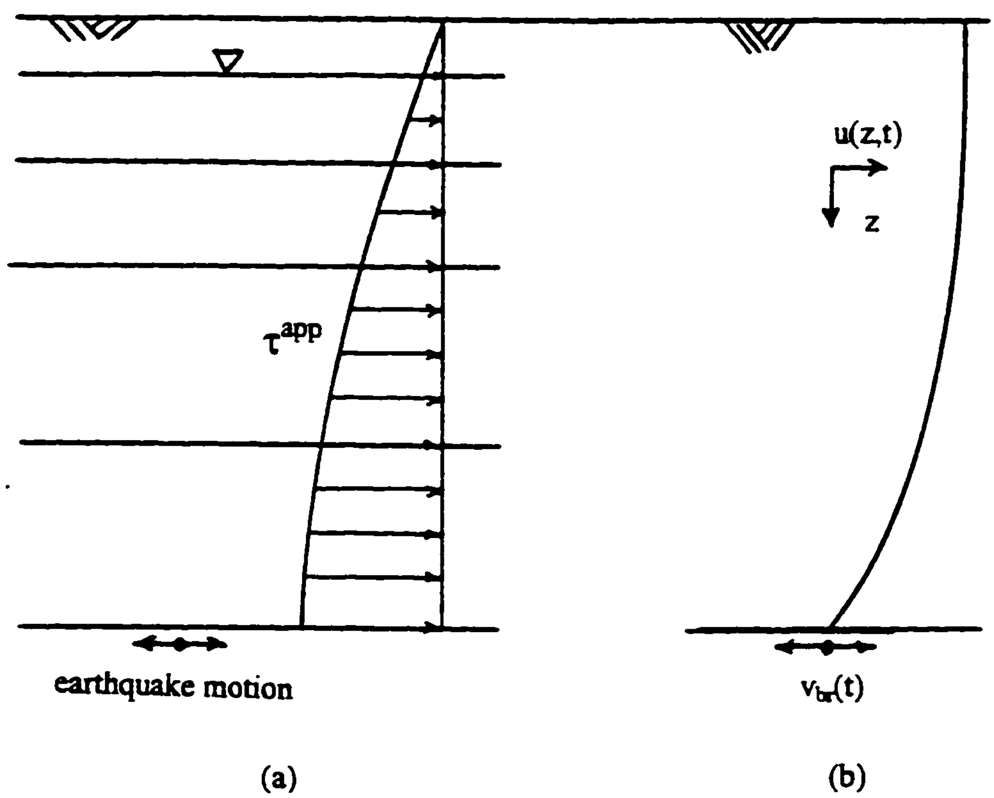


Figure 4.1 (a) Soil continuum considered for analysis, and (b) free-field displacement

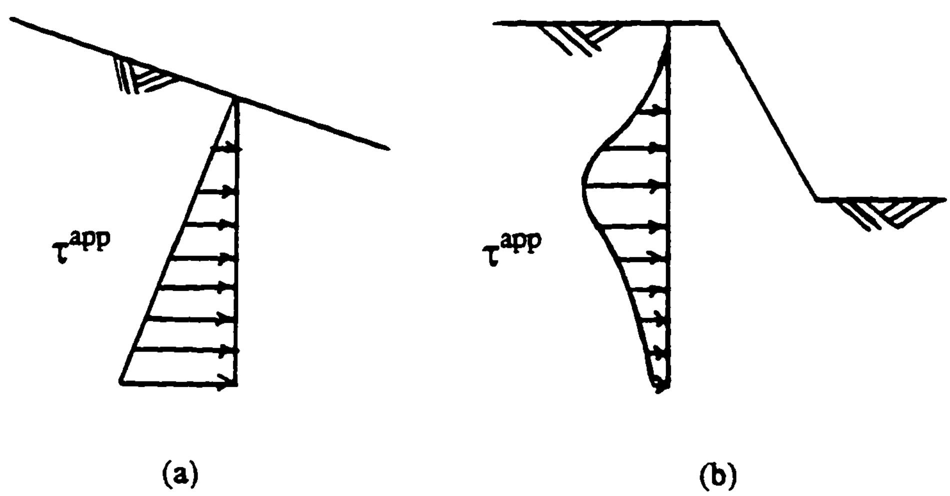


Figure 4.2 Initial shear stresses arising from (a) sloping, or (b) irregular ground surface

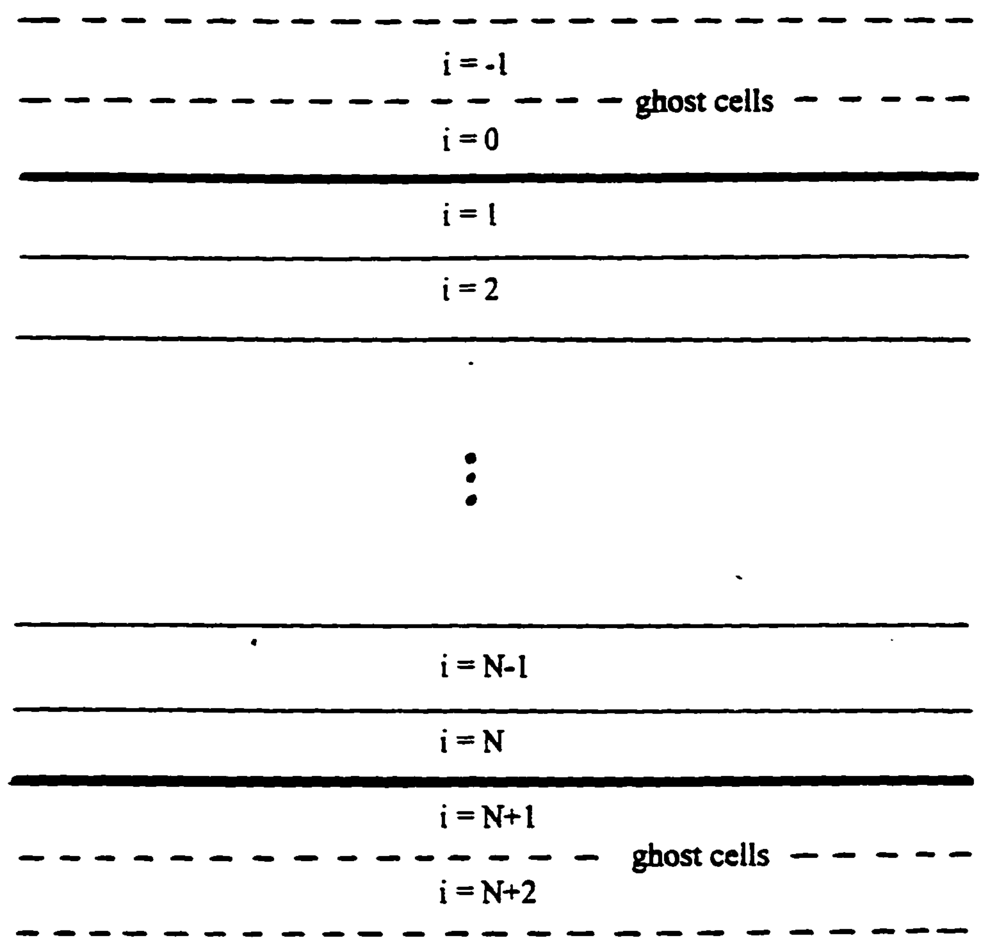


Figure 4.3 Discretized domain and ghost cells

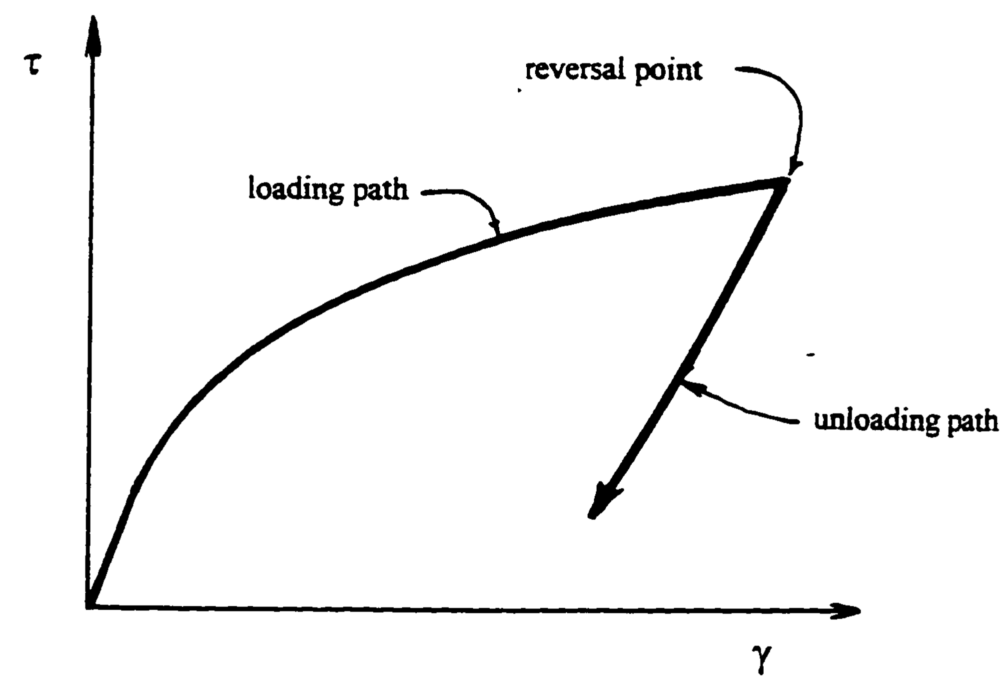


Figure 4.4 The effect of load reversal on stress-strain behavior

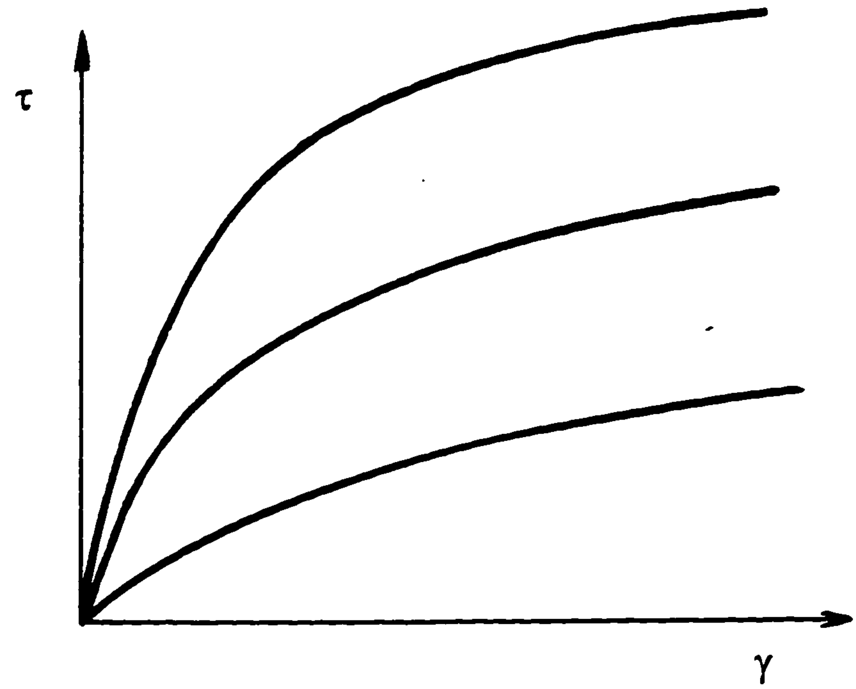


Figure 4.5 Backbone curves used to define stress strain behavior

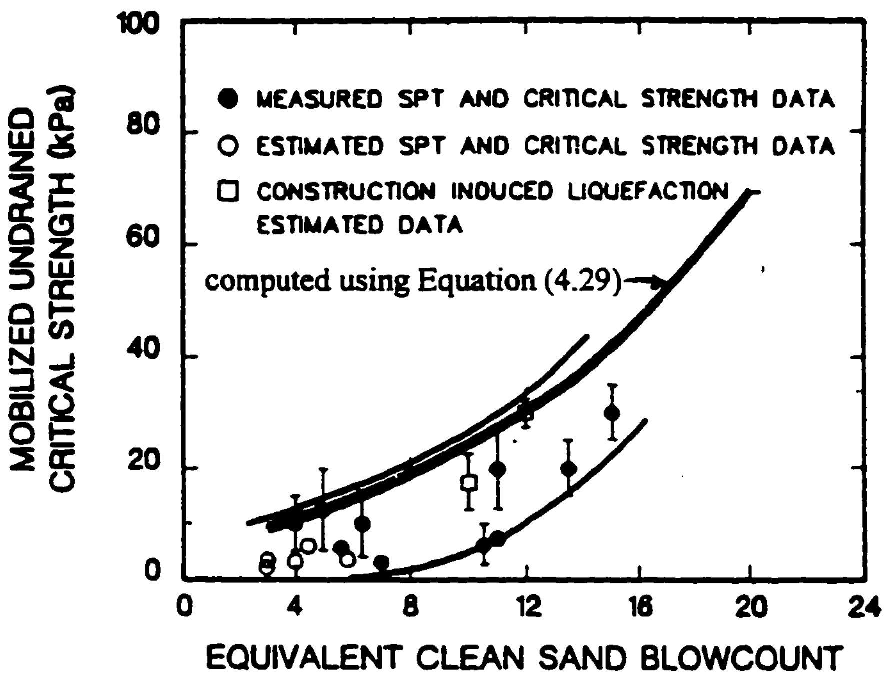


Figure 4.6 Equation (4.29) superimposed on the Seed and Harder (1992) data

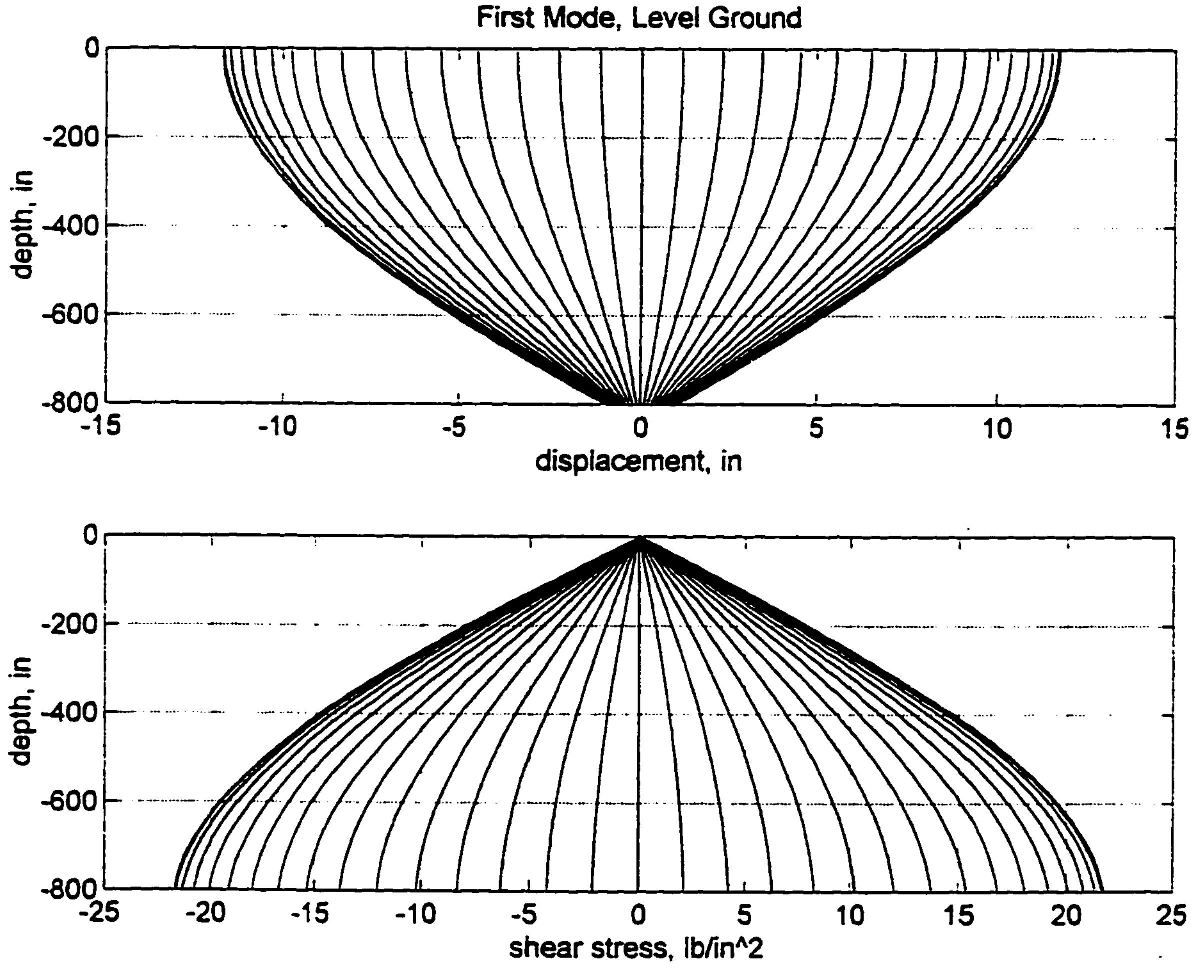


Figure 4.7 Level ground response to harmonic loading near the first mode

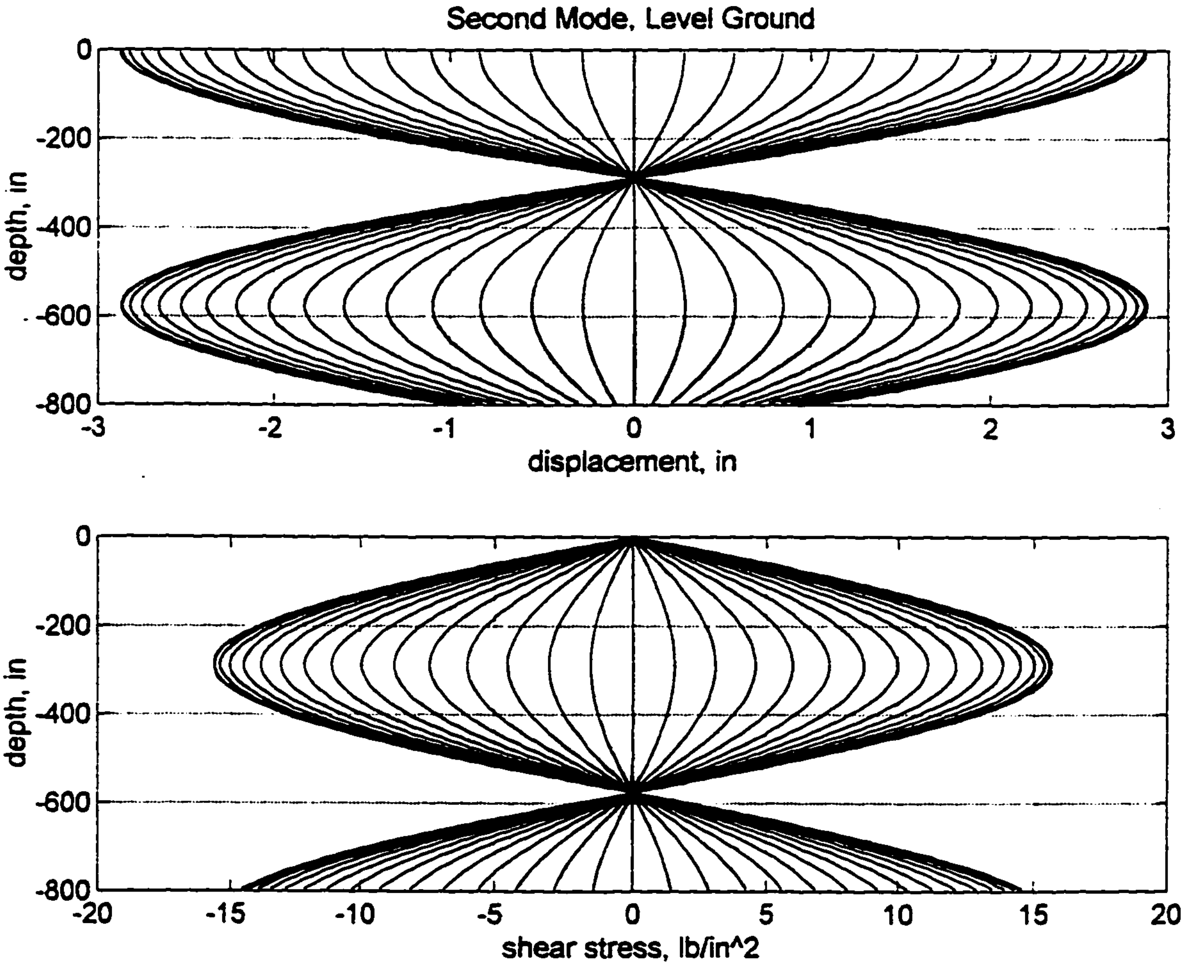


Figure 4.8 Level ground response to harmonic loading near the second mode

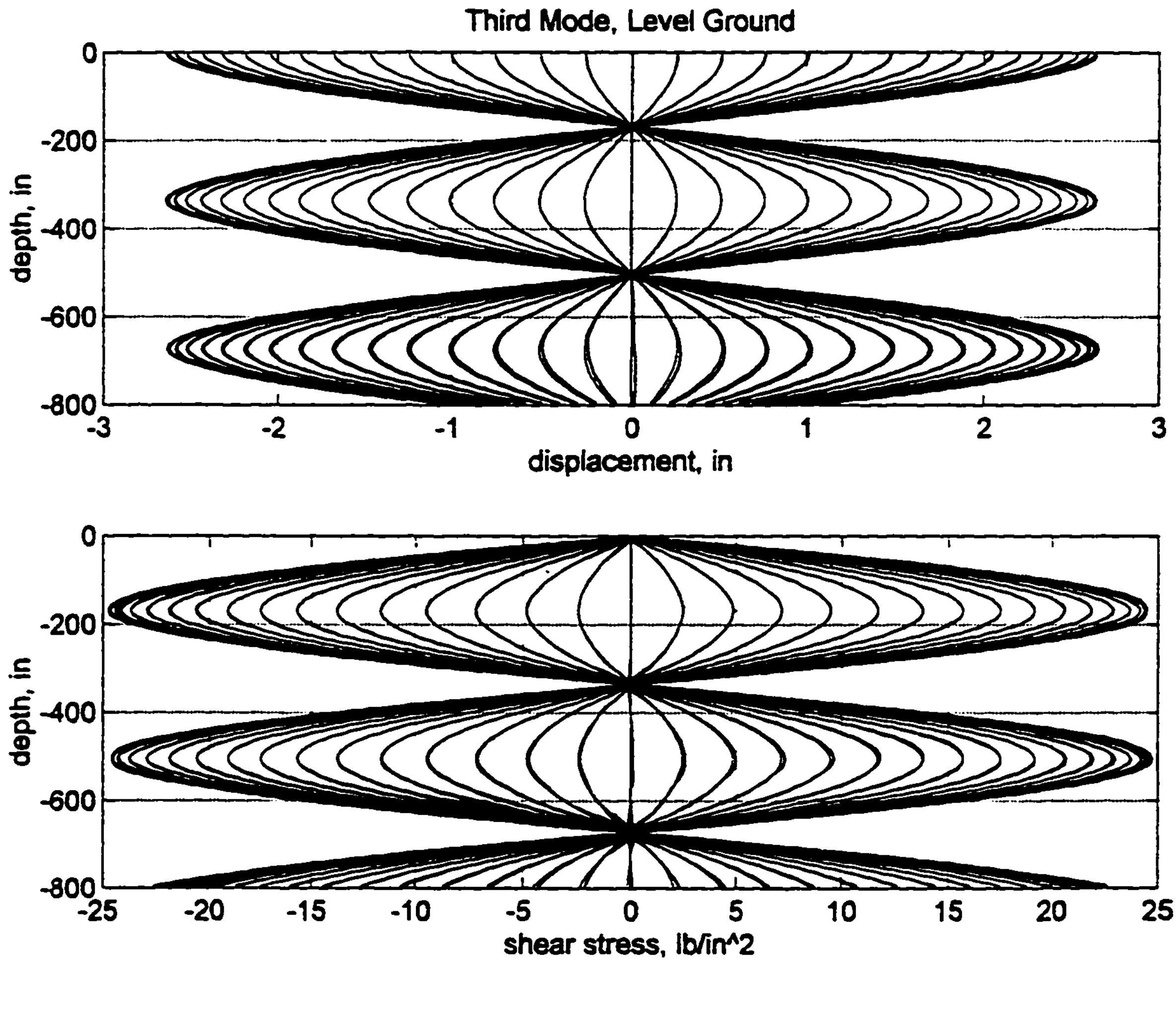


Figure 4.9 Level ground response to harmonic loading near the third mode

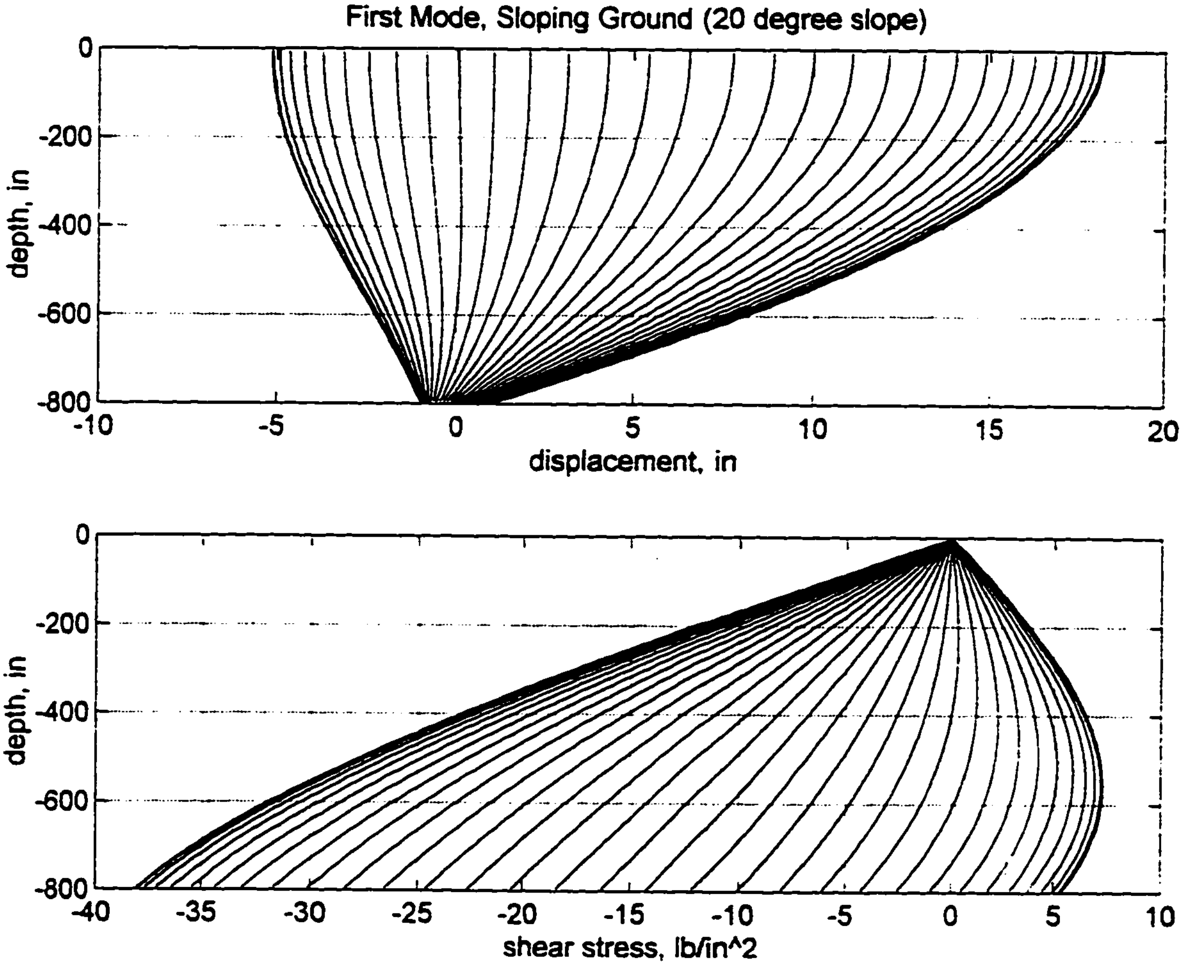


Figure 4.10 Sloping ground response to harmonic loading near the first mode

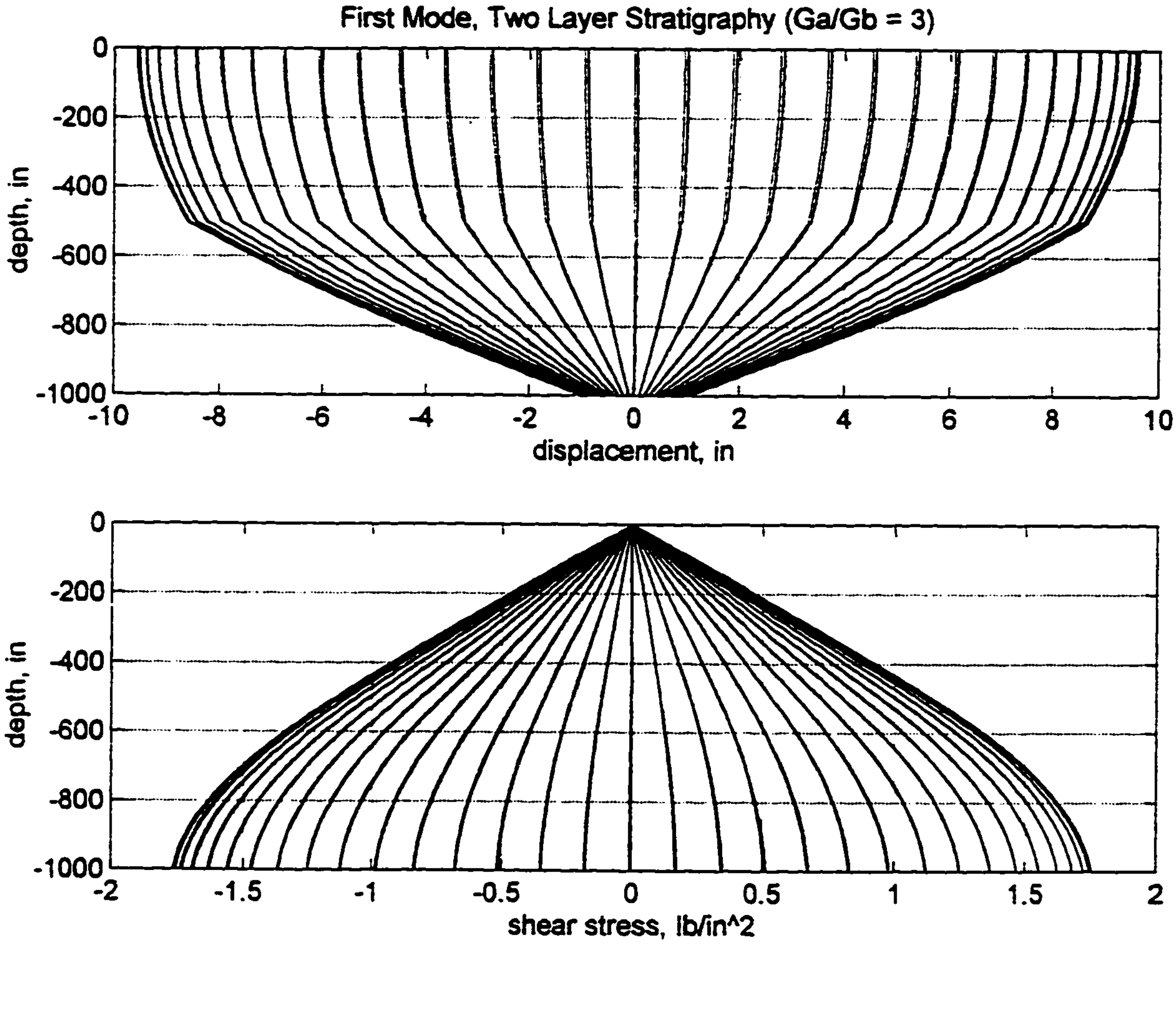


Figure 4.11 Two-layer ground response to harmonic loading near the first mode (upper layer has three times the shear modulus as the lower layer)

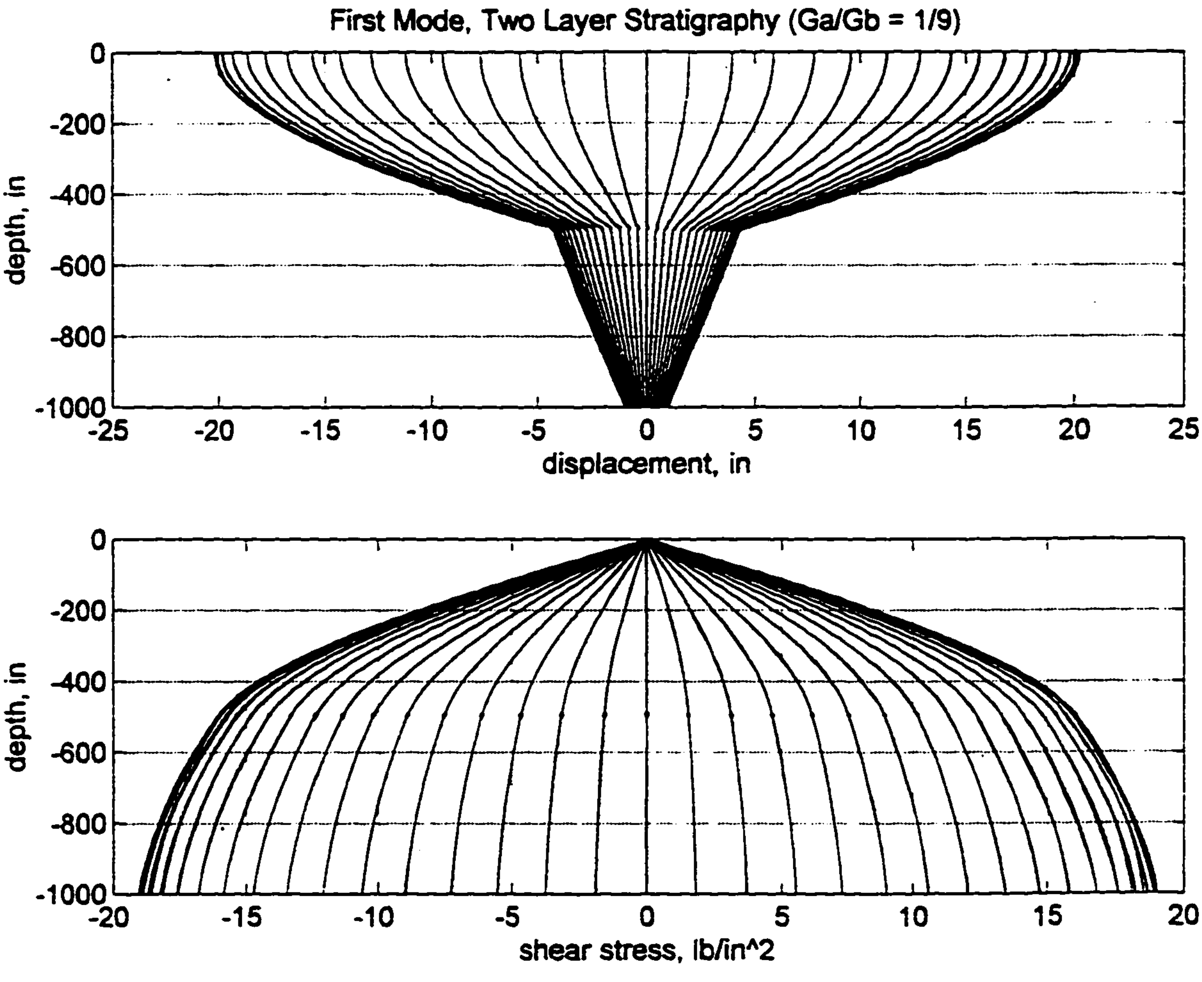


Figure 4.12 Two-layer ground response to harmonic loading near the first mode. (upper layer has one ninth the shear modulus as the lower layer.

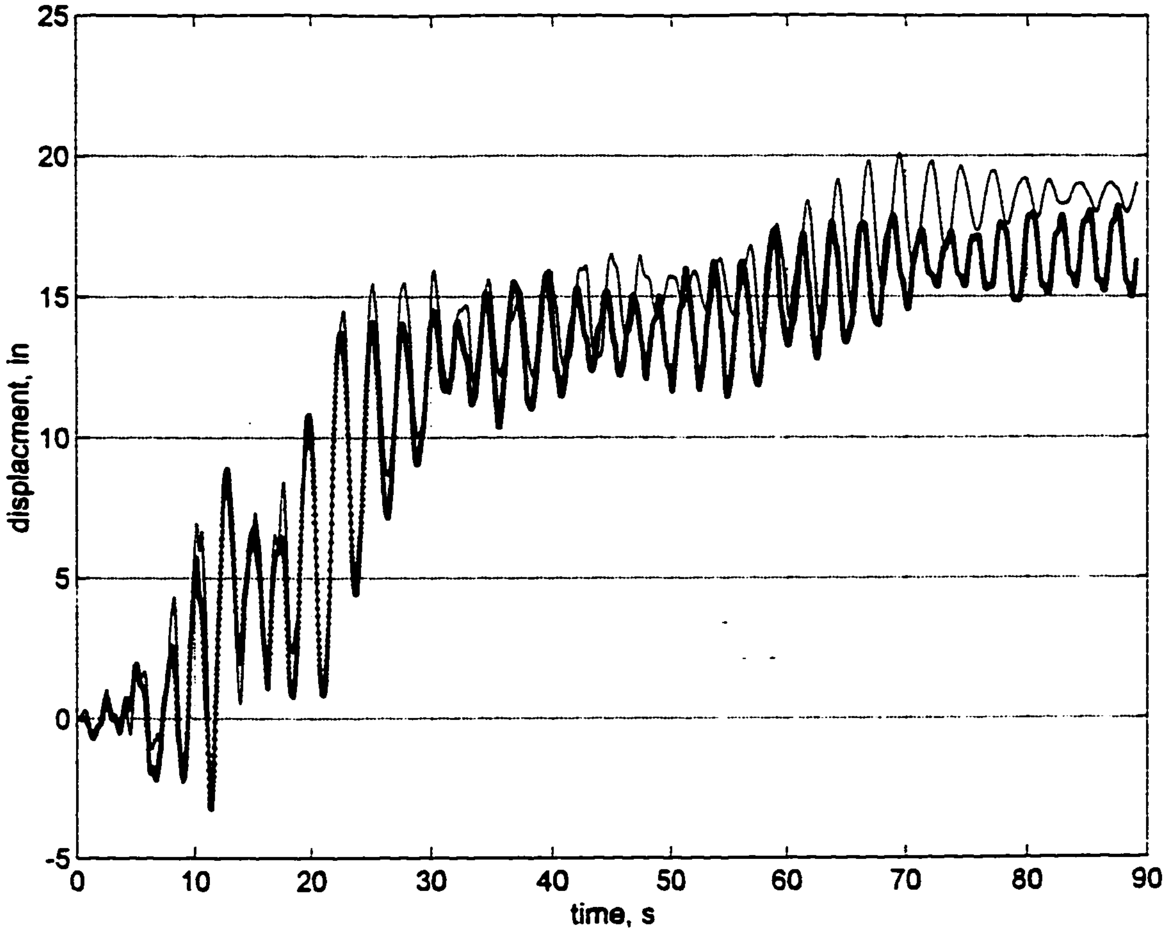


Figure 4.13 Comparison between ground surface displacements computed using the proposed model (bold line) and the commercially available program, TESS (light line)

# Chapter 5 Development of a Pile-Soil Interaction Model

## 5.1 INTRODUCTION

Chapter 3 described previous research that relates to pile-soil interaction. The deficiency of this work was discussed in Section 3.6. As described in Chapters 2 and 3, a useful procedure for evaluation of lateral spreading effects on piles must be able to predict the response of a pile to general loading. More specifically, the procedure must be able to compute pile displacements and internal forces both during strong ground shaking – when dynamic inertial forces are greatest, and after strong shaking -- when lateral spread displacements reach their maximum values. Such a procedure should also incorporate the effects of radiation damping and the effects of liquefaction-induced excess pore pressure on the pile-soil stiffness.

This chapter introduces a new model for prediction of the response of a pile to general lateral loading. The procedure is particularly effective for evaluating the effects of lateral spreading on pile foundations. The chapter contains three main sections. The first contains the analytical and numerical treatment of a one-dimensional Winkler beam model of a pile foundation. The second describes the method used to determine the pile-soil interaction behavior of an element of the model. The third section verifies the model against results published by other researchers.

## 5.2 DYNAMIC RESPONSE OF A LATERALLY LOADED PILE

Figure 5.1depicts the pile-soil system considered in the foregoing analysis. Figure 5.1(a) represents the actual system being modeled: a single, axially loaded pile embedded in a continuous soil half-space. Figure 5.1(b) shows the pile being deflected laterally by a general earthquake-induced free-field soil displacement. The free-field displacements induce bending moments in the pile along its length. Many analytical procedures have been developed for analysis of the response of a pile embedded in a continuum to lateral loads. A commonly used approach, which combines computational simplicity with sufficient flexibility to handle most practical problems is the beam-on-elastic foundation approach (Hetenyi, 1946). The beam-on-elastic-foundation approach is usually implemented in the idealized form of a Winkler foundation in which the continuum surrounding the pile was replaced by a series of independent springs. The Winkler model has become commonly used in geotechnical engineering practice for piles subjected to static, externally applied lateral loads. Extension to dynamic conditions, including the effects of free-field soil deformations, is relatively straightforward (e.g., Kavvadas and Gazetas, 1993). Figure 5.2 shows the Winkler beam, which is connected to the free-field along its length by a series of independent, rheologic models which characterize the pile-soil interaction. The characterization of the pile-soil interaction force – which involves the near-field and far-field models depicted in Figure 5.2 -- is the subject of the next section. The free-field motion – which includes the displacement, velocity, shear modulus, and pore pressure time histories -- may be computed using the methodology introduced in Chapter 4. The free-field motion provides the dynamic forcing function to the pile, and is assumed to be unaffected by the presence of the pile.

### 5.2.1 Governing Equation

The response of a pile to general dynamic loading is governed by a partial differential equation. In subsequent equations, the independent variables of depth and time appear as symbols, z and t, respectively. Subscripts z or t which appear on various terms imply spatial or temporal differentiation, respectively. The following fourth order PDE, derived by equilibrium consideration of a differential pile element, describes the response of the pile shown in Figure 5.1:

$$EIw_{zzzz} + Qw_{zz} + m_p w_{tt} = P(w, w_t, w_{tt}, u, u_t, G, r_u, \rho) \tag{5.1}$$

where: $w = w(z,t)$ = unknown absolute pile displacement

$u = u(z,t)$ = absolute free-field soil displacement

$m_p$ = mass per unit length of pile

$EI$ = flexural rigidity of the pile

Q = axial load on the pile

P = nonlinear pile-soil interaction force

G = G(z,t) = free-field shear modulus

$r_u = r_u(z,t)$ = free-field excess pore pressure ratio

$\rho = \rho(z,t)$ = free-field soil density

For the special case where the pile-soil interaction force is represented by the two parameter Kelvin model, (5.1) reduces to:

$$EIw_{zzzz}+Qw_{zz}+m_p w_{tt}+C(w_t-u_t)+K(w-u)=0 \qquad (5.2)$$

where: K = constant stiffness coefficient

C = constant damping coefficient

Equation (5.2) may be rearranged with Ku and $Cu_t$ on the right hand side. The right side of the resulting expression then represents known source terms arising from the free-field displacement and velocity time histories.

### 5.2.2 Initial and Boundary Conditions

Like the ground response model formulated in Chapter 4, the pile response model requires that initial and boundary conditions be satisfied. Because pile displacement is the only field variable in the preceding formulation of the governing equation, all initial and boundary conditions pertaining to the pile response problem are cast in terms of pile displacement or its derivatives. Appropriate initial conditions are discussed in Section 5.2.2.1 while several boundary condition options are explored in Section 5.2.2.2.

#### 5.2.2.1 Initial Conditions

The initial condition is satisfied trivially by specifying the initial displacement to be zero throughout the domain:

$$w(z,0) = 0 \qquad (5.3)$$

5.2.2.2 Boundary Conditions

There are many choices of boundary conditions which can be specified at the top of the pile (the "head", at z=0) and the bottom of the pile (the "toe", at z=L). These conditions typically relate to the fixity of these points with respect to displacement or rotation. Two sets of boundary conditions appear below. These include **Rotation and Moment** boundary conditions and **Displacement and Shear** boundary conditions.

**Rotation and Moment Boundary Conditions**: For a pile subjected to a known rotation time history, $\varphi(t)$, at either end, the appropriate boundary condition is:

$$w_z(t,z=0,L)=\varphi(t) \qquad (5.4)$$

A "fixed" boundary condition is a special case of (5.4) wherein rotation is precluded. This may be the case, say at a rigid pile cap connection:

$$w_z(t,z=0,L)=0 \qquad (5.4a)$$

Conversely, for a pile subjected to a specified bending moment time history, M(t) – perhaps during a dynamic lateral load test – the appropriate boundary condition becomes:

$$w_{zz}(t,z=0,L)=M(t)/EI \qquad (5.5)$$

A "pinned" boundary condition – which may exist at the top of a free head pile or at the bottom of relatively slender piles – is a special case of (5.5) whereby the bending moment is always zero:

$$w_{zz}(t,z=0,L)=0 \qquad (5.5a)$$

**Displacement and Shear Boundary Conditions**: Large diameter piles and belled caissons may experience very little relative displacement with respect to the free field. In this case it is appropriate to assign the known free field displacement time history, u(t), directly as indicated in (5.6):

$$w(t,z=0,L)=u(t) \qquad (5.6)$$

A special case of (5.6) exists if the pile is fixed against lateral displacement, in which the corresponding displacement boundary condition becomes:

$$w(t,z=0,L)=0 \tag{5.6a}$$

For a pile subjected to a known lateral force, V(t) – say from a lateral load test – the appropriate boundary condition is:

$$w_{zzz}(t,z=0,L)=V(t)/EI \tag{5.7}$$

For the special case of zero shear, (5.7) reduces to:

$$w_{zzz}(t,z=0,L)=0 \tag{5.7a}$$

Of the preceding boundary conditions, either (5.4) or (5.5) and either (5.6) or (5.7) must be specified at each end of the pile. There is one other type of boundary condition which does not appear above. This is the case of a compliant inertial structure placed on top of the pile. In this case, the boundary moment (or rotation) and shear (or deflection) would be coupled between the compliant structure and the underlying pile. Since these quantities would not be known a-priori, this would preclude their direct specification in the form of a boundary condition. However, the methodology presented below in Section 5.2.3 could easily be adapted to evaluate such a boundary condition.

### 5.2.3 Pile-Soil Interaction Force

Proper characterization of the pile-soil interaction force is crucial to the successful application of the method to lateral spread problems. As indicated in equation (5.1), the pile-soil interaction force effectively couples the pile to the free field. Previous research on this subject was reviewed in Chapter 3. In conclusion, there has been no attempt to create a model which incorporates radiation damping and liquefaction-induced softening in a time domain context for lateral spread problems. A pile-soil interaction model by Nogami and Konogai (1992) operates in the time domain but only considers pile response from forces applied at the pile head, and does not consider the effects of liquefaction on the pile-soil interaction force.

This section contains a novel description of the pile-soil interaction force. It does so by separating the force into two components: the near field and the far field. Each of these may behave in a nonlinear fashion. The near field captures damping behavior which is largely hysteretic in nature. It is a region of soil close to the pile - on the order of one or two diameters from the pile center. Conversely, the far field model replicates radiation damping behavior. It represents an absorbing boundary that accounts for acoustic energy emanating away from the pile. Taken together, they represent the most comprehensive pile-soil interaction model to date for use in studying lateral spreading effects on piles.

5.2.3.1 Near Field Model

The localized volume of soil adjacent to a pile determines the hysteretic behavior of pile-soil interaction. The width of this annular region -- sometimes called the "near field" -- is on the order of one or two pile diameters. Two primary attributes of the near field model – shown in Figure 5.3 -- are a nonlinear stiffness and a coupled inertia. The formulation of the near field model, including a description of its nonlinear stiffness and inertial terms, is described in the following paragraphs.

Traditional, non-linear p-y curves characterize the stiffness of the near field model (e.g. O'Neill and Murchison (1983)). However, in order to recover the correct static stiffness in the presence of the compliant far-field model, these curves must first be scaled upward by the amount:

$$c_{nf} = \left[1 - \frac{k^0{}_{py}}{k^0{}_{ff}}\right]^{-1} \qquad (5.8)$$

where $k_{py}{}^0$ = initial p-y stiffness

$k_{ff}{}^0$ = initial, equivalent static far-field (Section 5.2.3.2)

The tangent slope of the scaled p-y curve is the near field stiffness, $k_n$. The p-y curves scaled by (5.8) form the initial backbone curves for the non-linear near field model. These curves serve much the same function as the stress-strain backbone curves discussed in Chapter 4. That is, they describe the nonlinear displacement response to a monotonically-applied load. The extension of monotonic p-y behavior to dynamic loading is straightforward, and can be accomplished by incorporating the same hysteretic procedure that was described in Chapter 4.

Basic soil mechanics suggests that p-y curves should degrade as the excess pore pressure increases. Indeed, typical p-y curve formulations (e.g. O'Neill and Murchisson, 1983) cast the p-y behavior in terms of effective stress. The centrifuge data cited by Liu and Dobry (1995) suggests that p-y behavior strongly depends on the excess pore pressure ratio. Their results indicated that the build-up of excess pore pressure degraded the static p-y curves, and this degradation was characterized by a factor $C_u$ which varied linearly from 1.0 at $r_u$ = 0.0 to 0.0 at $r_u$ = 1.0 (Figure 3.18). The authors proposed multiplying the p-coordinates of static p-y curves by $C_u$ to account for the generation of excess pore pressure. Closer examination of Figure 3.18 indicates that their empirical expression ($C_u$ = 1.0 - $r_u$) represents somewhat of a lower bound of the experimental data. Alternatively, an expression in closer agreement with the average of the data is given by:

$$C_u = \min(1\,,\,1.1 - r_u) \tag{5.9}$$

in which the "min" expression implies the minimum of the two arguments appearing within the parentheses.

The near field also contributes coupled inertial effects to the pile-soil interaction. This is taken into account by the consistent mass matrix proposed by Nogami and Konagai (1992):

$$\overline{m}_n = \frac{\pi \rho_s r_0^2}{6}\left(\frac{r_1}{r_0} - 1\right)\begin{bmatrix} \frac{r_1}{r_0} + 3 & \frac{r_1}{r_0} + 1 \\ \frac{r_1}{r_0} + 1 & 3\frac{r_1}{r_0} + 1 \end{bmatrix} \tag{5.10}$$

where: $\rho_s$ = soil density

$r_0$ = radius of the pile

$r_1$ = radius of the near field

For numerical stability, a small amount of numerical damping is introduced into the numerical solution of the pile-soil interaction model. This damping is introduced through a near-field viscous dashpot in parallel with the nonlinear inelastic spring; the dashpot coefficient is given by:

$$c_n = 2\beta\sqrt{k_n m}_p \tag{5.11}$$

where: $\beta$ = desired damping ratio

$k_n$ = scaled, near field stiffness

5.2.3.2 Far Field model

The radiation damping behavior associated with a vibrating pile embedded in a continuum is accounted for by the far field model. This is a direct adaptation of the model first proposed by Nogami and Konagai (1988), which the authors verified for the case of a pile laterally loaded at the head. However, the current research extends the far field model to include free-field excitation and the softening effects of liquefaction. This section first describes the elements which make-up the far field model, and then discusses how these elements are characterized.

A diagram of the far field model appears in Figure 5.3. It consists of three Kelvin models arranged in series along with a single point mass. Although analytically quite simple, the far field model can be shown to accurately represent the complex impedance of a vibrating pile over a very wide frequency range. It is the first description to do so in a time-domain formulation. The appropriate mass, stiffness, and damping values were given by Nogami and Konagai (1992) as:

$$m_f = \pi\rho\, r_1^2 \xi_m(\nu) \tag{5.12a}$$

$$k_1 = 3.518G\xi_k(\nu) \tag{5.12b}$$

$$k_2 = 3.581G\xi_k(\nu) \tag{5.12c}$$

$$k_3 = 5.529G\xi_k(\nu) \quad (5.12d)$$

$$c_1 = 113.097G\xi_k(\nu)r_1/V_s \quad (5.12e)$$

$$c_2 = 25.133G\xi_k(\nu)r_1/V_s \quad (5.12f)$$

$$c_3 = 9.362G\xi_k(\nu)r_1/V_s \quad (5.12g)$$

where: $\rho$ = soil density

$r_1$ = outer radius of the near field

$G$ = shear modulus of the soil

$V_s$ = shear wave velocity of the soil

$\nu$ = Poisson's ratio of the soil

$\xi_m(\nu)$ = dimensionless mass factor (= 1.0 for $\nu$ = 0.5)

$\xi_k(\nu)$ is a dimensionless stiffness factor (= 2.0 for $\nu$ = 0.5)

Under static conditions, the far-field model exhibits an equivalent stiffness given by:

$$k_{ff} = \left[\frac{1}{k_1} + \frac{1}{k_2} + \frac{1}{k_3}\right]^{-1} \quad (5.13)$$

The model requires free field soil properties which include shear modulus, density, and Poisson's ratio. Shear moduli and density are known from the ground response analysis outlined in Chapter 4. This strategy automatically accounts for the effect of liquefaction because the shear moduli of the free-field soil elements are already degraded for the effects of excess pore pressure by the ground response analysis. Poisson's ratio for undrained response of soils is taken to be 0.5. The model also requires the size of the free field, $r_1$. The behavior of the far field model is fairly insensitive to the size of the free-field (Nogami and Konogai, 1992). Hence, a value of $r_1$ equal to twice the pile radius was chosen.

5.2.3.3 <u>Incremental Governing Equation of the Pile-Soil Interaction Model</u>

When combined, the near field and far field models represent a comprehensive description of the total pile soil interaction. In matrix form, the incremental governing equation of motion which describes this model is given by:

$$\begin{bmatrix} m_{n1,1} & m_{n1,2} & 0 & 0 & 0 \\ m_{n2,1} & m_{n2,2}+m_f & 0 & 0 & 0 \\ 0 & 0 & 0 & 0 & 0 \\ 0 & 0 & 0 & 0 & 0 \\ 0 & 0 & 0 & 0 & 0 \end{bmatrix} \begin{Bmatrix} da_p \\ da_{nf} \\ da_a \\ da_b \\ da_{ff} \end{Bmatrix} + \begin{bmatrix} c_n & -c_n & 0 & 0 & 0 \\ -c_n & c_n+c_1 & -c_1 & 0 & 0 \\ 0 & -c_1 & c_1+c_2 & -c_2 & 0 \\ 0 & 0 & -c_2 & c_2+c_3 & -c_3 \\ 0 & 0 & 0 & -c_3 & c_3 \end{bmatrix} \begin{Bmatrix} dv_p \\ dv_{nf} \\ dv_a \\ dv_b \\ dv_{ff} \end{Bmatrix} + \ldots$$

$$\ldots \begin{bmatrix} k_n & -k_n & 0 & 0 & 0 \\ -k_n & k_n+k_1 & -k_1 & 0 & 0 \\ 0 & -k_1 & k_1+k_2 & -k_2 & 0 \\ 0 & 0 & -k_2 & k_2+k_3 & -c_3 \\ 0 & 0 & 0 & -c_3 & k_3 \end{bmatrix} \begin{Bmatrix} du_p \\ du_{nf} \\ du_a \\ du_b \\ du_{ff} \end{Bmatrix} = \begin{Bmatrix} 0 \\ 0 \\ 0 \\ 0 \\ 0 \end{Bmatrix} \qquad (5.14)$$

in which the various matrix elements are given by expressions in the previous sections, and the five degrees of freedom are as shown on Figure 5.3.

For the purposes of analysis, it is appropriate to assume that at any point in time, the pile and free field motion is known. The resulting static condensation of Equation (5.14) becomes:

$$\begin{bmatrix} m_{n2,2}+m_f & 0 & 0 \\ 0 & 0 & 0 \\ 0 & 0 & 0 \end{bmatrix} \begin{Bmatrix} da_{nf} \\ da_a \\ da_b \end{Bmatrix} + \begin{bmatrix} c_n+c_1 & -c_1 & 0 \\ -c_1 & c_1+c_2 & -c_2 \\ 0 & -c_2 & c_2+c_3 \end{bmatrix} \begin{Bmatrix} dv_{nf} \\ dv_a \\ dv_b \end{Bmatrix} + \begin{bmatrix} k_n+k_1 & -k_1 & 0 \\ -k_1 & k_1+k_2 & -k_2 \\ 0 & -k_2 & k_2+k_3 \end{bmatrix} \begin{Bmatrix} du_{nf} \\ du_a \\ du_b \end{Bmatrix} = \begin{Bmatrix} dp_{nf} \\ 0 \\ dp_b \end{Bmatrix} \qquad (5.15)$$

where: $dp_{nf} = k_n du_p + c_n dv_p - m_{n1,2} da_p$

$dp_{ff} = k_3 du_{ff} + c_3 dv_{ff}$

Equation (5.15) may be written in short-hand as:

$$\overline{M}d\overline{a} + \overline{C}d\overline{v} + \overline{K}d\overline{u} = d\overline{p} \qquad (5.16)$$

5.2.3.4 Numerical Solution

Equations (5.15) or (5.16) represent a system of three second order ordinary differential equations, or ODE's, that are discrete in space and continuous in time. These equations must be solved to determine the internal degrees of freedom of the interaction model. The stiffness and damping coefficients are not constant, and hence the system cannot be solved using modal methods. Of the numerical methods available to solve this system, the Wilson Theta method (see Clough and Penzien, 1975) is well-suited. Wilson's method reduces (5.16) to the pseudostatic, linear system:

$$\overline{K}^{*}d\overline{u}^{*} = d\overline{p}^{*} \tag{5.17}$$

In this expression, the effective load vector is given by:

$$d\overline{p}^{*} = \theta d\overline{p} + \overline{M}\left[\frac{6}{\theta dt}\overline{v} + 3\overline{a}\right] + \overline{C}\left[3\overline{v} + \frac{\theta dt}{2}\overline{a}\right] \tag{5.18}$$

and the effective stiffness matrix is given by:

$$\overline{K}^{*} = \overline{K} + \frac{6}{(\theta dt)^{2}}\overline{M} + \frac{3}{\theta dt}\overline{C} \tag{5.19}$$

The variable dt represents the time step, while $\theta$ is used to compute an extended time step, $\theta$dt, over which the incremental equations of motion are solved. The numerical system is unconditionally stable for $\theta > 1.37$ (Clough and Penzien, 1975).

The effective stiffness matrix, (5.19), is easily inverted, and the pseudostatic relationship can be solved for the incremental displacements over the extended time step. These are then used to compute the incremental accelerations over the normal time step:

$$d\overline{a} = \frac{1}{\theta}\left[\frac{6}{(\theta dt)^{2}}d\overline{u}^{*} - \frac{6}{\theta dt}\overline{v} - 3\overline{a}\right] \tag{5.20}$$

The increments in velocity over the normal time step are given by:

$$d\overline{v} = dt\left(\overline{a} + \frac{d\overline{a}}{2}\right) \tag{5.21}$$

and the increments of displacement over the normal time step are:

$$d\overline{u} = dt\left(\overline{v} + \frac{dt}{2}\overline{a} + \frac{dt}{6}d\overline{a}\right) \tag{5.22}$$

Equations (5.20) through (5.22) are used with the incremental equation of motion (5.15) to compute the velocity at the end of the time step based on equilibrium:

$$\overline{v} = \overline{C}^{-1}\left[\left(\overline{p} + d\overline{p}\right) - \overline{K}\left(\overline{u} + d\overline{u}\right) - \overline{M}\left(\overline{a} + d\overline{a}\right)\right] \tag{5.23}$$

The updated pile-soil interaction force is given by:

$$\begin{aligned} p(i+1,j) = p(i,j) &- K_n(j)\,[du_p(j) - du_{nf}(j)] \ldots \\ &- C_n(j)\,[dv_p(j) - dv_{nf}(j)] \ldots \\ &- m_n(1,1)da_p(j) - m_n(1,2)da_{nf}(j) \end{aligned} \tag{5.24}$$

### 5.2.4 Numerical Discretization

It is possible to recast equation (5.1) as a system of four first order PDE's which can be solved numerically using the methodology presented in Chapter 4. Unlike the wave equation, however, Equation (5.1) cannot be put into diagonal form due to the singular coefficient matrices which would arise. For this reason, and because the pile displacement profile is expected to be smooth, the unknown displacement field will be directly solved for by discretizing the fourth order PDE, Equation (5.1), in z-t space using finite difference procedures. Using centered difference approximations for the derivatives in Equation (5.1), the pile displacement at depth j and time step i+1 can be computed explicitly. The resulting expression is given by:

$$w_j^{i+1} = -\left(\frac{dt^2}{m_p}\right)^{-1}\left\{\begin{array}{l} \dfrac{EI}{dz^4}\left[w_{j+2}^i - 4w_{j+1}^i + 6w_j^i - 4w_{j-1}^i + w_{j-2}^i\right] + \ldots \\ \dfrac{Q}{dz^2}\left[w_{j+1}^i - 2w_j^i + w_{j-1}^i\right] + \ldots \\ \dfrac{m_p}{dt^2}\left[w_j^{i-1} - 2w_j^i\right] + P_j^i \end{array}\right\} \tag{5.25}$$

The computation stencil of this finite difference method is shown in Figure 5.4. In the preceding discretization scheme, the indices j-1, j, and j+1 represent the previous, current, and next grid point in the spatial coordinate, respectively. Likewise, i-1, i and i+1 index the previous, current and next grid point in the temporal coordinate, respectively. Furthermore, dt and dz represent the time and space increments used to discretize the computational domain.

## 5.3 VERIFICATION OF THE PILE-SOIL INTERACTION MODEL

This section serves to verify the accuracy of the new procedure by comparison against published data involving pile-soil interaction. Two broad studies were performed. The first investigates the dynamic response of a pile embedded in a harmonically-excited, two layer half-space. The second verifies the that the complex impedances computed using the proposed procedure match those reported in the literature. Cases involving nonlinear soils behavior and lateral spreading are contained in Chapters 6 and 7.

### 5.3.1 Dynamic Response of a Single Pile

Kavvadas and Gazetas (1993) conducted a parametric study of a pile embedded in a two-layer elastic half-space subjected to harmonic base excitation. A broad array of 24 combinations of pile-soil stiffness and layer thicknesses were considered. Table 5.1 lists the parameters explored in the study. In the table, subscripts "a," "b," and "p" refer to the upper soil layer, lower soil layer, and pile, respectively. Table 5.1 also lists the properties used in the current study to replicate the authors' analyses.

The authors used a frequency-dependent impedance to represent the pile-soil interaction. The real and imaginary components of the impedance are given by:

$$K = 2.5E_s \tag{5.26a}$$

$$C = \omega\left\{2d\rho_s V_s\left[1 + \left(\frac{V_c}{V_s}\right)^{5/4}\right]\left(\frac{\omega d}{V_s}\right)^{-1/4} + 2K\,\frac{\beta}{\omega}\right\} \tag{5.26b}$$

where: $E_s$ = elastic modulus of the soil

$\omega$ = circular frequency of the applied base motion

d = pile diameter

The variable $V_c$ represents "the apparent velocity of the extension-compression waves," and is equal to:

$$V_c = \begin{Bmatrix} V_s & if \ \dfrac{z}{d} \leq 2.5 \\ \dfrac{3.4V_s}{\pi(1-\nu)} & if \ \dfrac{z}{d} > 2.5 \end{Bmatrix} \tag{5.27}$$

where: z = depth below the ground surface

All of the variables used in the analyses are listed in Table 5.1. The pile was discretized using dz = 6 in, and the free-field response was computed using the complex response method. The maximum normalized bending moments $M^{*}_{max}$, are listed on the last page of Table 5.1. On this page, "BDWF" denotes the model used by Kavaadas and Gazetas and "FEM" indicates results published by the authors that were based on a parallel finite element study. The results for the proposed model are listed under the column denoted "dynopile." The final column of Table 5.1 lists the relative error between the proposed model and the finite element results, and between the proposed model and the authors' BDWF results. In general, the agreement is excellent. Maximum bending moments computed using the proposed model agree with the author's model within 10% in all but one case (Case 9), in which the proposed model under-predicted the maximum bending moment by 55.3%. Upon close examination of the input and output data, no cause for this discrepancy could be determined. Case 9 does not contain the most severe impedance contrast of all the combinations investigated. The fact that the other 23 cases agree so well suggests a possible error in the authors' published value.

Several examples of computed bending moment and shear diagrams are presented in Figure 5.5 through Figure 5.10. The bending moments and shear forces were computed by numerically differentiating the displacement profiles at each time step. The figures show computed profiles at several snapshots in time over one cycle of steady-state dynamic response. In general, the maximum bending moment occurs near the interface of the two soil layers.

### 5.3.2 Verification of dynamic impedance

This section investigates the ability of the proposed model to replicate the frequency-dependent dynamic impedance values of Novak et al. (1978). As was mentioned previously, this is a crucial feature of the far-field model. This study was conducted by considering a single pile element excited at various frequencies. The resulting hysteretic behavior was used to compute the impedance values.

Figure 5.11 shows the results of this effort. It shows real and imaginary stiffness values for dimensionless frequencies ranging from 0.0 to 0.5, and Poisson's ratios of 0.25, 0.4, and 0.5. The solid lines represent the theoretical impedance values proposed by Novak et al. (1978), while the discrete points represent impedance values computed using the proposed model. The agreement is excellent, which verifies the ability of the proposed model to numerically replicate frequency-dependent stiffness values in a time-domain formulation.

## 5.4 SUMMARY

This chapter has introduced a new method to compute the dynamic response of a pile to general free-field loading. This included both the analytical and numerical treatment to the problem. Furthermore, the pile-soil interaction model is capable of correctly representing the frequency-dependent impedance in a time-domain formulation. Finally, the model was verified by direct comparison with published analytical and numerical results of dynamic pile response.

Table 5.1 Verification study described in Section 5.3.2

| Case | Vb / Va | Eb / Ea | Ep / Ea | Ha / Hb | L / d | RHOp/ RHOa | w1d/Va | Pile Length L (in) | Height Layer a Ha (in) | Height Layer b Hb (in) | Pile Diameter d (in) | Pile Inertia Ip (in^4) |
|---|---|---|---|---|---|---|---|---|---|---|---|---|
| 1 | 0.58 | 0.33 | 500 | 1.00 | 10 | 1.6 | 0.0964 | 240 | 120 | 120 | 24 | 1.63E+04 |
| 2 | 0.58 | 0.33 | 500 | 1.00 | 20 | 1.6 | 0.0482 | 240 | 120 | 120 | 12 | 1.02E+03 |
| 3 | 0.58 | 0.33 | 500 | 1.00 | 40 | 1.6 | 0.0241 | 240 | 120 | 120 | 6 | 6.36E+01 |
| 4 | 0.58 | 0.33 | 5000 | 1.00 | 10 | 1.6 | 0.0964 | 240 | 120 | 120 | 24 | 1.63E+04 |
| 5 | 0.58 | 0.33 | 5000 | 1.00 | 20 | 1.6 | 0.0482 | 240 | 120 | 120 | 12 | 1.02E+03 |
| 6 | 0.58 | 0.33 | 5000 | 1.00 | 40 | 1.6 | 0.0241 | 240 | 120 | 120 | 6 | 6.36E+01 |
| 7 | 1.50 | 2.25 | 1000 | 3.00 | 20 | 1.6 | 0.0916 | 240 | 180 | 60 | 12 | 1.02E+03 |
| 8 | 1.50 | 2.25 | 10000 | 0.33 | 20 | 1.6 | 0.1164 | 240 | 60 | 180 | 12 | 1.02E+03 |
| 9 | 1.50 | 2.25 | 10000 | 1.00 | 20 | 1.6 | 0.1058 | 240 | 120 | 120 | 12 | 1.02E+03 |
| 10 | 1.50 | 2.25 | 10000 | 3.00 | 20 | 1.6 | 0.0913 | 240 | 180 | 60 | 12 | 1.02E+03 |
| 11 | 1.73 | 3.00 | 500 | 1.00 | 10 | 1.6 | 0.2310 | 240 | 120 | 120 | 24 | 1.63E+04 |
| 12 | 1.73 | 3.00 | 500 | 1.00 | 20 | 1.6 | 0.1155 | 240 | 120 | 120 | 12 | 1.02E+03 |
| 13 | 1.73 | 3.00 | 500 | 1.00 | 40 | 1.6 | 0.0578 | 240 | 120 | 120 | 6 | 6.36E+01 |
| 14 | 1.73 | 3.00 | 5000 | 1.00 | 10 | 1.6 | 0.2310 | 240 | 120 | 120 | 24 | 1.63E+04 |
| 15 | 1.73 | 3.00 | 5000 | 1.00 | 20 | 1.6 | 0.1155 | 240 | 120 | 120 | 12 | 1.02E+03 |
| 16 | 1.73 | 3.00 | 5000 | 1.00 | 40 | 1.6 | 0.0578 | 240 | 120 | 120 | 6 | 6.36E+01 |
| 17 | 3.00 | 9.00 | 1000 | 3.00 | 20 | 1.6 | 0.1017 | 240 | 180 | 60 | 12 | 1.02E+03 |
| 18 | 3.00 | 9.00 | 10000 | 0.33 | 20 | 1.6 | 0.2117 | 240 | 60 | 180 | 12 | 1.02E+03 |
| 19 | 3.00 | 9.00 | 10000 | 1.00 | 20 | 1.6 | 0.1416 | 240 | 120 | 120 | 12 | 1.02E+03 |
| 20 | 3.00 | 9.00 | 10000 | 3.00 | 20 | 1.6 | 0.1019 | 240 | 180 | 60 | 12 | 1.02E+03 |
| 21 | 6.00 | 36.00 | 1000 | 3.00 | 20 | 1.6 | 0.1042 | 240 | 180 | 60 | 12 | 1.02E+03 |
| 22 | 6.00 | 36.00 | 10000 | 0.33 | 20 | 1.6 | 0.2697 | 240 | 60 | 180 | 12 | 1.02E+03 |
| 23 | 6.00 | 36.00 | 10000 | 1.00 | 20 | 1.6 | 0.1535 | 240 | 120 | 120 | 12 | 1.02E+03 |
| 24 | 6.00 | 36.00 | 10000 | 3.00 | 20 | 1.6 | 0.1045 | 240 | 180 | 60 | 12 | 1.02E+03 |

Table 5.1 Verification study described in Section 5.3.2 (cont.)

| Case | Elastic Moduli Layer a Ea (psi) | Elastic Moduli Layer b Eb (psi) | Elastic Moduli Pile Ep (psi) | Poisson' Ratios Layer a NUa (-) | Poisson' Ratios Layer b Nub (-) | Damping Layer a BETAa (-) | Damping Layer b BETAb (-) | Unit Weights Layer a GAMa (pci) | Unit Weights Layer b GAMb (pci) | Unit Weights Pile GAMp (pci) | Shear Modulus Layer a Ga (psi) | Shear Modulus Layer b Gb (psi) |
|---|---|---|---|---|---|---|---|---|---|---|---|---|
| 1 | 1000 | 333.33 | 5.00E+05 | 0.4 | 0.4 | 0.10 | 0.10 | 0.0543 | 0.0543 | 0.0868 | 357.1 | 119.0 |
| 2 | 1000 | 333.33 | 5.00E+05 | 0.4 | 0.4 | 0.10 | 0.10 | 0.0543 | 0.0543 | 0.0868 | 357.1 | 119.0 |
| 3 | 1000 | 333.33 | 5.00E+05 | 0.4 | 0.4 | 0.10 | 0.10 | 0.0543 | 0.0543 | 0.0868 | 357.1 | 119.0 |
| 4 | 1000 | 333.33 | 5.00E+06 | 0.4 | 0.4 | 0.10 | 0.10 | 0.0543 | 0.0543 | 0.0868 | 357.1 | 119.0 |
| 5 | 1000 | 333.33 | 5.00E+06 | 0.4 | 0.4 | 0.10 | 0.10 | 0.0543 | 0.0543 | 0.0868 | 357.1 | 119.0 |
| 6 | 1000 | 333.33 | 5.00E+06 | 0.4 | 0.4 | 0.10 | 0.10 | 0.0543 | 0.0543 | 0.0868 | 357.1 | 119.0 |
| 7 | 1000 | 2250.00 | 1.00E+06 | 0.4 | 0.4 | 0.10 | 0.10 | 0.0543 | 0.0543 | 0.0868 | 357.1 | 803.6 |
| 8 | 1000 | 2250.00 | 1.00E+07 | 0.4 | 0.4 | 0.10 | 0.10 | 0.0543 | 0.0543 | 0.0868 | 357.1 | 803.6 |
| 9 | 1000 | 2250.00 | 1.00E+07 | 0.4 | 0.4 | 0.10 | 0.10 | 0.0543 | 0.0543 | 0.0868 | 357.1 | 803.6 |
| 10 | 1000 | 2250.00 | 1.00E+07 | 0.4 | 0.4 | 0.10 | 0.10 | 0.0543 | 0.0543 | 0.0868 | 357.1 | 803.6 |
| 11 | 1000 | 3000.00 | 5.00E+05 | 0.4 | 0.4 | 0.10 | 0.10 | 0.0543 | 0.0543 | 0.0868 | 357.1 | 1071.4 |
| 12 | 1000 | 3000.00 | 5.00E+05 | 0.4 | 0.4 | 0.10 | 0.10 | 0.0543 | 0.0543 | 0.0868 | 357.1 | 1071.4 |
| 13 | 1000 | 3000.00 | 5.00E+05 | 0.4 | 0.4 | 0.10 | 0.10 | 0.0543 | 0.0543 | 0.0868 | 357.1 | 1071.4 |
| 14 | 1000 | 3000.00 | 5.00E+06 | 0.4 | 0.4 | 0.10 | 0.10 | 0.0543 | 0.0543 | 0.0868 | 357.1 | 1071.4 |
| 15 | 1000 | 3000.00 | 5.00E+06 | 0.4 | 0.4 | 0.10 | 0.10 | 0.0543 | 0.0543 | 0.0868 | 357.1 | 1071.4 |
| 16 | 1000 | 3000.00 | 5.00E+06 | 0.4 | 0.4 | 0.10 | 0.10 | 0.0543 | 0.0543 | 0.0868 | 357.1 | 1071.4 |
| 17 | 1000 | 9000.00 | 1.00E+06 | 0.4 | 0.4 | 0.10 | 0.10 | 0.0543 | 0.0543 | 0.0868 | 357.1 | 3214.3 |
| 18 | 1000 | 9000.00 | 1.00E+07 | 0.4 | 0.4 | 0.10 | 0.10 | 0.0543 | 0.0543 | 0.0868 | 357.1 | 3214.3 |
| 19 | 1000 | 9000.00 | 1.00E+07 | 0.4 | 0.4 | 0.10 | 0.10 | 0.0543 | 0.0543 | 0.0868 | 357.1 | 3214.3 |
| 20 | 1000 | 9000.00 | 1.00E+07 | 0.4 | 0.4 | 0.10 | 0.10 | 0.0543 | 0.0543 | 0.0868 | 357.1 | 3214.3 |
| 21 | 1000 | 36000.00 | 1.00E+06 | 0.4 | 0.4 | 0.10 | 0.10 | 0.0543 | 0.0543 | 0.0868 | 357.1 | 12857.1 |
| 22 | 1000 | 36000.00 | 1.00E+07 | 0.4 | 0.4 | 0.10 | 0.10 | 0.0543 | 0.0543 | 0.0868 | 357.1 | 12857.1 |
| 23 | 1000 | 36000.00 | 1.00E+07 | 0.4 | 0.4 | 0.10 | 0.10 | 0.0543 | 0.0543 | 0.0868 | 357.1 | 12857.1 |
| 24 | 1000 | 36000.00 | 1.00E+07 | 0.4 | 0.4 | 0.10 | 0.10 | 0.0543 | 0.0543 | 0.0868 | 357.1 | 12857.1 |

Table 5.1 Verification study described in Section 5.3.2 (cont.)

| Case | Shear Wave Velocities Va (in/s) | Vb (in/s) | Vp (in/s) | omega (rad/s) | delta (-) | Stiffness Values Layer a Ka (lb/in^2) | Layer b Kb (lb/in^2) | P-Y Curve Data Layer a PMAXa (lb/in) | Layer b PMAXb (lb/in) |
|---|---|---|---|---|---|---|---|---|---|
| 1 | 1594.9 | 920.8 | 2.82E+04 | 6.406 | 2.21 | 2207.6 | 735.9 | 4.415E+05 | 1.472E+05 |
| 2 | 1594.9 | 920.8 | 2.82E+04 | 6.406 | 2.41 | 2407.4 | 802.5 | 4.815E+05 | 1.605E+05 |
| 3 | 1594.9 | 920.8 | 2.82E+04 | 6.406 | 2.63 | 2625.2 | 875.1 | 5.250E+05 | 1.750E+05 |
| 4 | 1594.9 | 920.8 | 8.92E+04 | 6.406 | 1.66 | 1655.4 | 551.8 | 3.311E+05 | 1.104E+05 |
| 5 | 1594.9 | 920.8 | 8.92E+04 | 6.406 | 1.81 | 1805.3 | 601.8 | 3.611E+05 | 1.204E+05 |
| 6 | 1594.9 | 920.8 | 8.92E+04 | 6.406 | 1.97 | 1968.7 | 656.2 | 3.937E+05 | 1.312E+05 |
| 7 | 1594.9 | 2392.3 | 3.99E+04 | 12.174 | 2.27 | 2270.0 | 5107.5 | 4.540E+05 | 1.022E+06 |
| 8 | 1594.9 | 2392.3 | 1.26E+05 | 15.470 | 1.42 | 1417.5 | 3189.3 | 2.835E+05 | 6.379E+05 |
| 9 | 1594.9 | 2392.3 | 1.26E+05 | 14.061 | 1.55 | 1553.3 | 3495.0 | 3.107E+05 | 6.990E+05 |
| 10 | 1594.9 | 2392.3 | 1.26E+05 | 12.134 | 1.70 | 1702.3 | 3830.1 | 3.405E+05 | 7.660E+05 |
| 11 | 1594.9 | 2762.4 | 2.82E+04 | 15.351 | 2.05 | 2051.7 | 6155.0 | 4.103E+05 | 1.231E+06 |
| 12 | 1594.9 | 2762.4 | 2.82E+04 | 15.351 | 2.24 | 2237.3 | 6712.0 | 4.475E+05 | 1.342E+06 |
| 13 | 1594.9 | 2762.4 | 2.82E+04 | 15.364 | 2.44 | 2439.8 | 7319.5 | 4.880E+05 | 1.464E+06 |
| 14 | 1594.9 | 2762.4 | 8.92E+04 | 15.351 | 1.54 | 1538.5 | 4615.6 | 3.077E+05 | 9.231E+05 |
| 15 | 1594.9 | 2762.4 | 8.92E+04 | 15.351 | 1.68 | 1677.8 | 5033.3 | 3.356E+05 | 1.007E+06 |
| 16 | 1594.9 | 2762.4 | 8.92E+04 | 15.364 | 1.83 | 1829.6 | 5488.9 | 3.659E+05 | 1.098E+06 |
| 17 | 1594.9 | 4784.6 | 3.99E+04 | 13.517 | 2.17 | 2167.5 | 19507.6 | 4.335E+05 | 3.902E+06 |
| 18 | 1594.9 | 4784.6 | 1.26E+05 | 28.136 | 1.35 | 1353.4 | 12181.0 | 2.707E+05 | 2.436E+06 |
| 19 | 1594.9 | 4784.6 | 1.26E+05 | 18.806 | 1.48 | 1483.2 | 13348.8 | 2.966E+05 | 2.670E+06 |
| 20 | 1594.9 | 4784.6 | 1.26E+05 | 13.543 | 1.63 | 1625.4 | 14628.6 | 3.251E+05 | 2.926E+06 |
| 21 | 1594.9 | 9569.2 | 3.99E+04 | 13.849 | 2.07 | 2069.6 | 74506.5 | 4.139E+05 | 1.490E+07 |
| 22 | 1594.9 | 9569.2 | 1.26E+05 | 38.503 | 1.29 | 1292.3 | 46523.7 | 2.585E+05 | 9.305E+06 |
| 23 | 1594.9 | 9569.2 | 1.26E+05 | 20.401 | 1.42 | 1416.2 | 50984.0 | 2.832E+05 | 1.020E+07 |
| 24 | 1594.9 | 9569.2 | 1.26E+05 | 13.889 | 1.55 | 1552.0 | 55872.0 | 3.104E+05 | 1.117E+07 |

Table 5.1 Verification study described in Section 5.3.2 (cont.)

| | Damping Values | | | | max | actual | min | actual |
|---|---|---|---|---|---|---|---|---|
| | Layer a | Layer a | Layer b | Dynopile | Dynopile | Dynopile | Dynopile | Dynopile |
| | Ca1 | Ca2 | Cb | dz | dt | dt | ktime | ktime |
| Case | (lb-s/in^2) | (lb-s/in^s) | (lb-2/in^2) | (in) | (sec) | (sec) | (t-steps) | (t-steps) |
| 1 | 107.50 | 128.53 | 52.98 | 6 | 2.13E-04 | 6.E-05 | 16347. | 16400. |
| 2 | 98.10 | 110.61 | 42.89 | 6 | 2.13E-04 | 1.E-04 | 9808. | 9900. |
| 3 | 95.60 | 103.04 | 37.93 | 6 | 2.13E-04 | 2.E-04 | 4904. | 5000. |
| 4 | 90.26 | 111.30 | 47.23 | 6 | 6.73E-05 | 2.E-05 | 49041. | 49100. |
| 5 | 79.30 | 91.61 | 36.63 | 6 | 6.73E-05 | 3.E-05 | 32694. | 32800. |
| 6 | 75.10 | 82.54 | 31.09 | 6 | 6.73E-05 | 6.E-05 | 16347. | 16400. |
| 7 | 56.83 | 67.48 | 134.02 | 6 | 1.50E-04 | 5.E-05 | 10322. | 10600. |
| 8 | 36.73 | 46.76 | 88.43 | 6 | 4.76E-05 | 2.E-05 | 20307. | 20600. |
| 9 | 40.94 | 51.22 | 98.05 | 6 | 4.76E-05 | 2.E-05 | 22342. | 22600. |
| 10 | 47.61 | 58.27 | 113.29 | 6 | 4.76E-05 | 2.E-05 | 25690. | 26000. |
| 11 | 57.74 | 74.64 | 175.40 | 6 | 2.13E-04 | 5.E-05 | 8186. | 8400. |
| 12 | 47.59 | 57.64 | 144.06 | 6 | 2.13E-04 | 1.E-04 | 4093. | 4200. |
| 13 | 42.72 | 48.70 | 128.94 | 6 | 2.13E-04 | 2.E-04 | 2045. | 2100. |
| 14 | 51.05 | 67.96 | 155.34 | 6 | 6.73E-05 | 1.5E-05 | 27287. | 27600. |
| 15 | 40.30 | 50.35 | 122.19 | 6 | 6.73E-05 | 3.E-05 | 13644. | 13800. |
| 16 | 34.76 | 40.75 | 105.10 | 6 | 6.73E-05 | 6.E-05 | 6816. | 6900. |
| 17 | 51.11 | 61.48 | 404.77 | 6 | 1.50E-04 | 5.E-05 | 9297. | 9400. |
| 18 | 25.47 | 34.11 | 183.26 | 6 | 4.76E-05 | 2.E-05 | 11166. | 11400. |
| 19 | 33.30 | 42.85 | 248.88 | 6 | 4.76E-05 | 2.E-05 | 16705. | 17000. |
| 20 | 43.03 | 53.40 | 332.09 | 6 | 4.76E-05 | 2.E-05 | 23197. | 23400. |
| 21 | 48.81 | 59.12 | 1350.51 | 6 | 1.50E-04 | 5.E-05 | 9074. | 9200. |
| 22 | 21.36 | 29.35 | 454.25 | 6 | 4.76E-05 | 2.E-05 | 8159. | 8400. |
| 23 | 31.06 | 40.42 | 748.99 | 6 | 4.76E-05 | 2.E-05 | 15399. | 15600. |
| 24 | 41.25 | 51.56 | 1078.88 | 6 | 4.76E-05 | 2.E-05 | 22620. | 22800. |

Table 5.1 Verification study described in Section 5.3.2 (cont.)

| Case | K&G BDWF M*max (-) | K&G FEM M*max (-) | Error BDWF vs. FEM (%) | H&K Dynopile M*max (-) | Error Dynopile vs. FEM (%) | Error Dynopile vs. BDWF (%) |
|---|---|---|---|---|---|---|
| 1 | 760 | 709 | 7.2 | 780 | 10.0 | 2.6 |
| 2 | 1282 | 1253 | 2.3 | 1338 | 6.8 | 4.4 |
| 3 | 2196 | 2088 | 5.2 | 2379 | 13.9 | 8.3 |
| 4 | 1623 | 1854 | -12.5 | 1732 | -6.6 | 6.7 |
| 5 | 8019 | 7718 | 3.9 | 8358 | 8.3 | 4.2 |
| 6 | 13320 | 13120 | 1.5 | 14031 | 6.9 | 5.3 |
| 7 | 515 | 508 | 1.4 | 530 | 4.3 | 2.9 |
| 8 | 1097 | 1113 | -1.4 | 1123 | 0.9 | 2.4 |
| 9 | 1070 | 931 | 14.9 | 478 | -48.7 | -55.3 |
| 10 | 1433 | 1482 | -3.3 | 1455 | -1.8 | 1.5 |
| 11 | 79 | 86 | -8.1 | 79 | -8.1 | 0.0 |
| 12 | 253 | 269 | -5.9 | 264 | -1.9 | 4.3 |
| 13 | 577 | 656 | -12.0 | 592 | -9.8 | 2.6 |
| 14 | 266 | 273 | -2.6 | 253 | -7.3 | -4.9 |
| 15 | 860 | 998 | -13.8 | 864 | -13.4 | 0.5 |
| 16 | 2825 | 3054 | -7.5 | 2883 | -5.6 | 2.1 |
| 17 | 1075 | 1046 | 2.8 | 1080 | 3.3 | 0.5 |
| 18 | 896 | 875 | 2.4 | 940 | 7.4 | 4.9 |
| 19 | 3042 | 2949 | 3.2 | 3060 | 3.8 | 0.6 |
| 20 | 4911 | 4867 | 0.9 | 4924 | 1.2 | 0.3 |
| 21 | 1480 | 1486 | -0.4 | 1470 | -1.1 | -0.7 |
| 22 | 1274 | 1128 | 12.9 | 1356 | 20.2 | 6.4 |
| 23 | 4193 | 3809 | 10.1 | 4156 | 9.1 | -0.9 |
| 24 | 6831 | 6730 | 1.5 | 7091 | 5.4 | 3.8 |

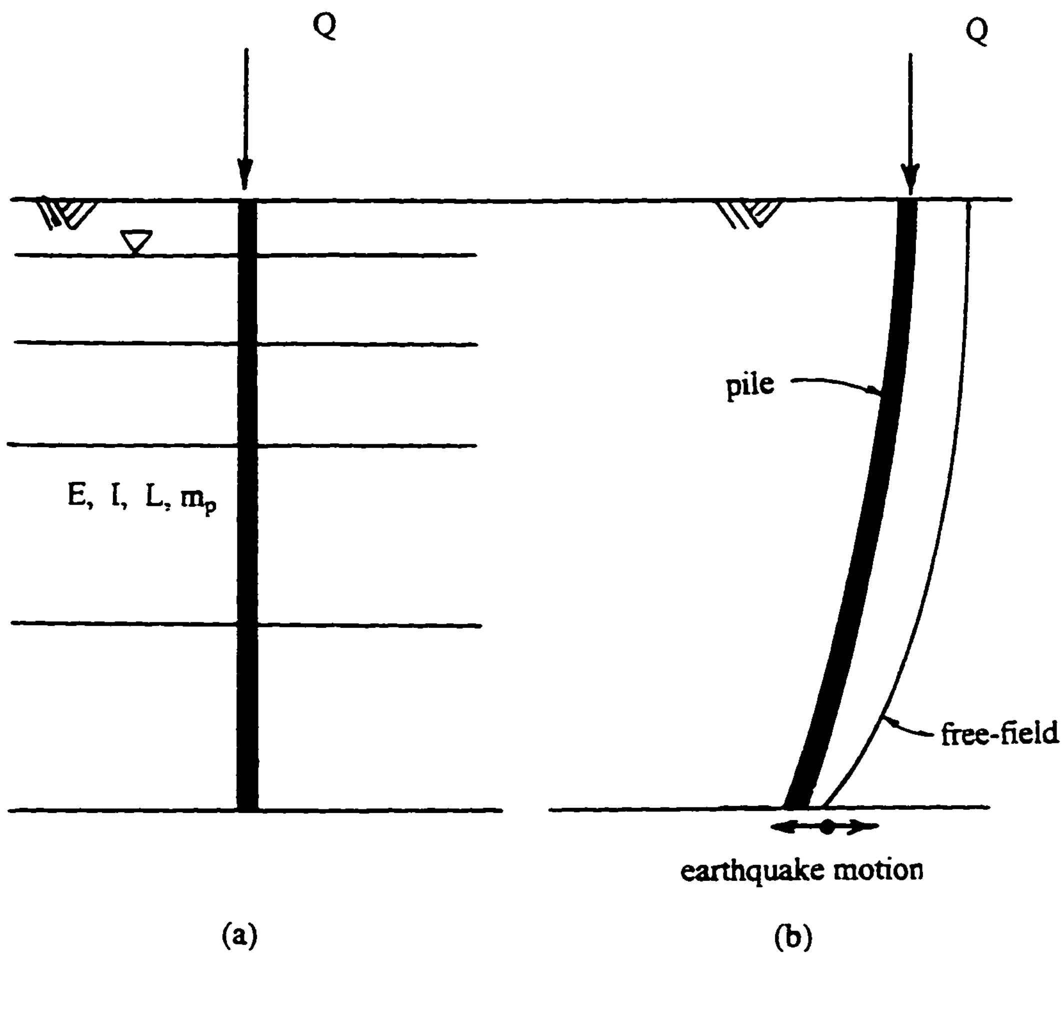


Figure 5.1 (a) Pile-soil system considered for analysis and (b) pile and free-field displacement profiles

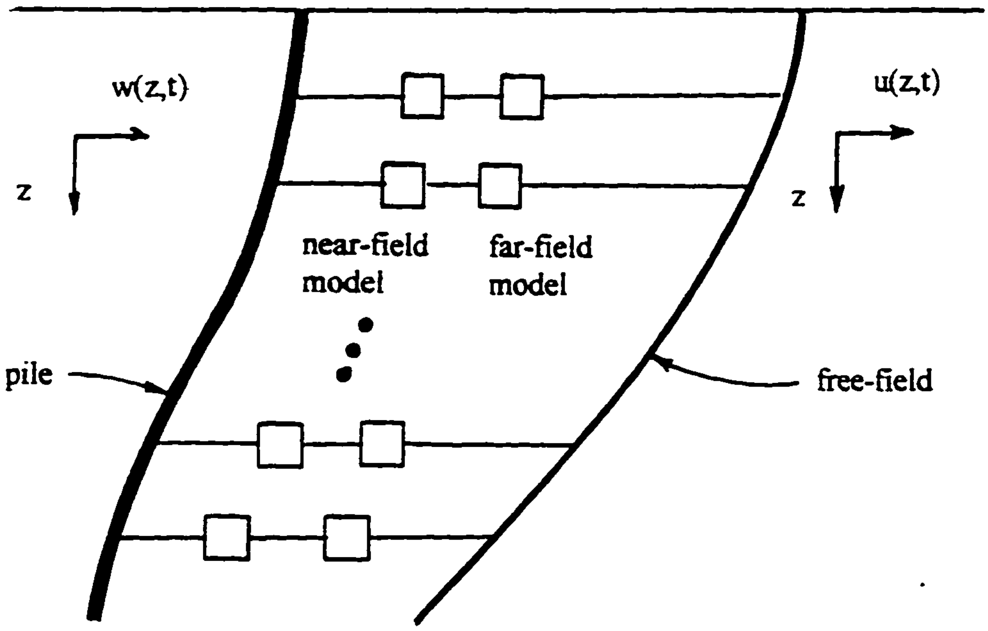


Figure 5.2 Winkler beam with rheologic pile-soil interaction model attached to the free field

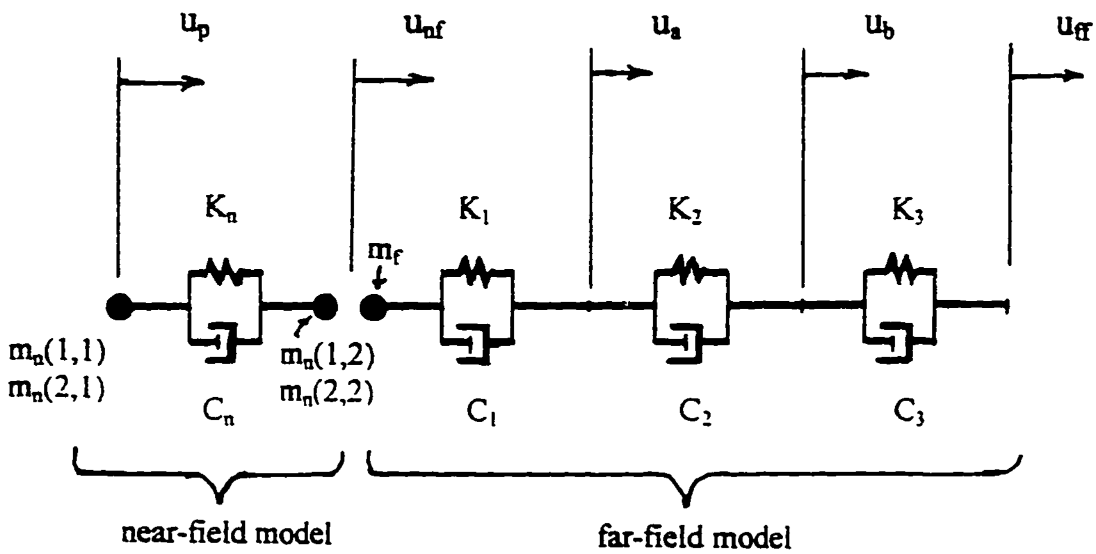


Figure 5.3 Elements of the pile-soil interaction model

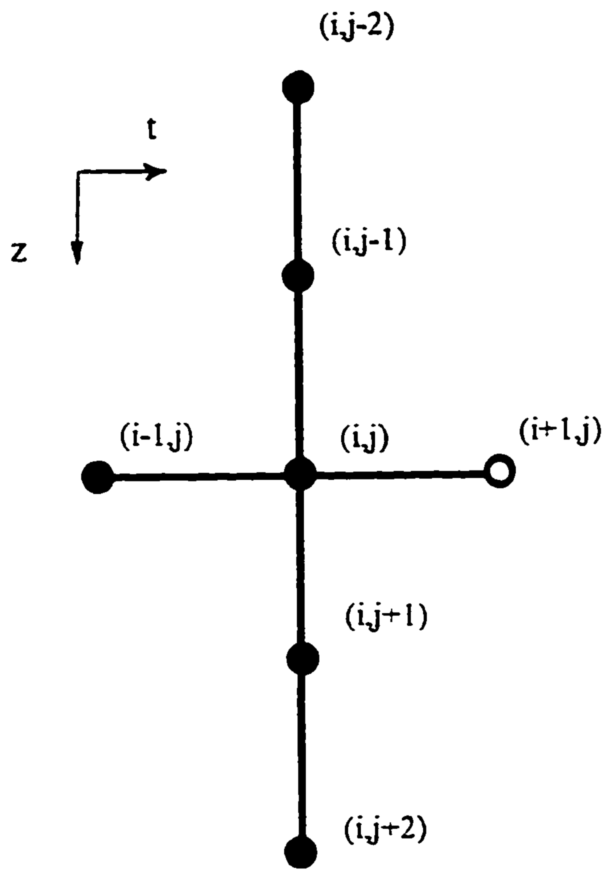


Figure 5.4 Computational stencil for the pile-soil interaction model

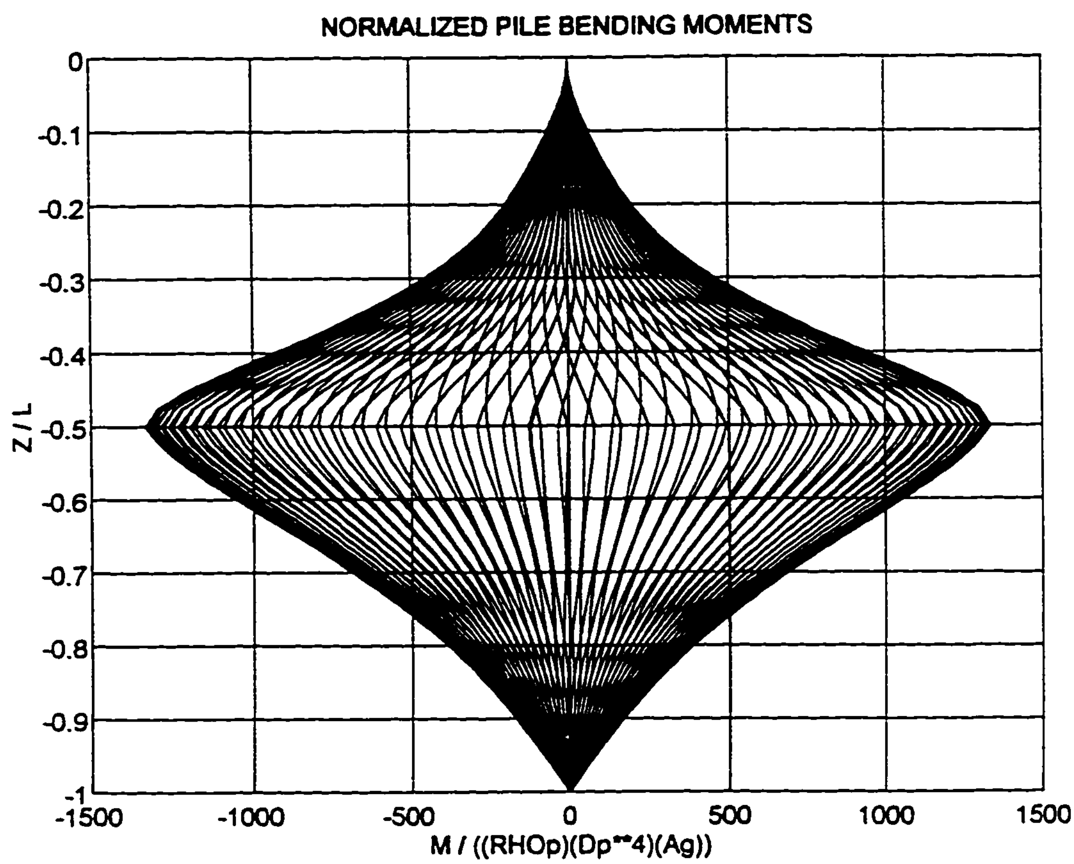


Figure 5.5 Normalized pile bending moment (corresponds to Case 2 of Table 5.1)

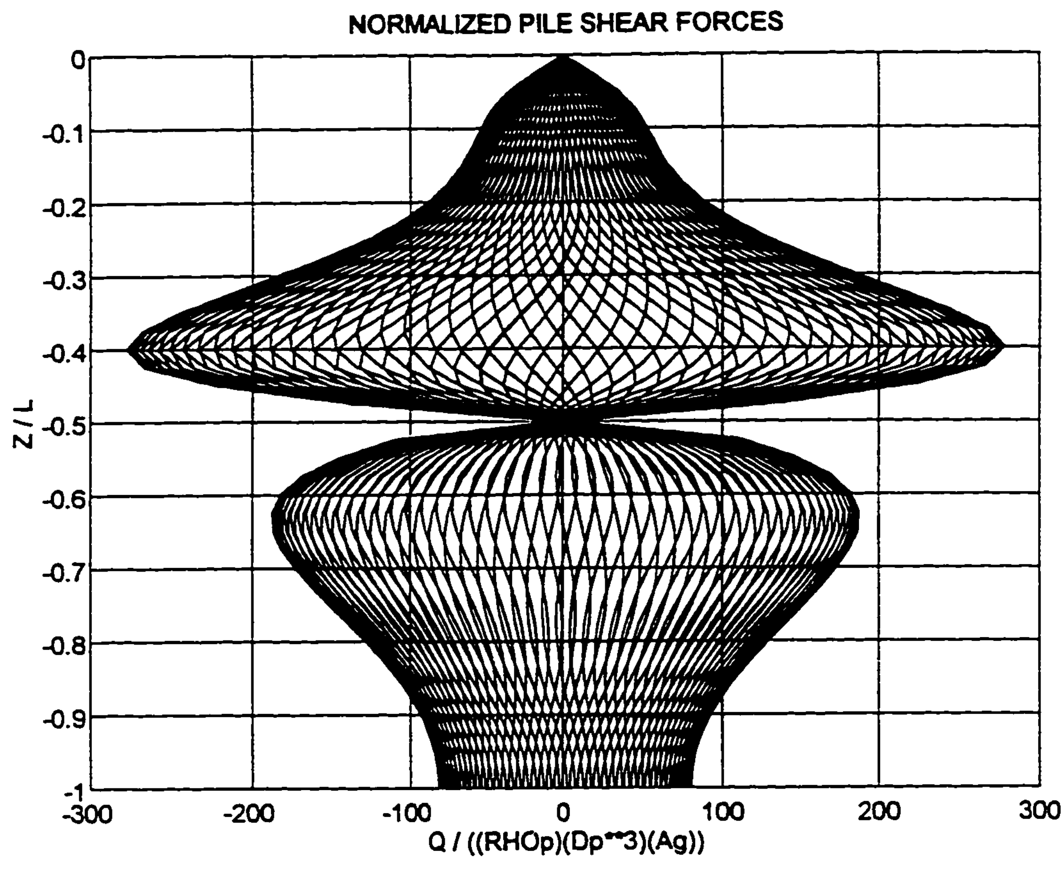


Figure 5.6 Normalized pile shear force (corresponds to Case 2 of Table 5.1)

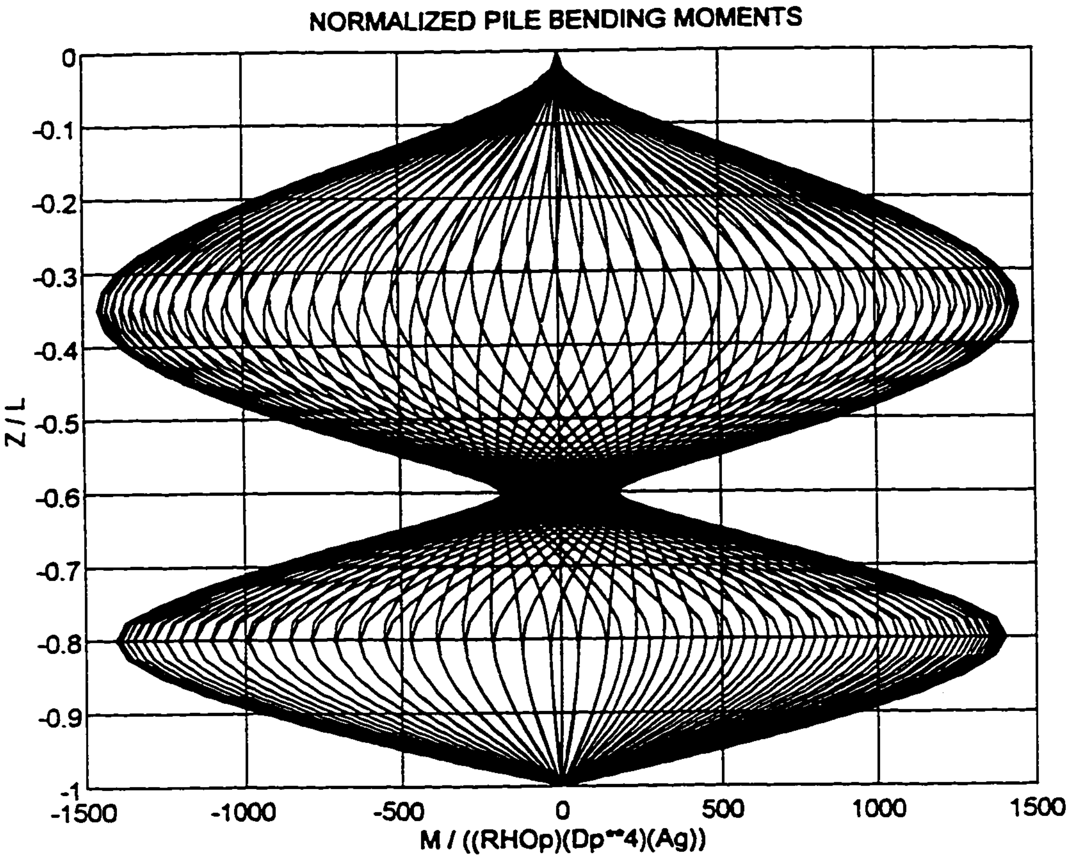


Figure 5.7 Normalized pile bending moment (corresponds to Case 10 of Table 5.1)

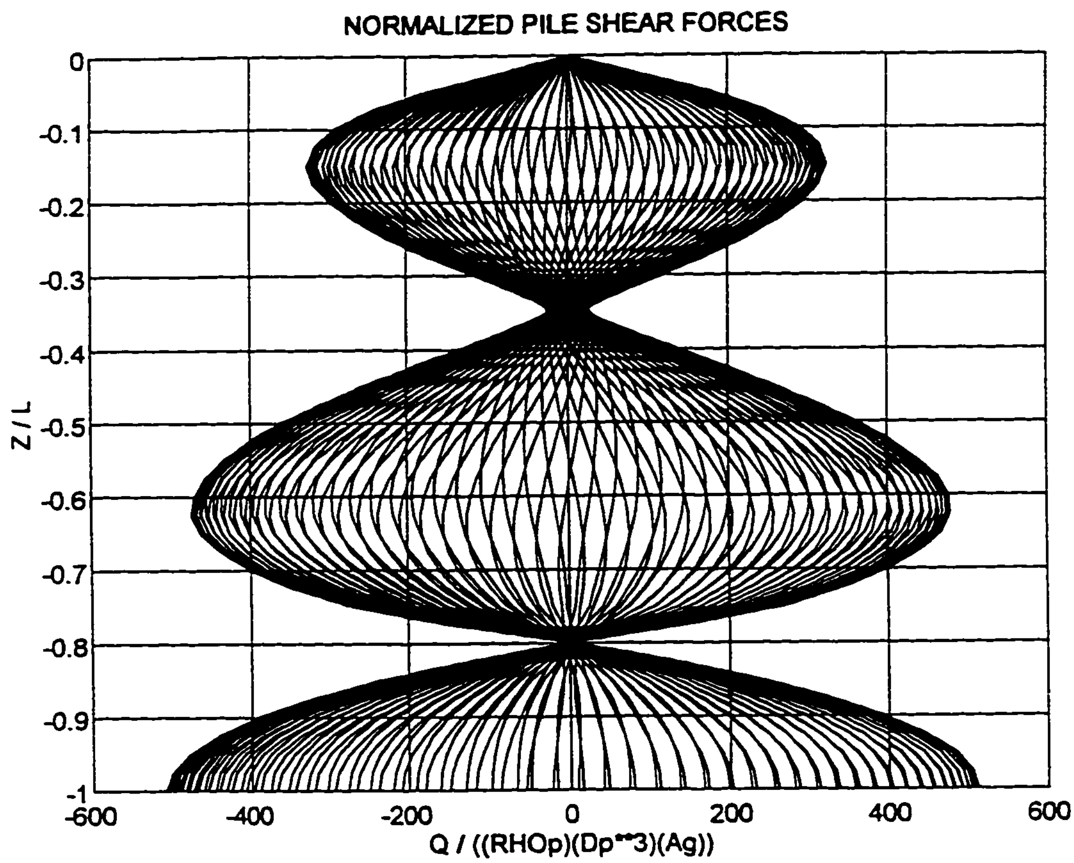


Figure 5.8 Normalized pile shear force (corresponds to Case 10 of Table 5.1)

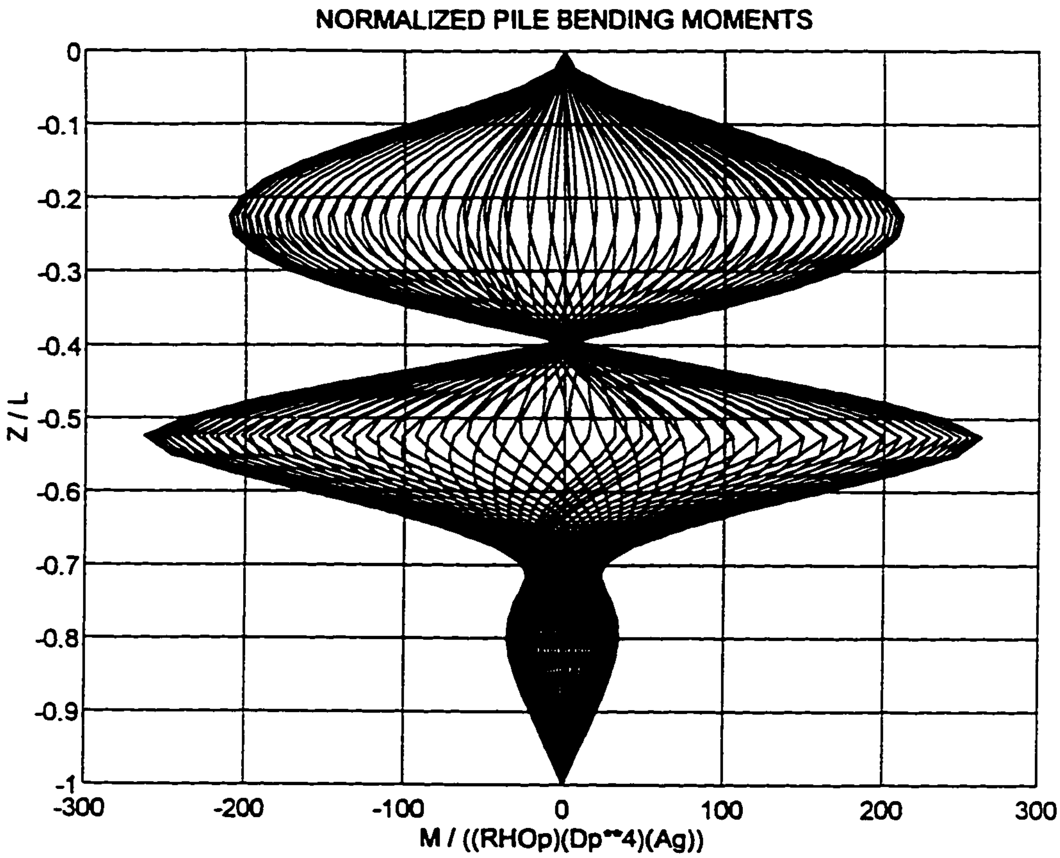


Figure 5.9 Normalized pile bending moment (corresponds to Case 12 of Table 5.1)

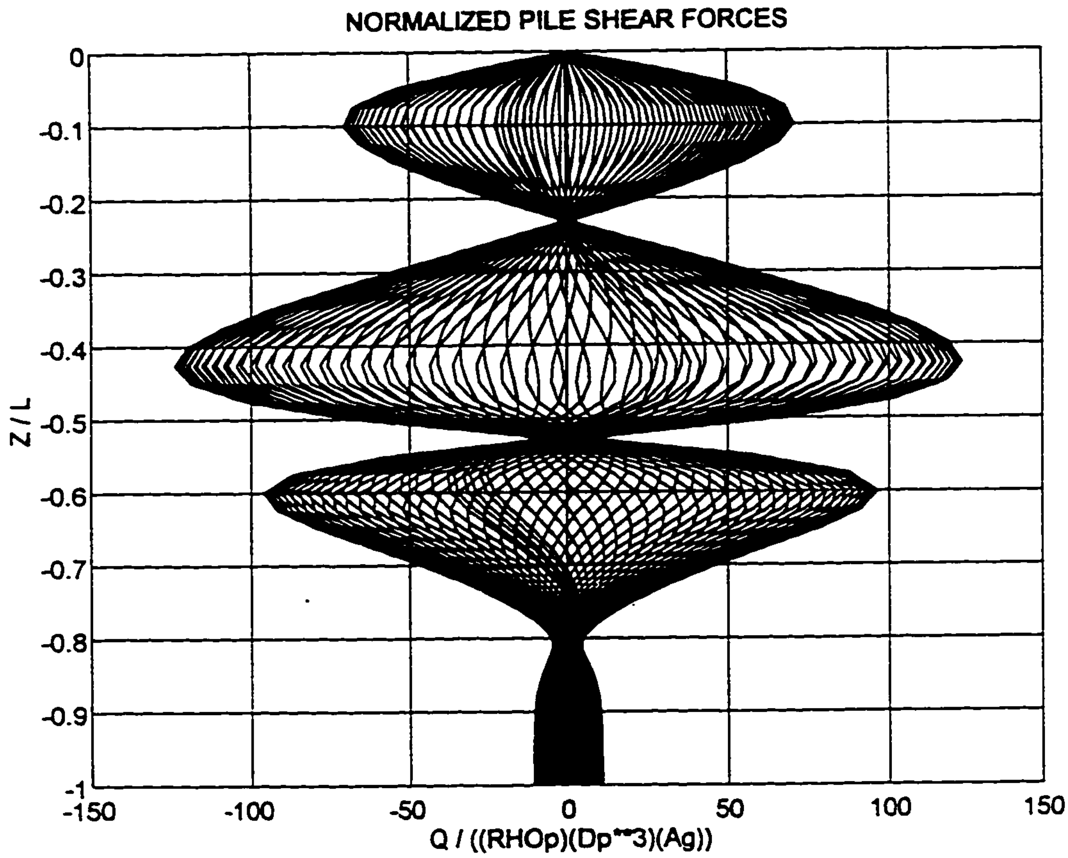


Figure 5.10 Normalized pile shear force (corresponds to Case 12 of Table 5.1)

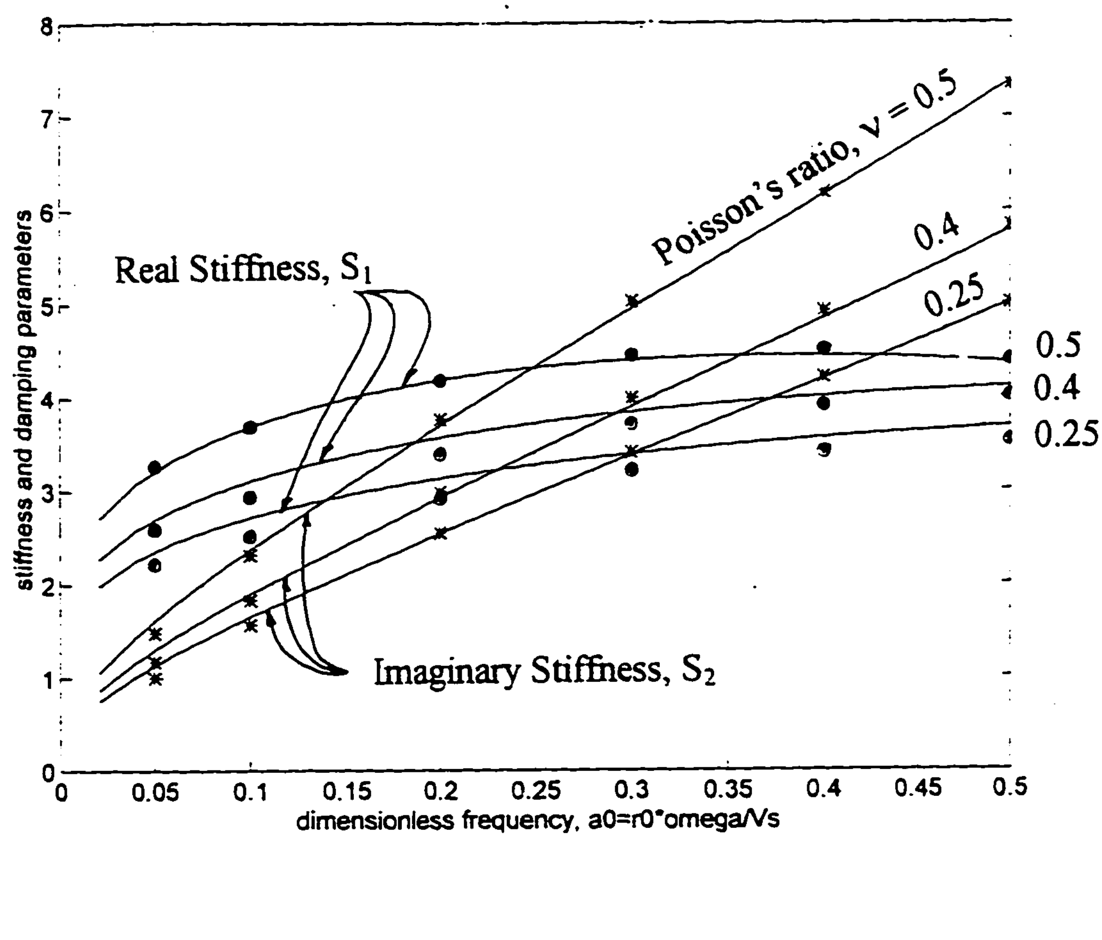


Figure 5.11 Impedance values computed using the proposed pile-soil interaction model (discrete points) compared with theoretical values (solid line) (after Novak et al. 1978)

# Chapter 6 Effects of Lateral Spreading on Pile Foundations

## 6.1 INTRODUCTION

The ground response and pile response models developed in the previous two chapters obviously require many input parameters. In large part, this is due to the complex, nonlinear behavior these models attempt to replicate. The development of a new method – and its eventual acceptance -- requires an understanding of its behavior. That is, the output must "make sense" under the scrutiny of engineering judgment. Equally important, the variation of the output caused by changes to the input must be broadly explored and thoroughly understood.

This chapter details the results of a comprehensive parameter study that illustrates the sensitivity of the proposed models to the input data. The parameter study contains two parts: the first explores the lateral spread model, while the second investigates the pile-soil interaction model.

## 6.2 FREE-FIELD GROUND RESPONSE ANALYSIS

### 6.2.1 Introduction

Soil deformations caused by lateral spreading depend on many factors. This section explores the effect of the three most significant parameters on lateral spread displacements: ground surface slope, soil strength, and groundwater table depth. In the field, each of these parameters can exhibit considerable variation. However, case studies involving lateral spreads give guidance as to practical limits these parameters may attain. Section 6.2.2 discusses how the study was performed, and is followed by Section 6.2.3, which presents input parameter selection in greater detail. Finally, Section 6.2.4 presents the output from the ground response analyses

### 6.2.2 Analytical Cases

The study was performed by first analyzing the baseline stratigraphy shown in Figure 6.1, which represen soil conditions typical of those observed at many lateral spread sites. The baseline site consists of a loose, alluvial sand deposit 10 m thick underlain by 10 m of glacial till composed of very dense sand. The (corrected) SPT blow-count of the upper layer is 10. The surface of the deposit is inclined at a gradual 20:1 slope, and the groundwater table is at a depth of 2.0 m. Other properties of the deposit are indicated on Figure 6.1.

Parallel analyses were conducted on stratigraphies with the parameter variation shown in Table 6.1, which indicates low-end, baseline, and high-end values for each parameter. The variation in each parameter reflects likely scenarios at lateral spread sites. For example, slopes greater than 10:1 are likely to exhibit flow failure (instead of lateral spread displacements) due to the fact that the static in situ shear stresses are greater than the residual strength of many liquefiable soils. Also, soils with SPT blow counts greater than 20 are unlikely to develop lateral spread displacements (Bartlett and Youd, 1995). Finally, the range of groundwater depths are typical of those encountered at lateral spread sites.

### 6.2.3 Preparation of Input Data

Although Figure 6.1 and Table 6.1 specify the problem geometry and general parameters that were investigated, detailed consideration had to be made to arrive at all the necessary input parameters to the ground response model. This section describes the development of the required input data. This includes parameters that characterize stress-strain behavior (Section 4.3.1) and excess pore pressure generation (Section 4.3.2), and the input ground motion used for dynamic excitation.

The basic sand properties of relative density and friction angle were estimated from the SPT blow count using the empirical correlations of Gibbs and Holtz (1957) and Meyerhof (1956), respectively. The relative densities were used with typical minimum and maximum void ratios given in Holtz and Kovacs (1981) to compute initial void ratios. The resulting data appears in Table 6.2.

A stress-strain backbone curve requires an initial or low-strain shear modulus. For this study, initial shear moduli of the loose upper sand layer were computed using the empirical relationship proposed by Seed et al. (1986):

$$G_{max} = 20000\left[(N_1)_{60}\right]^{1/3}\left(\sigma'_m\right)^{1/2} \tag{6.1}$$

where: $G_{max}$ = maximum or initial shear modulus of the soil (psf)

$(N_1)_{60}$ = SPT blow count corrected for overburden and efficiency

$\sigma'_m$ = mean effective stress of the soil (psf)

Alternatively, the initial modulus of the dense till layer was computed from its shear wave velocity and density:

$$G_{max} = \rho V_s^2 \tag{6.2}$$

where: $\rho$ = soil density

$V_s$ = soil shear wave velocity

Another important parameter of a backbone curve is the maximum shear strength. For this study, the shear strength of the sand was computed using the Mohr-Coulomb failure criterion given by Equation (4.28). The till, however, was intended to provide a strong impedance contrast with the liquefiable sand. Its strength, therefore, was not of prime importance for this parameter study, and was taken to be 300 kPa, a value sufficiently high that failure would not occur.

Individual backbone curves were defined at depths of 0.0, 0.5, 2.0, 6.0, 10.0, 10.1, and 20.0 m for each profile, using the procedure described in Section 4.3.1. The PI = 0 modulus reduction curve of Vucetic and Dobry (1991) was used to compute shear stress values for strains up to 0.005. At that point, the backbone curve was extended with a hyperbola which was asymptotic to the soil shear strength at a shear strain of 0.375.

Backbone curves for grid points intermediate to the seven discrete points were computed by linear interpolation. This provided a reasonable representation of the variation of both stiffness and strength with depth. Each backbone curve consisted of thirty six $\tau$-$\gamma$ pairs defining the first quadrant of each backbone curve. The discrete shear strains are presented in Table 6.3.

Slight modification was made to the backbone curves, based on the results obtained from several preliminary computer runs. First, the zero strength backbone curve at the ground surface resulted in unrealistic shear strains at this point. Therefore, the backbone curve at 0.5 m was also specified at the ground surface. This adjustment had the effect of artificially stiffening and strengthening the upper 0.5 m of soil. However, because this region of soil was above the groundwater table, the effect of this adjustment on the computed lateral spread response was negligible. Second, it was possible, when very near the strength envelope of a soil, to compute a shear stress which slightly and momentarily exceeded the strength. In such cases, the constitutive model cannot determine the appropriate shear modulus. To rectify this, the shear modulus at a strain of 0.375 was used to extend the backbone curve linearly to a very large strain value, arbitrarily taken to be 10. This adjustment introduces an artificial "residual" shear modulus to the backbone curve. However, in the analyses conducted for this chapter, this "residual" modulus was extremely small – about 5 orders of magnitude below the initial shear modulus. Additionally, since the residual modulus was only encountered momentarily, its effect on the overall lateral spread response is thought to be minor.

Section 4.3.2 defined several empirical parameters used in the energy-based pore pressure model. These include the five empirical coefficients: a, b, c, $\mu$, and n, which were taken to be 2.5, 1.1, 3.5, 0.001 kPa, and 0.5, respectively. These values were chosen such that the proposed pore pressure model closely replicated both the rate of excess pore pressure generation and the rate of backbone curve degradation of torsional shear test data presented by Figueroa et al. (1994). Since the till layer was not intended to liquefy, the degradation exponent, n (used in Equation 4.31) was set equal to 0.0, and the initial void ratio was set equal to the minimum void ratio, or 0.4. The use of these parameters with the energy-based pore pressure model ensured that no excess pore pressure would be generated by cyclic loading of the till.

A strong-motion acceleration record measured during the 1949 Olympia earthquake ($M = 7.1$, $a_{max} = 0.16$ g) provided the dynamic excitation for all of the ground response analyses. This earthquake was an intraplate event, with an epicentral distance of 26.4 km from the instrument (Site ID 2101OLY, Olympia Highway Test Lab). The record was obtained from the database maintained by the National Center for Earthquake Engineering Research (NCEER). It was first integrated once in time using the trapezoidal rule to compute an input velocity record, which was then applied at the bottom of the till layer as shown on Figure 6.1. Only the first 60 s of the record was used in the analyses, at which time the acceleration amplitude had subsided to about 0.01 g. Subsequent analyses indicated that the lateral spreading displacements had virtually ceased by this time.

Based on the results of preliminary analyses, the soil deposit was discretized using a regular grid with $dz = 0.4$ m. This provided good resolution of the displacement profile throughout the soil column.

### 6.2.4 Discussion of Results

The main results of this parameter study are illustrated by the displacement profiles shown in Figure 6.2 through Figure 6.4. Each figure refers to a separate parameter group described in Table 6.1, and contains a curve for the baseline case along with curves for the high-end and low-end variation. These are denoted BL, H, and L, respectively. The figures indicate the final displacement profiles for the 20 m soil deposit, and are plotted at the same scale to allow easy comparison among one another.

#### 6.2.4.1 Effect of Ground Surface Slope

The slope of the ground surface directly affects the initial state of shear stress. The initial shear stress creates the source term in Equation (4.11) which causes a yielding deposit to move in a down-slope direction. Figure 6.2 shows the final displaced shapes of the soil deposit for ground surface slopes of zero, 20:1, and 10:1. The permanent displacement of the till layer is negligible, but the level ground, 20:1 slope, and 10:1 slope all exhibit permanent ground surface displacements. The magnitudes of these displacements are strongly influenced by the ground surface slope. The level site has no static driving shear stress, consequently, permanent displacements are likely to be small and related to the asymmetry of the input motion; for this case, the computed permanent displacement is 0.02 m. The deposit with the 20:1 ground surface slope does have modest static shear stresses that tend to drive soil displacements in the downslope direction; the computed permanent displacement is 0.5 m. For the steepest case considered, the 10:1 slope, the relatively high static shear stresses produced permanent displacements of 1.3 m. Clearly, steeper slopes would be expected to induce larger lateral displacements and this result is verified by the proposed analysis. Figure 6.2 also shows that much of the strain is localized in a fairly thin region – about 2 m thick – immediately above the till layer.

6.2.4.2 Effect of Soil Strength

The SPT resistance is a purely empirical parameter that has been correlated to the strength and relative density of granular soils. Variation in soil strength directly affects the backbone curves that control stress strain behavior. Additionally, variation in relative density, and hence the initial void ratio – alters the rate of excess pore pressure generation. The proposed model incorporates both of these effects in the constitutive formulation discussed in Chapter 4. Figure 6.3 shows the final displaced shapes of the 20 m thick profile for SPT resistances of 5, 10, and 20. Again, the permanent displacements of the till layer are negligible, but the N = 5, N = 10, and N = 20 sand profiles all exhibit permanent downslope displacements. The magnitudes of these displacements are strongly influenced by the strength of the soil. The N = 20 deposit – the strongest of the three analyzed – displaced the least amount; for this case, the computed displacement was about 0.2 m at the surface. The baseline case, with a N = 10 sand deposit, resulted in larger permanent ground displacements; for this case, the final ground surface displacement was about 0.5 m. The weakest case, represented by the N = 5 sand deposit, displaced the greatest distance down slope; for this case, the final ground surface displacement was 1.5 m. It stands to reason that a weaker deposit should displace farther downslope, and this was confirmed by the proposed analysis. Examination of Figure 6.3 shows that the greatest shear strains tended to develop in the lower 2 to 3 m of the liquefiable sand.

6.2.4.3 Effect of Groundwater Table Depth

The depth of the groundwater table directly affects the initial state of effective stress in the soil and the thickness of liquefiable soil. The initial effective stress in turn affects the initial shear strength in accordance with the Mohr-Coulomb failure hypothesis. The residual shear strength, however, is not strongly dependent on the initial effective stress of a soil. Finally, a soil with a higher effective stress requires greater excess pore pressure to reach a fully liquefied state. Figure 6.4 shows the final displaced shapes of the soil deposit for groundwater depths of 0.5 m, 2.0 m, and 5.0 m. The striking observation is that the final displacement profiles are very similar among these three cases; each results in about 0.5 m of permanent displacement at the ground surface. Although the thickness of a potentially liquefiable soil is reduced as the groundwater table is lowered, the strains are so low in the upper portion that the displacement is not greatly influenced.

## 6.3 PILE-SOIL INTERACTION ANALYSIS

### 6.3.1 Introduction

Pile-soil interaction depends on many factors. This section considers the sensitivity of pile response to differences in seven input parameters that influence the effect of lateral spreading on pile foundations. These include the three soil parameters – surface slope, soil strength, and groundwater depth – considered in the previous section, along with four pile-based parameters – flexural stiffness, pile diameter, pile length, and p-y curve stiffness.

### 6.3.2 Analytical Cases

The baseline pile analysis case consists of a 12.0 m long pile embedded in the baseline stratigraphy illustrated in Figure 6.1. The pile has a flexural stiffness of 58,800 KN-m, which corresponds to a 40.6 cm diameter, 6.35 mm wall thickness steel pipe pile filled with normal strength concrete. Table 6.4 indicates the low-end and high-end variation for each of the six baseline parameters. The variation of soil parameters is the same as that used in the lateral spreading sensitivity analysis (Table 6.1). The pile parameters are typical of the ranges of flexural stiffnesses, pile lengths, and p-y curve stiffnesses for deep foundations that might be used to support structures on the baseline deposit. For example, the low-end length represents a pile barely embedded into the dense material, while the high-end length corresponds to a deeply driven or drilled pile.

### 6.3.3 Preparation of Input Data

The pile-soil interaction model described in Chapter 4 requires a comprehensive collection of input data, much of which comes directly from the lateral spread model of Chapter 3. Some of the input data, however, is independent of the free-field lateral spread response, and includes pile properties, parameters needed for the near-field and far-field pile-soil interaction model, and numerical discretization data.

The pile mass per unit length and flexural stiffness were computed assuming 6.35 mm wall thickness steel pipes ($E_s$ = 200 GPa) filled with normal strength concrete ($f'_c$ = 20.7 MPa). The low-end flexural stiffness of 21,400 KN-m$^2$ corresponds to a steel pipe with an outside diameter of 30.5 cm. Conversely, the high-end stiffness of 251,200 KN-m$^2$ represents a 61.0 cm diameter pile. The head and toe of the pile were assumed to be free with respect to translation and rotation, and the piles were assumed to carry no axial load. The spatial discretization of the pile was consistent with that used for the free-field grid, or, dz = 0.4 m.

The near-field and far-field models each require input paramters which affect their inertial, damping, and stiffness behavior. Data presented by Nogami and Konagai

(1992) indicate that near-field behavior is fairly insensitive to the size of the near-field. Therefore, the outer radius of the near field was assumed to be twice the outer radius of the pile, which is within the range investigated by Nogami and Konogai (1992). The generation of excess pore pressure through liquefaction represents essentially an undrained phenomenon. Therefore, Poisson's ratio of the soil was taken to be 0.5, which represents an incompressible medium.

The baseline p-y curves were developed at seven depths – 0.0, 0.5, 2.0, 6.0, 10.0, 10.1, and 15.2 m -- for each pile size/stratigraphy combination, using the procedure proposed by O'Neill and Murchison (1983). These curves were defined at the 14 discrete y-values listed in Table 6.5. The low-end stiffness p-y curves were computed by multiplying the baseline y-coordinates by a factor of 2.0, while the high-end curves were determined by applying a factor of 0.5 to the baseline y-values. In this way, the low-end, baseline, and high-end p-y curves retained the same ultimate strength, but exhibited a wide range of stiffness.

### 6.3.4 Discussion of Results

The results of the pile response analyses appear in Figure 6.5 through Figure 6.10, along with Table 6.6. Each figure consists of two subplots – one showing the final displaced shape of the pile, and another showing the pile bending moments corresponding to that displaced shape. Each subplot contains three curves which represent the low-end, baseline, and high-end data for each parameter, and are denoted L, BL, and H, respectively.

#### 6.3.4.1 Effect of Surface Slope

The ground response analyses revealed that lateral spread displacements are heavily dependent on ground surface slope. This strong influence carries over to the pile response, as shown in Figure 6.5. Figure 6.5(a) shows the final displaced shape of the baseline pile for the three ground surface slopes. As expected, the level ground condition produced very little permanent displacement of the pile. However, the 1:20 and 1:10

slopes induce significant permanent pile displacements – about 0.6 m and 1.8 m, respectively. The level ground and 1:20 slope cases suggest minimal yielding of the dense till soil situated at a depth of 10 m. In contrast, large deformations of the steep 1:10 slope caused severe rotation of the pile within the till layer. In all cases, the pile displacement at the ground surface was about the same as the ground surface displacement. However, considerable relative displacement between the pile and the free field developed deep in the liquefied zone.

The final bending moment diagrams are shown in Figure 6.5(b). The level ground case indicates final bending moments which were quite small, but the sloping ground cases resulted in much larger moments. Because the pile was embedded in the dense till layer, the very large strains which developed in the liquefied sand just above the till interface caused the bending moments to reach a local maximum near that location. As lateral spread displacements increase, a significant reversal of curvature may develop in a pile when non-liquefied soil (the soil above the water table in this case) exists near the ground surface. This behavior is evidenced by the large negative moment shown in Figure 6.5(b) for the 1:10 slope case. The proposed methodology successfully captures the dependency of pile response to changes in ground surface slope.

6.3.4.2 <u>Effect of Soil Strength</u>

Lateral spreading displacements were found to strongly depend on the strength of a soil. Figure 6.6 indicates that this effect carries over to pile response as well. The final displaced shapes for this case are shown in Figure 6.6(a), which shows a clear correlation between soil strength and pile movement. As the soil strength was decreased from SPT resistances of N = 20, to N = 10, and N = 5, the pile displacement increased from 0.2, to 0.6, to 1.5 m, respectively.

The final bending moment diagrams for this case are shown in Figure 6.6(b), which indicates that for all three soil strengths, the maximum bending moment occured near the sand-till interface. The effect of soil strength is further illustrated by the bending moments at a depth of 5 m. The strongest (N = 20) soil was able to hold the pile closer to a vertical position than the weaker soils. This caused the reverse curvature and large negative bending moment at a depth of 5 m for this soil strength, an effect noticeably absent in the weaker soils. Based on the preceding, it is apparent that pile response is strongly linked to soil strength, and the proposed methodology is able to model this dependency.

#### 6.3.4.3 Effect of Groundwater Table Depth

The effect of groundwater table depth on pile response is shown in Figure 6.7. Figure 6.7(a) shows the final displaced shape of the baseline pile for the various groundwater table depths. There appears to be very little difference in the three curves, although the 5.0 m case appears to induce more reverse curvature in the pile.

Examination of the bending moments shown in Figure 6.7(b) verifies this observation. It appears as though the upper 5 m of dry soil is strong enough to effectively "clamp" the pile, thus inducing the reverse curvature. Somewhat surprising is the result that of the three cases, the deepest groundwater table produces the highest bending moment. However, this is consistent with the simultaneous observations that the zone of liquefaction was thinnest when the groundwater table was deepest and the ground surface displacement was approximately equal for all groundwater table depths. It should be noted that the greatest bending moment still occurred near the sand-till interface.

#### 6.3.4.4 Effect of Pile Flexural Stiffness

Figure 6.8(a) shows final displaced shapes corresponding to the three flexural rigidities of Table 6.4. It is interesting to note that the pile displacement is very insensitive to pile stiffness over the range investigated. That is, the high stiffness pile experienced about the same total movement as the low stiffness pile; about 0.5 m. However, the final bending moments, as shown in Figure 6.8(b), are vastly different. Here, the low stiffness pile generated the greatest bending moment at the sand-till interface. This is because the stiff pile developed significant negative bending moment at the 5 m depth, which tended to relieve the flexure at the sand-till interface. In conclusion, this case illustrates that the pile flexural response is very sensitive to the pile rigidity.

6.3.4.5 Effect of Pile Diameter

This case is similar to the previous section, but the pile diameter was varied with the flexural rigidity held constant. The effect of pile diameter on pile response is shown in Figure 6.9. The displacement profiles for the three profiles are very similar; about 0.5 m of total displacement at the ground surface. Likewise, there isn't much difference in the bending moment profiles. This figure shows that pile response – both displacement and flexural – is very insensitive to pile diameter.

6.3.4.6 Effect of Pile Length

The extend to which a pile is embedded in non-liquefiable soil can be expected to influence its behavior. Figure 6.10(a) clearly shows that pile embedment has little effect on the maximum pile displacement. In contrast, the embedment strongly affects the maximum bending moments. Figure 6.10(b) indicates that the shortest pile, which barely penetrates the till, does not develop sufficient rotational resistance to produce a large bending moment at the sand-till interface – the pile is very nearly "pinned" at its base. As a result, the maximum bending moment occurs near the middle of the pile. The longer piles, with greater penetration into the till, develop large bending moments near the sand-till interface. Figure 6.10 shows that the 12.0 m long pile is practically "fixed" in the dense till layer -- it's bending moment and displacement diagrams closely follow those of the 15.2 m long pile. This indicates that no benefit, at least from the standpoint of resistance to lateral spreading, would accrue from the extra penetration of the 15.2 m long pile.

6.3.4.7 Effect of P-Y Curve Stiffness

The effect of p-y stiffness on pile response is illustrated in a different fashion than was done for the previous six cases. To evaluate the effect of this parameter, the maximum displacement and bending moment – computed using factored p-y curve – was corresponding response computed using the unfactored p-y curve. The result of this effort is presented in Table 6.6. In this table, the subscripts "low" and "high" refer to displacements and moments computed using the low stiffness and high stiffness p-y curves, respectively. Table 6.6 shows that for the vast majority of cases, the response is very insensitive to p-y stiffness. A few exceptions appear which are mostly associated with bending moments. The results of this table makes sense when the large relative displacements between the pile and the free-field are considered. At such large relative displacement, the individual p-y curves have fully yielded, resulting in a nearly uniform load on the pile.

## 6.4 SUMMARY AND CONCLUSIONS

The parameter study provides a strong indication as to the sensitivity of lateral spread analyses to variations in the input data. Several conclusions can be made based on the ground response and pile response analyses discussed above:

1. The amount of lateral spread displacement is strongly dependent on both the soil shear strength and ground surface slope.
2. The lateral spreading displacement profile is not strongly dependent on the thickness of the liquefied layer.
3. Much of the permanent strains develop in a relatively thin region within the liquefied zone. This zone is generally found near the bottom of the liquefied zone where the contrast between the impedances of the liquefied and underlying soil is large.
4. At the ground surface, the permanent pile displacement and permanent ground displacement are about equal.
5. The final pile displacement profile is independent of the pile diameter and length.
6. The final pile bending moment is strongly dependent on pile flexural rigidity.

7. The maximum positive pile bending moment generally occurs near the interface between liquefied and non-liquefied zones.

8. The geometry of the soil deposit and liquefied zone can result in large negative bending moments when a significant layer of non-liquefied soil exists near the ground surface.

9. Pile displacement and bending moment are largely independent of p-y curve stiffness.

Table 6.1 Ground Response Parameter Study

| Parameter | Low-End | Baseline | High-End |
|---|---|---|---|
| Surface Slope (H:V) | Level | 20:1 | 10:1 |
| Soil SPT $(N_1)_{60}$ | 5 | 10 | 20 |
| Groundwater Table Depth (m) | 0.5 | 2 | 5 |

Table 6.2 Basic Soil Properties of the Sand

| $(N_1)60$ | $D_r$ (%) | $\phi$ (degrees) | $e_{min}$ | $e_o$ | $e_{max}$ |
|---|---|---|---|---|---|
| 5 | 20 | 30 | 0.40 | 0.88 | 1.00 |
| 10 | 35 | 32 | 0.40 | 0.79 | 1.00 |
| 20 | 50 | 36 | 0.40 | 0.70 | 1.00 |

Table 6.3 Discrete Shear Strain Values Used to Define Backbone Curves

| $\gamma$ (-) | $\gamma$ (-) | $\gamma$ (-) | $\gamma$ (-) | $\gamma$ (-) | $\gamma$ (-) |
|---|---|---|---|---|---|
| 0.00 | 2.75 e -4 | 2.15 e -3 | 3.00 e -2 | 1.25 e -1 | 2.75 e -1 |
| 1.00 e -6 | 4.53 e -4 | 3.59 e -3 | 4.00 e -2 | 1.50 e -1 | 3.00 e -1 |
| 2.05 e -5 | 5.82 e -4 | 5.00 e -3 | 5.00 e -2 | 1.75 e -1 | 3.25 e -1 |
| 5.75 e -5 | 7.70 e -4 | 1.00 e -2 | 6.00 e -2 | 2.00 e -1 | 3.50 e -1 |
| 1.02 e -4 | 1.00 e -3 | 1.50 e -2 | 8.00 e -2 | 2.25 e -1 | 3.75 e -1 |
| 1.74 e -4 | 1.44 e -3 | 2.00 e -2 | 1.00 e -1 | 2.50 e -1 | 10.0 |

Table 6.4 Pile Response Parameter Study

| Parameter | Low-End | Baseline | High-End |
|---|---|---|---|
| Surface Slope (H:V) | Level | 20:1 | 10:1 |
| Soil SPT $(N_1)_{60}$ | 5 | 10 | 20 |
| Groundwater Table Depth (m) | 0.5 | 2 | 5 |
| Pile Flexural Stiffness (KN-m$^2$) | 21,400 | 58,800 | 251,200 |
| Pile Diameter (m) | 0.305 | 0.406 | 0.610 |
| Pile Length (m) | 10.4 | 12.0 | 15.2 |
| Relative P-Y Curve Stiffness (-) | 0.5 | 1 | 2 |

Table 6.5 Discrete Y-Values Used to Define Baseline P-Y Curves

| y (m) | y (m) | y (m) |
|---|---|---|
| 0.00 | 3.125 e -4 | 1.000 e -2 |
| 1.953 e -5 | 6.250 e -4 | 2.000 e -2 |
| 3.906 e -5 | 1.250 e -3 | 4.000 e -2 |
| 7.813 e -5 | 2.500 e -3 | 1.500 e 0 |
| 1.563 e -4 | 5.000 e -3 | |

Table 6.6 Pile Response Analysis: Effect of P-Y Curve Stiffness

| **Analysis Cases** | | **Effect on Pile Displacement at the Ground Surface** | | **Effect on the Maximum Bending Moment** | |
|---|---|---|---|---|---|
| Parameter | Variation | $D_{low} / D_{bl}$ | $D_{high} / D_{bl}$ | $M_{low} / M_{bl}$ | $M_{high} / M_{bl}$ |
| Baseline | (-) | 0.99 | 1.00 | 0.91 | 1.21 |
| Slope | low | 1.03 | 0.93 | 0.79 | 1.23 |
| | high | 0.97 | 0.95 | 1.02 | 0.70 |
| Soil SPT | low | 1.08 | 0.96 | 1.02 | 0.99 |
| | high | 1.01 | 1.00 | 0.87 | 1.09 |
| Groundwater Depth | low | 0.97 | 1.25 | 0.89 | 1.53 |
| | high | 0.99 | 1.03 | 0.89 | 1.09 |
| Flexural Stiffness | low | 0.99 | 0.97 | 0.93 | 1.33 |
| | high | 1.01 | 1.01 | 0.81 | 1.15 |
| Pile Length | low | 0.99 | 1.10 | 0.50 | 1.16 |
| | high | 0.99 | 1.01 | 0.93 | 1.21 |

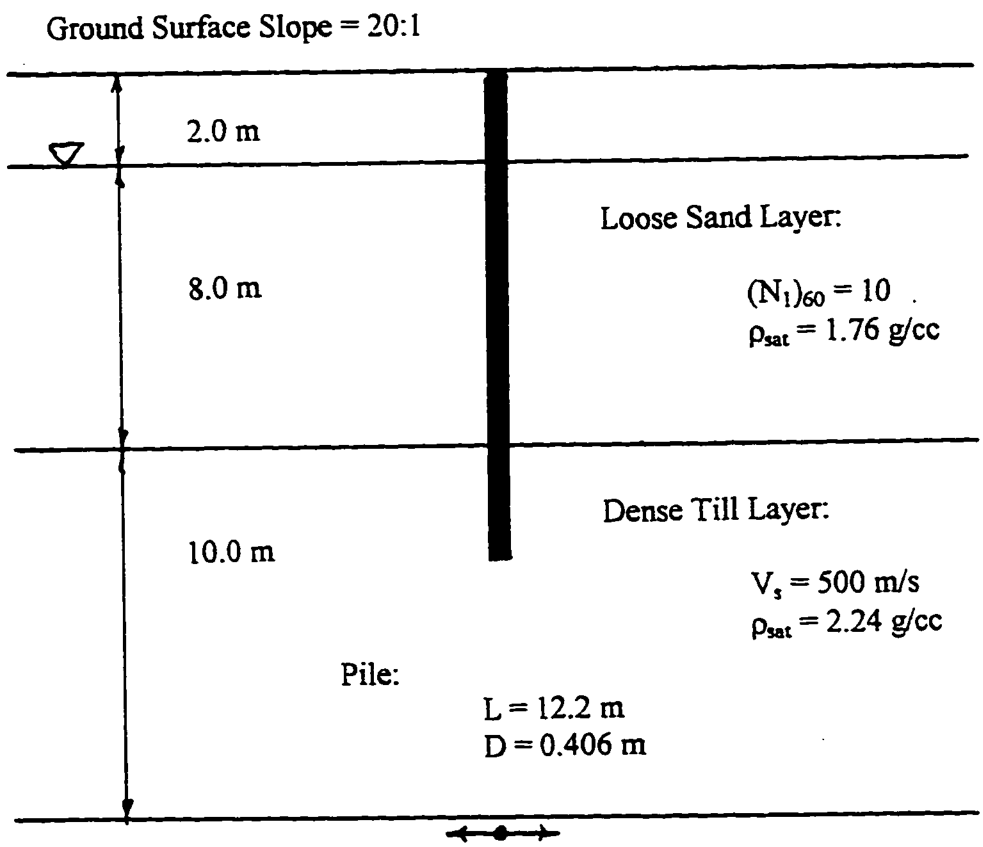


Figure 6.1 Baseline stratigraphy and pile properties

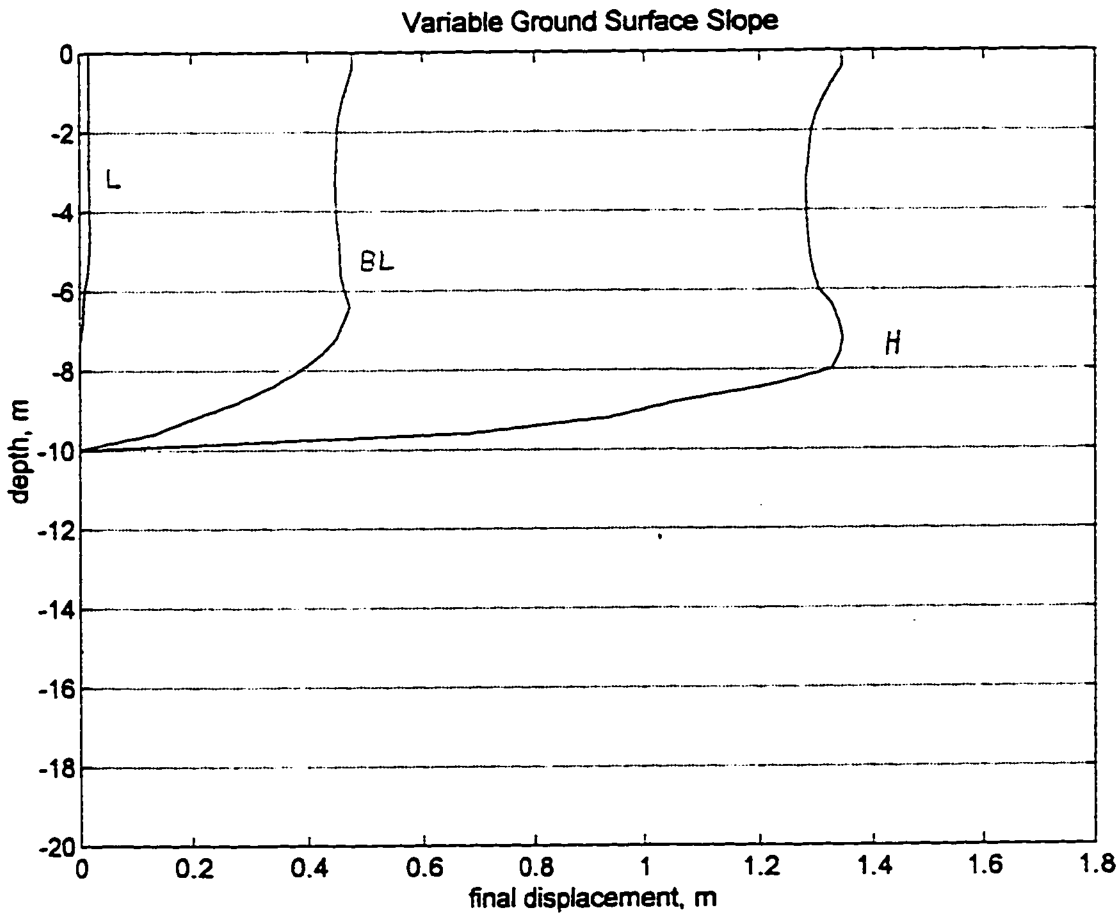


Figure 6.2 Ground response analysis: effect of ground surface slope on final displacement profile

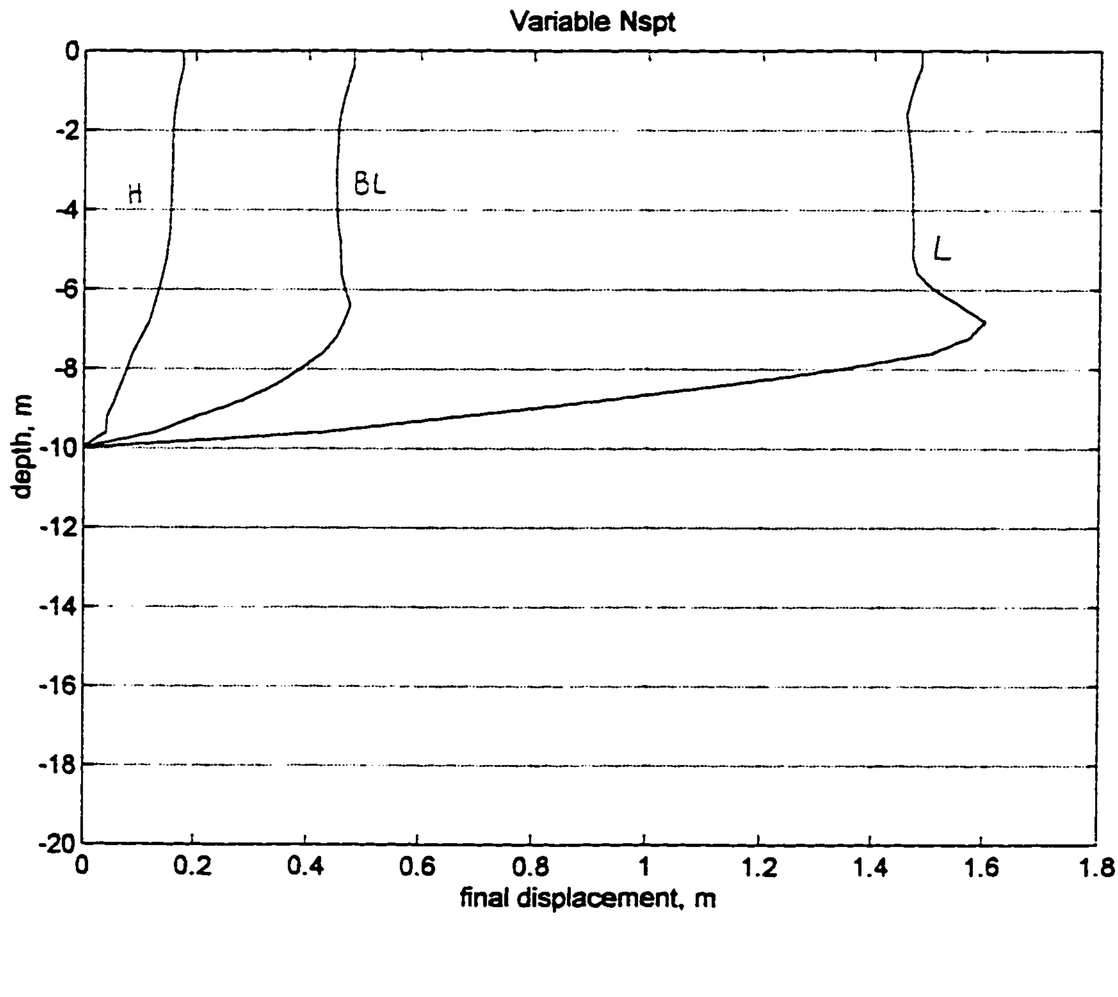


Figure 6.3 Ground response analysis: effect of soil strength on final displacement profile

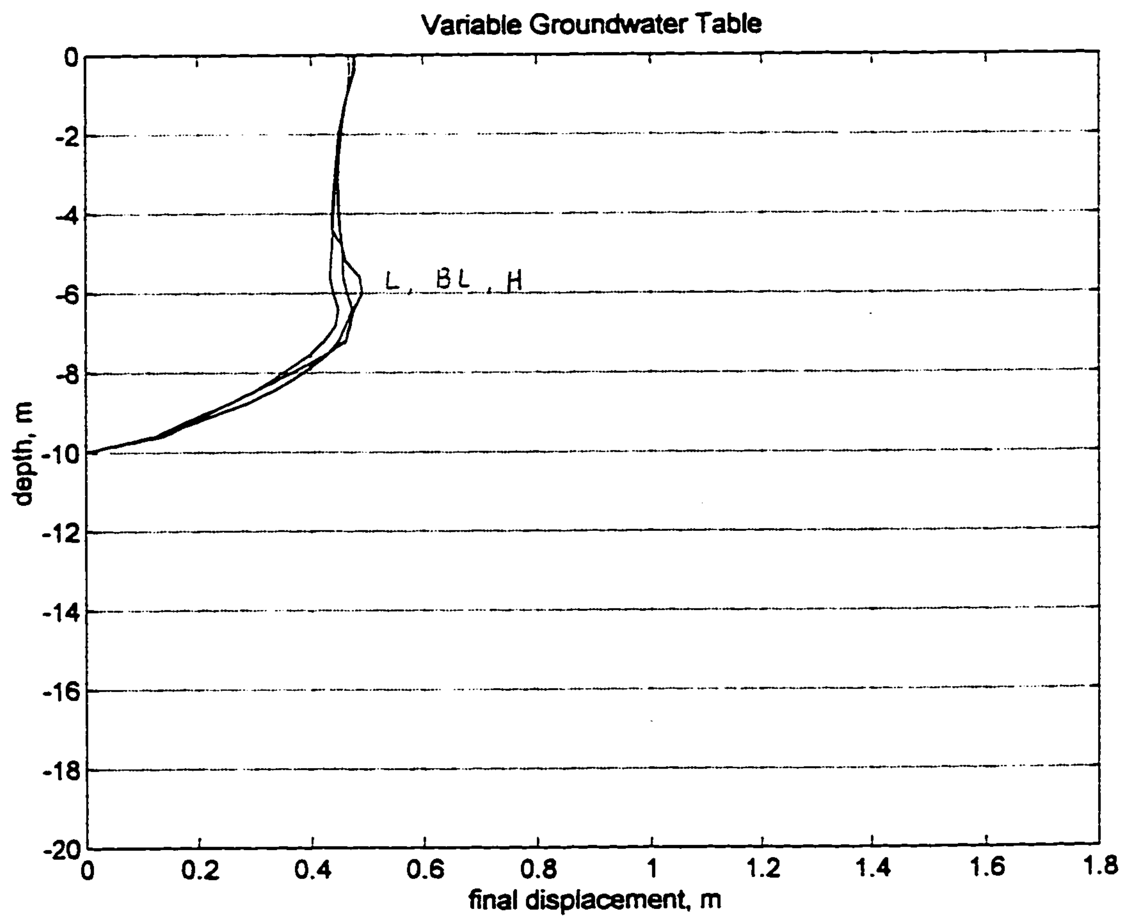


Figure 6.4 Ground response analysis: effect of groundwater table depth on final displacement profile

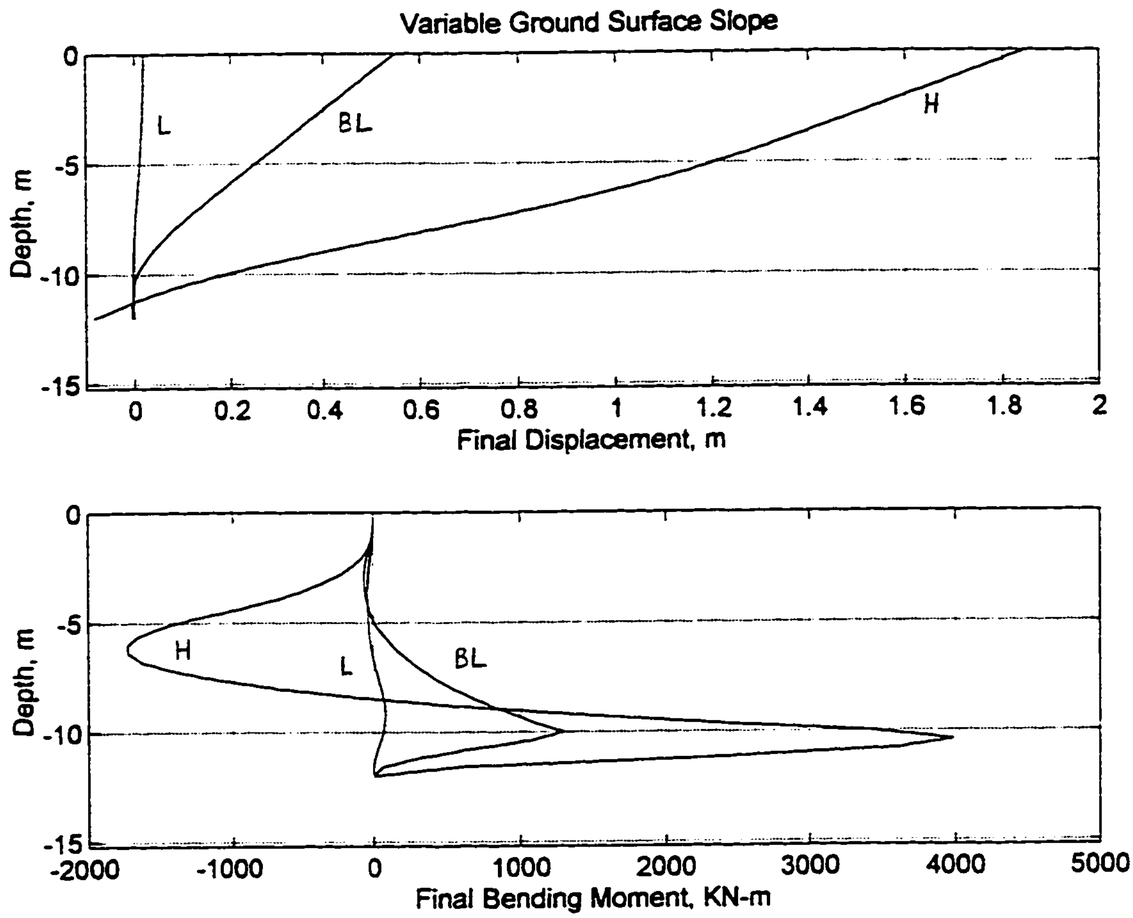


Figure 6.5 Pile response analysis: effect of ground surface slope on (a) final displacement profile and (b) final bending moment profile

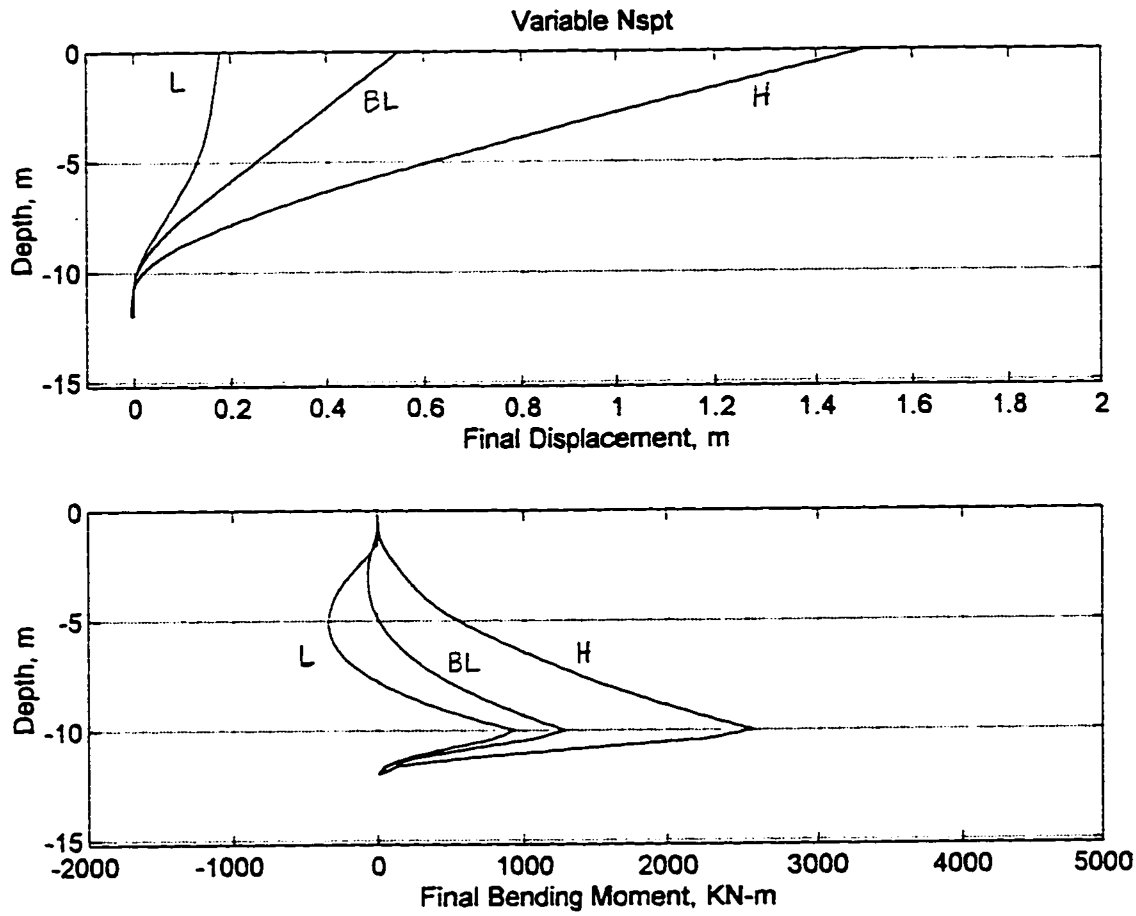


Figure 6.6 Pile response analysis: effect of soil strength on (a) final displacement profile and (b) final bending moment profile

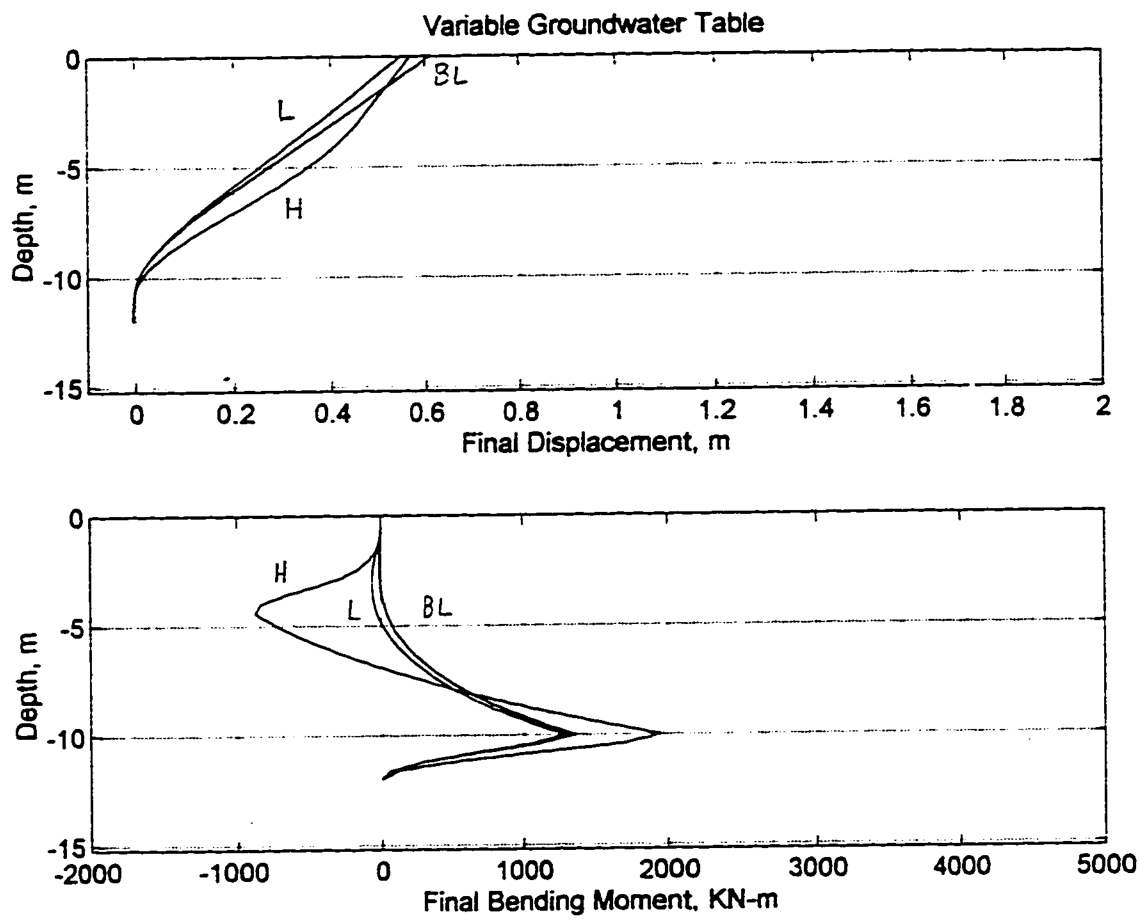


Figure 6.7 Pile response analysis: effect of groundwater table depth on (a) final displacement profile and (b) final bending moment profile

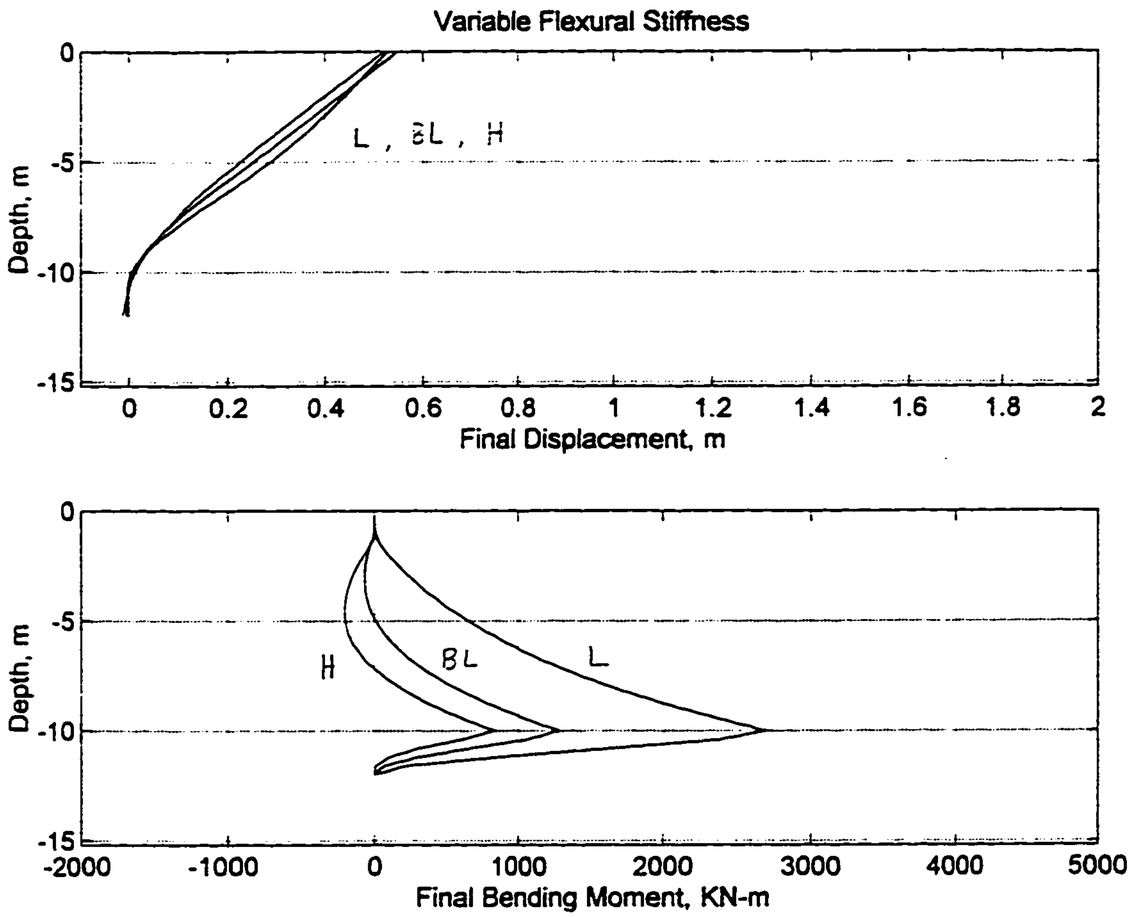


Figure 6.8 Pile response analysis: effect of pile flexural stiffness on (a) final displacement profile and (b) final bending moment profile

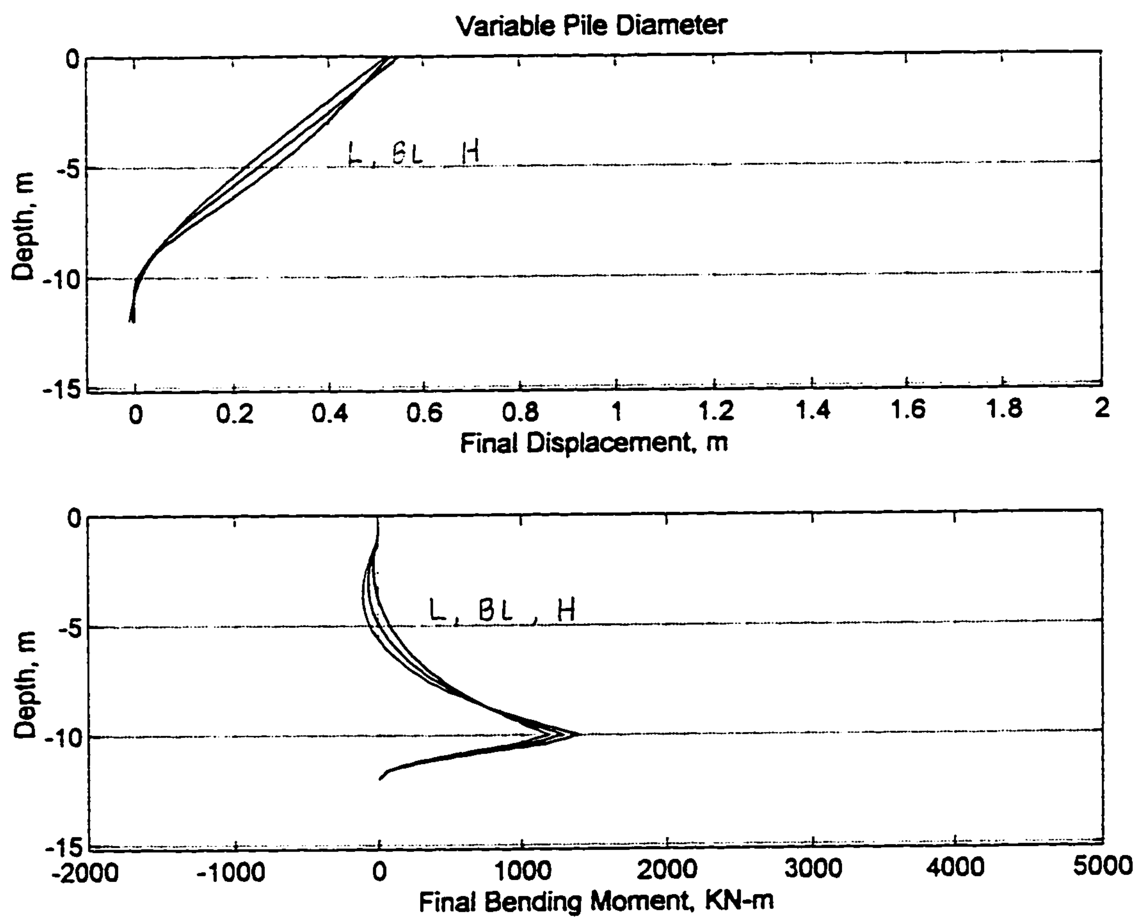


Figure 6.9 Pile response analysis: effect of pile diameter on (a) final displacement profile and (b) final bending moment profile

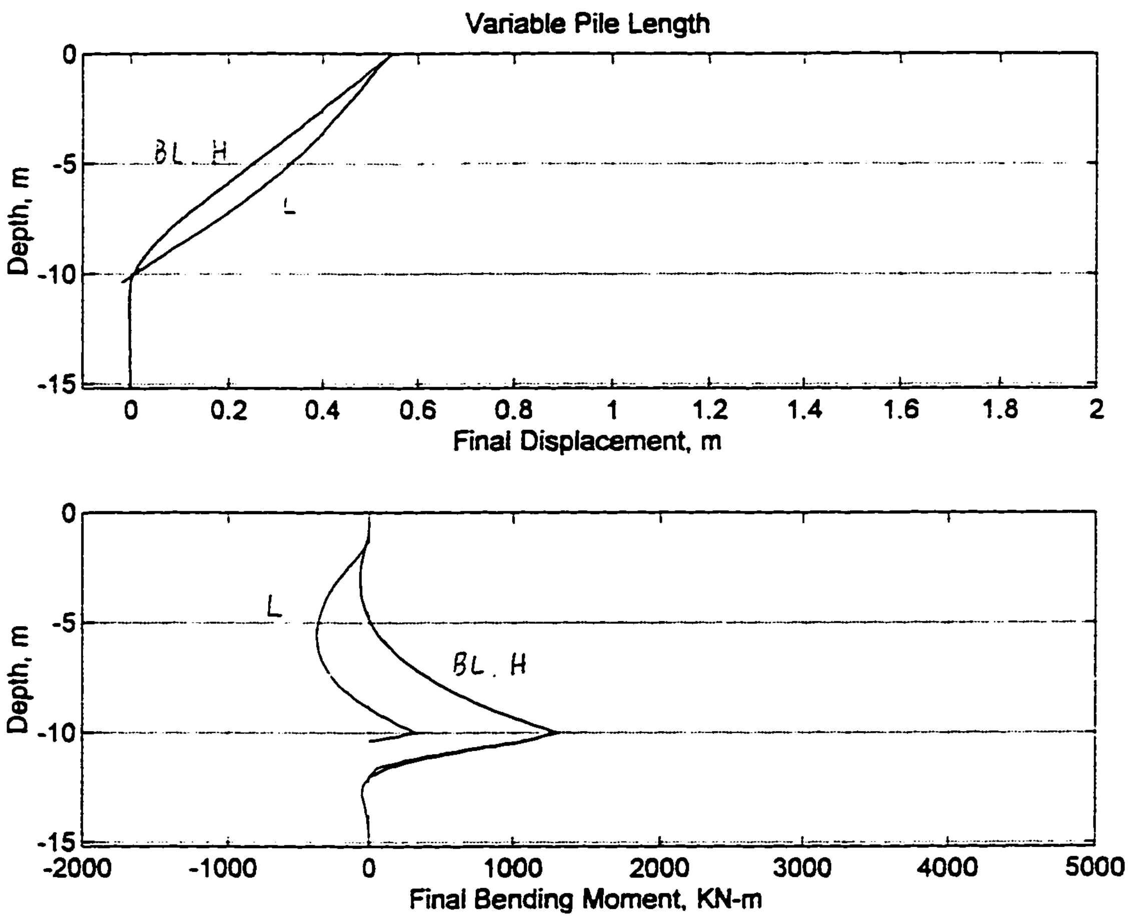


Figure 6.10 Pile response analysis: effect of pile length on (a) final displacement profile and (b) final bending moment profile

# Chapter 7 Application to Case Histories

## 7.1 INTRODUCTION

The sensitivity of the proposed methodology to a wide variation of important input parameters was explored in Chapter 6. The parametric analysis presented in that chapter established the dominant trends of ground and pile response behaviors. However, all of the cases investigated in Chapter 6 – while realistic – were purely hypothetical. Chapter 7 provides additional verification of the proposed methods by comparison with some of the published case histories discussed in Chapters 2 and 3.

Unfortunately, the lack of detailed geotechnical, seismological, and structural data precludes hind-cast analyses of most of these cases. Despite this difficulty, there are several cases which merit detailed analysis with the lateral spread and pile response models. Section 7.2 illustrates the efficacy of the ground response model through comparison with the empirical MLR method proposed by Barlett and Youd (1992), and Section 7.3 applies both models to several of the Niigata case histories discussed in Chapter 2.

## 7.2 CASE HISTORIES OF LATERAL SPREADING

One of the most important attributes of the proposed lateral spread model is its ability to predict the variation of soil displacement with respect to depth. Unfortunately, virtually all case histories regarding lateral spreading only report measured ground surface displacements. As a result, it is not possible to comprehensively verify the displacement profiles that the model can predict. Surprisingly, even the published case histories of lateral spreading at the Wildlife array contain virtually no information regarding subsurface deformations – an inclinometer installed at the site was apparently not read before the earthquake.

The paucity of data has led the profession toward empirical predictions based on numerous case histories. The parameters within these empirical expressions are chosen because of their statistical significance and, as such, reflect trends in lateral spread behavior that have been observed in the field. In this section, the MLR procedure of Barlett and Youd (1992) (see Section 2.5.1.2) is used to calibrate the proposed ground response model against the two parameters that are common to both analyses: the ground surface slope (S), and the thickness of liquefiable soils ($T_{15}$, in which the subscript 15 denotes only those layers with SPT resistances of 15 or less). Bartlett and Youd's method was chosen because of the breadth of the database that was used in its development – a compilation of 467 sites that experienced lateral spread displacements during eight western U.S. and Japanese earthquakes.

### 7.2.1 Effect of Ground Surface Slope

The parametric study of Chapter 6 revealed a strong dependency of lateral spread displacement on ground surface slope. To compare Bartlett and Youd's procedure with the proposed methodology, the baseline profile of Chapter 6 was analyzed at slopes of 0.1, 1.0, 2.0, 3.0, 4.0, 5.0, and 6.0 percent. The same soil properties and earthquake ground motion described in Chapter 6 were used. Chapter 6 also indicated a strong dependency between lateral spread displacement and blow count, however, Bartlett and Youd's procedure makes no distinction between blow counts less than 15 – in other words, it would predict the same displacement for a slope with N = 2 as for an otherwise identical slope with N = 14. It is highly likely that the soils represented in their database comprise a wide range of penetration resistances, and that their final regression smears this fact. As a result, separate analyses were performed using penetration resistances of 5 and 10 in order to bracket the likely average of the Bartlett and Youd database. An epicentral distance of 61 km was assumed so that the MLR and proposed procedures were in close agreement for the baseline case of S = 5%. Because the relative, rather than the absolute, effects of ground surface slope were being investigated by these analyses, this assumption was deemed reasonable. In addition, the following parameters of the MLR model were assumed:

- Moment magnitude, $M_w$ — 7.1
- Fines content of soils with $N < 15$, $F_{15}$ — 0.0 %
- Mean grain size of soils with $N < 15$, $D_{50_{15}}$ — 0.1 mm

The results of these analyses are shown in Figure 7.1, which indicates that the displacements predicted by Bartlett and Youd's method generally fall within the bounds computed using the proposed method. In particular, the two methods agree for shallow slopes comprised of weaker (N = 5) soils and steep slopes comprised of stronger (N = 10) slopes. This suggests that the empirical method of Bartlett and Youd contains significant bias with respect to soil strength, and as a result, fails to capture the obvious sensitivity of lateral spread displacement with penetration resistance. It is interesting to note that the MLR method predicts displacements that increase at a decreasing rate with increasing surface slope. For liquefiable soils -- which are highly nonlinear -- this trend is unrealistic, as it implies strain-stiffening behavior. The proposed method predicts more realistic behavior -- one that allows for lateral spread displacements to become unbounded as the surface slope approaches an asymptotic maximum value. However, the MLR predictions may reflect the fact that the case studies from which it was derived are not infinite slopes, as assumed in the proposed method. For slopes of finite extent, the development of significant deformations generally results in decreased driving stresses, an effect that is not present in the infinite slope model incorporated in the proposed method.

### 7.2.2 Effect of Thickness of Liquefied Soil

The parameter study of Chapter 6 indicated little dependency of lateral spread displacement on the thickness of the liquefied layer. However, the analyses of Chapter 6 varied the thickness of the liquefied soil only by varying the depth of the groundwater table. At many sites where lateral spreading has been observed, the groundwater depth is constant, but the depth to a nonliquefying layer is variable. This latter case was studied to investigate the effect of liquefied soil thickness using the MLR and proposed procedures. This was accomplished by conducting a series of six analyses in which the groundwater table of the baseline stratigraphy was held constant at a depth of 0.5 m, and the depth to the nonliquefiable layer was varied from depths of 1.0, 2.0, 4.0, 7.0, 10.0 and 15.0 m. As was done for the previous comparison, these six analyses were conducted for profiles possessing penetration resistances of 5 and 10. In all analyses, the ground surface slope was held constant at 5%.

The results of these of analyses are presented in Figure 7.2. The data points computed from the proposed method reveal a much greater sensitivity to T15 than those computed using the MLR procedure. Additionally, Figure 7.2 suggests that the MLR procedure tends to over-predict lateral spread displacements at lower values of T15, and under-predict the displacements within the upper range of T15. The trends shown in Figure 7.2 are in sharp contrast to the data computed in the parameter study of Chapter 6 -- reproduced in Figure 7.3 -- that suggests lateral spread displacements determined using the proposed method are rather insensitive to T15. Furthermore, Figure 7.3 indicates that the MLR procedure tends to under-predict the displacements at low T15 and over-predict the displacements at high T15 – behavior opposite to that observed in Figure 7.2. This seeming contradiction is discussed in the following paragraph.

It is important to remember that T15 was varied in Figure 7.2 by changing the depth to the nonliquefiable layer, while T15 was varied in Figure 7.3 by changing the depth to the groundwater. It is apparent that the manner in which T15 is varied has a direct influence on the observed trends in lateral spread displacement computed using the proposed methodology. This makes sense from a physical standpoint, because the two schemes result in vastly different initial states of effective stress as well as applied shear stresses at the bottom of the liquefiable layer. However, the database from which the MLR procedure was developed contains both (and other) conditions. As a result, the averaging tendency of the MLR procedure smears this distinction, and thus fails to reflect the behavior suggested by the proposed methodology.

### 7.2.3 Discussion

Direct comparison of the permanent displacements predicted by the MLR procedure and the proposed model is complicated by the fact that the former is based on a large database that contains many different combinations of site conditions and earthquake ground motions. The limited number of analyses performed with the proposed model cannot begin to reflect the wide range of conditions that exist in the MLR database. In addition, although the MLR procedure is based on a robust collection of observed field behavior, it tends to greatly oversimplify lateral spread behavior by considering only a small subset of important independent variables. In spite of these difficulties, the comparisons do show that the proposed model predicts trends that exist in this large database of actual lateral spreading movements. This consistency provides additional verification of the proposed model.

## 7.3 CASE HISTORIES OF PILE DAMAGE

There have been limited field measurements of lateral spread-induced pile damage but, as with the ground response problem, there are no case histories which contain all the data required for a detailed analysis. Of the case histories presented in Chapter 3, the Showa Bridge and NHK Building cases contain the most detailed information. At both sites, some of the failed piles were extracted and examined. The structural details and resulting damage of these piles are known to a higher degree of certainty than those of the other case histories discussed in Chapter 3. Also, data obtained from aerial surveys gives a broad indication of the magnitude and direction of the free-field deformations at the ground surface. Finally, borehole data and inferred stratigraphies give a fairly reliable assessment of the geotechnical setting at the time of the earthquake. Unfortunately, there are no good strong motion accelerograms from the Niigata earthquake. As a result, researchers have been forced to use either scaled ground motions from other events, or synthetic ground motions based on the source parameters of the earthquake. Another source of uncertainty is the initial state of shear stress at the two sites, because of a lack of detailed topographic and bathymetric information.

In light of the uncertainty surrounding the ground motion and initial shear stress, the lateral spread displacements at the sites were analyzed by the following procedure. First, the initial shear stresses were estimated using the information available in the literature. Following this, idealized stratigraphies were constructed, and appropriate soil properties were assigned to the various layers based on the known geotechnical conditions. Third, the lateral spread response was determined with the proposed method using an appropriately scaled ground motion, and the computed ground surface displacement was then compared with the observed surface displacement. Finally, the initial shear stress distribution was scaled, and the site reanalyzed, until the computed ground surface displacement was in agreement with the observed displacement. This revised free-field response was then used to compute the pile response. Alternatively, the MLR procedure could be used to scale the ground response computed using the proposed methodology. However, for the two sites considered in this chapter, the MLR procedure severely under-predicts the observed displacements.

### 7.3.1 Showa Bridge

The known geotechnical conditions beneath the Showa Bridge are illustrated in Figure 7.4. SPT test results were used to identify the shaded zone of expected liquefaction (Hamada et al., 1992). The bridge consisted of 10 simply-supported spans founded on pile-supported bents. The piles -- 60.9 cm diameter steel pipes – extended to a depth of about 16 m below the river bottom. During the 1964 earthquake, the river bank adjacent to the north abutment displaced up to about 4 m towards the channel. The pile bents were displaced about 1 m at the pile caps, which caused five of the spans to collapse into the river.

#### 7.3.1.1 Soil Properties

This site was analyzed using the idealized stratigraphy shown in Figure 7.5, which includes a single pile embedded in a two-layer soil profile. This roughly corresponds to conditions which existed below the river bottom at the north bank of the river. Based on previous subsurface investigations, the 6.0 m thick upper layer of loose sand was assumed to have an average penetration resistance of 5, while the 10.0 m thick lower layer of medium-dense sand was characterized with an average penetration resistance of 30. This and other pertinent soil properties are listed in Table 7.1, and the relevant pile data is contained in Table 7.2. Details regarding these parameters are discussed in the following paragraphs.

The stress-strain behavior of the soil is controlled by the initial shear modulus, the initial shear strength, the rate of pore pressure generation, and the residual shear strength. The initial shear strength of the soil depends on the friction angle and initial state of effective stress, in accordance with the Mohr-Coulomb failure hypothesis presented in Chapter 4. For this case study, the former was estimated from the penetration resistance data of Figure 7.4, while the latter was computed based on assumed values of soil density and lateral earth pressure coefficient, which are listed in Table 7.1. The rate of pore pressure generation is strongly dependent on the initial void ratio of the soil, which was computed using the assumed values of relative density, minimum void ratio, and maximum void ratio listed in Table 7.1. This table also indicates the residual strengths used for the analysis, which were derived from the Seed and Harder (1990) correlation that was shown graphically in Figure 2.5.

#### 7.3.1.2 Initial Shear Stresses

As discussed in Chapter 4, lateral spread displacements are driven by initial shear stresses on horizontal planes. For this case study, the initial state of shear stress was estimated using the commercially available finite difference program, FLAC (Itasca Consulting Group, 1994) with linear elastic soil properties. The finite difference mesh developed for this analysis is shown in Figure 7.6, and the computed shear stress contours in the vicinity of the north river bank appear in Figure 7.7. The maximum vertical gradient of shear stress is indicated along line A-A' in this figure, and the data along this section was used to establish the initial state of shear stress for the subsequent analysis.

#### 7.3.1.3 Pile Properties

No data concerning the wall thickness, steel grade, and axial load of the 60.9 cm diameter pipe piles located at each bent is available. In order to compute the flexural stiffness and mass per unit length, the piles were assumed to be hollow with a wall thickness of 9.5 mm. Based on an oblique photograph of the failed structure (Seed and Idriss, 1966), eight piles were assumed to be located at each bent of the bridge. This implies a pile spacing of about 5 diameters, center to center. The pile axial load was estimated from the known configuration of the bridge. Information presented in Hamada (1992) indicates that the bridge deck was about 25 m wide and that the pile bents were spaced 27.6 m apart. Based on these dimensions, each pile supported a tributary area of about 90 $m^2$. Assuming an effective dead plus live load of 9 kPa applied from the bridge deck, the axial load is about 800 kN. Alternatively, if the piles were fabricated from low carbon steel with a yield stress of 250 MPa, and assuming the piles were designed using an allowable stress equal to 35 percent of this value (UBC, 1994), then the design capacity would be about 1600 kN. Furthermore, if the typical service load were about half the design load, then the axial force in each pile was likely to be around 800 kN. Finally, a yield moment of 550 kN-m was computed for this magnitude of axial load.

#### 7.3.1.4 Input Motion

There are no reliable strong motion acceleration records from the Niigata earthquake, although a post-earthquake liquefaction analysis performed by Seed and Idriss (1966) estimated that the peak bedrock acceleration was on the order of 0.12 to 0.13 g. Based on this, the ground motion used for this case study consisted of the 1940 El Centro earthquake record scaled to a peak acceleration of 0.125 g (Figure 7.8). The El Centro data (M = 7.1) was recorded at an epicentral distance of only 9 km, while the Niigata event (M = 7.3) was located somewhat farther from the source, about 43 km. Therefore, there is probably more high frequency motion in the record used for the analysis than actually existed at the time of the Niigata event. However, the highly nonlinear nature of liquefaction tends to drastically attenuate high frequency energy, so the effect of this discrepancy is minimal.

#### 7.3.1.5 Results of Analysis

The MLR procedure cannot be used to analyze this site, because the displacements of interest occurred in front of – rather than behind – the free face created by the bank of the Shinano River. Using the proposed methodology with the unscaled shear stress distribution, a free-field surface displacement of 0.45 m was computed, which is considerably smaller than the 4 to 6 meters reported by Hamada (1992). By scaling the initial shear stress distribution upward by a factor of 1.03, and decreasing the residual shear strength to 5 kPa, a free-field surface displacement of 5.1 m was computed using the proposed methodology.

The resulting profile is plotted along with the final pile displacement in the upper half of Figure 7.9. This figure shows that the free-field displacements developed primarily in a thin region just above the interface between the loose and medium dense sands. In a fully liquefied state, the static shear stresses in this region were nearly equal to the residual shear strength of the soil, and the soil possessed practically no shear stiffness. As a result, the zone of soil from about 4.5 m to 6.0 m displaced farther than the overlying soil, producing the spike shown on the figure. The lower half of Figure 7.9 shows the final displacement profile of the pile plotted to a different scale. Additionally, a straight line was drawn that extends from the top of the pile (depth = 0 m) to the top of the pier (depth = +9 m), at the same slope as the top of the deformed pile. This simulation indicates a predicted pier cap displacement of about 0.42 m, which is somewhat less than the 0.93 m reported by Hamada (1992), and previously shown in Figure 3.7(b). The computed bending moment profile for this displacement is shown in Figure 7.10. The maximum bending moment is about 850 kN-m, and occurs just below the liquefiable soil, at a depth of about 6.5 m. This exceeds the yield moment of 550 kN-m for the section, and suggests that the pile sustained flexural failure at this location.

### 7.3.2 NHK Building

The NHK Building was a four-story reinforced concrete structure situated about 1 km southeast of the Showa Bridge. The site occupied a former channel of the Shinano

River that had been filled during land reclamation efforts in the city of Niigata. The building was founded on 35 cm diameter reinforced concrete piles ranging from 11 to 12 m in length. Neither the column spacing, nor the individual pile spacing within each cap are known. Aerial survey data gathered after the earthquake indicated that the ground surface of the site moved laterally between 1 and 2 m in a south-easterly direction due to lateral spreading. After the earthquake, minor repairs were made to the structure which was then reoccupied until 1985. During demolition of the structure at that time, it was discovered that many of the foundation piles had sustained severe damage due to the earthquake. The typical pile deformation and observed damage was previously shown in Figure 3.8.

#### 7.3.2.1 Soil Properties

The known geotechnical conditions beneath the NHK Building are shown in Figure 7.11, which shows SPT test data and the inferred zone of liquefaction. The idealized model used in this case study (Figure 7.12) consisted of three soil layers and a single 11 m long pile. An upper 3.0 m thick layer was underlain by a 5.5 m thick liquefiable layer, which in turn overlay medium dense soil to the bottom of the pile. The relevant soil and pile properties used for the analyses are listed in Table 7.3 and Table 7.4, respectively. These are discussed in greater detail in the following paragraphs.

The strength properties and void ratio data that was used to model the stress-strain behavior of the three soil layers are shown in Table 7.3. As was done for the Showa Bridge case study, these values were chosen to be consistent with the penetration resistance data at the site.

#### 7.3.2.2 Initial Shear Stresses

Unlike the Showa Bridge site, the NHK building was situated well-beyond the influence of the existing river channel. However, the site possessed a very gradual slope of about 1.5% downward in a south-easterly direction, which corresponded to the general direction of permanent ground surface displacements measured after the earthquake. An infinite slope of 1.5% was used to compute the initial shear stress distribution for the analyses.

#### 7.3.2.3 Pile Properties

Table 7.4 contains the pertinent pile data that was used for the case study. Although the pile diameter and length are known, no information pertaining to the pile reinforcement is available. The pile flexural stiffness was computed assuming normal strength concrete ($f'_c$ = 20 MPa), and that the longitudinal reinforcement consisted of four 20 mm steel bars with 8 cm of clear cover. The pile axial load was taken to be 75 kN, a value reported by others that have performed post-earthquake pile analyses at this site (Dobry, 1994). Using these properties, the yield moment of the pile was computed to be about 80 kN-m.

#### 7.3.2.4 Input Motion

The input ground motion was the same motion that was used for the Showa Bridge analysis. The motion was described in Section 7.3.1.4.

#### 7.3.2.5 Results of Analyses

The MLR procedure predicted a free-field surface displacement of about 0.3 m at this site, which is considerably lower than the 1 to 2 m reported by Hamada (1992). Additionally, the surface displacement computed using the proposed methodology – with unscaled initial shear stresses - was about 0.07 m, which was also much lower than observed. By scaling the initial shear stress distribution upward by a factor of 3.0, a free-field displacement of about 1.2 m was computed using the proposed methodology.

The resulting profile is plotted along with the final pile displacement profile in Figure 7.13. Because a nonliquefiable surface layer existed at the NHK site, the pile and free-field displacements at the ground surface indicate a much lower relative displacement than was observed at Showa Bridge (Figure 7.9). This figure shows that the computed pile displacement is about 1.4 m at the ground surface, and that a good part of the displacement resulted from rotation of the pile within the nonliquefiable surface layer. The computed pile displacement is in general agreement with the 1.0 to 1.2 m displacement reported by Hamada (1992). The final bending moment profile for this case is plotted in Figure 7.14. Large positive and negative bending moments that reach local maxima near the interface between liquefiable and non-liquefiable layers were computed. The large bending moments shown on this figure far exceed the actual flexural yield capacity of the pile, thus indicating that flexural failure of the piles should have occurred in the vicinities of the top and bottom of the liquefied layer. This result is consistent with the damage observed when the pile were exhumed (Figure 3.8). In reality, the pile moments would not be expected to increase beyond about 100 kN-m. This behavior is due to the linear moment-curvature constitutive relation assumed in the pile-soil interaction model. In spite of this, the proposed methodology is able to predict both when and where yielding is likely to occur within a pile due to lateral spread displacements.

## 7.4 SUMMARY AND CONCLUSIONS

The analyses described in first part of this chapter demonstrate that the proposed lateral spread model is able to replicate dominant trends observed in actual earthquakes. Furthermore, the case studies of pile damage contained in the latter part of the chapter verify that the pile response model can predict if and where pile damage will likely occur when subjected to lateral spread displacements.

Finally, this chapter illustrates the need for high-quality, well-documented case studies with which to calibrate and verify these and other predictive procedures. Even the best available case histories require estimation of several important parameters. More measurements of pile and free-field displacements are needed – especially the vertical profile of lateral spread displacements.

Table 7.1 Soil properties used for the Showa Bridge site

| **Property** | **Layer 1** | **Layer 2** |
|---|---|---|
| Layer thickness, m | 6.0 | 10.0 |
| Saturated unit weight, $kN/m^3$ | 15.7 | 20.4 |
| SPT Resistance, blows/ft | 5 | 30 |
| Residual Strength, kPa | 5 | n/a |
| Friction angle, degrees | 30 | 38 |
| Relative density, % | 20 | 65 |
| Minimum void ratio, - | 0.4 | 0.4 |
| Maximum void ratio, - | 1.0 | 1.0 |
| Lateral earth pressure coefficient, - | 0.5 | 0.5 |
| Poisson's ratio | 0.5 | 0.5 |

Table 7.2 Pile properties used for the Showa Bridge site

| **Property** | **Value** |
|---|---|
| Length, m | 16.0 |
| Diameter, cm | 60.4 |
| Flexural stiffness, $kN\text{-}m^2$ | 162000. |
| Mass per unit length, $kN\text{-}s^2/m^2$ | 0.140 |
| Axial force, kN | 800. |
| Boundary condition at head | pinned |
| Boundary condition at toe | pinned |

Table 7.3 Soil properties used for the NHK Building site

| Property | Layer 1 | Layer 2 | Layer 3 |
|---|---|---|---|
| Layer thickness, m | 3.0 | 5.5 | 2.5 |
| Saturated unit weight, $kN/m^3$ | 14.2 | 15.7 | 19.7 |
| SPT Resistance, blows/ft | 9 | 9 | 20 |
| Residual Strength, kPa | n/a | 6.0 | 60.0 |
| Friction angle, degrees | 32 | 32 | 37 |
| Relative density, % | 35 | 35 | 55 |
| Minimum void ratio, - | 0.4 | 0.4 | 0.4 |
| Maximum void ratio, - | 1.0 | 1.0 | 1.0 |
| Lateral earth pressure coefficient, - | 0.5 | 0.5 | 0.5 |
| Poisson's ratio, - | 0.5 | 0.5 | 0.5 |

Table 7.4 Pile properties used for the NHK Building site

| Property | Value |
|---|---|
| Length, m | 11.0 |
| Diameter, cm | 35.0 |
| Flexural stiffness, $kN\text{-}m^2$ | 20000. |
| Mass per unit length, $kN\text{-}s^2/m^2$ | 0.231 |
| Axial force, kN | 75.0 |
| Boundary condition at head | pinned |
| Boundary condition at toe | pinned |

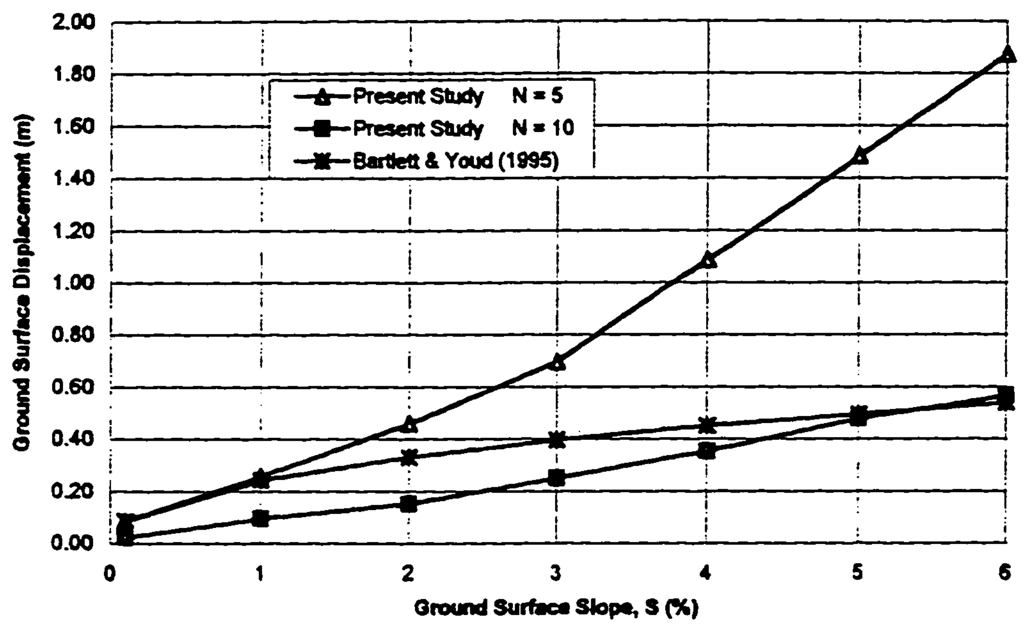


Figure 7.1 The effect of ground surface slope on surface displacement using the proposed method and the MLR procedure of Bartlett and Youd (1995)

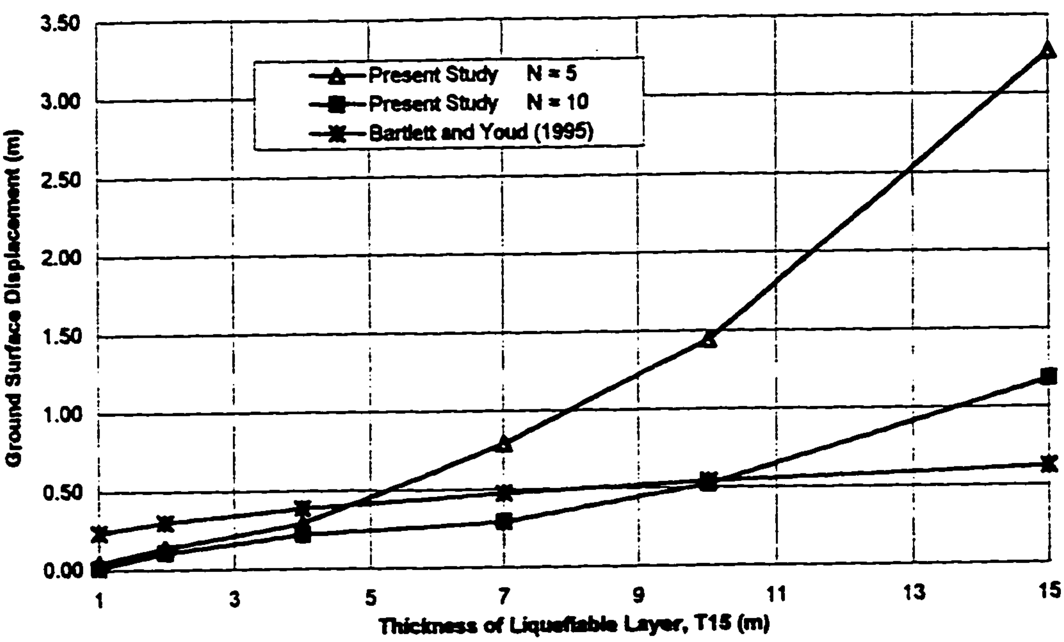


Figure 7.2 The effect of thickness of liquefiable soil on surface displacement using the proposed method and the MLR procedure of Bartlett and Youd (1995) For the proposed method, $T_{15}$ was varied by holding the depth to groundwater constant at 0.5 m and varying the depth to a nonliquefiable layer.

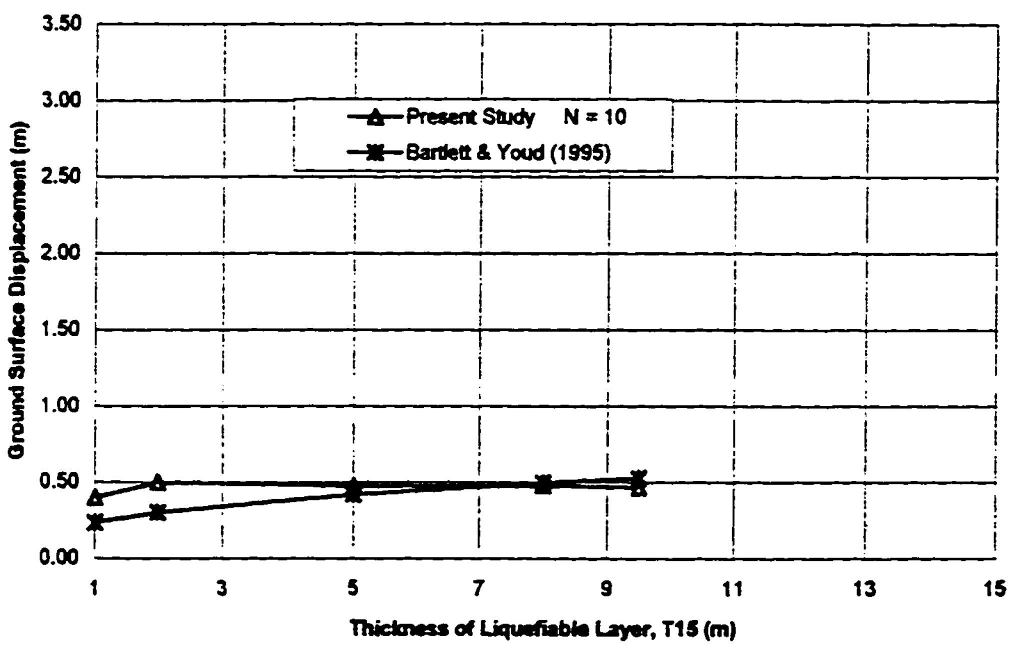


Figure 7.3 The effect of thickness of liquefiable soil on surface displacement using the proposed method and the MLR procedure of Bartlett and Youd (1995). For the proposed method, $T_{15}$ was varied by holding the depth to a nonliquefiable layer constant at 10.0 m, and varying the depth to groundwater.

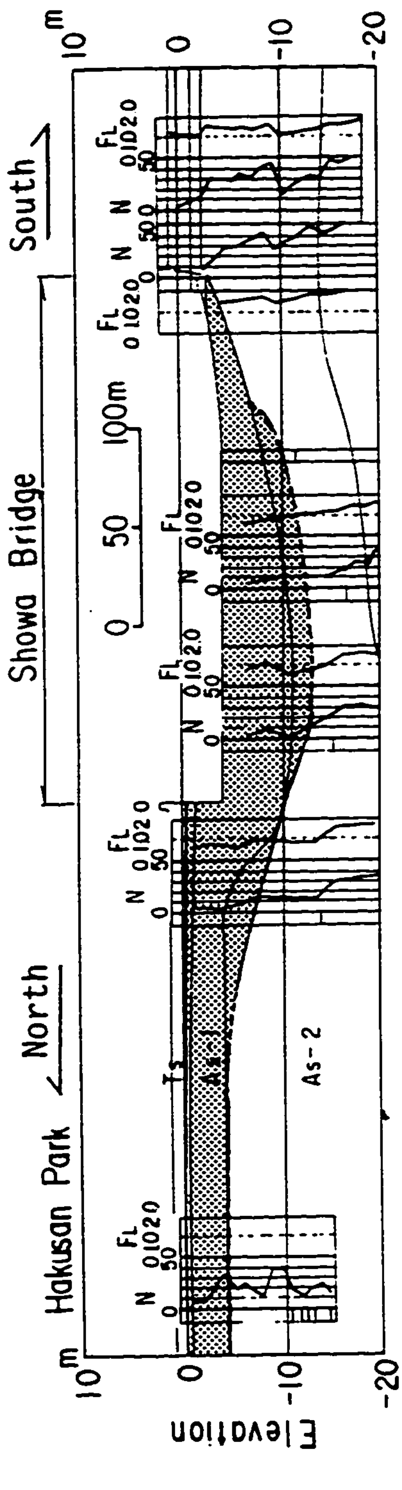


Figure 7.4 Geotechnical setting at the Showa Bridge site (adapted from Hamada, 1992)

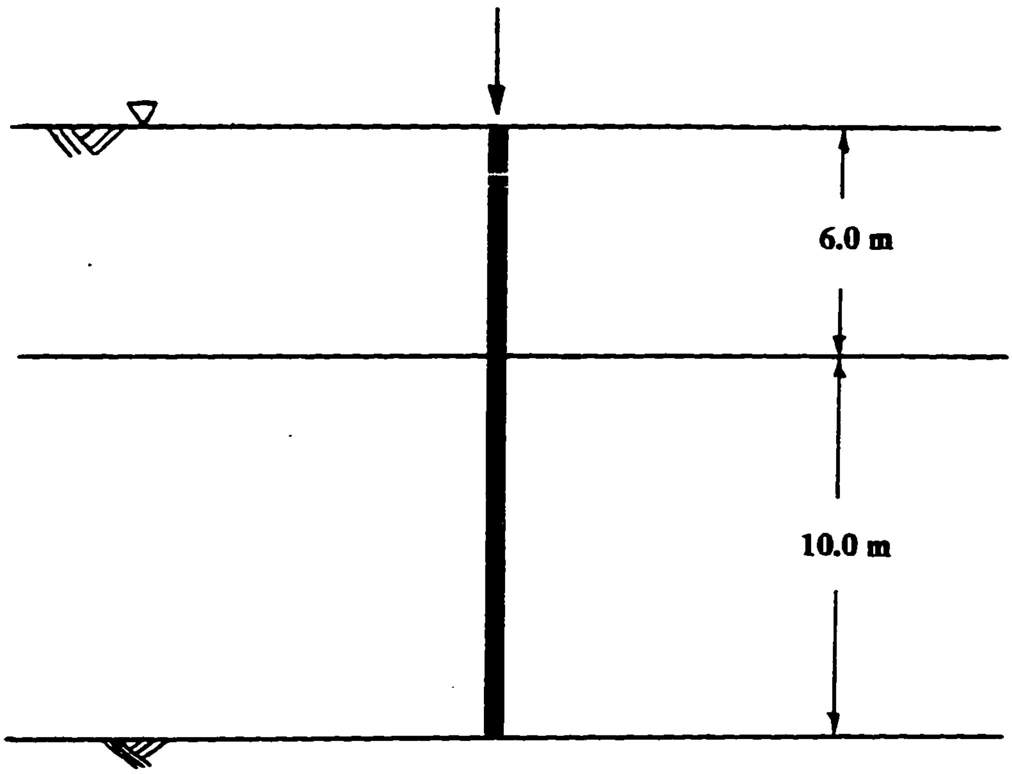


Figure 7.5 Idealized stratigraphy used for the Showa Bridge case study

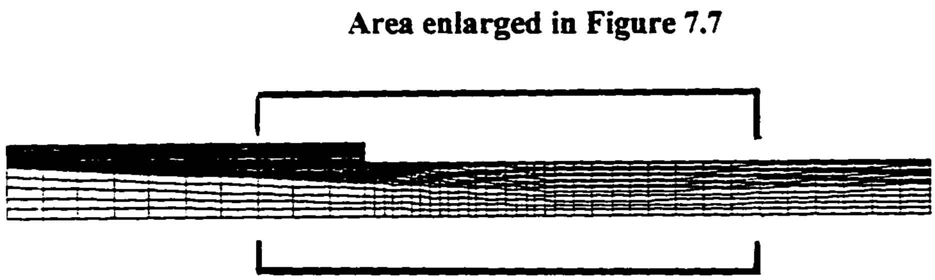


Figure 7.6 Finite difference mesh used to compute initial shear stresses

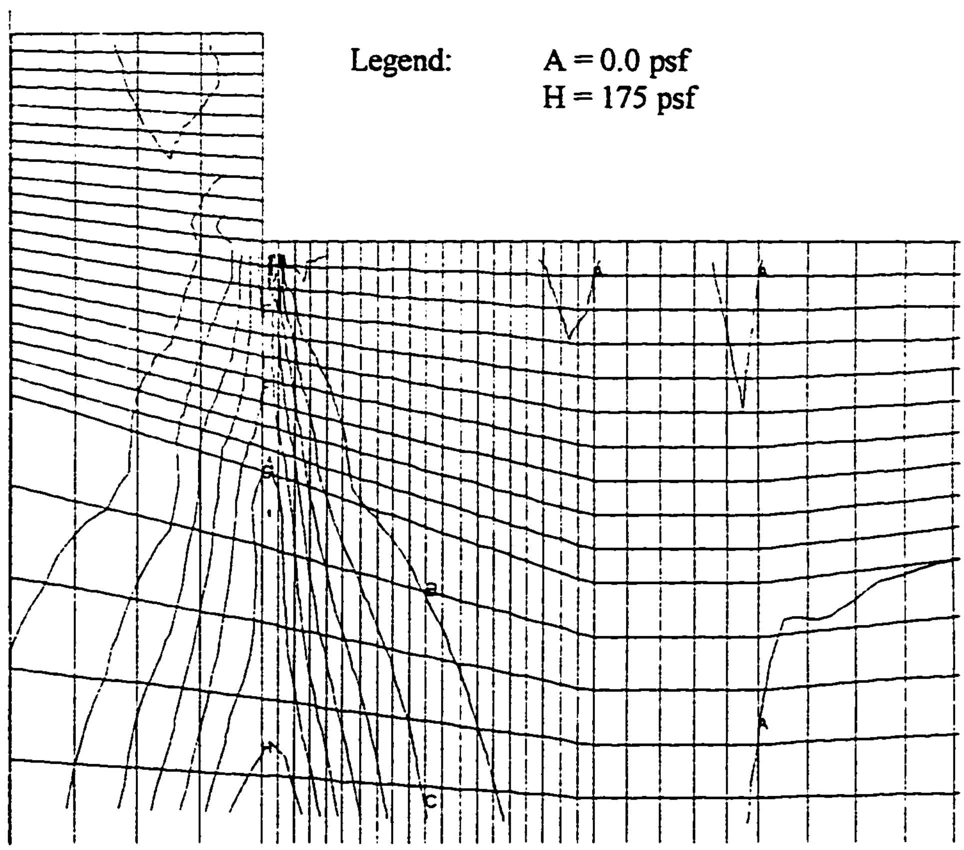


Figure 7.7 Shear stress contours near the north bank computed using FLAC

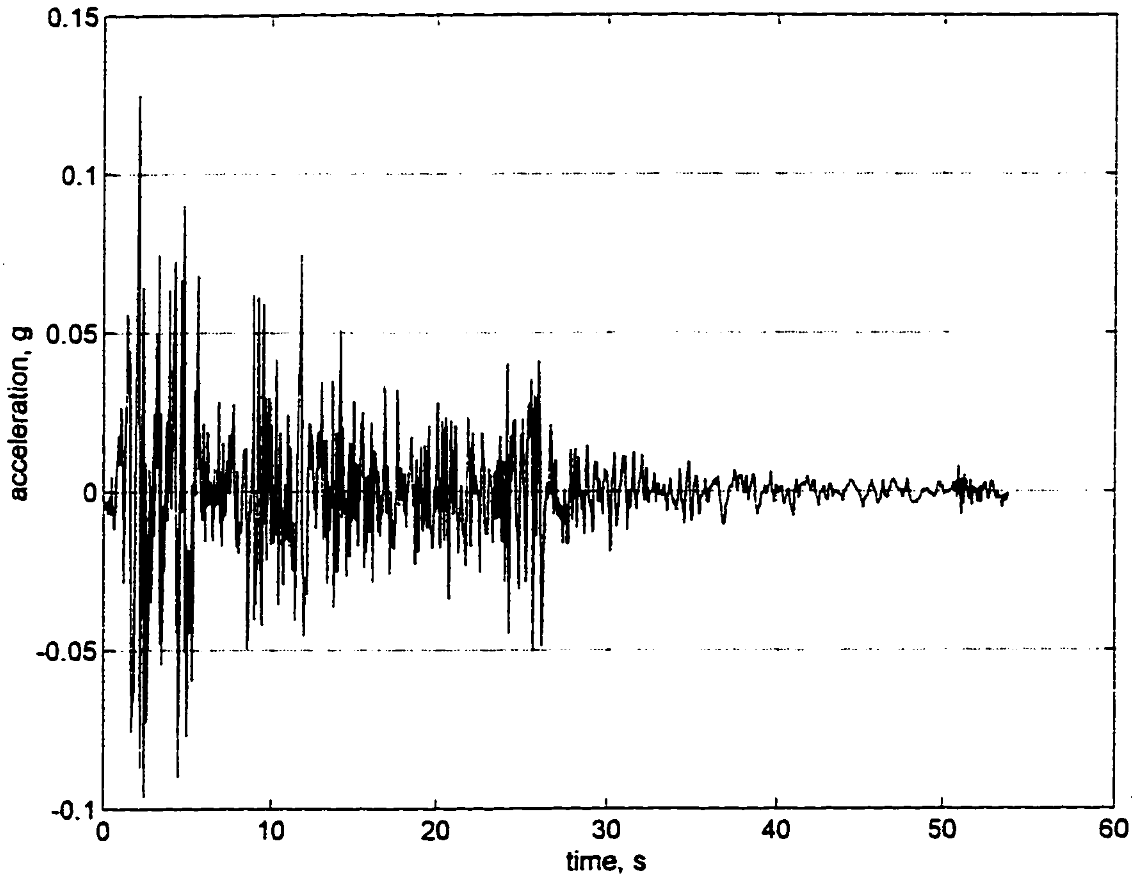


Figure 7.8 Ground motion used for analysis of the Niigata case studies

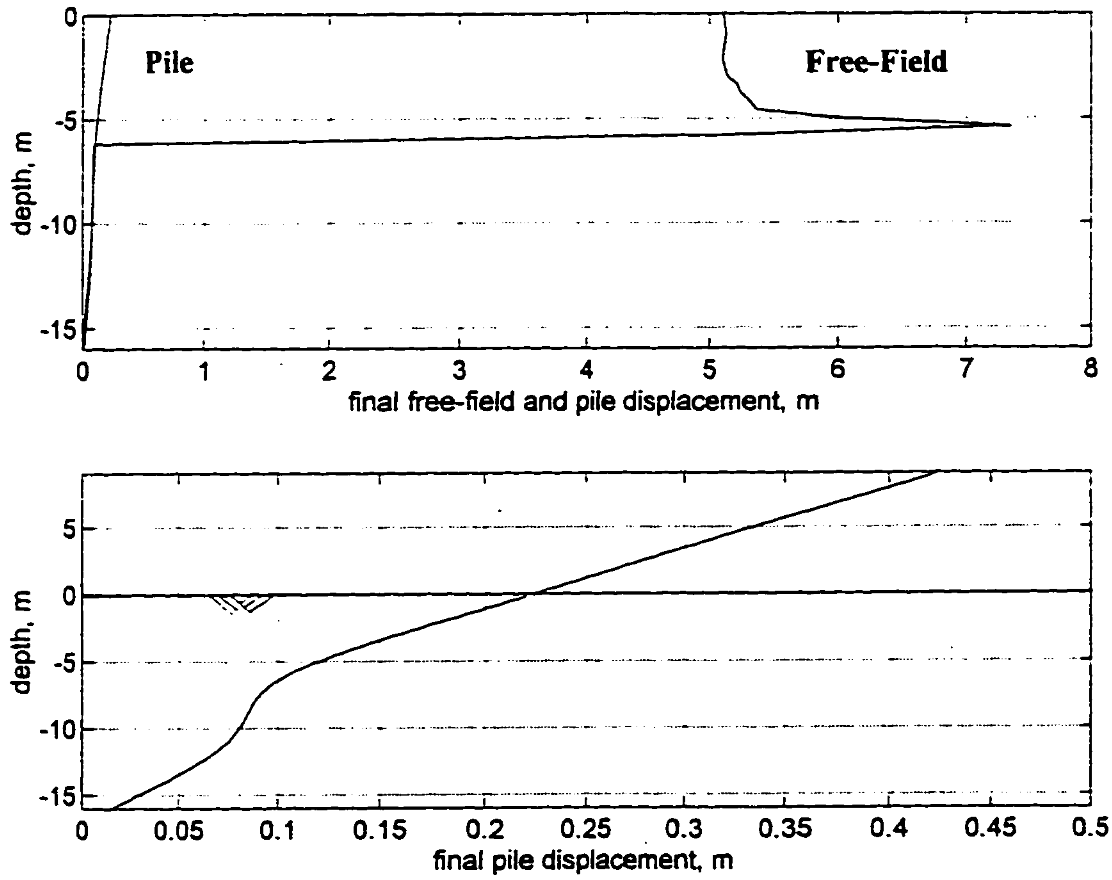


Figure 7.9 Computed pile and free-field displacements at the Showa Bridge site

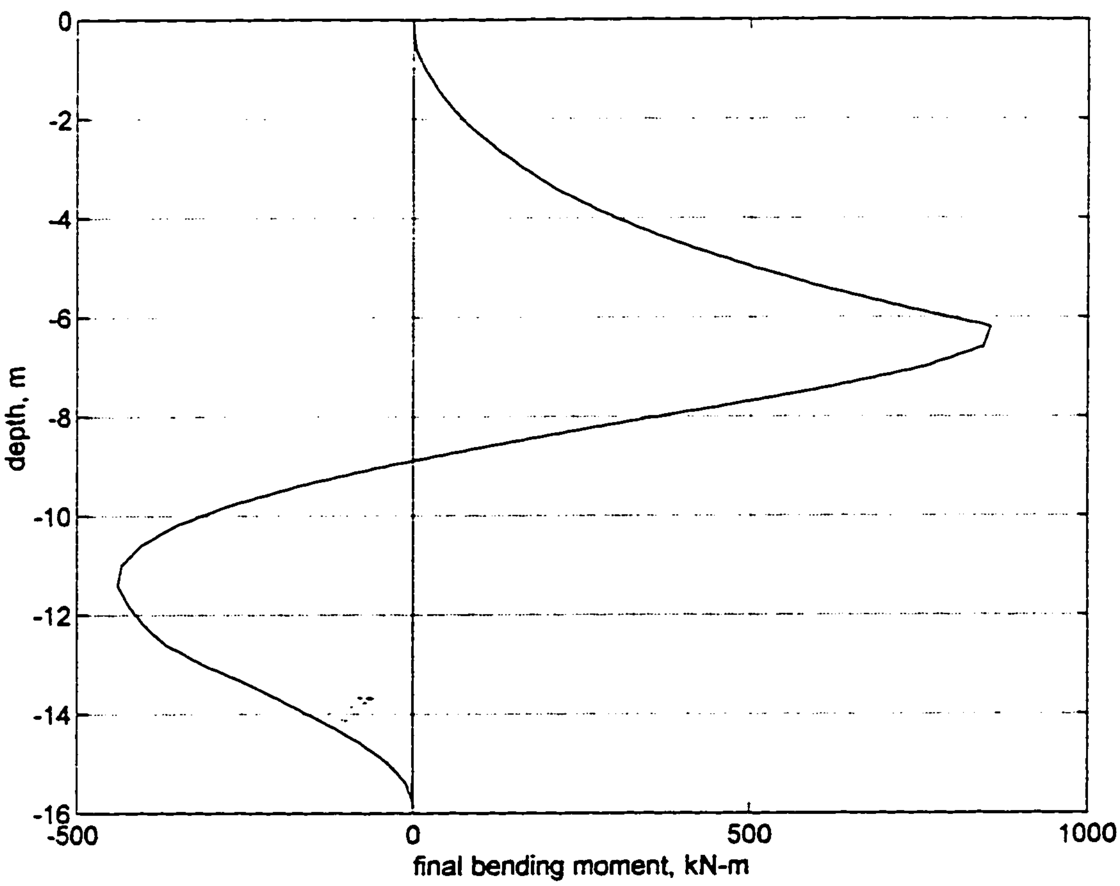


Figure 7.10 Computed pile bending moments at the Showa Bridge site

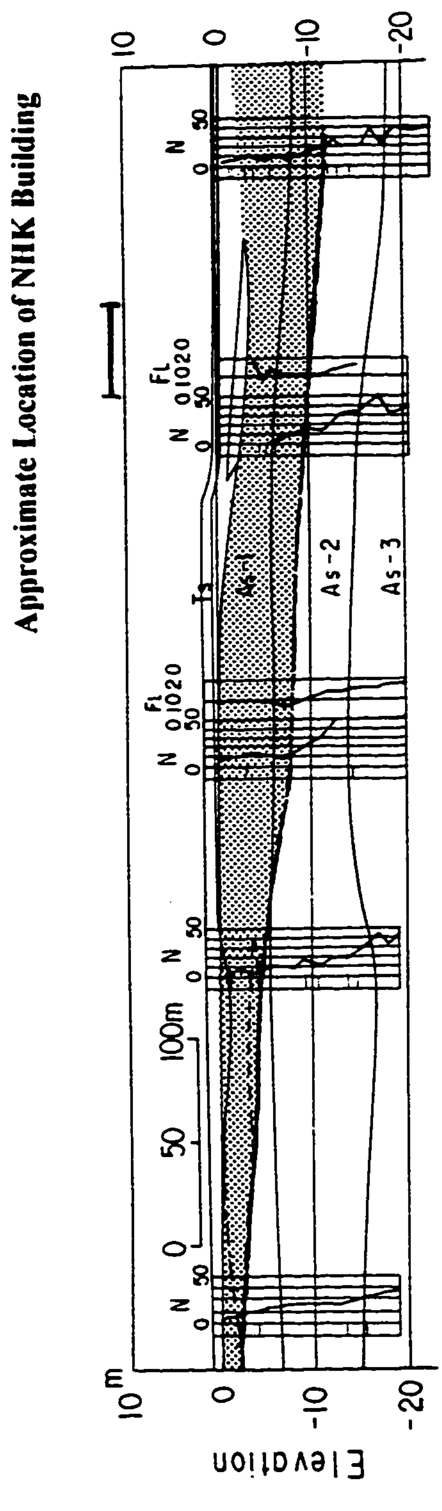


Figure 7.11 Geotechnical setting at the NHK Building site (adapted from Hamada, 1992)

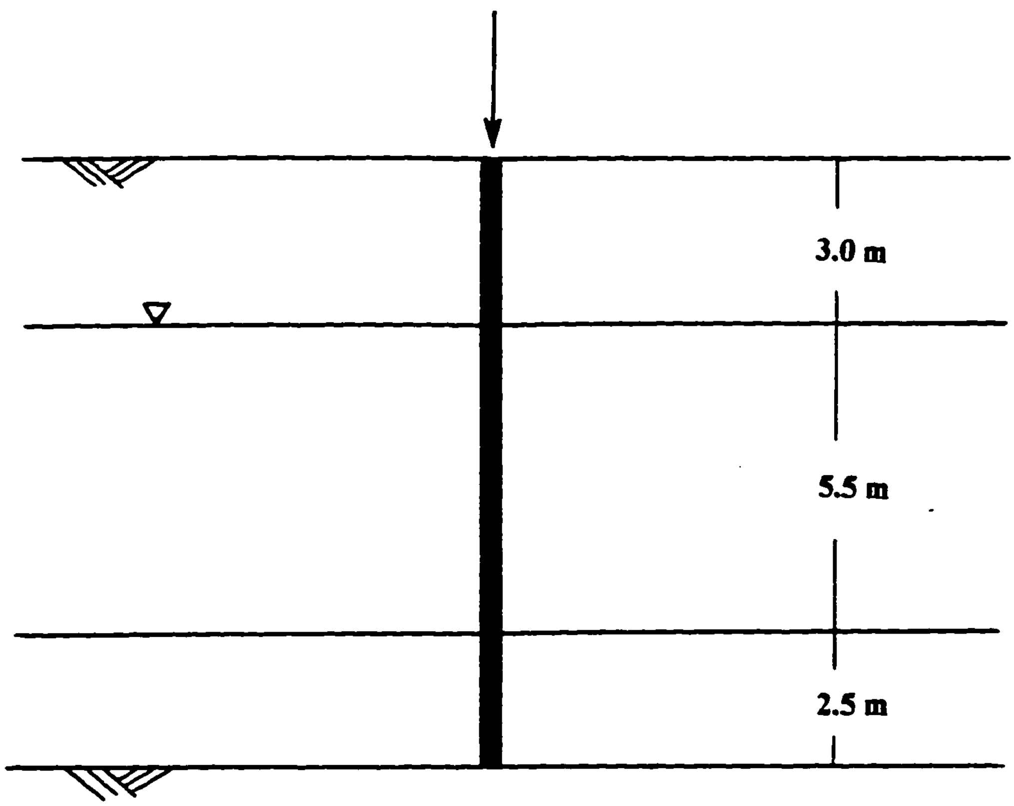


Figure 7.12 Idealized stratigraphy used for the NHK Building case study

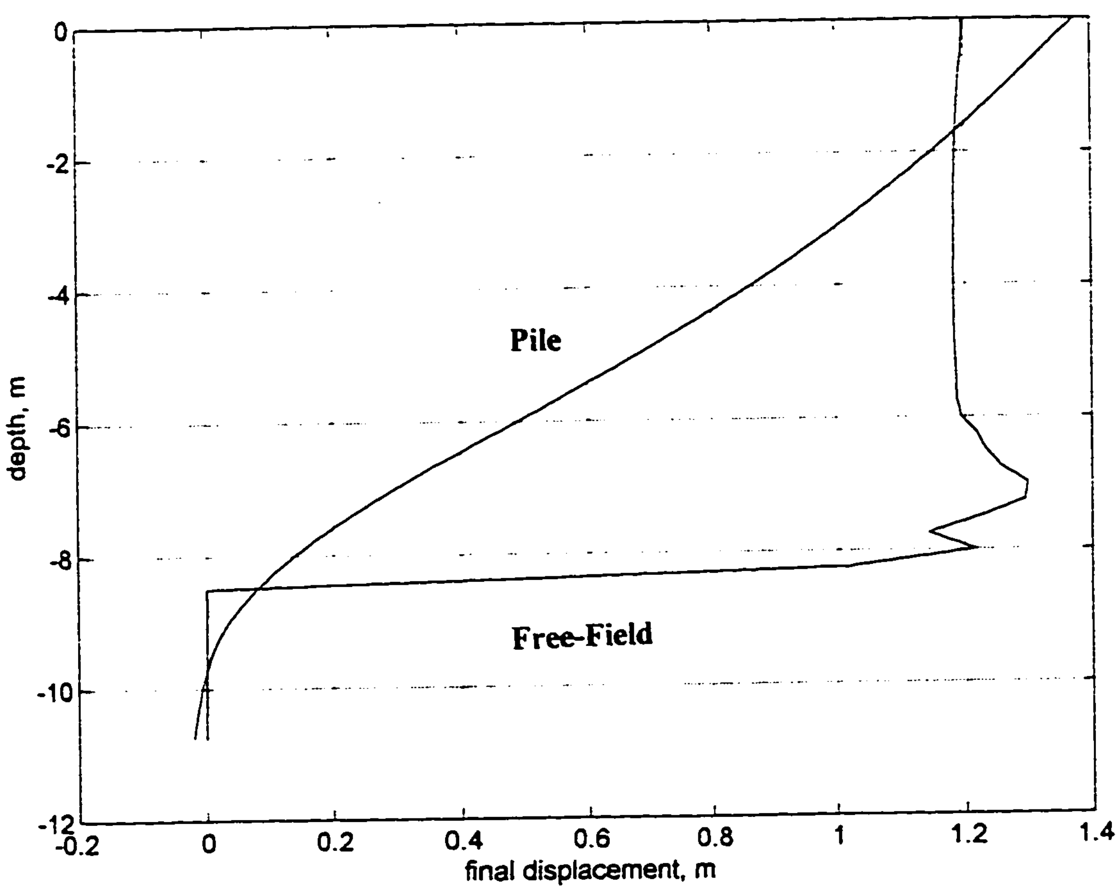


Figure 7.13 Computed pile and free-field displacements at the NHK Building site

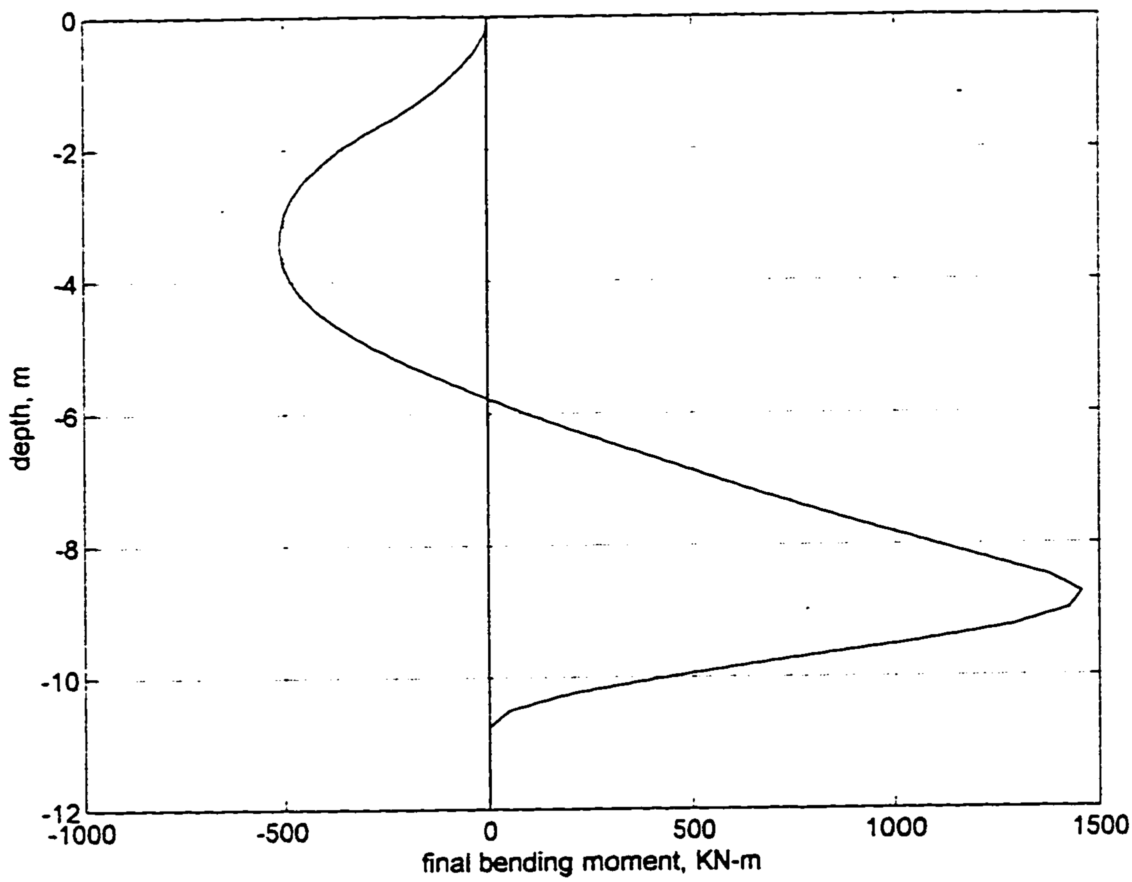


Figure 7.14 Computed pile bending moments at the NHK Building site

# Chapter 8 Summary and Conclusions

This dissertation has described the current state of knowledge regarding the effects of liquefaction-induced lateral spreading on pile foundations, and has presented a new methodology for evaluation of those effects. The research described in this dissertation and the conclusions that can be drawn from that research are described in the following sections. Finally, suggested topics for future research are described.

## 8.1 SUMMARY

The dissertation reviewed the phenomena that result in significant lateral soil movements during earthquakes in Chapter 2. The basic principles of liquefaction and cyclic mobility were described. The influence of initial shear stresses, residual shear strengths, and the relationship between those two quantities were discussed in detail. Several case histories involving liquefaction-induced lateral spreading were presented. The results of pertinent experimental research, including centrifuge and shaking table model tests, were reviewed. Empirical, semi-empirical, and analytical approaches to prediction of lateral spreading displacements were also described. Based on this literature review, the limitations of the existing state of knowledge on lateral spreading deformations were evaluated.

The response of piles to lateral loads was reviewed in Chapter 3. Static and dynamic loading were distinguished and considered. A series of case histories in which piles were damaged by liquefaction-induced lateral spreading during earthquakes were reviewed. The case histories involved sites in Alaska, California, Japan, and Costa Rica. Limitations in the certainty with all of the important parameters of the case histories were noted. Previous experimental investigations, including both shaking table and centrifuge tests, of the response of piles to lateral soil movements were described. The experimental investigations included studies of dynamic response and of the ultimate resistance of piles to soil movements. Analytical studies of the pile-soil interaction problem were also reviewed. Based on this literature review, the limitations of the existing state of knowledge on pile response to lateral soil movement was evaluated.

A one-dimensional ground response model was developed. The model was formulated to allow it to consider nonlinear, inelastic soil behavior, the effects of initial shear stresses on planes perpendicular to the direction of wave propagation, the generation of excess pore water pressure, and degradation of soil properties based on changes in effective stresses. The model can accept any backbone curve that describes nonlinear stress-strain behavior and incorporates the efficient Cundall-Pyke hypothesis for unloading-reloading behavior. Chapter 4 describes the development and verification of this model.

The development of a dynamic Winkler beam model for analysis of pile-soil interaction was described in Chapter 5. The model features nonlinear, inelastic p-y behavior in the near-field, time-domain representation of frequency-dependent radiation damping behavior in the far-field, and near- and far-field degradation based on changes in effective stresses. The model allows the use of any p-y curve and uses the Cundall-Pyke hypothesis for pile unloading-reloading behavior. The model was verified by comparison of its response with that of frequency domain solution for the case of linear p-y behavior.

An extensive parametric study was performed to evaluate the sensitivity of the ground response and pile-soil interaction models to a series of soil and pile characteristics. The results of these parametric analyses were described in Chapter 6. Free-field lateral spreading displacements were investigated with respect to ground surface slope, standard penetration resistance of the liquefiable soil, and groundwater table depth. Pile-soil interaction behavior was investigated with respect to ground surface slope, standard penetration resistance, groundwater table depth, pile flexural stiffness, pile diameter, pile length, and p-y curve stiffness.

The ground response and pile-soil interaction models were also validated by comparison with field observations. Two forms of field observations were used: (1) an empirical predictive relationship based on regression of a very large database of lateral spreading ground surface displacements, and (2) two case histories for which most, but not all, of the information needed for a detailed back-analysis were available.

## 8.2 CONCLUSIONS

The research described in this dissertation has considered the important problem of pile response in soil deposits subject to lateral spreading. After reviewing the state of knowledge in this area and developing and verifying new methods of analysis, the following conclusions can be drawn:

1. Lateral spreading has been observed in many past earthquakes. It is commonly observed in low-lying areas near bodies of water where significant deposits of loose, saturated granular soils are found.

2. Free-field displacements produced by lateral spreading vary widely, but have been shown to be influenced most strongly by the initial and residual shear strength of the liquefiable soil, the gradation of the liquefiable soils, the initial state of shear stress within the deposit, the earthquake magnitude, and the distance from the site to the fault rupture zone.

3. Empirical procedures are currently available for estimation of ground surface movements due to lateral spreading. However, these estimates have significant uncertainty, and are only considered accurate to within a factor of two for most sites.

4. The empirical procedures are based on large databases of observed field behavior that includes a wide variety of topographic conditions, soil conditions and earthquake loading conditions.

5. None of the existing procedures for estimation of lateral spreading displacements provide information regarding the distribution of displacements with respect to depth.

6. Lateral spreading displacements are driven by static shear stresses. Many sites can be idealized as infinite slopes which simplifies the analysis.

7. Lateral spreading has caused considerable damage to pile-supported structures in past earthquakes. The pile damage generally occurs as flexural failure which has often been observed near the top and bottom of the liquefied layer.

8. The flexural demands that are placed on a pile in soil undergoing lateral spreading are strongly influenced by the distribution of lateral soil movement with respect to depth.

9. Relatively simple one-dimensional ground response analyses can be conducted with initial static shear stresses on planes perpendicular to the direction of wave propagation. The initial state of shear stress can be computed analytically for infinite slopes and from multi-dimensional numerical models for other shapes. In a straight forward way, such ground response analyses can consider the parameters most important to lateral spread displacements.

10. The use of a Godunov-based numerical scheme provides a model that is second order accurate and able to resolve discontinuous strain fields and extremely large strain gradients.

11. The nonlinear stress-strain behavior of the soil and the generation of excess pore water pressures require that the ground response analyses be conducted in the time domain.

12. The dynamic Winkler beam formulation provides an attractive balance between generality and simplicity. It allows the main processes to be represented in a physically relevant manner.

13. Pile response is influenced by nonlinear, inelastic pile-soil interaction effects in the near-field and radiation damping effects in the far-field.

14. Pile response is also influenced by the generation of excess pore pressures during the earthquake. The pore water pressure influences both the near-field and the far-field response.

15. The nonlinear nature of pile-soil interaction requires that the analyses be conducted in the time domain.

16. Frequency-dependent radiation damping behavior can be represented over a significant range of frequencies using a discrete far-field model that allows computation of pile response in the time domain.

17. Lateral spread response is strongly-dependent on ground surface slope and soil strength, but relatively insensitive to groundwater table depth.

18. Pile displacement response to lateral spreading is strongly dependent on surface slope and soil strength, but relatively independent of groundwater table depth, pile flexural stiffness, pile diameter, pile length, and p-y curve stiffness.

19. Pile flexural response is strongly dependent on surface slope, soil strength, groundwater table depth, pile length, and pile flexural stiffness, but relatively independent of pile diameter and p-y curve stiffness.

20. The breadth of conditions that exist in databases from which empirical predictive relations for lateral spreading displacements complicates the interpretation of individual analyses.

21. The effect of surface slope on permanent displacements predicted by the proposed model is consistent with that predicted the empirical MLR method.

22. The consistency of the effect of liquefiable soil thickness given by the proposed and empirical methods is difficult to evaluate. The range of conditions that could exist in the empirical method database brackets the displacements predicted by the empirical method.

23. The ability of the proposed ground response model to predict observed free-field displacements of a specific cases history is limited, given the paucity of available data for those case histories. For the two cases studied in detail, free-field ground surface displacements were under-predicted.

24. For practical analyses of the effects of lateral spreading on pile foundations, the initial shear stresses can be scaled such that the ground response model produces the best estimate of the final ground surface displacement. In the absence of other data, the MLR model may be used to estimate these free-field displacements. This approach combines the ability of the proposed method to compute relative displacements throughout the thickness of a soil deposit with the ability of the MLR model to predict absolute ground surface displacements that are consistent with historical observations.

25. For the two case histories studied in detail, this procedure correctly predicted the occurrence and location of yielding.

26. The proposed model, by allowing computation of free-field displacements both at and below the ground surface and by considering the effects of those motions on the pile throughout earthquake shaking, offers a practical, rational tool for the evaluation of lateral spreading effects on pile foundations.

## 8.3 FUTURE RESEARCH DIRECTIONS

There are several avenues of further exploration that could add significantly to the knowledge gained in this research. The group effect on pile response was not addressed, and could have a strong influence on pile response at low center to center spacing. Additionally, the effect of pore pressure redistribution was not considered in the preceding analyses. Dissipating excess pore pressures could cause a temporary reduction in pile capacity at depth, and could also induce significant down-drag loads on a pile as the soil consolidates. The lateral spread response and pile response models could benefit from a multidimensional formulation. This would allow direct consideration of complex site geometry, group effects, directional effects of wave propagation, or flow around a pile. The parameters which control the rate of pore pressure generation are based on a limited number of laboratory tests. As such, the proposed model could be improved if the sensitivity of pore pressure response due to variations of these parameters were investigated further. The pile-soil interaction model would be improved if it were generalized to include nonlinear moment-curvature behavior. This would allow the procedure to more accurately predict the post-yield response of a pile to severe lateral spread displacements. The pile-soil interaction model could also be improved by considering a compliant mass at the pile head and large deflection or "P-Δ" effects within the pile. The former would allow for the consideration of pile-soil-structure interaction during dynamic loading while the latter would account for geometric nonlinearities.

Finally, more comprehensive field data is needed so that the proposed model can be calibrated in a more rigorous fashion. The required data includes measures of permanent lateral soil movements, pore pressure generation and dissipation, surface and down-hole strong motion accelerograms, pile displacements at and below the ground surface, and axial stresses along the length of the pile.

## Appendix A REFERENCES


Ambraseys, (1988), "Engineering Seismology," Earthquake Engineering and Structural Dynamics, v 17, pp 1-105

Arulanandan, K., and Scott, R.F., eds. (1994), "Verification of Numerical Procedures for the Analysis of Soil Liquefaction Problems," A.A. Balkema Publishers, ISBN 90 5410 360 4, v 1&2, pp 1-1801

Bardet, J.P., Oka, F., Sugito, M., and Yashima, A. (1995), "The Great Hanshin Earthquake Disaster, (The 1995 South Hyogo Prefecture Earthquake), Preliminary Investigation Report," February 10, 1995, pp 29-36

Bardet, J.P., Kapuskar, M., Martin, G.R., and Proubert, J. (1991), "Preliminary Results on the Dynamic Response of the Marina District of San Francisco During the Loma Prieta Earthquake," Proceedings from the Third Japan-US Workshop on Earthquake Resistant Design of Lifeline Facilities and Countermeasures for Soil Liquefaction, O'Rourke & Hamada ed., Technical Report NCEER-91-0001, pp 109-128

Bartlett, S.F., and Youd, T.L. (1992), "Case Histories of Lateral Spreads Caused by the 1964 Alaska Earthquake," Case Studies of Liquefaction and Lifeline Performance During Past Earthquakes, O'Rourke, T.D., and Hamada, M., ed., National Center for Earthquake Engineering Research, technical report NCEER-92-0002, v 2, c 2, pp 1-127

Bartlett, S.F. and Youd, T.L. (1992), "Empirical Prediction of Lateral Spread Displacement," Proceedings from the Fourth Japan-U.S. Workshop on Earthquake Resistant Design of Lifeline Facilities and Countermeasures for Soil Liquefaction, Hamada, M., and O'Rourke, T.D., ed., National Center for Earthquake Engineering Research, technical report NCEER-92-0019, pp 351-366

Baziar, M.H., Dobry, R., and Elgamal, A.W.M (1992), "Engineering Evaluation of Permanent Ground Deformations Due to Seismically-Induced Liquefaction," National Center for Earthquake Engineering Research, technical report NCEER-92-0007

Berg, G.V. (1989), Elements of Structural Dynamics, Prentice Hall, ISBN 0 13 272493 6, pp 76-77

Biot, M.A. (1956), "Theory of Propagation of Elastic Waves in a Fluid Saturated Porous Solid," Journal of the Acoustical Society of America, v 28, pp 168-191

Biot, M.A. (1962a), "Generalized Theory of Acoustic Propagation in Porous Dissipation Media," Journal of the Acoustical Society of America, v 34, pp 1254-1264

Biot, M.A. (1962b), "Mechanics of Deformation and Acoustic Propagation in Porous Media," Journal of Applied Physics, v 33, pp 1482-1498

Brandow, G.E., and Leeds, D.J. (1980), "Reconnaissance Report, Imperial County, California, Earthquake, October 15, 1979," Earthquake Engineering Resarch Institute, Berkeley, California

Cook, R.D. (1981), "Concepts and Applications of Finite Element Analysis, Second Edition," John Wiley & Sons, ISBN 0 471 03050 3, pp 455-472

Cox, W.R., Reese, L.C., and Grubbs, B.R. (1974), "Field Testing of Laterally Loaded Piles in Sand," Proceedings of the Sixth Annual Offshore Technology Conference, Houston, Texas

Dafalias, Y.F. (1994), "Overview of Constitutive Models Used in VELACS," Verification of Numerical Procedures for the Analysis of Soil Liquefaction Problems, Arulanandan & Scott (eds), A.A. Balkema Publishers, ISBN 90 5410 360 4, v 2, pp 1293-1303

Dobry, R., and Baziar, M.H., (1992), "Liquefaction and Ground Failure in the Imperial Valley, Southern California During the 1979, 1981, and 1987 Earthquakes," Case Studies of Liquefaction and Lifeline Performance During Past Earthquakes, O'Rourke, T.D., and Hamada, M., ed., National Center for Earthquake Engineering Research, technical report NCEER-92-0002, v 2, c 4, pp 1-85

Dobry, R., and Baziar, M.H., (1991), "Evaluation of Ground Deformation Caused by Lateral Spreading," Proceedings from the Third Japan-US Workshop on Earthquake Resistant Design of Lifeline Facilities and Countermeasures for Soil Liquefaction, O'Rourke & Hamada ed., Technical Report NCEER-91-0001, pp. 209-223

Earth Technology Corporation, (1981), "Full-Scale Pile Vibration Tests," NSF Grant PFR 7900193-A02

Egan, J.A., and Wang, Z.L, (1991), "Liquefaction-Related Ground Deformation and Effects on Facilities at Treasure Island, San Francisco, during the 17 October 1989 Loma Prieta Earthquake," Proceedings from the Third Japan-US Workshop on Earthquake Resistant Design of Lifeline Facilities and Countermeasures for Soil Liquefaction, O'Rourke & Hamada ed., Technical Report NCEER-91-0001, pp. 57-76

Elgamal, A.W., and Zeghal, M., "Analysis of Wildlife Site Liquefaction During the 1987 Superstition Hills Earthquake," Proceedings from the Fourth Japan-US. Workshop on Earthquake Resistant Design of Lifeline Facilities and Countermeasures for Soil Liquefaction, Hamada & O'Rourke ed., Technical Report NCEER-92-0019, pp 87-96

El Nagger, M.H., and Novak, M. (1994), "Non-Linear Model for Dynamic Axial Pile Response," Journal of Geotechnical Engineering, ASCE, v 120, n 2, pp 308-329

Fan, K., Gazetas, G., Kaynia, A., Kausel, E., and Ahmad, S. (1991), "Kinematic Seismic Response of Single Piles and Pile Groups," Journal of Geotechnical Engineering, ASCE, v 117, n 12, pp 1860-1879

Famiglietti & Prevost (1992), "Recent Work on Numerical Modeling of Flow Failure Induced by Soil Liquefaction," pp. 301-315, Proceedings from the Fourth Japan-US Workshop on Earthquake Resistant Design of Lifeline Facilities and Countermeasures for Soil Liquefaction, O'Rourke & Hamada ed., Technical Report NCEER-92-0019

Fiegel, G.L., and Kutter, B.L. (1994), "Liquefaction-Induced Lateral Spreading of Mildly Sloping Ground," Journal of Geotechnical Engineering, ASCE, v 120, n 12, pp 2236-2243

Finn, L. (1991), "Assessment of Liquefaction Potential and Post-Liquefaction Behavior of Earth Structures: Developments 1981-1991 (State of the Art Paper), Proceedings: Second International Conference on Recent Advances in Geotechnical Earthquake Engineering and Soil Dynamics, St. Louis, MO

Gazetas, G. (1991), "Foundation Vibrations," Foundation Engineering Handbook, 2nd Edition, Fang, H.Y., ed., Van Nostrand Reinhold

Glaser, S. (1993), "Estimating In-Situ Liquefaction Potential and Permanent Ground Displacements Due to Liquefaction for the Siting of Lifelines," NIST 5150, Building and Fire Research Laboratory, Department of Commerce

Grashuis, A.J., Dieterman, H.A., and Zorn, N.F. (1990), "Calculation of Cyclic Response of Laterally Loaded Piles," Computers and Geotechnics, v 10, n 4, pp 287-305

Gu, W.H., Morgenstern, N.R., and Robertson, P.K. (1994), "Post Earthquake Deformation Analysis of Wildlife Site," Journal of Geotechnical Engineering, ASCE, v 120 n 2, pp 274-289

Hamada, M., Sato, H. and Nakamura, T. (1994), "An Experimental and Numerical Study on Liquefaction-Induced Ground Displacement," Fifth U.S. National Conference of Earthquake Engineering, Chicago, v 4, pp 169-178

Hamada, M., Ohtomo, K., Sato, H., and Iwatate, T. (1992e), "Experimental Study of Effects of Liquefaction-Induced Ground Displacement on In-Ground Structures," Proceedings from the Fourth Japan-US. Workshop on Earthquake Resistant Design of Lifeline Facilities and Countermeasures for Soil Liquefaction, Hamada & O'Rourke ed., Technical Report NCEER-92-0019, pp 481-492

Hamada, M., Wakamatsu, K., and Yasuda, S. (1992d), "Liquefaction-Induced Ground Deformations During the 1923 Kanto Earthquake," Case Studies of Liquefaction and Lifeline Performance During Past Earthquakes, O'Rourke, T.D., and Hamada, M., ed., National Center for Earthquake Engineering Research, technical report NCEER-92-0002, v 1, c 1, pp 1-39

Hamada, M.,.Yasuda, S., and Wakamatsu, K (1992c), "Large Ground Deformations and Their Effects on Lifelines: 1948 Fukui Earthquake," Case Studies of Liquefaction and Lifeline Performance During Past Earthquakes, O'Rourke, T.D., and Hamada, M., ed., National Center for Earthquake Engineering Research, technical report NCEER-92-0002, v 1, c 2, pp 1-41

Hamada, M. (1992a), "Large Ground Deformations and Their Effects on Lifelines: 1964 Niigata Earthquake," Case Studies of Liquefaction and Lifeline Performance During Past Earthquakes, O'Rourke, T.D., and Hamada, M., ed., National Center for Earthquake Engineering Research, technical report NCEER-92-0002, v 1, c 3, pp 1-123

Hamada, M. (1992b), "Large Ground Deformations and Their Effects on Lifelines: 1983 Nihonkai-Chubu Earthquake," Case Studies of Liquefaction and Lifeline Performance During Past Earthquakes, O'Rourke, T.D., and Hamada, M., ed., National Center for Earthquake Engineering Research, technical report NCEER-92-0002, v 1, c 4, pp 1-85

Hamada, M., Towhata, I., Yasuda, S., and Isoyama, R. (1987), "Study on Permanent Ground Displacement Induced by Seismic Liquefaction," Computers and Geotechnics, Vol. 4, No. 4, pp. 197-220

Hungr, O. (1988), "Notes on Dynamic Analysis of Flowslides," Proceedings of the Fifth International Symposium on Landslides, Lausanne, Switzerland, v 1, pp 679-683

Ishihara, K., and Yoshimine, M. (1991), "Evaluation of Settlements in Sand Deposits Following Liquefaction During Earthquakes," Soils and Foundations, v 32, n 1, pp 173-188

Ishihara, K. (1993), "Liquefaction and flow Failure During Earthquakes," Geotechnique, v 43, n 3, pp 351-415

Joyner, W.B., and Boore, D.M. (1988), "Measurement, Characterization, and Prediction of Strong Ground Motion," Proceedings, Earthquake Engineering & Soil Dynamics, Park City, Utah, ASCE, pp 43-102

Joyner, W.B., and Chen, A.T.F. (1975), "Calculation of Nonlinear Ground Response in Earthquakes," Bulletin of the Seismological Society of America, v 65, n 5, pp 1315-1336

Kagawa, T., Minowa, C., Mizuno, H., and Abe, A. (1994), "Shaking Table Tests on Piles in Liquefying Sands," Fifth U.S. National Conference of Earthquake Engineering, Chicago, v 4, pp 107-116

Kagawa, T. (1992), "Lateral Pile Response in Liquefying Sand," Earthquake Engineering, Tenth World Conference, Balkema, pp 1761-1766

Kavvadas, M. and Gazetas, G. (1993), "Kinematic Seismic Response and Bending of Free-Head Piles in Layered Soil," Geotechnique, v 43, n 2, pp 207-222

Keane, C.M., and Prevost, J.H. (1991), "Preliminary Results of a Numerical Technique to Model Flow Failure Induced by Soil Liquefaction," Proceedings from the Third Japan-US Workshop on Earthquake Resistant Design of Lifeline Facilities and Countermeasures for Soil Liquefaction, O'Rourke & Hamada ed., Technical Report NCEER-91-0001, pp. 253-267

Kramer S.L. (1995), <u>Geotechnical Earthquake Engineering</u>, Prentice Hall

Lacy, S.J., Aubry, D., Benzenati, I., Modaressi, A., Roth, W., and Inel, S. (1994) "Overview of VELACS Model No. 2," Verification of Numerical Procedures for the Analysis of Soil Liquefaction Problems, Arulanandan, K., and Scott, R.F., eds. A.A. Balkema Publishers, ISBN 90 5410 360 4, v 2, pp 1369-1381

LeVeque, R.J. (1992), "Numerical Methods for Conservation Laws, Second Edition," Birkhauser

Liu, L, and Dobry, R. (1995), "Effect of Liquefaction on Lateral Response of Piles by Centrifuge Model Tests," National Center for Earthquake Engineering Research, NCEER Bulletin, v 9, n 1, pp 7-11

Makdisi, F., and Seed, H.B. (1978), "Simplified Procedure for Estimating Dam and Embankment Earthquake-Induced Deformations," Journal of the Geotechnical Engineering Division, ASCE, v 104, n 7, pp 849-867

Makris, N., and Gazetas, G. (1991), "Phase Wave Velocities and Displacement Phase Differences in a Harmonically Oscillating Pile," National Center for Earthquake Engineering Research, Technical Report NCEER-91-0010

Martin, G.R., Finn, W.D.L., and Seed, H.B. (1975), "Fundamentals of Liquefaction Under Cyclic Loading," Journal of the Geotechnical Engineering Division, ASCE, v 101, n 5, pp 423-438

Matlock, H., Foo, S.H.C., and Bryant, L.M. (1978), "Simulation of Lateral Pile Behavior Under Earthquake Motion," Proceedings of the ASCE Geotechnical Engineering Division Specialty Conference on Earthquake Engineering and Soil Dynamics, Pasadena, CA, v 2, pp 600-619

McCulloch, D.S., and Bonilla, M.G. (1970), "Effects of the Earthquake of March 27, 1964 on the Alaska Railroad," U.S.G.S. Professional Paper No. 545-D, Government Printing Office, Washington D.C.

Meyersohn, W.D. (1994), "Pile Response to Liquefaction-Induced Lateral Spread," Ph.D. thesis, School of Civil and Environmental Engineering, Cornell University, Ithaca, New York

Miura, F., and O'Rourke, T.D. (1991), "Nonlinear Analysis of Piles Subjected to Liquefaction-Induced Large Ground Deformation," Proceedings from the Third Japan-US Workshop on Earthquake Resistant Design of Lifeline Facilities and Countermeasures for Soil Liquefaction, O'Rourke and Hamada ed., Technical Report NCEER-91-0001, pp 497-512

Miyajima, Kitaura, and Ando, (1991), "Experiments on Liquefaction-Induced Large Ground Deformation", Proceedings from the Third Japan-US Workshop on Earthquake Resistant Design of Lifeline Facilities and Countermeasures for Soil Liquefaction, O'Rourke and Hamada ed., Technical Report NCEER-91-0001, pp 269-292

Newmark, N.M. (1965), "Effect of Earthquakes on Dams and Embankments," Geotechnique, Vol. 5, No. 2, pp 139-160

Nogami, T., and Konagai, K. (1989), "Time Domain Flexural Response of Dynamically Loaded Single Piles," Journal of Engineering Mechanics, ASCE, v 114, n 9, pp 1512-1525

Nogami, T., and Konagai, K. (1986), "Time Domain Axial Response of Dynamically Loaded Single Piles," Journal of Engineering Mechanics, ASCE, v 112, n 11, pp 1241-1252

Nogami, T., Konagai, K., and Otani, J.(1986), "Time Domain Response Analysis of Nonlinear Deep Foundations Subjected to Axial Dynamic Load," Proceedings of the Third U.S. National Conference on Earthquake Engineering, Charleston, SC, pp 647-658

Nomura, S., Tokimatsu, K., and Shamoto, Y. (1991), "Soil-Pile-Structure Interaction During Liquefaction," Proceedings of the Second International Conference on Recent Advances in Geotechnical Earthquake Engineering and Soil Dynamics, Prakash, S., ed., St. Louis, pp 742-750

Novak, M. (1993), "Pile-Soil-Pile Interaction Under Small and Large Displacements," Developments in Dynamic Soil Structure Interaction, Bulkan, P., and Clough, R.W., eds., Kluwer Academic Publishers, pp 361-380

Novak, M. (1991), "Piles Under Dynamic Loads," Proceedings, Second International Conference on Recent Advances in Geotechnical Earthquake Engineering and Soil Dynamics, Prakash, S., ed., St. Louis, v 3, pp 2433-2455

Ohtomo, K., and Hamada, M. (1994), "Soil force Acting on Pile in Laterally Flowing Ground by Soil Liquefaction," Fifth U.S. National Conference of Earthquake Engineering, Chicago, v 4, pp 241-250

O'Rourke, T.D., Beaujon, P.A., and Scawthorn, C.R. (1992), "Large Ground Deformations and Their Effects on Lifeline Facilities: 1906 San Francisco Earthquake," Case Studies of Liquefaction and Lifeline Performance During Past Earthquakes, O'Rourke, T.D., and Hamada, M., ed., National Center for Earthquake Engineering Research, technical report NCEER-92-0002, v 2, c 1, pp 1-130

O'Rourke, T.D., and Roth, B.L. (1992), "Large Ground Deformations and Their Effects on Lifeline Facilities: 1971 San Fernando Earthquake," Case Studies of Liquefaction and Lifeline Performance During Past Earthquakes, O'Rourke, T.D., and Hamada, M., ed., National Center for Earthquake Engineering Research, technical report NCEER-92-0002, v 2, c 3, pp 1-85

O'Rourke, T.D., and Pease, J.W. (1992), "Large Ground Deformations and Their Effects on Lifeline Facilities: 1989 Loma Prieta Earthquake," Case Studies of Liquefaction and Lifeline Performance During Past Earthquakes, O'Rourke, T.D., and Hamada, M., ed., National Center for Earthquake Engineering Research, technical report NCEER-92-0002, v 2, c 5, pp 1-85

Orense & Towhata, (1992), "Prediction of Liquefaction-Induced Permanent Ground Displacements: A Three Dimensional Approach," Proceedings from the Fourth Japan-US Workshop on Earthquake Resistant Design of Lifeline Facilities and Countermeasures for Soil Liquefaction, O'Rourke and Hamada ed., Technical Report NCEER-92-0019, pp 335-349

Pyke, R. (1979), "Nonlinear Soil Models for Irregular Cyclic Loadings," Journal of the Geotechnical Engineering Division, ASCE, v 105, n 6, pp 715-726

Reese, L.C., Cox, W.R., and Koop, F.D. (1974), "Analysis of Laterally Loaded Piles in Sand," Proceedings of the Sixth Annual Offshore Technology Conference, Houston, Texas

Roth, W.H., Fong, H., and DeRubertis, C. (1992), "Batter Piles and the Seismic Performance of Pile-Supported Wharves," Ports 92 Conference, Torseth, D., ed., ASCE, v1, pp 336-349

Sasaki, Tokaida, Matsumoto, and Saya, (1991) "Shake Table Tests on Lateral Ground Flow Induced by Soil Liquefaction," Proceedings from the Third Japan-US Workshop on Earthquake Resistant Design of Lifeline Facilities and Countermeasures for Soil Liquefaction, O'Rourke and Hamada ed., Technical Report NCEER-91-0001, February 1, 1991, pp 371-385

Sato, H. Hamada, M., and Doi, M., (1994), "A Study on Mechanical Properties of Liquefied Soil as a Fluid," Fifth U.S. National Conference of Earthquake Engineering, Chicago, v 4, pp 189-198

Seed, H.B., Idriss, I.M., Arango, I. (1983), "Evaluation of Liquefaction Potential Using Field Performance Data," Journal of Geotechnical Engineering, ASCE, v 109, n 3, pp 458-482

Seed, H.B. and Wilson, S.D. (1967), "Turnagain Heights Landslide," Journal of the Soil Mechanics and Foundation Divsion, ASCE, vol 93, no 7, pp 1053-1122

Shiomi, T., Shigeno, Y., Sugimoto, M., Suzuki, Y. (1992), "Influence of Liquefaction to Pile-Soil-Structure Interaction," Takenaka Technical Research Report, n 47, pp 99-117

Shiomi, T., Tsukuni, S., Hatanaka, M., Tanaka, Y., Suzuki, Y., and Hirose, T. (1987), "Simulation Analysis of Ground Liquefaction Induced by Earthquake," Computers and Geotechnics, Vol. 4, No. 4, pp. 221-245

Sladen, J.A., D'Hollander, R.D. and Krahn, J. (1985), "The Liquefaction of Sands, a Collapse Surface Approach," Canadian Geotechnial Journal, v 22, pp 564-578

Slyh, R.J., and Jackura, K.A. (1993), "Soil-Pile Interaction Effects on Modifying Free Field Motion of Soft Soil Sites," Proceedings of the Second Annual Seismic Research Workshop, California Department of Transportation, Sacramento

Succarieh, M.F., and Elgamal, A.W.M. (1991), "Seismically Induced Stick-Slip Large Displacements in Earth Structures," Proceedings from the Third Japan-US Workshop on Earthquake Resistant Design of Lifeline Facilities and Countermeasures for Soil Liquefaction, O'Rourke and Hamada ed., Technical Report NCEER-91-0001, pp 317-332

Taylor, R.N., ed. (1995), Geotechnical Centrifuge Technology, by Blackie Academic and Professional, an imprint of Chapman & Hall, Glasgow

Ting, J.M., Kauffman, C.R., and Lovicsek, M. (1987), "Centrifuge Static and Dynamic Lateral Pile Behavior," Canadian Geotechnical Journal, v 24, no 2, pp 198-207

Tokida, K., Matsumoto, H., and Iwasaki, H. (1992), "Experimental Study on Drag Acting on Piles in Ground Flowing by Soil Liquefaction," Proceedings from the Fourth Japan-US. Workshop on Earthquake Resistant Design of Lifeline Facilities and Countermeasures for Soil Liquefaction, Hamada & O'Rourke ed., Technical Report NCEER-92-0019, pp 511-523

Tokimatsu, K., Kojima, H., Kuwayama, S, Abe, A, and Midorikawa, S. (1994), "Liquefaction-Induced Damage to Buildings in 1990 Luzon Earthquake," Journal of Geotechnical Engineering, ASCE, v 120, n 2, pp 290-307,

Tokimatsu, K, and Seed, H.B. (1987), "Evaluation of Settlements in Sands Due to Earthquake Shaking," Journal of Geotechnical Engineering, ASCE, v 113, n 8, pp 861-878

Towhata & Matsumoto (1992), "Analysis on Development of Permanent Displacement with Time in Liquefied Ground," Proceedings from the Fourth Japan-US Workshop on Earthquake Resistant Design of Lifeline Facilities and Countermeasures for Soil Liquefaction, O'Rourke and Hamada ed., Technical Report NCEER-92-0019, pp 285-299

Towhata, Tokaida, Tamari, Matsumoto, and Yamada, (1991), "Prediction of Permanent Lateral Displacement of Liquefied Ground by Means of Variational Principle," Proceedings from the Third Japan-US Workshop on Earthquake Resistant Design of Lifeline Facilities and Countermeasures for Soil Liquefaction, O'Rourke and Hamada ed., Technical Report NCEER-91-0001, pp 237-251

Vucetic, M., and Zorapapel, G.T. (1991), "The Effects of Liquefaction Process on the Spectral Content of Strong Ground Motion," Proceedings from the Third Japan-US Workshop on Earthquake Resistant Design of Lifeline Facilities and Countermeasures for Soil Liquefaction, O'Rourke and Hamada ed., Technical Report NCEER-91-0001, pp 403-418

Wakamatsu, K., Yoshida, N., Suzuki, N., and Tazoh, T. (1992), "Liquefaction-Induced Large Ground Deformations and Their Effects on Lifelines During the 1990 Luzon, Philippines Earthquake," Case Studies of Liquefaction and Lifeline Performance During Past Earthquakes, O'Rourke, T.D., and Hamada, M., ed., National Center for Earthquake Engineering Research, technical report NCEER-92-0002, v 1, c 5, pp 1-52

Wang, Z.L., Dafalias, Y.F., and Shen, C.K. (1990), "Bounding Surface Hypoplasticity Model for Sand," Journal of Engineering Mechanics, ASCE, v 116, n 5, pp 983-1001

Yasuda, S., Nagase, H. Kiku, H., Uchida, Y., and Kiyota, M. (1992), "Shaking Table Tests on Countermeasures Against Large Ground Displacement due to Liquefaction," Proceedings from the Fourth Japan-US. Workshop on Earthquake Resistant Design of Lifeline Facilities and Countermeasures for Soil Liquefaction, Hamada & O'Rourke ed., Technical Report NCEER-92-0019, pp 367-380

Yasuda, S., Nagase, H., Kiku, H., and Uchida Y., (1991), "A Simplified Procedure for the Analysis of the Permanent Ground Displacement," Proceedings from the Third Japan-US. Workshop on Earthquake Resistant Design of Lifeline Facilities and Countermeasures for Soil Liquefaction, O'Rourke & Hamada ed., Technical Report NCEER-91-0001, pp. 225-236

Yegian, M.K., Ghanhraman, V.G., and Harutiunyan, R.N. (1994), "Liquefaction and Embankment Failure Case Histories, 1988 Armenia Earthquake," Journal of Geotechnical Engineering, ASCE, v 120, n 3, pp 581-596

Yegian, M.K., Ghanhraman, V.G., and Gazetas, G. (1994), "Ground Motion and Soil Response Analysis for Leninakan, 1988 Armenia Earthquake," Journal of Geotechnical Engineering, ASCE, v 120, n 2, pp 330-348

Youd, T.L., and McMullin, S.R. (1991),"Ground Deformation in Anchorage During the 1964 Alaska Earthquake," Proceedings from the Third Japan-US Workshop on Earthquake Resistant Design of Lifeline Facilities and Countermeasures for Soil Liquefaction, O'Rourke & Hamada ed., Technical Report NCEER-91-0001, pp 93-107

Youd T.L, and Perkins, (1987), "Mapping of Liquefaction Severity Index," Journal of Geotechnical Engineering, ASCE, Vol. 113, No. 11, pp. 1374-1392

Yoshida, N., Watanabe, H., Yasuda, S., and S. Mora, C. (1992) "Liquefaction-Induced Ground Failure and Related Damage to Structures During 1991 Telire-Limon, Costa Rica, Earthquake," Proceedings from the Fourth Japan-US. Workshop on Earthquake Resistant Design of Lifeline Facilities and Countermeasures for Soil Liquefaction, Hamada & O'Rourke ed., Technical Report NCEER-92-0019, pp 37-52

Yoshida, N., and Hamada, M. (1991), "Damage to Foundation Piles and Deformation Pattern of Ground due to Liquefaction-Induced Permanent Ground Deformations," Proceedings from the Third Japan-US Workshop on Earthquake Resistant Design of Lifeline Facilities and Countermeasures for Soil Liquefaction, O'Rourke & Hamada ed., Technical Report NCEER-91-0001, pp 147-161

Yoshikawa, M., and Arano, M. (1988), "Dynamic Behavior of Model Pile Foundation Ground Systems in the Liquefaction Process," Proceedings of the Ninth World Conference on Earthquake Engineering, Tokyo, Kyoto, v 3, pp 599-604

Zienkiewicz, O.C., and Shiomi, T. (1984), "Dynamic Behavior of Saturated Porous Media: The Generalized Biot Formulation and its Numerical Solution," International Journal for Numerical and Analytical Methods in Geomechanics, v 8, pp 71-96

Zienkiewicz, O.C., Chang, C.T., and Hinton, E. (1978), "Non-Linear Seismic Response and Liquefaction," International Journal for Numerical and Analytical Methods in Geomechanics, v 2 p 381-404

## Appendix B: FORTRAN Listing - Lateral Spreading Response Code

```
cccccccccccccccccccccccccccccccccccccccccccccccccccccccccccccccccccccccc
c Program WAVE
c University of Washington
c John Horne and Professor Steven Kramer
c 1996
cccccccccccccccccccccccccccccccccccccccccccccccccccccccccccccccccccccccc
      program driver
      implicit double precision (a-h,o-z)
      parameter (maxmx = 50)        !# maxinum number of soil elements
      parameter (meqn = 2)          !# 2nd order PDE (a system of 2 first order PDE's)
      parameter (mwaves = 2)        !# number of eigenvalues
      parameter (mbc = 2)           !# number of bc ghost cells at either end of
c                                   !# computational domain
      parameter (maux = 3)          !# density, wave speed, and shear modulus
      parameter (mwork = 8064)      !# work space size
      parameter (nsoil = 2)         !# maximum number of soil layers
      parameter (nptsmax = 71)      !# max number of t-g pairs per curve
      parameter (maux2  = 14)       !# max number of soil parameters for constitutive
c                                   !# model and 1D consolidation model
c
      dimension q(1-mbc:maxmx+mbc, meqn)
      dimension aux(1-mbc:maxmx+mbc, maux)
      dimension work(mwork)
      dimension x(1-mbc:maxmx+mbc)
      dimension mthlim(mwaves),method(7),dtv(5),cflv(4),nv(2)
      dimension rho(nsoil),g(nsoil),h(nsoil),xif(nsoil)
      dimension beo(nsoil),bemin(nsoil),bnu(nsoil)
      dimension br1(nsoil),bn1(nsoil),bq(nsoil),bdeg(nsoil)
      dimension bnblow(nsoil),bko(nsoil),bm(nsoil)
      dimension cv(nsoil),ck(nsoil),cr(nsoil)
      dimension disp(maxmx),ru(maxmx),dtau(2,maxmx),sold(maxmx)
      dimension u(1-mbc:maxmx+mbc)
      dimension vold(maxmx),told(maxmx),tnew(maxmx),gmod(maxmx)
      dimension tbb0(maxmx,nptsmax),gbb0(maxmx,nptsmax)
      dimension tbb(maxmx,nptsmax),gbb(maxmx,nptsmax)
      dimension tcur(maxmx,nptsmax),gcur(maxmx,nptsmax),strn(maxmx)
      dimension deg(maxmx),auxmat(maxmx,maux2)
      dimension sigvtot(maxmx),sigveff(maxmx),ffu(maxmx),tau0(maxmx)
      dimension sigvold(maxmx)
      integer*2 mh1,mm1,ms1,md1,mh2,mm2,ms2,md2
      character bcutop*6,bcubot*6
c
```

```
      common /bcsrc/ beta,grav
      common /bedrock/ vbr
c
      open(21,file='soil.dat',status='unknown',form='formatted')
      open(22,file='tgcurve.dat',status='unknown',form='formatted')
      open(23,file='quak.dat',status='unknown',form='formatted')
      open(24,file='c_velo.ini',status='unknown',form='formatted')
      open(25,file='c_strs.ini',status='unknown',form='formatted')
      open(26,file='c_disp.ini',status='unknown',form='formatted')
c
      open(30,file='echo.out',status='unknown',form='formatted')
      open(31,file='depth.out',status='unknown',form='formatted')
      open(32,file='velo.out',status='unknown',form='formatted')
      open(33,file='stress.out',status='unknown',form='formatted')
      open(34,file='disp.out',status='unknown',form='formatted')
      open(35,file='strain.out',status='unknown',form='formatted')
      open(36,file='gmod.out',status='unknown',form='formatted')
      open(37,file='pore.out',status='unknown',form='formatted')
      open(38,file='diffuse.out',status='unknown',form='formatted')
cccccccccccccccccccccccccccccccccccccccccccccccccccccccccccccccccccc
cccccccccccccccccccccccccccccccccccccccccccccccccccccccccccccccccccc
cccc -------------------------------------------------------- ccccccccc
cccc  PROBLEM DEFINITION AND INITIALIZATION SECTION  ccccccccc
cccc -------------------------------------------------------- ccccccccc
cccccccccccccccccccccccccccccccccccccccccccccccccccccccccccccccccccc
cccccccccccccccccccccccccccccccccccccccccccccccccccccccccccccccccccc
      write(*,*) 'input gravity and unit weight of water'
      read(21,*) grav,gamh2o        !# Units:  L/T^2 and F/L^3, respec.
      write(*,*) grav,gamh2o
c
      write(*,*) 'input ax, bx'
      read(21,*) ax,bx              !# Units: L and L, respec.
      write(*,*) ax,bx
c
      write(*,*) 'input number of soil layers, nlayer'
      read(21,*)nlayer
      write(*,*)nlayer
      if(nlayer.gt.nsoil)then
        write(*,*)'NUMBER OF SOIL LAYERS EXCEEDS ARRAY DIMENSION'
        write(*,*)'TO FIX, DO ONE OF THE FOLLOWING:'
        write(*,*)'  1) reduce the number of soil layers so that'
        write(*,*)'     nlayer is no greater than ',nsoil
        write(*,*)'  2) recompile the source code with an increased'
        write(*,*)'     value for nsoil'
```

```
   goto 200
  endif
c
  write(*,*) 'input layer thicknesses'
  read(21,*) (h(n), n=1,nlayer)              !# Units:  L
  write(*,*) (h(n), n=1,nlayer)
c
  write(*,*) 'input layer shear moduli'
  read(21,*) (g(n), n=1,nlayer)          !# Units: F/L^2
  write(*,*) (g(n), n=1,nlayer)
c
  write(*,*) 'input layer densities'
  read(21,*) (rho(n), n=1,nlayer)          !# Units: FT^2/L^4
  write(*,*) (rho(n), n=1,nlayer)
c
  write(*,*) 'input layer coefficients of consolidation'
  read(21,*) (cv(n), n=1,nlayer)          !# Units: L^2/T
  write(*,*) (cv(n), n=1,nlayer)
  cvmax = 0.d0
  do 42 n=1,nlayer
   cvmax = dmax1(cvmax,cv(n))
42   continue
c
  write(*,*) 'input layer permeabilities'
  read(21,*) (ck(n), n=1,nlayer)          !# Units: L/T
  write(*,*) (ck(n), n=1,nlayer)
c
  write(*,*) 'input layer rebound moduli'
  read(21,*) (cr(n), n=1,nlayer)          !# Units: dimensionless
  write(*,*) (cr(n), n=1,nlayer)
c
  write(*,*) 'input drainage boundary conditions'
  read(21,*)bcutop,bcubot
  write(*,*)bcutop,bcubot
c
  write(*,*) 'input tend and tcon'
  read(21,*) tend,tcon               !# Units: T
  write(*,*) tend,tcon
c
  write(*,*) 'input dxi, dti'
  read(21,*) dxi,dti                 !# Units: L and T, respec.
  write(*,*) dxi,dti
c
  write(*,*) 'input nout, the number of output points desired'
```

```
      read(21,*) nout
      write(*,*) nout
c
c     comnpute the consolication time step and the number of time steps
c     beyond the earthquake to compute the consolidation response
c
      dtcon = 0.1d0*dxi**2.d0/cvmax
      ncon  = max(1,idint((tcon-tend)/dtcon))
      write(*,*)' '
      write(*,*)'Number of Post-EQ Consolidation Time Steps: ',ncon
      write(*,*)' '
c
c     determine the maximum dt based on the initial wave speeds
c     and the desired cfl condition.  NOTE:  this assumes that
c     for nonlinear runs, the shear moduli will never be greater
c     than it's initial value.
c
      smax = 0.d0      !# maxinum wave speed of the layered deposit
      do 44 n=1,nlayer
        if(dsqrt(g(n)/rho(n)).gt.smax) smax = dsqrt(g(n)/rho(n))
 44   continue
      dtmax = dmin1(0.95d0*dxi/smax,dtcon)  !# maxinum dt such that cfl .le. 0.95
c                                           !# and consolidation equation time
c                                           !# step is not exceeded
      ndiv = max(1,idint(dti/dtmax)+1)      !# number of divisions to achieve this
      dtcfl = dti / dfloat(ndiv)            !# new dt based on cfl condition
      write(*,*)'done recomputing time step based on CFL and consol...'
      write(*,*)'    initial dt ',dti
      write(*,*)'          ndiv ',ndiv
      write(*,*)' recomputed dt ',dtcfl
c
      write(*,*) 'input slope angle'        !# Units:  degrees
      read(21,*) beta
      write(*,*) beta
c
c     determine what type of material behavior is desired
c
      write(*,*)'input material analysis type'
      read(21,*)ntype
      if(ntype.eq.1) then
        write(*,*)'linear run: initial shear moduli remain constant'
      elseif(ntype.eq.2) then
        write(*,*)'nonlinear run: hysteretic tracking and degradation'
      elseif(ntype.eq.3) then
```

```
      write(*,*)'nonlinear run: stress-path constitutive model'
     endif
c
c    determine the type of loading the soil deposit will be subjected to
c
     write(*,*)'input earthquake data type'
     read(21,*)nquake
     if(nquake.eq.1) then
      read(21,*) f                    !# Units:  1/T
      write(*,*)'harmonic bedrock motion - freqency (hz) = ',f
     elseif(nquake.eq.2) then
      write(*,*)'bedrock velocities read from input file'
     endif
c
c    initialize some variables (most are passed to the CLAW1 subroutine)
c
     pi = 4.d0*datan(1.d0)        !# 3.14...
     amp = 1.d0                   !# desired displacement amplitude (nquake=1 only)
     vbr1 = 0.d0                  !# bedrock velocity at t
     vbr2 = 0.d0                  !# bedrock velocity at t+dti
     t0 = 0.d0                    !# initial time
     cflv(1) = 1.0d0              !# largest cfl to allow before rejecting step
     cflv(2) = 0.95d0             !# desired cfl
     dtv(1) = dtcfl               !# dt to try in first step
     dtv(2) = dtcfl               !# dt can not be greater than the initial time step
     nv(1) = 500                  !# maximum number of time steps allowed
c
c    see CLAW1 comment statments for background of method(n) array
c
     method(1) = 0        !# variable time stepping is NOT envoked (dt is adjusted
c                         !# initially above, and remains constant throughout the analysis)
     method(2) = 2        !# 2nd order correction terms added
     method(4) = 0        !# don't print dt and cfl every time step
     method(5) = 1        !# source term is active (from initial shear stresses)
     method(6) = 0        !# no capacity function is used
     method(7) = 3        !# auxiliary variables for rho, c, and G
c                          # aux(i,1) = density rho in i'th cell
c                          # aux(i,2) = sound speed c in i'th cell
c                          # aux(i,3) = shear modulus gmod in i'th cell
c
c    see function PHILIM and subroutine CLAW1 comment statements for
c    details on limiters
c
     mthlim(1) = 1     !# minmod limiter for 1-wave
```

```
      mthlim(2) = 1     !# ditto for 2-wave
      dx = dxi
      mx= (bx - ax + 1d-12)/dx
c
c     Initialize grid, material properties, and dependent variables
c
      xtot = 0.d0
      do 5 n=1,nlayer
       xtot = xtot + h(n)
       xif(n)=xtot
       write(*,*)' INTERFACE ELEVATION: ',n,' IS ',xif(n)
 5     continue
c
       do 12 i=1-mbc,mx+mbc
        x(i) = ax + (i-0.5d0) * dx
        do 10 n=1,nlayer
         if (x(i).lt.xif(n)) then
          aux(i,1) = rho(n)                !# density
          aux(i,2) = dsqrt(g(n)/rho(n))    !# wave speed
          aux(i,3) = g(n)                  !# shear modulus
          goto 11
         endif
 10     continue
 11     continue
 12     continue
c
      aux(mx+1,1) = aux(mx,1)          !# same as the previous soil layer
      aux(mx+1,2) = aux(mx,2)
      aux(mx+1,3) = aux(mx,3)
      aux(mx+2,1) = aux(mx,1)          !# same as the previous soil layer
      aux(mx+2,2) = aux(mx,2)
      aux(mx+2,3) = aux(mx,3)
      write(*,*)'done initializing aux(i,m) and x(i) arrays'
      write(31,1000) (x(i), i=1,mx)
 1000 format(100e15.8)
c
      write(*,*)' '
      write(*,*)'Reading Initial Velocity Profile'
      read(24,*)(q(i,2), i=1,mx)       !# intial velocity profile
c
      write(*,*)' '
      write(*,*)'Reading Initial Shear Stress Profile'
      read(25,*)(q(i,1), i=1,mx)       !# initial shear stress profile
c
```

```
      write(*,*)' '
      write(*,*)'Reading Initial Displacement Profile'
      read(26,*)(disp(i), i=1,mx)        !# initial displacement profile
c
      do 15 i=1,mx
c
       told(i) = 0.d0
       tnew(i) = q(i,1)
       tau0(i) = q(i,1)
       dtau(1,i) = 0.d0
       dtau(2,i) = q(i,1)
c
       vold(i) = q(i,2)
       u(i) = 0.d0
       ru(i)= 0.d0
 15    continue
      t1 = 0.d0
      t2 = 0.d0
      t3 = 0.d0
      t4 = 0.d0
ccccccccccccccccccccccccccccccccccccccccccccccccccccccccccccccccccccccc
c  initialize the t-g curves and degradation parameters if the
c  hysteretic model is used
ccccccccccccccccccccccccccccccccccccccccccccccccccccccccccccccccccccccc
      if(ntype.eq.2) then
c
c      input material properites for the layers
c
       read(21,*)xgwt                             !# groundwater table depth
       read(21,*) (beo(n),   n=1,nlayer)          !# initial void ratio
       read(21,*) (bemin(n), n=1,nlayer)          !# minimum void ratio
       read(21,*) (bnu(n),   n=1,nlayer)          !# parameter "nu"
       read(21,*) (br1(n),   n=1,nlayer)          !# parameter "r1"
       read(21,*) (bn1(n),   n=1,nlayer)          !# parameter "n1"
       read(21,*) (bq(n),    n=1,nlayer)          !# parameter "q"
       read(21,*) (bdeg(n),  n=1,nlayer)          !# parameter "n_deg"
       read(21,*) (bnblow(n),  n=1,nlayer)        !# (N1)60_ys (SPT N, corrected
c                                                 !# for overburden, energy, and
c                                                 !# (yield-strength) fines content)
       read(21,*) (bko(n),   n=1,nlayer)          !# lateral earth pressure coeff.
       read(21,*) (bm(n),    n=1,nlayer)          !# slope of q-p' envelope
c
c      assign material properties and effective stresses from the layers to the grid
c
```

```
c     first layer...
c
      sigvtot(1)  = aux(i,1)*grav*dx/2.d0              !# total stress
      ffu(1)      = max((gamh2o*(x(1)-xgwt)),0.d0)    !# initial pore pressure
      sigveff(1)  = sigvtot(1) - ffu(1)                !# effective stress
      auxmat(1,1)  = beo(1)                            !# initial void ratio
      auxmat(1,2)  = bemin(1)                          !# minimum void ratio
      auxmat(1,3)  = sigveff(1)                        !# initial effective stress
      auxmat(1,4)  = bnu(1)                            !# pore pressure model param
      auxmat(1,5)  = br1(1)                            !#     ditto
      auxmat(1,6)  = bn1(1)                            !#     ditto
      auxmat(1,7)  = bq(1)                             !#     ditto
      auxmat(1,8)  = bdeg(1)                           !# degradation exponent
c      auxmat(1,9)  = .001d0*bnblow(1)*sigveff(1)/bm(1)  !# critical state p'
c                                                        !# (based on critical
c                                                        !# state shear strength
c                                                        !# correlation of Stark &
c                                                        !# Mesri, '92)
      auxmat(1,9)  = (10.d0+0.15d0*(bnblow(1))**2.d0)/bm(1)     !# ~upper bound
c                                                               !# critical state p'
c                                                               !#(based on critical
c                                                               !# state shear strength
c                                                               !# of Seed & Harder,
c                                                               !# '90)
c      auxmat(1,9)   = bnblow(1)/bm(1)   !# here, bnblow is interpreted as tau_cs = q_cs
      auxmat(1,10) = bko(1)                   !# lat. earth press. coef.
      auxmat(1,11) = bm(1)                    !# slope of q-p' envelope
      auxmat(1,12) = cv(1)                    !# coeff. of consol.
      auxmat(1,13) = ck(1)                    !# permeability
      auxmat(1,14) = cr(1) / ( 1.d0 + beo(1) ) !# modified rebound modulus
      if(x(1).lt.xgwt)then                !# then we don't want degredation
       auxmat(1,1) = auxmat(1,2)
       auxmat(1,8) = 0.d0
      endif
c
c     ... and subsequent layers
c
      do 25 i=2,mx
       ffu(i) = max((gamh2o*(x(i)-xgwt)),0.d0)              !# initial pore pressure
       sigvtot(i)=sigvtot(i-1)+(aux(i-1,1)+aux(i,1))*grav*dx/2.d0  !# total stress
       sigveff(i) = sigvtot(i) - ffu(i)                    !# effective stress
       auxmat(i,3) = sigveff(i)                            !# initial effective stress
       do 20 n=1,nlayer
        if(x(i).lt.xif(n))then
```

```
          auxmat(i,1)  = beo(n)                          !# initial void ratio
          auxmat(i,2)  = bemin(n)                        !# minimum void ratio
          auxmat(i,4)  = bnu(n)                          !# pore pressure model param
          auxmat(i,5)  = br1(n)                          !#    ditto
          auxmat(i,6)  = bn1(n)                          !#    ditto
          auxmat(i,7)  = bq(n)                           !#    ditto
          auxmat(i,8)  = bdeg(n)                         !# degradation exponent
c          auxmat(i,9)  = .005d0*bnblow(n)*sigveff(n)/bm(n)        !# S&M '92
          auxmat(i,9)  = (10.d0+0.15d0*(bnblow(n))**2.d0)/bm(n)  !# S&H, '90
c          auxmat(i,9)  = bnblow(i)/bm(i)  !# here, bnblow is interpreted as tau_cs = q_cs
          auxmat(i,10) = bko(n)                          !# lat. earth press. coef.
          auxmat(i,11) = bm(n)                           !# slope of q-p' envelope
          auxmat(i,12) = cv(n)                           !# coeff. of consol.
          auxmat(i,13) = ck(n)                           !# permeability
          auxmat(i,14) = cr(n) / ( 1.d0 + beo(n) )           !# modified rebound modulus
          goto 21
        endif
 20     continue
 21     continue
       if(x(i).lt.xgwt)then              !# we're above the gwt!!!
        auxmat(i,1)=auxmat(i,2)          !# no pore press. gen. if e0=emin
        auxmat(i,8)=0.d0                 !# no degradation if n_deg=0.
       endif
c
c      Determine the depth index, i which lies just below the gwt.
c      This defines the upper boundary of the computational domain
c      used in consolidation computations.
c
       if(x(i-1).lt.xgwt.and.x(i).ge.xgwt) icon=i
 25    continue
c      do 26 i=1,mx
c        write(*,*) (auxmat(i,n),n=12,14)
c 26    continue
c
c     initialilze the backbone curves
c
      call tginput(maxmx,mx,mbc,nptsmax,npt,x,tbb0,gbb0,
   &            tbb,gbb,tcur,gcur,gmod)
      write(*,*)' '
      write(*,*)'t-g and shear moduli initialized'
c
c     initialize the shear strain...
c
       call hyster(maxmx,mbc,mx,meqn,nptsmax,npt,tbb,gbb,
```

```
     &              tcur,gcur,dtau,q,strn,gmod,
     &              maux2,auxmat,sigveff)
        do 29 i=1,mx
          sold(i)=strn(i)
          told(i)=tnew(i)
 29     continue
c
c     ...and update the shear moduli and wave speed
c
        do 30 i=1,mx
          aux(i,3) = gmod(i)                        !# shear modulus
            aux(i,2) = dsqrt(aux(i,3)/aux(i,1))     !# wave speed
c         write(*,600)' Layer ',i,' depth = ',x(i),' rho = ',
c    &              aux(i,1),' c = ',aux(i,2),' G = ',aux(i,3)
 30     continue
        aux(mx+1,1) = aux(mx,1)         !# same as the previous soil layer
        aux(mx+1,2) = aux(mx,2)
        aux(mx+1,3) = aux(mx,3)
        aux(mx+2,1) = aux(mx,1)         !# same as the previous soil layer
        aux(mx+2,2) = aux(mx,2)
        aux(mx+2,3) = aux(mx,3)
        write(*,*)'done re-initializing aux(i,m) for ntype=2'
        do 27 i=1,mx
          write(30,101)x(i),sigvtot(i),ffu(i),auxmat(i,3),auxmat(i,1),
     &            auxmat(i,2),auxmat(i,4),auxmat(i,5),auxmat(i,6),
     &            auxmat(i,7),auxmat(i,8),auxmat(i,9),auxmat(i,10),
     &            auxmat(i,11)
     &           ,(tbb0(i,j),j=npt,2*npt-1)
     &           ,(gbb0(i,j),j=npt,2*npt-1)
 27     continue
 101    format(100f9.4)
      endif
ccccccccccccccccccccccccccccccccccccccccccccccccccccccccccccccccccccccc
      call outjch(maxmx,meqn,mbc,mx,aux,q,disp,strn,u)
      dtout = (tend - t0)/dfloat(nout)
      write(*,*)'DONE INITIALIZING DATA, icon = ',icon
ccccccccccccccccccccccccccccccccccccccccccccccccccccccccccccccccccccccc
ccccccccccccccccccccccccccccccccccccccccccccccccccccccccccccccccccccccc
ccccccccccccccccccccccccccccccccccccccccccccccccccccccccccccccccccccccc
ccccccccc-------------------------------------ccccccccccccccccccccccccc
ccccccccc MAIN LOOP OF THE PROGRAM cccccccccccccccccccccccccccccccc
ccccccccc-------------------------------------ccccccccccccccccccccccccc
ccccccccccccccccccccccccccccccccccccccccccccccccccccccccccccccccccccccc
ccccccccccccccccccccccccccccccccccccccccccccccccccccccccccccccccccccccc
```

```
cccccccccccccccccccccccccccccccccccccccccccccccccccccccccccccccccccc
      do 100 n=1,nout
        call gettim(mh1,mm1,ms1,md1)
        if(mod(n,100).eq.0)write(*,5999)dfloat(n)*dti,' SECONDS, OUT OF'
     &                        ,dfloat(nout)*dti,' SECONDS'
 5999   format(f8.2,a16,f8.2,a8)
        if(nquake.eq.2) read(23,*) vbr2
        call gettim(mh2,mm2,ms2,md2)
        t1 = t1 + getdt(mh2-mh1,mm2-mm1,ms2-ms1,md2-md1)
      do  95 n2 = 1,ndiv
        tstart = t0 + dti*(n-1) + dtcfl*(n2-1)
        tend   = t0 + dti*(n-1) + dtcfl*n2
ccc        tstart = t0 + (n-1) * dtout
ccc        tend = t0 + n*dtout
        if(nquake.eq.1) then
          vbr = -2.d0 * pi * f * amp * dsin(2.d0*pi*f*tend)
        elseif(nquake.eq.2) then
          vbr = vbr1 + (vbr2 - vbr1)*n2/ndiv
        endif
c      ---------------------------------------
c      # main call to claw1
c      ---------------------------------------
        call gettim(mh1,mm1,ms1,md1)
        call claw1(maxmx,meqn,mwaves,mbc,mx,
     &          q,aux,dx,tstart,tend,dtv,cflv,nv,method,mthlim,
     &        work,mwork,info)
c         write(*,6001) nv(2),tend,info
c 6001    format(' CLAW1 returning after ',i3,' steps,  t =',e10.5,
c    &        ' info =',i3,/)
        dtv(1) = dtv(5)  !# set dt to start next call
        call gettim(mh2,mm2,ms2,md2)
        t2 = t2 + getdt(mh2-mh1,mm2-mm1,ms2-ms1,md2-md1)
c      --------------------------------------------------
c      # Constitutive Models are Envoked Here
c      --------------------------------------------------
c
        call gettim(mh1,mm1,ms1,md1)
        if(ntype.eq.1) then          !# linear analysis
          do 50 i=1,mx
            strn(i) =  q(i,1)/aux(i,3)
 50       continue
c
        elseif(ntype.eq.2) then   !# hysteresis loops and degradation
          do 60 i=1,mx
```

```
        tnew(i) = q(i,1)
        dtau(2,i) = tnew(i) - told(i)
 60     continue
       call hyster(maxmx,mbc,mx,meqn,nptsmax,npt,tbb,gbb,
     &             tcur,gcur,dtau,q,strn,gmod,
     &             maux2,auxmat,sigveff)
       call pore(maxmx,mbc,mx,maux2,auxmat,told,sold,tnew,strn,
     &           tau0,u,deg)
       do 70 i=1,mx
        ru(i) = u(i) / auxmat(i,3)
        told(i) = tnew(i)
        sold(i) = strn(i)
        sigveff(i) = auxmat(i,3) - u(i)
 70     continue
       call degrade(maxmx,mx,maux2,nptsmax,npt,auxmat,tbb0,deg,tbb)
c
c     elseif(ntype.eq.3) then   !# stress-path constitutive model
c       call sladen(args...)
      endif
c     ----------------------------------------
c     update excess pore pressure for diffusion problem
c     ----------------------------------------
      call bccon(bcutop,bcubot,icon,mbc,maxmx,mx,u)          !# drainage bc's applied
here
      call constep(mbc,maxmx,mx,maux2,icon,auxmat,dxi,dtcfl,u)  !# time step taken
here
c     ----------------------------------------
c     update auxiliary array here (nonlinear runs only)
c     ----------------------------------------
      if(ntype.eq.2.or.ntype.eq.3)then
       do 90 i=1,mx
c         gmod(i)  = dmax1(gmod(i),1.d-10)
        aux(i,3) = gmod(i)                          !# new shear modulus
        if(gmod(i).lt.0.d0)write(*,*)'NEGATIVE MODULUS',tend,i,g(i)
        aux(i,2) = dsqrt(aux(i,3)/aux(i,1))  !# new wave speed
 90     continue
       aux(0,2)   = aux(1,2)           !# ghost cells above ground surface
       aux(0,3)   = aux(1,3)
       aux(-1,2)  = aux(1,2)
       aux(-1,3)  = aux(1,3)
       aux(mx+1,2) = aux(mx,2)            !# ghost cells below bedrock level
       aux(mx+1,3) = aux(mx,3)
       aux(mx+2,2) = aux(mx,2)
       aux(mx+2,3) = aux(mx,3)
```

```
      endif
      call gettim(mh2,mm2,ms2,md2)
      t3 = t3 + getdt(mh2-mh1,mm2-mm1,ms2-ms1,md2-md1)
c     ------------------------------
c      integrate velocities to get displacements
c     ------------------------------
      call gettim(mh1,mm1,ms1,md1)
      call integrate(maxmx,meqn,mbc,mx,dtcfl,q,vold,disp)
      call gettim(mh2,mm2,ms2,md2)
      t4 = t4 + getdt(mh2-mh1,mm2-mm1,ms2-ms1,md2-md1)
 95   continue
     call gettim(mh1,mm1,ms1,md1)
      vbr1 = vbr2    !# update the bedrock velocity when loop 95 is completed
c     ------------------------
c      output data only at dti time steps
c     ------------------------
      call outjch(maxmx,meqn,mbc,mx,aux,q,disp,strn,u)
c
         if (info .ne. 0) then
           write(*,*) 'ERROR in claw1... info =', info
           stop
           endif
     call gettim(mh2,mm2,ms2,md2)
     t1 = t1 + getdt(mh2-mh1,mm2-mm1,ms2-ms1,md2-md1)
  100 continue
c
     write(*,*)'CPU Time (sec) for MACRO LOOP  = ',int(t1)
     write(*,*)'  (includes earthquake reads & data writes)'
     write(*,*)'CPU Time (sec) for MICRO LOOP  = ',int(t2+t3+t4)
     write(*,*)'  (subroutine CLAW)        = ',int(t2)
     write(*,*)'  (material behavior)      = ',int(t3)
     write(*,*)'  (integrate velocity)     = ',int(t4)
c
c    ******************************************************************
c    CONSOLIDATION COMPUTATIONS CONTINUE HERE AFTER THE
c    EARTHQUAKE COMPUTATIONS ARE COMPLETED, BUT LIKELY
c    AT A LARGER TIME STEP
c    ******************************************************************
c
     write(*,*)'DONE WITH EARTHQUAKE COMPUTATIONS, CONTINUE WITH'
     write(*,*)'CONSOLIDATION COMPUTATIONS UNTIL TIME,',tcon
c    ------------------------------------------
c    first, initialize the "old" value of effective stress as the
c    "current" value of effective stress
```

```
c   ------------------------------------------------
    do 165 i=1,mx
     sigvold(i) = sigveff(i)
 165  continue
c   ------------------------------------------------
c   second, perform the diffusion computations
c   ------------------------------------------------
    do 170 n=1,ncon
     if(mod(n,100).eq.0)write(*,5999)tend+dfloat(n)*dtcon,
   &                ' SECONDS, OUT OF',tcon,' SECONDS'
c
c     ----------------------------------------
c     apply b.c.'s and update excess pore pressure
c     ----------------------------------------
      call bccon(bcutop,bcubot,icon,mbc,maxmx,mx,u)
      call constep(mbc,maxmx,mx,maux2,icon,auxmat,dxi,dtcon,u)
c     ------------------------------------------
c     update the effective stress based on the current value
c     of excess pore pressure
c     -------------------------------------------
      do 175 i=1,mx
       sigveff(i) = sigvtot(i) - u(i)
 175   continue
c     ----------------------------------------
c     compute settlement at the ground surface
c     ----------------------------------------
      call settle(maxmx,mx,maux2,auxmat,dxi,sigvold,sigveff,delh)
c     ----------------------------------------
c     update the "old" value of vertical effective stress
c     ----------------------------------------
      do 177 i=1,mx
       sigvold(i) = sigveff(i)
 177   continue
c     ----------------------------------------
c     output settlement and pore pressure data
c     ----------------------------------------
      write(38,1001) delh,(u(i), i=1,mx)
 1001  format(100e15.8)
 170  continue
    write(*,*)'Consolidation Computations Complete'
    write(*,*)'Total Settlement = ',delh
c
c   ******************************************************************
c   CONSOLIDATION COMPUTATIONS COMPLETE
```

```
c   *****************************************************************
c
 200  stop
      end
cccccccccccccccccccccccccccccccccccccccccccccccccccccccccccccccccccccc
cccccccccccccccccccccccccccccccccccccccccccccccccccccccccccccccccccccc
cccccccccccccccccccccccccccccccccccccccccccccccccccccccccccccccccccccc
cccc ------------------------------------------------------------- cccc
cccc  SUBROUTINES AND FUNCTION SUBPROGRAMS BEGIN HERE  cccc
cccc ------------------------------------------------------------- cccc
cccccccccccccccccccccccccccccccccccccccccccccccccccccccccccccccccccccc
cccccccccccccccccccccccccccccccccccccccccccccccccccccccccccccccccccccc
cccccccccccccccccccccccccccccccccccccccccccccccccccccccccccccccccccccc
c   =================================================================
      subroutine rp1jch(maxm,meqn,mwaves,mbc,mx,ql,qr,auxl,auxr,
     &                  wave,s,amdq,apdq)
c   =================================================================
c
c   # Riemann solver for the acoustics equations in 1d,
c
c
c   # On input, ql contains the state vector at the left edge of each cell
c   #           qr contains the state vector at the right edge of each cell
c
c   # auxl(i,1) holds rho,
c   # auxl(i,2) holds sound speed c,
c   #   Here it is assumed that auxl=auxr gives the cell values.
c
c   # On output, wave contains the waves,
c   #            s the speeds,
c   #
c   #            amdq = A^- Delta q,
c   #            apdq = A^+ Delta q,
c   #                 the decomposition of the flux difference
c   #                    f(qr(i-1)) - f(ql(i))
c   #                 into leftgoing and rightgoing parts respectively.
c   #
c
c   # Note that the i'th Riemann problem has left state qr(i-1,:)
c   #                                    and right state ql(i,:)
c   # From the basic clawpack routines, this routine is called with ql = qr
c
c
      implicit double precision (a-h,o-z)
```

```
c
      dimension wave(1-mbc:maxm+mbc, meqn, mwaves)
      dimension   s(1-mbc:maxm+mbc, mwaves)
      dimension  ql(1-mbc:maxm+mbc, meqn)
      dimension  qr(1-mbc:maxm+mbc, meqn)
      dimension auxl(1-mbc:maxm+mbc, 3)
      dimension auxr(1-mbc:maxm+mbc, 3)
      dimension apdq(1-mbc:maxm+mbc, meqn)
      dimension amdq(1-mbc:maxm+mbc, meqn)
c
c     local arrays
c     ----------
      dimension delta(2)
c
c
c     # split the jump in q at each interface into waves
c
c     # find a1 and a2, the coefficients of the 2 eigenvectors:
      do 20 i = 2-mbc, mx+mbc
         delta(1) = ql(i,1) - qr(i-1,1)
         delta(2) = ql(i,2) - qr(i-1,2)
         rhol = auxl(i,1)
         rhor = auxr(i-1,1)
         cl = auxl(i,2)
         cr = auxr(i-1,2)
c           write(*,*)'divisions ahead'
         det = cr/rhol + cl/rhor
         a1 = (-delta(1)/rhol - delta(2)*cl) / det
         a2 =  (delta(1)/rhor - delta(2)*cr) / det
c           write(*,*)'done with divisions'
c
c        # Compute the waves.
c
         wave(i,1,1) = -a1*cr
         wave(i,2,1) = -a1/rhor
         s(i,1) = -cr
c
         wave(i,1,2) = a2*cl
         wave(i,2,2) = -a2/rhol
         s(i,2) = cl
c
   20    continue
c
c
```

```
c    # compute the leftgoing and rightgoing flux differences:
c    # Note s(i,1) < 0   and   s(i,2) > 0.
c
     do 220 m=1,meqn
       do 220 i = 2-mbc, mx+mbc
         amdq(i,m) = s(i,1)*wave(i,m,1)
         apdq(i,m) = s(i,2)*wave(i,m,2)
 220     continue
c
     return
     end
c
c =====================================================================
     subroutine claw1(maxmx,meqn,mwaves,mbc,mx,
    &            q,aux,dx,tstart,tend,dtv,cflv,nv,method,mthlim,
    &          work,mwork,info)
c =====================================================================
c
c  Solves a hyperbolic system of conservation laws in one space dimension
c  of the general form
c
c    capa * q_t + A q_x = psi
c
c  The "capacity function" capa(x) and source term psi are optional
c  (see below).
c
c  For a more complete description see the documentation in the directory
c  claw/doc,  especially note1.ps and note2.ps.
c
c  Sample driver programs and user-supplied subroutines are available.
c  see the the directory claw/clawpack/1d/example for one example, and
c  codes in claw/applications for more extensive examples.
c
c --------------------------------------------------------
c
c  The user must supply the following subroutines:
c
c   bc1, rp1       subroutines specifying the boundary conditions and
c                  Riemann solver.
c                  These are described in greater detail below.
c
c  In addition, if the equation contains source terms psi, then the user
c  must provide:
c
```

```
c  src1          subroutine that solves capa * q_t = psi
c                over a single time step.
c
c These routines must be declared EXTERNAL in the main program.
c For description of the calling sequences, see below.
c
c
c
c Description of parameters...
c ------------------
c
c
c  maxmx is the maximum number of interior grid points in x,
c      and is used in declarations of the array q.
c
c  meqn is the number of equations in the system of
c      conservation laws.
c
c  mwaves is the number of waves that result from the
c       solution of each Riemann problem.  Often mwaves = meqn but
c       for some problems these may be different.
c
c  mbc is the number of "ghost cells" that must be added on to each
c    side of the domain to handle boundary conditions.  The cells
c    actually in the physical domain are labelled from 1 to mx in x.
c    The arrays are dimensioned actually indexed from 1-mbc to mx+mbc.
c    For the methods currently implemented, mbc = 2 should be used.
c    If the user implements another method that has a larger stencil and
c    hence requires more ghost cells, a larger value of mbc could be used.
c    q is extended from the physical domain to the ghost cells by the
c    user-supplied routine bc1.
c
c  mx is the number of grid cells in the x-direction, in the
c    physical domain.  In addition there are mbc grid cells
c    along each edge of the grid that are used for boundary
c    conditions.
c    Must have mx .le. maxmx
c
c  q(1-mbc:maxmx+mbc, meqn)
c     On input:  initial data at time tstart.
c     On output: final solution at time tend.
c     q(i,m) = value of mth component in the i'th cell.
c     Values within the physical domain are in q(i,m)
c           for i = 1,2,...,mx
```

```
c     mbc extra cells on each end are needed for boundary conditions
c     as specified in the routine bc1.
c
c  aux(1-mbc:maxmx+mbc, maux)
c     Array of auxiliary variables that are used in specifying the problem.
c     If method(7) = 0 then there are no auxiliary variables and aux
c              can be a dummy variable.
c     If method(7) = maux > 0 then there are maux auxiliary variables
c              and aux must be dimensioned as above.
c
c     Capacity functions are one particular form of auxiliary variable.
c     These arise in some applications, e.g. variable coefficients in
c     advection or acoustics problems.
c     See Clawpack Note # 5 for examples.
c
c     If method(6) = 0 then there is no capacity function.
c     If method(6) = mcapa > 0  then there is a capacity function and
c        capa(i), the "capacity" of the i'th cell, is assumed to be
c        stored in aux(i,mcapa).
c        In this case we require method(7).ge.mcapa.
c
c  dx = grid spacing in x.
c     (for a computation in ax <= x <= bx,  set dx = (bx-ax)/mx.)
c
c  tstart = initial time.
c
c  tend = Desired final time (on input).
c     = Actual time reached (on output).
c
c  dtv(1:5) = array of values related to the time step:
c          (Note: method(1)=1 indicates variable size time steps)
c     dtv(1) = value of dt to be used in all steps if method(1) = 0
c          = value of dt to use in first step if method(1) = 1
c     dtv(2) = unused if method(1) = 0.
c          = maximum dt allowed if method(1) = 1.
c     dtv(3) = smallest dt used (on output)
c     dtv(4) = largest dt used (on output)
c     dtv(5) = dt used in last step (on output)
c
c  cflv(1:4) = array of values related to Courant number:
c     cflv(1) = maximum Courant number to be allowed.  With variable
c            time steps the step is repeated if the Courant
c            number is larger than this value.  With fixed time
c            steps the routine aborts.  Usually cflv(1)=1.0
```

```
c             should work.
c       cflv(2) = unused if method(1) = 0.
c            = desired Courant number if method(1) = 1.
c             Should be somewhat less than cflv(1), e.g. 0.9
c       cflv(3) = largest Courant number observed (on output).
c       cflv(4) = Courant number in last step (on output).
c
c    nv(1:2) = array of values related to the number of time steps:
c       nv(1) = unused if method(1) = 0
c            = maximum number of time steps allowed if method(1) = 1
c       nv(2) = number of time steps taken (on output).
c
c    method(1:7) = array of values specifying the numerical method to use
c       method(1) = 0 if fixed size time steps are to be taken.
c                 In this case, dt = dtv(1) in all steps.
c             = 1 if variable time steps are to be used.
c                 In this case, dt = dtv(1) in the first step and
c                 thereafter the value cflv(2) is used to choose the
c                 next time step based on the maximum wave speed seen
c                 in the previous step. Note that since this value
c                 comes from the previous step, the Courant number will
c                 not in general be exactly equal to the desired value
c                 If the actual Courant number in the next step is
c                 greater than 1, then this step is redone with a
c                 smaller dt.
c
c       method(2) = 1 if Godunov's method is to be used, with no 2nd order
c                 corrections.
c             = 2 if second order correction terms are to be added, with
c                 a flux limiter as specified by mthlim.
c             = 3 if "third order" correction terms are to be added,
c                 based on my paper my paper "A high-resolution
c                 conservative algorithm for advection in
c                 incompressible flow".
c                 This is currently recommended only for problems
c                 with smooth solutions, using no limiter (mthlim = 0)
c
c       method(3)  is not used in one-dimension.
c
c       method(4) = 0 to suppress printing
c             = 1 to print dt and Courant number every time step
c
c       method(5) = 0 if there is no source term psi. In this case
c                 the subroutine src2 is never called so a dummy
```

```
c              parameter can be given.
c           = 1 if there is a source term.  In this case
c              the subroutine src2 must be provided.
c
c    method(6) = 0 if there is no capacity function capa.
c           = mcapa > 0 if there is a capacity function.  In this case
c              aux(i,mcapa) is the capacity of the i'th cell and you
c              must also specify method(7) .ge. mcapa and set aux.
c
c    method(7) = 0 if there is no aux array used.
c           = maux > 0  if there are maux auxiliary variables.
c
c
c    The recommended choice of methods for most problems is
c      method(1) = 1,  method(2) = 2.
c
c  mthlim(1:mwaves) = array of values specifying the flux limiter to be used
c             in each wave family mw.  Often the same value will be used
c             for each value of mw, but in some cases it may be
c             desirable to use different limiters.  For example,
c             for the Euler equations the superbee limiter might be
c             used for the contact discontinuity (mw=2) while another
c             limiter is used for the nonlinear waves.  Several limiters
c             are built in and others can be added by modifying the
c             subroutine philim.
c
c    mthlim(mw) = 0 for no limiter
c           = 1 for minmod
c           = 2 for superbee
c           = 3 for van Leer
c           = 4 for monotonized centered
c
c
c  work(mwork) = double precision work array of length at least mwork
c
c  mwork = length of work array.  Must be at least
c        (maxmx + 2*mbc) * (2 + 3*meqn + mwaves + meqn*mwaves)
c      If mwork is too small then the program returns with info = 4
c      and prints the necessary value of mwork to unit 6.
c
c
c  info = output value yielding error information:
c     = 0 if normal return.
c     = 1 if mx.gt.maxmx   or  mbc.lt.2
```

```
c        = 2 if method(1)=0 and dt doesn't divide (tend - tstart).
c        = 3 if method(1)=1 and cflv(2) > cflv(1).
c        = 4 if mwork is too small.
c        = 11 if the code attempted to take too many time steps, n > nv(1).
c             This could only happen if method(1) = 1 (variable time steps).
c        = 12 if the method(1)=0 and the Courant number is greater than 1
c             in some time step.
c
c         Note: if info.ne.0, then tend is reset to the value of t actually
c         reached and q contains the value of the solution at this time.
c
c   User-supplied subroutines
c   ------------------------
c
c   bc1 = subroutine that specifies the boundary conditions.
c       This subroutine should extend the values of q from cells
c       1:mx to the mbc ghost cells along each edge of the domain.
c
c         The form of this subroutine is
c -------------------------------------------------
c    subroutine bc1(maxmx,meqn,mbc,mx,q,aux,t)
c    implicit double precision (a-h,o-z)
c    dimension   q(1-mbc:maxmx+mbc, meqn)
c    dimension aux(1-mbc:maxmx+mbc, *)
c -------------------------------------------------
c
c
c   rp1 = user-supplied subroutine that implements the Riemann solver
c
c         The form of this subroutine is
c -------------------------------------------------
c    subroutine rp1(maxmx,meqn,mwaves,mbc,mx,ql,qr,auxl,auxr,wave,s,amdq,apdq)
c    implicit double precision (a-h,o-z)
c    dimension   ql(1-mbc:maxmx+mbc, meqn)
c    dimension   qr(1-mbc:maxmx+mbc, meqn)
c    dimension auxl(1-mbc:maxmx+mbc, *)
c    dimension auxr(1-mbc:maxmx+mbc, *)
c    dimension wave(1-mbc:maxmx+mbc, meqn, mwaves)
c    dimension    s(1-mbc:maxmx+mbc, mwaves)
c    dimension amdq(1-mbc:maxmx+mbc, meqn)
c    dimension apdq(1-mbc:maxmx+mbc, meqn)
c -------------------------------------------------
c
c       On input, ql contains the state vector at the left edge of each cell
```

```
c            qr contains the state vector at the right edge of each cell
c           auxl contains auxiliary values at the left edge of each cell
c           auxr contains auxiliary values at the right edge of each cell
c
c      Note that the i'th Riemann problem has left state qr(i-1,:)
c                              and right state ql(i,:)
c      In the standard clawpack routines, this Riemann solver is
c      called with ql=qr=q along this slice.  More flexibility is allowed
c      in case the user wishes to implement another solution method
c      that requires left and rate states at each interface.

c      If method(7)=maux > 0 then the auxiliary variables along this slice
c      are passed in using auxl and auxr.  Again, in the standard routines
c      auxl=auxr=aux in the call to rp1.
c
c       On output,
c          wave(i,m,mw) is the m'th component of the jump across
c                    wave number mw in the ith Riemann problem.
c          s(i,mw) is the wave speed of wave number mw in the
c                    ith Riemann problem.
c          amdq(i,m) = m'th component of A^- Delta q,
c          apdq(i,m) = m'th component of A^+ Delta q,
c               the decomposition of the flux difference
c                  f(qr(i-1)) - f(ql(i))
c               into leftgoing and rightgoing parts respectively.
c
c       It is assumed that each wave consists of a jump discontinuity
c       propagating at a single speed, as results, for example, from a
c       Roe approximate Riemann solver.  An entropy fix can be included
c       into the specification of amdq and apdq.
c
c   src1 = subroutine for the source terms that solves the equation
c           capa * q_t = psi
c       over time dt.
c
c       If method(5)=0 then the equation does not contain a source
c       term and this routine is never called.  A dummy argument can
c       be used with many compilers, or provide a dummy subroutine that
c       does nothing (such a subroutine can be found in
c       clawpack/1d/misc/src1xx.f)
c
c      The form of this subroutine is
c -------------------------------------------------
c    subroutine src1(maxmx,meqn,mbc,mx,q,aux,t,dt)
```

```
c   implicit double precision (a-h,o-z)
c   dimension  q(1-mbc:maxmx+mbc, meqn)
c   dimension aux(1-mbc:maxmx+mbc, *)
c ------------------------------------
c    If method(7)=0  or the auxiliary variables are not needed in this solver,
c    then the latter dimension statement can be omitted, but aux should
c    still appear in the argument list.
c
c    On input, q(i,m) contains the data for solving the
c          source term equation.
c    On output, q(i,m) should have been replaced by the solution to
c           the source term equation after a step of length dt.

c
c
c NOTES:
c -----
c
c -- This code is written for clarity rather than efficiency in many
c   respects.
c
c -- Most of this routine is concerned with checking for errors and
c   choosing time steps. The main work of each time step is done in step1.
c
c -- Strang splitting is used to handle the source term. This works well
c   and can be used to achieve second order accuracy on smooth solutions
c   provided that the source terms are not "stiff". If they are, meaning
c   that the time scale on which solutions to the ODE vary are much faster
c   than the time scales of the homogeneous conservation law, then to
c   obtain good results it may be necessary to take dx and dt small enough
c   that the rapid transients are well-resolved.
c
c -- Note that with variable time steps, the value dtv(2)
c   may be used to limit the time step to some maximum value, independent
c   of the Courant number. This may be chosen based on the source terms.
c
c
c
c =====================================================================
c
c Copyright 1994 R. J. LeVeque
c
c This software is made available for research and instructional use only.
c You may copy and use this software without charge for these non-commercial
```

```
c purposes, provided that the copyright notice and associated text is
c reproduced on all copies. For all other uses (including distribution of
c modified versions), please contact the author at the address given below.
c
c *** This software is made available "as is" without any assurance that it
c *** will work for your purposes. The software may in fact have defects, so
c *** use the software at your own risk.
c
c ----------------------------
c  CLAWPACK Version 2.1, October, 1995
c  available from netlib@research.att.com in pdes/claw
c  Homepage: http://www.amath.washington.edu/~rjl/clawpack.html
c ----------------------------
c  Author: Randall J. LeVeque
c          Applied Mathematics
c          Box 352420
c          University of Washington,
c          Seattle, WA 98195-2420
c          rjl@amath.washington.edu
c ==================================================================
c  Beginning of claw1 code
c ==================================================================
c
   implicit double precision (a-h,o-z)
   dimension q(1-mbc:maxmx+mbc, meqn)
   dimension aux(1-mbc:maxmx+mbc, *)
   dimension work(mwork)
   dimension mthlim(mwaves),method(7),dtv(5),cflv(4),nv(2)
c
   info = 0
   t = tstart
   maxn = nv(1)
   dt = dtv(1)   !# initial dt
   cflmax = 0.d0
   dtmin = dt
   dtmax = dt
   nv(2) = 0
c
c   # check for errors in data:
c
   if (mx .gt. maxmx) then
      info = 1
      go to 900
      endif
```

```
c
      if (method(1) .eq. 0) then
c        # fixed size time steps.  Compute the number of steps:
         maxn = (tend - tstart + 1d-10) / dt
         if (dabs(maxn*dt - (tend-tstart)) .gt. 1d-8) then
c           # dt doesn't divide time interval integer number of times
            info = 2
            go to 900
            endif
         endif
c
      if (method(1).eq.1 .and. cflv(1).gt.1.d0) then
         info = 3
         go to 900
         endif
c
c     # partition work array into pieces for passing into step1:
      i0f = 1
      i0wave = i0f + (maxmx + 2*mbc) * meqn
      i0s = i0wave + (maxmx + 2*mbc) * meqn * mwaves
      i0dtdx = i0s + (maxmx + 2*mbc) * mwaves
      i0qwork = i0dtdx + (maxmx + 2*mbc)
      i0amdq = i0qwork + (maxmx + 2*mbc) * meqn
      i0apdq = i0amdq + (maxmx + 2*mbc) * meqn
      i0dtdx = i0apdq + (maxmx + 2*mbc) * meqn
      i0end = i0dtdx + (maxmx + 2*mbc) - 1
c
      if (mwork .lt. i0end) then
         write(*,*) 'mwork must be increased to ',i0end
         info = 4
         go to 900
         endif
c
c     ---------
c     # main loop
c     ---------
c
      if (maxn.eq.0) go to 900
      do 100 n=1,maxn
         told = t
         if (told+dt .gt. tend) dt = tend - told
         if (method(1).eq.1) then
c           # save old q in case we need to retake step with smaller dt:
            call copyq1(maxmx,meqn,mbc,mx,q,work(i0qwork))
```

```
          endif
c
  40   continue
         dt2 = dt / 2.d0
         thalf = t + dt2  !# midpoint in time for Strang splitting
         t = told + dt    !# time at end of step
c
c      ------------------------------------------------
c      # main steps in algorithm, using Strang splitting for source term:
c      ------------------------------------------------
c
c      # extend data from grid to bordering boundary cells:
c-jch   call bc1jch(maxmx,meqn,mbc,mx,q,aux,told)
       call bc1jch(maxmx,meqn,mbc,mx,q)
c
         if (method(5).eq.1) then
c         # with source term:   use Strang splitting
           call src1jch(maxmx,meqn,mbc,mx,q,dt2)
           endif
c
c      # take a step on the homogeneous conservation law:
       call step1(maxmx,meqn,mwaves,mbc,mx,q,aux,dx,dt,
     &         method,mthlim,cfl,work(i0f),work(i0wave),
     &         work(i0s),work(i0amdq),work(i0apdq),work(i0dtdx))
c
         if (method(5).eq.1) then
c         # source terms over second half time step:
           call src1jch(maxmx,meqn,mbc,mx,q,dt2)
           endif
c
c      ------------------------------------------------
c
       if (method(4) .eq. 1) write(*,601) n,cfl,dt,t
 601   format('CLAW1... Step',i4,
     &          ' Courant number =',f6.3,' dt =',d12.4,
     &          ' t =',d12.4)
c
       if (method(1) .eq. 1) then
c        # choose new time step if variable time step
         if (cfl .gt. 0.d0) then
              dt = dmin1(dtv(2), dt * cflv(2)/cfl)
              dtmin = dmin1(dt,dtmin)
              dtmax = dmax1(dt,dtmax)
           else
```

```
               dt = dtv(2)
            endif
           endif
c
c     # check to see if the Courant number was too large:
c
         if (cfl .le. cflv(1)) then
c          # accept this step
             cflmax = dmax1(cfl,cflmax)
            else
c          # reject this step
               t = told
             call copyq1(maxmx,meqn,mbc,mx,work(i0qwork),q)
c
               if (method(4) .eq. 1) then
                 write(*,602)
 602             format('CLAW1 rejecting step... ',
   &                         'Courant number too large')
                 endif
             if (method(1).eq.1) then
c              # if variable dt, go back and take a smaller step
                  go to 40
              else
c              # if fixed dt, give up and return
                cflmax = dmax1(cfl,cflmax)
                go to 900
              endif
            endif
c
c     # see if we are done:
         nv(2) = nv(2) + 1
         if (t .ge. tend) go to 900
c
 100   continue
c
 900  continue
c
c     # return information
c
      if (method(1).eq.1 .and. t.lt.tend .and. nv(2) .eq. maxn) then
c        # too many timesteps
         info = 11
         endif
c
```

```
      if (method(1).eq.0 .and. cflmax .gt. cflv(1)) then
c        # Courant number too large with fixed dt
          info = 12
          endif
      tend = t
      cflv(3) = cflmax
      cflv(4) = cfl
      dtv(3) = dtmin
      dtv(4) = dtmax
      dtv(5) = dt
      return
      end
c
c
c=====================================================================
      subroutine step1(maxmx,meqn,mwaves,mbc,mx,q,aux,dx,dt,
     &           method,mthlim,cfl,f,wave,s,amdq,apdq,dtdx)
c=====================================================================
c
c     # Take one time step, updating q.
c
c     method(1) = 1   ==>  Godunov method
c     method(1) = 2   ==>  Slope limiter method
c     mthlim(p)  controls what limiter is used in the pth family
c
c
c     amdq, apdq, wave, s, and f are used locally:
c
c     amdq(1-mbc:maxmx+mbc, meqn) = left-going flux-differences
c     apdq(1-mbc:maxmx+mbc, meqn) = right-going flux-differences
c        e.g. amdq(i,m) = m'th component of A^- \Delta q from i'th Riemann
c                       problem (between cells i-1 and i).
c
c     wave(1-mbc:maxmx+mbc, meqn, mwaves) = waves from solution of
c                                           Riemann problems,
c           wave(i,m,mw) = mth component of jump in q across
c                          wave in family mw in Riemann problem between
c                          states i-1 and i.
c
c     s(1-mbc:maxmx+mbc, mwaves) = wave speeds,
c           s(i,mw) = speed of wave in family mw in Riemann problem between
c                     states i-1 and i.
c
c     f(1-mbc:maxmx+mbc, meqn) = correction fluxes for second order method
```

```
c        f(i,m) = mth component of flux at left edge of ith cell
c   ---------------------------------------------------------------
c
      implicit double precision (a-h,o-z)
      dimension    q(1-mbc:maxmx+mbc, meqn)
      dimension  aux(1-mbc:maxmx+mbc, *)
      dimension    f(1-mbc:maxmx+mbc, meqn)
      dimension    s(1-mbc:maxmx+mbc, mwaves)
      dimension wave(1-mbc:maxmx+mbc, meqn, mwaves)
      dimension amdq(1-mbc:maxmx+mbc, meqn)
      dimension apdq(1-mbc:maxmx+mbc, meqn)
      dimension dtdx(1-mbc:maxmx+mbc)
      dimension method(7),mthlim(mwaves)
      logical limit
c
c     # check if any limiters are used:
      limit = .false.
      do 5 mw=1,mwaves
         if (mthlim(mw) .gt. 0) limit = .true.
   5     continue
c
      mcapa = method(6)
      do 10 i=1-mbc,mx+mbc
         if (mcapa.gt.0) then
            if (aux(i,mcapa) .le. 0.d0) then
               write(*,*) 'Error -- capa must be positive'
               stop
               endif
         dtdx(i) = dt / (dx*aux(i,mcapa))
          else
         dtdx(i) = dt/dx
          endif
  10     continue
c
c     # solve Riemann problem at each interface
c     -----------------------------------------
c
      call rp1jch(maxmx,meqn,mwaves,mbc,mx,q,q,aux,aux,wave,s,amdq,
     &            apdq)
c
c     # Modify q for Godunov update:
c     # Note this may not correspond to a conservative flux-differencing
c     # for equations not in conservation form.  It is conservative if
c     # amdq + apdq = f(q(i)) - f(q(i-1)).
```

```
c
    do 40 i=1,mx+1
      do 40 m=1,meqn
        q(i,m) = q(i,m) - dtdx(i)*apdq(i,m)
        q(i-1,m) = q(i-1,m) - dtdx(i-1)*amdq(i,m)
  40    continue

c
c   # compute maximum wave speed:
    cfl = 0.d0
    do 50 i=1,mx+1
         cfl = dmax1(cfl, dtdx(i)*dabs(s(i,1)), dtdx(i)*dabs(s(i,mwaves)))
  50   continue
c
    if (method(2) .eq. 1) go to 900
c
c   # compute correction fluxes for second order q_{xx} terms:
c   ----------------------------------------------
c
    do 100 m = 1, meqn
        do 100 i = 1-mbc, mx+mbc
          f(i,m) = 0.d0
 100      continue
c
c   # apply limiter to waves:
    if (limit) call limiter(maxmx,meqn,mwaves,mbc,mx,wave,s,mthlim)
c
    do 120 i=1,mx+1
        do 120 m=1,meqn
          do 110 mw=1,mwaves
            dtdxave = 0.5d0 * (dtdx(i-1) + dtdx(i))
            f(i,m) = f(i,m) + 0.5d0 * dabs(s(i,mw))
   &             * (1.d0 - dabs(s(i,mw))*dtdxave) * wave(i,m,mw)
c
c          # third order corrections:
c          # (still experimental... works well for smooth solutions
c          # with no limiters but not well with limiters so far.
c

          if (method(2).lt.3) go to 110
          if (s(i,mw) .gt. 0.d0) then
            dq2 = wave(i,m,mw) - wave(i-1,m,mw)
           else
            dq2 = wave(i+1,m,mw) - wave(i,m,mw)
```

```
          endif
         f(i,m) = f(i,m) - s(i,mw)/6.d0 *
   &              (1.d0 - (s(i,mw)*dtdxave)**2) * dq2

  110       continue
  120     continue
c
c
  140 continue
c
c    # update q by differencing correction fluxes
c    ============================================
c
c    # (Note:  Godunov update has already been performed above)
c
      do 150 m=1,meqn
         do 150 i=1,mx
           q(i,m) = q(i,m) - dtdx(i) * (f(i+1,m) - f(i,m))
  150     continue
c
  900 continue
      return
      end
c
c
c =====================================================================
      subroutine copyq1(maxmx,meqn,mbc,mx,q1,q2)
c =====================================================================
c
c    # copy the contents of q1 into q2
c
      implicit double precision (a-h,o-z)
      dimension q1(1-mbc:maxmx+mbc, meqn)
      dimension q2(1-mbc:maxmx+mbc, meqn)
c
      do 10 i = 1-mbc, mx+mbc
        do 10 m=1,meqn
            q2(i,m) = q1(i,m)
   10     continue
      return
      end
c
c
c    ===================================================================
```

```
      subroutine limiter(maxm,meqn,mwaves,mbc,mx,wave,s,mthlim)
c     =============================================================
c
c     # Apply a limiter to the waves.
c     # The limiter is computed by comparing the 2-norm of each wave with
c     # the projection of the wave from the interface to the left or
c     # right onto the current wave.  For a linear system this would
c     # correspond to comparing the norms of the two waves.  For a
c     # nonlinear problem the eigenvectors are not colinear and so the
c     # projection is needed to provide more limiting in the case where the
c     # neighboring wave has large norm but points in a different direction
c     # in phase space.
c
c     # The specific limiter used in each family is determined by the
c     # value of the corresponding element of the array mthlim, as used in
c     # the function philim.
c     # Note that a different limiter may be used in each wave family.
c
c     # dotl and dotr denote the inner product of wave with the wave to
c     # the left or right.  The norm of the projections onto the wave are then
c     # given by dotl/wnorm and dotr/wnorm, where wnorm is the 2-norm
c     # of wave.
c
      implicit real*8(a-h,o-z)
      dimension mthlim(mwaves)
      dimension wave(1-mbc:maxm+mbc, meqn, mwaves)
      dimension    s(1-mbc:maxm+mbc, mwaves)
c
c
      do 50 mw=1,mwaves
         if (mthlim(mw) .eq. 0) go to 50
         dotr = 0.d0
         do 40 i = 0, mx+1
            wnorm = 0.d0
            dotl = dotr
            dotr = 0.d0
            do 20 m=1,meqn
               wnorm = wnorm + wave(i,m,mw)**2
               dotr = dotr + wave(i,m,mw)*wave(i+1,m,mw)
   20          continue
            if (i.eq.0) go to 40
            wnorm = dsqrt(wnorm)
         if (wnorm.eq.0.d0) go to 40
c
```

```
          if (s(i,mw) .gt. 0.d0) then
               wlimitr = philim(wnorm, dotl/wnorm, mthlim(mw))
            else
               wlimitr = philim(wnorm, dotr/wnorm, mthlim(mw))
            endif
c
          do 30 m=1,meqn
         wave(i,m,mw) = wlimitr * wave(i,m,mw)
  30       continue
  40     continue
  50   continue
c
    return
    end
c
c   =====================================================================
    double precision function philim(a,b,meth)
c   =====================================================================
    implicit real*8(a-h,o-z)
c
c   # Compute a limiter based on wave strengths a and b.
c   # meth determines what limiter is used.
c   # a is assumed to be nonzero.
c
    r = b/a
    go to (10,20,30,40) meth

c
  10 continue
c   ------
c   # minmod
c   ------
    philim = dmax1(0.d0, dmin1(1.d0, r))
    return
c
  20 continue
c   --------
c   # superbee
c   --------
    philim = dmax1(0.d0, dmin1(1.d0, 2.d0*r), dmin1(2.d0, r))
    return
c
  30 continue
c   --------
```

```
c   # van Leer
c   --------
    philim = (r + dabs(r)) / (1.d0 + dabs(r))
    return
c
 40 continue
c   ----------------------
c   # monotinized centered
c   ----------------------
    c = (1.d0 + r)/2.d0
    philim = dmax1(0.d0, dmin1(c, 2.d0, 2.d0*r))

    return
    end
c
c
c
c =====================================================================
    subroutine bc1jch(maxmx,meqn,mbc,mx,q)
c =====================================================================
c
c   # Extend the data from the computational region
c   #     i = 1, 2, ..., mx2
c   # to the virtual cells outside the region, with
c   #     i = 1-ibc  and   i = mx+ibc   for ibc=1,...,mbc
c
    implicit double precision (a-h,o-z)
    dimension q(1-mbc:maxmx+mbc, meqn)
    common /bedrock/ vbr
c
c bc's applied here:  note that q(i,1) = shear stress and q(i,2) = velocity
c
c bc's at the top of the soil layer
c
    q(0,1) =     -q(1,1)    !# tau: zero always at boundary
    q(-1,1) =    -q(2,1)    !# (for the limiter)
c
    q(0,2) =      q(1,2)    !# velo: 0-order extrapolation
    q(-1,2) =     q(1,2)    !# (for the limiter)
c
c bc's at bottom of soil layer
c
    q(mx+1,1) = 2.d0*q(mx,1) -      q(mx-1,1)          !# tau: 1st-order extrap
    q(mx+2,1) = 3.d0*q(mx,1) - 2.d0*q(mx-1,1)  !# (for the limiter)
```

```
c
      q(mx+1,2) = 2.d0*vbr   -    q(mx,2)      !# velo: 1st-order extrap
      q(mx+2,2) = q(mx+1,2) !#4.d0*vbr   - 3.d0*q(mx,2)   !# (for the limiter)
c
      return
      end
cccccccccccccccccccccccccccccccccccccccccccccccccccccccccccccccccccccccc
c  This routine integrates the computed velocities at the end of each
c  time step to obtain the displacments. The trapezoidal rule is used
c  to perform the integration.
cccccccccccccccccccccccccccccccccccccccccccccccccccccccccccccccccccccccc
      subroutine integrate(maxmx,meqn,mbc,mx,dt,q,vold,d)
      implicit double precision (a-h,o-z)
      dimension q(1-mbc:maxmx+mbc, meqn)
      dimension vold(maxmx),d(maxmx)
      do 11 i=1,mx
        d(i) = d(i) + .5d0 * dt * ( q(i,2) + vold(i) )
        vold(i) = q(i,2)
 11   continue
      return
      end
cccccccccccccccccccccccccccccccccccccccccccccccccccccccccccccccccccccccc
c  Output the results
c
c  Note that mx max = 100 is implied by the 1000 format statement below.
c  If mx > 100, then change the field specification accordingly.
c
cccccccccccccccccccccccccccccccccccccccccccccccccccccccccccccccccccccccc
      subroutine outjch(maxmx,meqn,mbc,mx,aux,q,d,s,p)
      implicit double precision (a-h,o-z)
      dimension q(1-mbc:maxmx+mbc, meqn),aux(1-mbc:maxmx+mbc, 3)
      dimension d(maxmx),s(maxmx),p(maxmx)
c
      write(32,1000) (q(i,2),    i=1,mx)        !# velocities
      write(33,1000) (q(i,1),    i=1,mx)        !# shear stresses
      write(34,1000) (d(i),      i=1,mx)        !# displacements
      write(35,1000) (s(i),   i=1,mx)           !# shear strains
      write(36,1000) (aux(i,3), i=1,mx)         !# shear moduli
      write(37,1000) (p(i),      i=1,mx)        !# pore pressures
c
 1000 format(100e15.8)
      return
      end
c
```

```
c ====================================================================
      subroutine src1jch(maxmx,meqn,mbc,mx,q,dt)
c ====================================================================
      implicit double precision (a-h,o-z)
      dimension q(1-mbc:maxmx+mbc, meqn)
      common /bcsrc/ beta,grav
c
c     infinite slope source term
c
      pi=4.d0*datan(1.d0)        !# 3.14...
      do 10 i=1-mbc,mx+mbc
       q(i,2) = q(i,2) + grav*dsin(beta*pi/180.d0)*dt  !# velocity integrated here
       q(i,1) = q(i,1)                          !# no change to shear stress
 10   continue
      return
      end
ccccccccccccccccccccccccccccccccccccccccccccccccccccccccccccccccccccc
c This subroutine develops initial t-g backbone curves for each soil
c element. This is done by first reading t-g data pairs defined at up
c to 10 depths within the stratum. Each t-g curve may be constructed
c of up to "nptsmax" first quadrant t-g data pairs. Secondly, this first
c quadrant data is extended to the third quadrant. Finally, linear
c interpolation is used to obtain tbb-gbb curves between the depths at
c which the individual t-g curves are defined.
c
c Note the following variables and units:
c   ntg = number of t-g curves in the stratum
c   npt = number of first quadrant t-g data points for each curve
c   ztg(jj) = depth of the jjth t-g curve (L)
c   ginp(jj,n) = nth shear strain of the jjth t-g curve (L)
c   tinp(jj,n) = nth shear stress of the jjth t-g curve (F/L^2)
c   tbb0(mx,2*npt-1) = interpolated tau-values for each soil element
c   gbb0(mx,2*npt-1) = corresponding gamma-values for each soil element
c   gi(mx) = initial shear moduluis for the jth soil element
c   mx =  number of soil elements for which interpolated curves
c           will be constructed
c   2*npt-1 = number of interpolated tbb-gbb data pairs at each soil
c           element
ccccccccccccccccccccccccccccccccccccccccccccccccccccccccccccccccccccc
      subroutine tginput(maxmx,mx,mbc,nptsmax,npt,z,tbb0,gbb0,
     &                tbb,gbb,tcur,gcur,gi)
      implicit double precision (a-h,o-z)
      parameter (ntgmax=25)          !# max number of tg backbone curves
      parameter (nptsinpmax=100)     !# max number of 1st quadrant input t-g pairs
```

```
c                                  !# (must be .ge. nptsmax)
      dimension ztg(ntgmax)
      dimension tinp(ntgmax,nptsinpmax),ginp(ntgmax,nptsinpmax)
      dimension z(1-mbc:maxmx+mbc),gi(maxmx)
      dimension tbb0(maxmx,nptsmax),gbb0(maxmx,nptsmax)
      dimension  tbb(maxmx,nptsmax), gbb(maxmx,nptsmax)
      dimension tcur(maxmx,nptsmax),gcur(maxmx,nptsmax)
c
c  initialize resident arrays
c
      do 10 jj=1,ntgmax
       ztg(jj) = 0.d0
       do 9 n=1,nptsmax
        tinp(jj,n) = 0.d0
        ginp(jj,n) = 0.d0
 9     continue
 10   continue
c
c  read the first quadrant t-g data
c
      read(22,*) ntg,npt
      do 11 jj=1,ntg
       read(22,*) ztg(jj)
 11   continue
      do 12 jj=1,ntg
       read(22,*) (ginp(jj,n),n=npt,2*npt-1)
       read(22,*) (tinp(jj,n),n=npt,2*npt-1)
 12   continue
c
c  extend the backbone curves to the third quadrants
c
      do 14 jj=1,ntg
       do 13 n=npt,2*npt-1
        tinp(jj,2*npt-n) = -tinp(jj,n)
        ginp(jj,2*npt-n) = -ginp(jj,n)
 13     continue
 14   continue
c
c  Interpolate to get backbone t-g curve at each soil element. Also,
c  make the current backbone curves (tcur,gcur) equal to the initial
c  backbone curves (tbb,gbb).  Finally, compute the initial stiffness.
c
      do 20 j=1,mx
       kdum=1
```

```
 17   continue
     if(z(j).ge.ztg(kdum).and.z(j).le.ztg(kdum+1)) then
      kk=kdum
      go to 18
     else
      kdum=kdum+1
      go to 17
     endif
 18   continue
     do 19 n=1,2*npt-1
      tbb0(j,n) = tinp(kk,n) + (tinp(kk+1,n)-tinp(kk,n))
   &          * (z(j)-ztg(kk)) / (ztg(kk+1)-ztg(kk))
      gbb0(j,n) = ginp(kk,n)
      tbb(j,n)  = tbb0(j,n)
      gbb(j,n)  = gbb0(j,n)
      tcur(j,n) = tbb0(j,n)
      gcur(j,n) = gbb0(j,n)
 19   continue
     gi(j) = tbb0(j,npt+1)/gbb0(j,npt+1)
 20  continue
    return
    end
cccccccccccccccccccccccccccccccccccccccccccccccccccccccccccccccccccc
c This subroutine keeps track of the hysteretic t-g behavior for all
c the soil elements. It evaluates the slope of the current t-g curves,
c g(j), and the current shear strain s(j), and returns these vectors
c back to the main loop of the program.
c
c In its current form (2/13/96), this routine is based on shear stress
c as the independent variable (tau(i) = q(i,1) in this formulation). Shear
c strain (s) and shear modulus (g) are computed via the modified Cundall
c Pyke hypothesis.
c
c Arrays passed to this routine are as follows:
c
c    tbb(j,m) gbb(j,m)  the backbone curves defining tau-gamma behavior
c    tcur(j,m) gcur(j,m) the current loading curve
c    dtau(1,j), the shear stress increment in the previous time step
c    dtau(2,j), the shear stress increment in the most recent time step
c    q(j,1) the shear stress in the most recent time step
c    q(j,2) the velocity in the most recent time step (not used here)
c
c Arrays returned to the Main Loop are as follows:
c
```

```
c     s(j) the shear strain in the most recent time step
c     g(j) the shear modulus in the most recent time step
c
c  Steve Kramer (BASIC). Modified and converted to FORTRAN by John Horne
cccccccccccccccccccccccccccccccccccccccccccccccccccccccccccccccccc
      subroutine hyster(maxmx,mbc,mx,meqn,nptsmax,npt,tbb,gbb,
     &             tcur,gcur,dtau,q,s,g,
     &             maux2,auxmat,sigveff)
      implicit double precision (a-h,o-z)
      dimension dtau(2,maxmx)
      dimension s(maxmx),g(maxmx)
      dimension q(1-mbc:maxmx+mbc,meqn)
      dimension tbb(maxmx,nptsmax),gbb(maxmx,nptsmax)
      dimension tcur(maxmx,nptsmax),gcur(maxmx,nptsmax)
      dimension auxmat(maxmx,maux2),sigveff(maxmx)
c
c     constants
c
      pi = 4.d0*datan(1.d0)
c
c     MAIN LOOP OF SUBROUTINE
c
      do 22 j=1,mx
c
c      STEP 0:  determine if we're out of range of the defined shear stresses
c             (This can happen with an explicit scheme)  If we are, then scale
c             the current curve upwards so that it's maximum is just 1% above
c             the shear stress value.
c
        mflag = 0
        ratio = dabs(q(j,1)) / tbb(j,2*npt-1)
        if(ratio.gt.1.d0)then
          write(*,*)'OUT OF RANGE: depth = ',j,' STRESS = ,',q(j,1)
          mflag = 1
          do 13, mrat=1,2*npt-1
            tcur(j,mrat) = tcur(j,mrat) * (1.001d0 * ratio)
 13       continue
        endif
c
c      determine direction of displacement in most recent time step.
c
        if(dtau(2,j).ge.0.d0)then
          dir =  1.d0        !# tau is increasing
        else
```

```
       dir = -1.d0         !# tau is decreasing
      endif
c
c     DETERMINE IF A REVERSAL HAS OCCURED IN THE
c     MOST RECENT TIME STEP
c
      if(dtau(1,j)*dtau(2,j).ge. -1.0d-100 )then
c
c     No Reversal!
c
c      STEP 1:  determine where we are on the current backbone curve:
c
       mdum=1
 14     continue
       if(q(j,1).ge.tcur(j,mdum).and.q(j,1).lt.tcur(j,mdum+1))
     &  then
        mm=mdum
        go to 15
       else
        mdum=mdum+1
        go to 14
       endif
 15     continue
c
c      STEP 2:  compute the tangent shear modulus and shear strain
c
       s(j) = s(j) + dtau(2,j)/g(j)
c
       ghyst = (tcur(j,mm+1) - tcur(j,mm)) /
     &         (gcur(j,mm+1) - gcur(j,mm))
       g(j)=dmin1(g(j)*2.d0,ghyst)
c
       if  ( dabs(q(j,1)/tbb(j,2*npt-2)) .gt. 1.d0
     &        .and. dir*q(j,1)         .gt. 0.d0)
     &     g(j) = (tcur(j,2*npt-1) - tcur(j,2*npt-2)) /
     &            (gcur(j,2*npt-1) - gcur(j,2*npt-2))
c
       g(j)  = dmax1(g(j),1.d0)
c
      else
c
c     A reversal has occured!
c
c      STEP 1: determine the reversal point (grev,trev)
```

```
c
      trev = q(j,1) - dtau(2,j)
      mdum=1
 16    continue
      if(trev.ge.tcur(j,mdum).and.trev.lt.tcur(j,mdum+1))
   &   then
       mm=mdum
       go to 17
      else
       mdum=mdum+1
       go to 16
      endif
 17    continue
      grev = gcur(j,mm) + (trev - tcur(j,mm)) *
   &   (gcur(j,mm+1) - gcur(j,mm)) / (tcur(j,mm+1) - tcur(j,mm))
c
c      STEP 2:  determine the scaling factor,
c      and re-compute the current backbone curve:
c
      c = dabs( dir - trev / tbb(j,2*npt-2) )     !# note the 2*npt-2 index!!!
c       c = dmax1(1.d0,dabs( dir - trev / tbb(j,2*npt-1) ) )
c
      do 18 m=1,2*npt-1
       gcur(j,m) = grev + c * gbb(j,m)
       tcur(j,m) = trev + c * tbb(j,m)
 18    continue
c-jch-5/28/96c
c-jch-5/28/96c      STEP 3:  adjust the new backbone curve to account for p'/pcs < 1
c-jch-5/28/96c
      bpcs = auxmat(j,9)          !# i.e. p'cs
      bko  = auxmat(j,10)         !# i.e. ko
      pp = (1.d0+bko)/2.d0*sigveff(j) !# i.e. p'
c-jch-5/28/96      if(pp/bpcs.le.1.d0.and.tcur(j,1)/tcur(j,2*npt-1).le.0.d0)then
c-jch-5/28/96       write(*,*)'BACKBONE CURVE ADJUST FOR LOW pp/pcs
AHEAD!!!!'
c-jch-5/28/96c
c-jch-5/28/96c       STEP 3(a): determine point 1
c-jch-5/28/96c
c-jch-5/28/96       mdum = npt + int(dir)
c-jch-5/28/96 30     if(dir*tcur(j,mdum).gt.0.d0)then
c-jch-5/28/96        m1 = mdum
c-jch-5/28/96        goto 35
c-jch-5/28/96       else
c-jch-5/28/96        mdum = mdum + int(dir)
```

```
c-jch-5/28/96          goto 30
c-jch-5/28/96         endif
c-jch-5/28/96 35       t1 = tcur(j,m1)
c-jch-5/28/96         g1 = gcur(j,m1)
c-jch-5/28/96c
c-jch-5/28/96c         STEP 3(b): determine point 2
c-jch-5/28/96c
c-jch-5/28/96         mdum = m1 + int(dir)
c-jch-5/28/96 40       if(dir*gcur(j,mdum).gt.-dir*grev)then
c-jch-5/28/96          m2 = mdum
c-jch-5/28/96          goto 45
c-jch-5/28/96         else
c-jch-5/28/96          mdum = mdum + int(dir)
c-jch-5/28/96          goto 40
c-jch-5/28/96         endif
c-jch-5/28/96 45       t2 = tcur(j,m2)
c-jch-5/28/96         g2 = gcur(j,m2)
c-jch-5/28/96c
c-jch-5/28/96c         STEP 3(c): compute coeffients for polynomial
c-jch-5/28/96c
c-jch-5/28/96         gchord = ( t2 - t1 ) / ( g2 - g1 )
c-jch-5/28/96         gi     = (tcur(j,npt+1) - tcur(j,npt))/
c-jch-5/28/96    &             (gcur(j,npt+1) - gcur(j,npt))
c-jch-5/28/96         gmax = 0.8 * gi
c-jch-5/28/96         gmin = 0.05 * gi
c-jch-5/28/96         ymax = gmax / gchord
c-jch-5/28/96c         ymin = gmin / gchord
c-jch-5/28/96         ymin = .1
c-jch-5/28/96         rat  = pp / bpcs
c-jch-5/28/96         ba   = rat + (1.-rat)*ymin
c-jch-5/28/96         bn   = rat + (1.-rat)*min(10.,(ymax-ymin)/(1.-ymin))
c-jch-5/28/96c
c-jch-5/28/96c         STEP 3(d): compute new tau-values from g1 to g2
c-jch-5/28/96c
c-jch-5/28/96         do 50 m=m1,m2,int(dir)
c-jch-5/28/96          x = (gcur(j,m)-g1) / (g2-g1)
c-jch-5/28/96          y = ba*x + (1.-ba)*x**bn
c-jch-5/28/96          tcur(j,m) = (t2-t1)*y + t1
c-jch-5/28/96 50       continue
c-jch-5/28/96        endif
c
c      STEP 4:  determine where along the new current curve we are located
c
      mdum=1
```

```
 19     continue
       if(q(j,1).ge.tcur(j,mdum).and.q(j,1).lt.tcur(j,mdum+1))
     &  then
        mm = mdum
        go to 21
       else
        mdum = mdum + 1
        go to 19
       endif
 21     continue
c
c       STEP 5:  compute the tangent shear modulus and shear strain
c
       s(j) = s(j) + dtau(2,j)/g(j)
c
       ghyst = (tcur(j,mm+1) - tcur(j,mm)) /
     &          (gcur(j,mm+1) - gcur(j,mm))
      g(j) = dmin1(g(j)*1.1d0,ghyst)
c
       if  ( dabs(q(j,1)/tbb(j,2*npt-2)) .gt. 1.d0
     &     .and.  dir*q(j,1)             .gt. 0.d0)
     &     g(j) = (tcur(j,2*npt-1) - tcur(j,2*npt-2)) /
     &            (gcur(j,2*npt-1) - gcur(j,2*npt-2))
c
       g(j) = dmax1(g(j),1.d0)
c
      endif
c
c     BEFORE YOU GO:  update "delta-tau" for the next time step
c
      dtau(1,j) = dtau(2,j)
 22  continue
 222  format(3e15.8)
     return
     end
ccccccccccccccccccccccccccccccccccccccccccccccccccccccccccccccccccccc
c Subroutine pore for computing pore pressure using energy based method
c
c       Robert Mitchell, 1994
c       slight modification by John Horne, 1996
c
c Integers Passed to this Subroutine:
c
c     jmax                  maxinum number of soil elements
```

```
c     jtot              actual number of soil elements
c     matmax            maxinum number of material parameters
c
c Material properties (which may vary with depth) are passed to this
c subroutine via an auxilliary array, auxm(j,m) (see the code below):
c
c       eo              initial void ratio
c       emin            minimum void ratio
c       sigvo           initial vertical effective overburden pressure
c       nu              coefficient from Nemat-Nasser paper(=0.001)
c       r1              coefficient from Nemat-Nasser paper(=2.5)
c       n1              coefficient from Nemat-Nasser paper(=3.5)
c       q_exp           exponent used in f2 funciton below  (=1.1)
c       n_deg           degradation exponent                (=0.5)
c
c Recent stress and strain history passed to this subroutine:
c
c       tauave(j)       average shear stress in the most recent time step
c     strdif(j)  incremental shear strain in the most recent time step
c
c Resident Variables Computed in this Subroutine:
c
c       r_u             pore pressure ratio
c       f2              funciton = (1+r_u)**r1*(1-r_u)**q_exp
c       d_wk            incremental work done
c       d_u             incremental pore pressure
c
c Arrays returned to the subroutine call
c
c       deg(j)          tau-gamma curve degradation coefficient
c       u(j)            excess pore pressure
c
cccccccccccccccccccccccccccccccccccccccccccccccccccccccccccccccccccccc
      subroutine pore(jmax,mbc,jtot,matmax,auxm,told,gold,tnew,gnew,
     &             t0,u,deg)
      implicit double precision (a-h,o-z)
      dimension auxm(jmax,matmax),tnew(jmax),gnew(jmax)
      dimension gold(jmax),told(jmax)
      dimension u(1-mbc:jmax+mbc),deg(jmax),t0(jmax)
c
      do 30 j=1,jtot
c
c      recover material properties from the auxm array
c
```

```
      eo    = auxm(j,1) !# initial void ratio
      emin  = auxm(j,2)       !# minimum void ratio
      sigvo = auxm(j,3)       !# initial vertical eff. stress
      anu   = auxm(j,4)       !# parameter "nu"
      ar1   = auxm(j,5)       !# parameter "r1"
      an1   = auxm(j,6)       !# parameter "n1"
      aq    = auxm(j,7)       !# parameter "q"
      adeg  = auxm(j,8)       !# parameter "n_deg"
c
c     compute incremental work via trapezoidal rule
c
        d_wk = ((tnew(j) + told(j))/2.d0  - t0(j))* (gnew(j) - gold(j))
c
c     compute incremental pore pressure
c
c     Note the following about the f2 function:
c      1. use f(1+p) function equal to (1+p)^r*(1-p)^q
c      2. this is a modified f(1+p) function from Nemat-Nassar paper
c
      r_u = u(j)/sigvo
        f2 = (1.d0 + r_u)**ar1 * (dmax1(1.d0 - r_u,0.d0))**aq
        d_u = sigvo * (f2*(eo-emin)**an1) * d_wk/(anu*eo)
c
c     compute degradation parameter
c
        deg(j) = (dmax1(1.d0-r_u,0.d0))**adeg
c
c     update excess pore pressure
c
        u(j) = u(j) + d_u
        u(j) = dmax1(u(j),0.d0)
c
 30   continue
      return
      end
cccccccccccccccccccccccccccccccccccccccccccccccccccccccccccccccccc
c This routine degrades the backbone curves as pore pressure increases
c
c It does so by knocking down the tau-coordinates of the original back-
c bone curves, tbb0(i,j).  However, the amount of degradation is limited
c by the steady state shear strength, tss.
c
c Note that deg(i) is 1.0 initially, and degrades to zero when u_excess
c approaches sig'_vo.
```

```
c
c Variables passed to degrade():
c  maxmx       integer      maxinum no. of soil elements
c  mx          integer      actual number of soil elements
c  maux2       integer      no. of parameters stored in auxmat array
c  nptsmax     integer      maxinum no. of pairs per backbone curve
c  npt         integer      actual no. of pairs per backbone curve
c  auxmat      real array   auxillary array which stores the material
c                           properties for each soil element
c  tbb0        real array   initial tau-coordinates of each bb curve
c
c Variables returned to main loop:
c  tbb         real array   degraded tau-coordinates of each bb curve
c
cccccccccccccccccccccccccccccccccccccccccccccccccccccccccccccccccccc
      subroutine degrade(maxmx,mx,maux2,nptsmax,npt,auxmat,tbb0,deg,tbb)
      implicit double precision (a-h,o-z)
      dimension deg(maxmx)
      dimension tbb(maxmx,nptsmax),tbb0(maxmx,nptsmax)
      dimension auxmat(maxmx,maux2)
      do 20 i=1,mx
        tss = auxmat(i,9)*auxmat(i,11)          !# i.e. t_ss = q_cs = M*p'_cs
        rat = dmin1(tss/tbb0(i,2*npt-2),1.d0)      !# ratio of t_ss / t_max0
        do 10 j=1,2*npt-1
          tbb(i,j) = tbb0(i,j) * (1.d0 -(1.d0-deg(i))*(1.d0-rat))
 10     continue
 20   continue
      return
      end
cccccccccccccccccccccccccccccccccccccccccccccccccccccccccccccccccccc
c This subroutine envokes the user-specified drainage b.c.'s
c  for the consolidation computations
cccccccccccccccccccccccccccccccccccccccccccccccccccccccccccccccccccc
      subroutine bccon(bctop,bcbot,icon,mbc,maxmx,mx,u)
      implicit double precision (a-h,o-z)
      dimension u(1-mbc:maxmx*mbc)
      character bctop*6,bcbot*6
      if(bctop.eq.'drain1') u(0)    = -u(icon)     !# drained
      if(bctop.eq.'drain0') u(0)    =  u(icon)     !# undrained
      if(bcbot.eq.'drain1') u(mx+1) = -u(mx)     !# drained
      if(bcbot.eq.'drain0') u(mx+1) =  u(mx)     !# undrained
      return
      end
cccccccccccccccccccccccccccccccccccccccccccccccccccccccccccccccccccc
```

```
c This subroutine takes a time step on the parabolic consolidation
c PDE. (based on FDE procedure in SK notes)
cccccccccccccccccccccccccccccccccccccccccccccccccccccccccccccccc
      subroutine constep(mbc,maxmx,mx,maux2,icon,auxmat,dx,dt,u)
      implicit double precision (a-h,o-z)
      dimension u(1-mbc:maxmx*mbc),auxmat(maxmx,maux2)
c
c     COMPUTE THE RESPONSE FOR THE FIRST GRID POINT BELOW THE GWT
c
c     compute constants used in the FDE
c
      alpha1 = auxmat(icon,13)/dx           !# Note: column 13 = K
      beta1  = auxmat(icon,12)*dt/dx**2.d0   !# Note: column 12 = Cv
      alpha2 = auxmat(icon+1,13)/dx
      beta2  = auxmat(icon+1,12)*dt/dx**2.d0
      coeff = 2.d0 * beta1*beta2 / (beta2*alpha1 + beta1*alpha2)
      anum  = coeff * alpha1
      bnum  = coeff * (alpha1+alpha2)/2.d0
      cnum  = coeff * alpha2
c
c     update u via the FDE
c
      du = anum*u(0) - 2.d0*bnum*u(icon) + cnum*u(icon+1)
      u(icon) = u(icon) + du
c
c     COMPUTE THE RESPONSE FOR THE REMAINING GRID POINTS
c
      do 20 i=icon+1,mx
c
c      compute constants used in the FDE
c
       alpha1 = auxmat(i,13)/dx           !# Note: column 13 = K
       beta1  = auxmat(i,12)*dt/dx**2.d0   !# Note: column 12 = Cv
       if(i.lt.mx) then
        alpha2 = auxmat(i+1,13)/dx
        beta2  = auxmat(i+1,12)*dt/dx**2.d0
c         write(*,*)'alpha2,beta2 = ',alpha2,beta2
       else
        alpha2 = alpha1
        beta2  = beta1
       endif
c
       coeff = 2.d0 * beta1*beta2 / (beta2*alpha1 + beta1*alpha2)
c
```

```
      anum  = coeff * alpha1
      bnum  = coeff * (alpha1+alpha2)/2.d0
      cnum  = coeff * alpha2
c
c      update u via the FDE
c
      du = anum*u(i-1) - 2.d0*bnum*u(i) + cnum*u(i+1)
      u(i) = u(i) + du
c
 20   continue
     return
     end
cccccccccccccccccccccccccccccccccccccccccccccccccccccccccccccccccc
c This routine computes the cumulative settlement at the ground surface
c as the excess pore pressures dissapate
cccccccccccccccccccccccccccccccccccccccccccccccccccccccccccccccccc
     subroutine settle(maxmx,mx,maux2,auxmat,dx,sigold,signew,dhtot)
     implicit double precision (a-h,o-z)
     dimension auxmat(maxmx,maux2)
     dimension signew(maxmx),sigold(maxmx)
     do 20 i=1,mx
      cre = auxmat(i,14)      !# rebound modulus
      if(sigold(i).le.0.d0) then
       pratio = 1.d0
      else
       pratio = signew(i)/sigold(i)
      endif
      dhtot = dhtot + dx * cre * dlog10(pratio)
 20   continue
     return
     end
cccccccccccccccccccccccccccccccccccccccccccccccccccccccccccccccccc
c    This function computes the increment in time (cpu sec)
c    based on the hrs, min, sec, hundredths, passed to it
c    in the argument list
cccccccccccccccccccccccccccccccccccccccccccccccccccccccccccccccccc
     double precision function getdt(ihr,imin,isec,ihun)
     implicit real*8(a-h,o-z)
      getdt = dfloat(ihr)*3600.d0
    &       + dfloat(imin)*60.d0
    &       + dfloat(isec)
    &       + dfloat(ihun)/100.d0
     return
     end
```

**Appendix C: FORTRAN Listing - Pile Response Code**

```
cccccccccccccccccccccccccccccccccccccccccccccccccccccccccccccccccccc
c  Program DYNOPILE
c  University of Washington
c  John Horne and Professor Steven Kramer
c  1996
cccccccccccccccccccccccccccccccccccccccccccccccccccccccccccccccccccc
      program dynopile
      implicit double precision (a-h,o-z)
      parameter (jmax=50)
      parameter (nptsmax=27)
c
      real emod,inert,length,diam,area,axload,wpile,rhopile,mpile,dz,dt
      real dr,r0,dt0
c
      integer jtot,npile,kt,ktime
      integer kprint0,ktime0,icount
      integer npt,mtype,ndiv,iflag
c
      character bchead*3,bctoe*3
c
      dimension z(jmax),v(3,jmax),ydel(2,jmax)
      dimension unf(2,jmax),vnf(2,jmax)
      dimension ddp(jmax), dvp(jmax), dap(jmax)
      dimension ddff(jmax),dvff(jmax)
      dimension ffd(2,jmax),ffv(2,jmax),ffu(2,jmax),gmod(jmax)
      dimension bend(jmax),shear(jmax),rho(jmax)
      dimension pbb0(jmax,nptsmax),ybb0(jmax,nptsmax)
      dimension pbb(jmax,nptsmax),ybb(jmax,nptsmax)
      dimension pcur(jmax,nptsmax),ycur(jmax,nptsmax)
      dimension stiff(jmax),damp(jmax),ppile(jmax)
      dimension d1(jmax),v1(jmax),u1(jmax),g1(jmax)
      dimension d2(jmax),v2(jmax),u2(jmax),g2(jmax)
      real*8 mn11(jmax),gini(jmax),stiffini(jmax)
c
      common /piledat/ emod,inert,length,diam,area,axload,
     &             wpile,rhopile,mpile,dz,dt
      common /gravity/ grav
c
c   INPUT FILES
c
      open(21,file='pile.dat',status='unknown')      !# The basic pile data file
      open(22,file='ground.dat',status='unknown')  !# only used if mytype = 2 or 3
```

```
      open(23,file='py.dat',status='unknown')        !# py backbone curves
c
c     the following are only used for ntype=1 (far-field model envoked)
c
      open(31,file='freedisp.dat',status='unknown')  !# free field displacement
      open(32,file='freevelo.dat',status='unknown')  !# free field velocitie
      open(33,file='freepore.dat',status='unknown')  !# free field excess pore pressure ratio
      open(34,file='freegmod.dat',status='unknown') !# free field shear modulus
      open(35,file='freegamm.dat',status='unknown') !# free field soil unit weight
      open(36,file='freegini.dat',status='unknown')  !# free field initial shear moduli
c
c     OUTPUT FILES:
c
      open(24,file='pdepth.out',status='unknown')    !# pile depth vector
      open(25,file='pdisp.out',status='unknown')     !# pile displacement response
      open(26,file='pbend.out',status='unknown')     !# pile bending moment response
      open(27,file='pshear.out',status='unknown')    !# pile shear force response
      open(28,file='pyforce.out',status='unknown')   !# pile-soil interaction force response...
...   (at selected elements only - see the MAIN LOOP for details here)
c
c     Read the pile data.  Note units!
c     (F,L,T = Force, Length, and Time, respectively)
c
c     mtype, -      ntype, -
c     grav, L/T^2
c     emod, F/L^2   inert, L^4    length, L    diam, L
c     axload, F     wpile, F/L^3
c     dz, L         dt, sec       ktime, -     kprint, -
c     dr, -
c
c     Axload is positive for compressive loads
c     For fixed head(toe) - zero rotation, bchead(bctoe) = 'fix'
c     For pinned head(toe) - zero moment,  bchead(bctoe) = 'pin'
c     Length must be a multiple of dz  (npile = length/dz)
c
      read(21,*) mtype,ntype
      read(21,*) grav
      read(21,*) emod,inert,length,diam
      read(21,*) axload,wpile
      read(21,*) dz,dt0,ktime0,kprint0
      read(21,*) bchead
      read(21,*) bctoe
      read(21,*) dr
      write(*,*)'done reading pile data'
```

```
c
c   Initialize the grid, boundary conditions, and other arrays
c
c   compute area of pile, radius of pile, density of pile (per unit volume)
c   and mass of mass per unit length
c
      area    = datan(1.d0)*diam**2.d0
      r0      = diam/2.d0
      rhopile = wpile/grav
      mpile   = rhopile*area
      write(*,*)'pile   total length is',length
      write(*,*)'pile element length is',dz
      npile = idint((length+1.d-6)/dz) + 1
      write(*,*)'number of pile elements is',npile
c
c   these parameters are initialized here, but change if an instability is encountered
c
      iflag = 1
      ndiv  = 1
      dt    = dt0
      ktime  = ktime0
c
c   construct the depth vector
c
      jtot = npile + 4
      do 13 j=3,jtot-2
        z(j) = (dfloat(j)-3.d0)*dz
 13   continue
      write(24,1000) (z(j), j=3,jtot-2)   !# output the depth vector
 1000 format(100e15.8)
c
c   flow returns here if instability is encountered
c
 14   continue
      do 17 j=1,jtot
        mn11(j)     = 0.d0
        ppile(j)    = 0.d0
        stiff(j)    = 0.d0
        rho(j)      = 0.d0
        gmod(j)     = 0.d0
        ddp(j)      = 0.d0
        dvp(j)      = 0.d0
        dap(j)      = 0.d0
        ddff(j)     = 0.d0
```

```
      dvff(j)    = 0.d0
      bend(j)    = 0.d0
      shear(j)   = 0.d0
      d1(j) = 0.d0
      v1(j) = 0.d0
      u1(j) = 0.d0
      g1(j) = 0.d0
      d2(j) = 0.d0
      v2(j) = 0.d0
      u2(j) = 0.d0
      g2(j) = 0.d0
      do 15 i=1,3
       v(i,j)  = 0.d0
 15    continue
      do 35 i=1,2
       unf(i,j)  = 0.d0
       vnf(i,j)  = 0.d0
       ffd(i,j)  = 0.d0
       ffv(i,j)  = 0.d0
       ffu(i,j)  = 0.d0
       ydel(i,j) = 0.d0
 35    continue
      do 16 n=1,nptsmax
       pbb0(j,n) = 0.d0
       ybb0(j,n) = 0.d0
       pbb(j,n)  = 0.d0
       ybb(j,n)  = 0.d0
       pcur(j,n) = 0.d0
       ycur(j,n) = 0.d0
 16    continue
 17   continue
     call bc(v,jtot,bchead,bctoe)
     write(*,*)'done initializing arrays and boundary conditions'
ccccccccccccccccccccccccccccccccccccccccccccccccccccccccccccccccccccc
c  Input p-y data which defines the backbone of hysteretic p-y curves.
c  This data is then extended to the third quadrant in p-y space and
c  finally interpolated to obtain a p-y curve for each pile element.
c  Additionally, the initial (pcur,ycur) arrays are returned.
ccccccccccccccccccccccccccccccccccccccccccccccccccccccccccccccccccccc
     call pyinput(jtot,z,npt,pbb0,ybb0,pbb,ybb,pcur,ycur)
     write(*,*)'done inputting p-y curves'
     if(ntype.eq.1)then
      read(36,*)(gini(j),j=3,jtot-2)
      call pyscale(jtot,npt,gini,pbb0,ybb0,ybb,ycur)
```

```
     write(*,*)'done scaling p-y curves to account for far field'
    endif
    do 18, j=3,jtot-2
     stiffini(j)= pcur(j,npt+1)/ycur(j,npt+1)  !# initial p-y stiffness
     damp(j) = dr*2.d0*dsqrt(stiffini(j)*mpile) !# dashpot coefficient
 18  continue
cccccccccccccccccccccccccccccccccccccccccccccccccccccccccccccccccccc
c
c  MAIN LOOP
c
cccccccccccccccccccccccccccccccccccccccccccccccccccccccccccccccccccc
    call output(jtot,v,bend,shear)       !# write initial conditions
    vmax=0.d0
c
c    BEGIN MACRO LOOP
c
    do 27 kt=1,ktime0
     call field(kt,dt,jtot,mtype,z,d2,v2,u2,g2,rho)     !# free field motion
c
c     BEGIN MICRO LOOP
c
     do 25 i=1,ndiv
      ti=dfloat(i)/dfloat(ndiv)
      icount = ndiv*(kt-1) + i
      if(mod(icount,1000).eq.0) write(*,*)'STEP',icount,' OF',ktime
      do 19 j=3,jtot-2
c
c       linear interpolation is used to obtain values in the micro timesteps
c
       ffd(2,j) = d1(j) + (d2(j)-d1(j)) * i / ndiv !# displacement
       ffv(2,j) = v1(j) + (v2(j)-v1(j)) * i / ndiv !# velocity
       if(kt.eq.1) then
        gmod(j)  = g2(j) !# shear modulus
        ffu(2,j) = u2(j) !# pore pressure ratio
       else
        ffu(2,j) = u1(j) + (u2(j)-u1(j)) * i / ndiv !# pore pressure ratio
        gmod(j)  = g1(j) + (g2(j)-g1(j)) * i / ndiv !# shear modulus
       endif
c
c       compute the increments of free-field displacement and velocity
c
       ddff(j)  = ffd(2,j) - ffd(1,j)
       dvff(j)  = ffv(2,j) - ffv(1,j)
 19    continue
```

```
c
c      IF ntype = 1, THEN THE FAR FIELD MODEL IS ENVOKED HERE
c
       if(ntype.eq.1) then
        do 20 j=3,jtot-2
         ydel(2,j) = unf(2,j) - v(2,j)
 20      continue
        call kvalue(jtot,icount,npt,pbb,ybb,pcur,ycur,ydel,stiff)  !# near field stiffness
        do 22 j=3,jtot-2
         if(stiff(j).gt.stiffini(j)) stiff(j)=stiffini(j)
 22      continue
        call nogami(jtot,icount,dt,r0,dr,mpile,mn11,damp,stiff,ddp,
    &             dvp,dap,ddff,dvff,gmod,rho,unf,ppile,vnf)  !# pile load & near field
              displacement
        call tstep(jtot,icount,ppile,mn11,damp,v,vnf,ddp,dvp,dap)  !# pile displacement
        call degrade(jtot,npt,ffu,pbb0,pbb)
c
c      IF ntype = 2 THEN NO FAR FIELD MODEL IS USED
c
       elseif(ntype.eq.2) then                              !# no far-field model
        do 23 j=3,jtot-2
         ydel(2,j) = ffd(2,j) - v(2,j)
 23      continue
        call kvalue(jtot,icount,npt,pbb,ybb,pcur,ycur,ydel,stiff)  !# near field stiffness
        call nofar(jtot,stiff,ddp,ddff,ppile)                  !# pile load
        call tstep(jtot,icount,ppile,mn11,damp,v,ffv,ddp,dvp,dap)  !# pile displacement
        call degrade(jtot,npt,ffu,pbb0,pbb)
       endif
c
c      OUTPUT PILE-SOIL INTERACTION FORCE AT SELECTED DEPTHS
c
       if(i.eq.ndiv) then
        write(28,110)
    &    ppile(7),  ffd(2,7)-v(2,7),  ppile(23), ffd(2,23)-v(2,23),
    &    ppile(28), ffd(2,28)-v(2,28), ppile(29), ffd(2,29)-v(2,29)
       endif
 110    format(8e12.5)
c
c      APPLY APPROPRIATE BOUNDARY CONDITIONS
c
       call bc(v,jtot,bchead,bctoe)
c
c      COMPUTE SHEAR FORCES AND BENDING MOMENTS
c
```

```
      call forces(jtot,v,bend,shear)
c
c      UPDATE MICRO TIME STEP VARIABLES HERE
c
      do 24 j=3,jtot-2
       if(abs(v(3,j)).gt.vmax) vmax=abs(v(3,j))      !# used for instabilty check
       ffd(1,j)  = ffd(2,j)                  !# free field displacement
       ffv(1,j)  = ffv(2,j)                  !# free field velocity
       ffu(1,j)  = ffu(2,j)                  !# free field pore pressure
       ydel(1,j) = ydel(2,j)                 !# pile/ff or pile/nf relative displacement
 24    continue
c
c      CHECK FOR INSTABILITY HERE
c
      if(vmax.gt.10.)then                              !# instability detection
       write(*,*)' '
       write(*,*)'UNSTABLE: t-step = ',kt,' max disp = ',int(vmax)
       iflag  = iflag + 1
       ndiv   = 2**(iflag-1)
       dt     = dt0 / dfloat(ndiv)
       ktime  = ndiv * ktime0
       write(*,*)'ndiv =',ndiv,'  new dt=',dt,'  new ktime =',ktime
       if(ndiv.gt.2000) then
        write(*,*)'NDIV exceeds 4000 - program terminating'
        goto 28
       endif
       rewind(21)
       rewind(22)
       rewind(23)
       rewind(24)
       rewind(25)
       rewind(26)
       rewind(27)
       rewind(28)
       rewind(31)
       rewind(32)
       rewind(33)
       rewind(34)
       rewind(35)
       rewind(36)
       goto 14
      endif
c
 25   continue
```

```
c
c    END OF MICRO LOOP
c
c    WRITE SELECTED OUTPUT
c
      if(mod(kt,kprint0).eq.0) then
        call output(jtot,v,bend,shear)
      endif
c
c    UPDATE MACRO TIME STEP VARIABLES HERE
c
      do 26 j=3,jtot-2
       d1(j) = d2(j)
       v1(j) = v2(j)
       u1(j) = u2(j)
       g1(j) = g2(j)
 26    continue
 27   continue
c
c   END MACRO LOOP
c
 28   continue
     stop
     end
cccccccccccccccccccccccccccccccccccccccccccccccccccccccccccccccccccccc
cccccccccccccccccccccccccccccccccccccccccccccccccccccccccccccccccccccc
cccccccccccccccccccccccccccccccccccccccccccccccccccccccccccccccccccccc
ccccc                                  ccccccccccccccccccccccccccccccc
ccccc  SUBROUTINES APPEAR BELOW        ccccccccccccccccccccccccccccccc
ccccc                                  ccccccccccccccccccccccccccccccc
cccccccccccccccccccccccccccccccccccccccccccccccccccccccccccccccccccccc
cccccccccccccccccccccccccccccccccccccccccccccccccccccccccccccccccccccc
cccccccccccccccccccccccccccccccccccccccccccccccccccccccccccccccccccccc
c
cccccccccccccccccccccccccccccccccccccccccccccccccccccccccccccccccccccc
c This subroutine develops initial p-y backbone curves for each pile
c element.  This is done by first reading p-y data pairs defined at up
c to 10 depths within the stratum.  Each p-y curve may be constructed
c of up to (nptsmax+1)/2 first quadrant p-y data pairs.  Secondly, this first
c quadrant data is extended to the third quadrant.  Finally, linear
c interpolation is used to obtain pbb-ybb curves between the depths at
c which the individual p-y curves are defined.
c
c Note the following variables and units:
```

```
c   npy = number of p-y curves in the stratum
c   npt = number of first quadrant p-y data points for each curve
c   zpy(jj) = depth of the jjth p-y curve (L)
c   y(jj,n) = nth displacment of the jjth p-y curve (L)
c   p(jj,n) = nth 'force' of the jjth p-y curve (F/L)
c   pbb0(jtot-4,2*npt-1) = interpolated p-values for each pile element
c   ybb0(jtot-4,2*npt-1) = corresponding y-values for each pile element
c   jtot-4 =  number of pile elements for which interpolated curves
c           will be constructed
c   2*npt-1 = number of interpolated pbb-ybb data pairs at each pile
c           element
cccccccccccccccccccccccccccccccccccccccccccccccccccccccccccccccccccccc
      subroutine pyinput(jtot,z,npt,pbb0,ybb0,pbb,ybb,pcur,ycur)
      implicit double precision (a-h,o-z)
      parameter (jmax=50)
      parameter (nptsmax=27)
      parameter (npymax=8)
      integer npt,jtot
      dimension zpy(npymax),p(npymax,nptsmax),y(npymax,nptsmax)
      dimension z(jmax),pbb0(jmax,nptsmax),ybb0(jmax,nptsmax)
      dimension pbb(jmax,nptsmax),ybb(jmax,nptsmax)
      dimension pcur(jmax,nptsmax),ycur(jmax,nptsmax)
c
c    initialize resident arrays
c
      do 10 jj=1,npymax
        zpy(jj) = 0.d0
        do 9 n=1,nptsmax
          p(jj,n) = 0.d0
          y(jj,n) = 0.d0
 9      continue
 10   continue
c
c    read the first quadrant p-y data
c
      read(23,*) npy,npt
      do 11 jj=1,npy
        read(23,*) zpy(jj)
 11   continue
      do 12 jj=1,npy
        read(23,*) (y(jj,n),n=npt,2*npt-1)
        read(23,*) (p(jj,n),n=npt,2*npt-1)
 12   continue
c
```

```
c    This allows for preliminary scaling of y-coordinates.  Currently, the
c    factor is set at 1.0
c
      factor = 1.d0
      do 25 jj=1,npy
       do 24 n=npt,2*npt-1
        y(jj,n) = y(jj,n)*factor
 24    continue
 25   continue
c
c    extend the backbone curves to the third quadrants
c
      do 14 jj=1,npy
       do 13 n=npt,2*npt-1
        p(jj,2*npt-n) = -p(jj,n)
        y(jj,2*npt-n) = -y(jj,n)
 13    continue
 14   continue
c
c    Interpolate to get backbone p-y curve at each pile element. Also,
c    make the current backbone curves (pcur,ycur) equal to the initial
c    backbone curves (pbb,ybb).  Finally, compute the initial stiffness.
c
      do 20 j=3,jtot-2
       kdum=1
 17    continue
       if(z(j).ge.zpy(kdum).and.z(j).le.zpy(kdum+1)) then
        kk=kdum
        go to 18
       else
        kdum=kdum+1
        go to 17
       endif
 18    continue
       do 19 n=1,2*npt-1
        pbb0(j,n) = p(kk,n) + (p(kk+1,n)-p(kk,n))
     &            * (z(j)-zpy(kk)) / (zpy(kk+1)-zpy(kk))
        ybb0(j,n) = y(kk,n)
        pcur(j,n) = pbb0(j,n)
        pbb(j,n)  = pbb0(j,n)
        ycur(j,n) = ybb0(j,n)
        ybb(j,n)  = ybb0(j,n)
 19    continue
 20   continue
```

```
      return
      end
cccccccccccccccccccccccccccccccccccccccccccccccccccccccccccccccccccc
c  This routine is only called for runs using the Nogami far field model
c
c  This subroutine scales the original py curves so that when they are
c  used with the stiffness of the far-field model, the correct static
c  stiffness is retained.
cccccccccccccccccccccccccccccccccccccccccccccccccccccccccccccccccccc
      subroutine pyscale(jtot,npt,gmod,pbb0,ybb0,ybb,ycur)
      implicit double precision (a-h,o-z)
      parameter(jmax=50)
      parameter(nptsmax=27)
      dimension pbb0(jmax,nptsmax),ybb0(jmax,nptsmax)
      dimension ybb(jmax,nptsmax),ycur(jmax,nptsmax)
      dimension gmod(jmax)
      real*8 kpy,kff,kfac,sf
c
c   This constant also appears in subroutine NOGAMI, so if it
c   is changed here, it MUST be changed there (and vice-versa)
c
      kfac = 2.d0                    !# assumes poisson's ratio = 1/2
c
c   MAIN LOOP OF THE SUBROUTINE
c
      do 40 j=3,jtot-2
       kpy = pbb0(j,npt+1)/ybb0(j,npt+1)  !# unscaled py-curve initial stiffness
       kff = kfac*gmod(j)/0.744d0         !# far-field static stiffness
       if(kpy/kff.lt.1.d0)then
        sf = 1.d0/(1.d0-kpy/kff)          !# scaling factor
       else
        write(*,*)' At depth index = ',j,', the initial py stiffness'
        write(*,*)' is greater than the initial far field stiffness'
        write(*,*)' (which is based on the initial shear moduli).'
        write(*,*)' The scale factor (in theory) is negative.'
        write(*,*)' Program is setting the scale factor to 1.0'
        sf = 1.d0                         !# scaling factor
       endif
       do 30 n=1,2*npt-1
        ybb0(j,n) = ybb0(j,n)/sf          !# scaled, original backbone curve
        ybb(j,n)  = ybb0(j,n)             !# ditto for the degraded-curve-to-be
        ycur(j,n) = ybb0(j,n)             !# ditto for the current curve
30     continue
40    continue
```

```
      return
      end
ccccccccccccccccccccccccccccccccccccccccccccccccccccccccccccccccc
c  subroutine DEGRADE degrades the backbone curves as a function of
c  excess pore pressure ratio in the free field
ccccccccccccccccccccccccccccccccccccccccccccccccccccccccccccccccc
      subroutine degrade(jtot,npt,u,pbb0,pbb)
      implicit double precision (a-h,o-z)
      parameter(jmax=50)
      parameter(nptsmax=27)
      dimension u(2,jmax),pbb(jmax,nptsmax),pbb0(jmax,nptsmax)
      do 40 j=3,jtot-2
c
c       BACKBONE CURVE DEGRADATION DUE TO PORE PRESSURES
c
c       This is done by scaling-down the p-coordinates of the original
c       backbone curves.
c
c       A simple linear relation suggested by the centrifuge work of
c       Liu & Dobry at RPI is used
c
       cu = dmin1( 1.d0 , 1.1d0 - u(2,j) )   !# with this expression, note that: at u=0%
c                                                cu=100%, and at u=100%, cu=10%
       do 30 n=1,2*npt-1
        pbb(j,n) = cu*pbb0(j,n)
 30     continue
 40    continue
      return
      end
ccccccccccccccccccccccccccccccccccccccccccccccccccccccccccccccccc
c This subroutine inputs or computes the free field motion for the next
c time step, depending on the value of mtype passed to it.
c
c Note that not all arrays are needed for all values of ntype: For a
c linear free field with harmonic loading (mtype=2)
ccccccccccccccccccccccccccccccccccccccccccccccccccccccccccccccccc
      subroutine field(kt,dt,jtot,mtype,z,dnew,vnew,unew,gnew,rho)
      implicit double precision (a-h,o-z)
      parameter (jmax=50)
      dimension dnew(jmax),vnew(jmax),unew(jmax)
      dimension gnew(jmax),rho(jmax),z(jmax)
      common /gravity/ grav
      real dt
      integer jtot,kt
```

```
      integer mtype
      if(mtype.eq.1)  then
        read(31,*) (dnew(j) , j=3,jtot-2)   !# displacement
        read(32,*) (vnew(j) , j=3,jtot-2)   !# velocity
        read(33,*) (unew(j) , j=3,jtot-2)   !# pore pressure ratio
        read(34,*) (gnew(j) , j=3,jtot-2)   !# shear modulus
        if(kt.eq.1) then
          read(35,*) (rho(j) , j=3,jtot-2)     !# note this is a unit weight, not a density
          do 11 j=3,jtot-2
            rho(j)=rho(j)/grav                 !# convert from unit weight to density
 11         continue
        endif
      elseif(mtype.eq.2) then
        call comrespo(jtot,kt,dt,z,dnew,vnew,rho)
      elseif(mtype.eq.3) then
        call lateral(jtot,kt,ktime,z,dnew)
      endif
      return
      end
ccccccccccccccccccccccccccccccccccccccccccccccccccccccccccccccccccccc
c  This subroutine was written to aid in the verification runs of
c  program DYNOPILE.  It uses the complex response method to compute the
c  displacements induced by vertically-propagating shear waves in a two
c  layer soil stratum.
c
c  jtot, kt, dt, and z(j) are passed to the routine. ffd(2,j) is
c  calculated and returned to the main program.
c
c  version 6 9/95 - subroutine also computes the free field velocity
c  ffv(2,j) and returns this as well
ccccccccccccccccccccccccccccccccccccccccccccccccccccccccccccccccccccc
      subroutine comrespo(jtot,kt,dt,z,ffd,ffv,rho)
      implicit double precision (a-h,o-z)
      parameter (jmax=50)
      dimension ffd(2,jmax),ffv(2,jmax),z(jmax),rho(jmax)
      complex*16 eye,one,cg1,cg2,ck1,ck2,calpha,canum,cbnum,ccnum,cdnum
      complex*16 u(jmax),v(jmax)
      real dt,omega,amp,g1,gam1,d1,h1,g2,gam2,d2,h2
      real c1,c2,tfact
      integer jtot,kt
      common /cmplxdat/ amp,omega
      common /gravity/ grav
c
c     input data for the first time step only
```

```
c
c    omega (rad/s) = circular frequency of the bedrock motion
c    amp (in) = displacment amplitude of the bedrock motion
c    g1, g2 (psi) = shear moduli of layers 1 & 2, respectively
c    gam1, gam2 (pci) = unit weight of soil in layers 1 & 2, respectively
c    d1, d2 (-) = damping ratios of soil in layers 1 & 2, respectively
c    h1, h2 (in) = thickness of soil layers 1 & 2, respectively
c
c    constants are computed for the first time step, and are left
c    unchanged for all subsequent time steps.
c
      if(kt.eq.1)then
        read(22,*)omega,amp
        read(22,*)g1,gam1,d1,h1
        read(22,*)g2,gam2,d2,h2
        do 11 j=3,jtot-2
          if(z(j).le.h1) rho(j)=gam1/grav
          if(z(j).gt.h1) rho(j)=gam2/grav
 11       continue
        eye = (0.,1.)
        one = (1.,0.)
        cg1 = g1*(one + 2.*d1*eye)
        cg2 = g2*(one + 2.*d2*eye)
        ck1 = omega*one*cdsqrt(gam1/grav/cg1)
        ck2 = omega*one*cdsqrt(gam2/grav/cg2)
        calpha = (ck1*cg1)/(ck2*cg2)
        canum = (one+calpha)*cdexp(eye*ck1*h1)
     &        + (one-calpha)*cdexp(-eye*ck1*h1)
        cbnum = (one-calpha)*cdexp(eye*ck1*h1)
     &        + (one+calpha)*cdexp(-eye*ck1*h1)
        ccnum = canum*cdexp(eye*ck2*h2) + cbnum*cdexp(-eye*ck2*h2)
      endif
c
c    for each time step, the response is calculated throughout the two
c    soil layers using the following statements.
c
c    tfact is the butterworth filter which varies from 0 at t=0 to one
c    over approximately 2*c1 time steps.
c
      cdnum = amp*one*cdexp(eye*omega*kt*dt)
      c1 = 16.d0*dt
      c2 = 1.5d0
      tfact = 1.d0
c       tfact = (1.d0 - 1.d0/((1.d0 + (dt*(kt-1)/c1)**c2)**.5d0))
```

```
      do 12 j=3,jtot-2
        if(z(j).le.h1)then
          u(j) = 2.*one*(cdexp(eye*ck1*z(j))
     &        + cdexp(-eye*ck1*z(j)))*cdnum/ccnum
        else
          u(j) = (canum*cdexp(eye*ck2*(z(j)-h1))
     &        + cbnum*cdexp(-eye*ck2*(z(j)-h1)))*cdnum/ccnum
        endif
        v(j) = tfact*eye*omega*u(j)
        ffd(2,j) = tfact*real(u(j))
        ffv(2,j) = tfact*real(v(j))
 12   continue
      return
      end
cccccccccccccccccccccccccccccccccccccccccccccccccccccccccccccccccccc
c  this subroutine computes intermediate free-field soil displacements
c  based on a user-specified ultimate lateral spread profile
cccccccccccccccccccccccccccccccccccccccccccccccccccccccccccccccccccc
      subroutine lateral(jtot,kt,ktime,z,ffd)
      implicit double precision (a-h,o-z)
      parameter (jmax=50)
      parameter (nffmax=20)
      dimension ffd(2,jmax),z(jmax)
      dimension zff(nffmax),uff(nffmax),ffult(jmax)
      real ffmax
      real pi,tfact
      integer jtot,ktime,nff
c
c     if this is the first time step, input the lateral spread data...
c
c     then determine where within the lateral spread each pile element is
c     located, and interpolate to determine the maximum lateral spread
c     displacement each pile element will be subjected to
c
      if(kt.eq.1) then
        pi = 4.d0*datan(1.d0)
        read(22,*)ffmax
        read(22,*)nff
        read(22,*) (zff(n),n=1,nff)
        read(22,*) (uff(n),n=1,nff)
        do 13 j=3,jtot-2
          kdum=1
 11       continue
          if(z(j).ge.zff(kdum).and.z(j).lt.zff(kdum+1)) then
```

```
        kk=kdum
         go to 12
        else
         kdum=kdum+1
         go to 11
        endif
 12      continue
        ffult(j) = ffmax * (uff(kk) + (uff(kk+1)-uff(kk))
   &            * (z(j)-zff(kk)) / (zff(kk+1)-zff(kk)))
c
c       This creates a lateral spread with a parabolic shape.
c
        if(z(j).ge.120.d0) then
         ffult(j) = ffmax * ( -0.001616d0*(30.d0 - z(j)/12.d0)**2.d0
   &                     +0.085*(30.d0 - z(j)/12.d0)
   &                     -0.08338d0)
        endif
 13    continue
      endif
c
c    for all time steps, this portion calculates the amount of free-field
c    lateral spread displacement at each pile element
c
      if(kt.le.ktime-1) then
       tfact = .5d0 * (1.d0 - dcos(pi*(kt-1)/(ktime-1)))
      else
       tfact = 1.0d0
      endif
c
      do 14 j=3,jtot-2
       ffd(2,j) = tfact * ffult(j)
 14   continue
      return
      end
ccccccccccccccccccccccccccccccccccccccccccccccccccccccccccccccccccc
c  This subroutine keeps track of the hysteretic p-y behavior for all
c  the pile elements.  Additionally, it evaluates the slope of the
c  current p-y curves, stiff(j),  and returns this vector back to the
c  main loop of the program.
c
c  Steve Kramer (BASIC). Modified and converted to FORTRAN by John Horne
ccccccccccccccccccccccccccccccccccccccccccccccccccccccccccccccccccc
      subroutine kvalue(jtot,kt,npt,pbb,ybb,pcur,ycur,ydel,stiff)
      implicit double precision (a-h,o-z)
```

```
      parameter (jmax=50)
      parameter (nptsmax=27)
      dimension delta1(jmax),delta2(jmax)
      dimension ydel(2,jmax)
      dimension pbb(jmax,nptsmax),ybb(jmax,nptsmax),stiff(jmax)
      dimension prev(jmax),yrev(jmax),p(jmax)
      dimension pcur(jmax,nptsmax),ycur(jmax,nptsmax)
      real dir,c
      integer npt
      if(kt.eq.1)then
       do 11 j=3,jtot-2
        p(j) = 0.d0
        delta1(j) = ydel(2,j) - ydel(1,j)
        delta2(j) = ydel(2,j) - ydel(1,j)
        prev(j)  = 0.d0
        yrev(j)  = 0.d0
        stiff(j)  = pcur(j,npt+1) / ycur(j,npt+1)
 11     continue
       return
      else
       goto 12
      endif
c
c     calculate direction of displacement in most recent time step.
c
 12    do 22 j=3,jtot-2
       delta2(j) = ydel(2,j) - ydel(1,j)
       if(delta2(j).ge.0.d0)then
        dir =  1.d0        !# y is increasing
       else
        dir = -1.d0         !# y is decreasing
       endif
c
c      determine the current p-value based on the most recent displacement increment
c
       p(j) = p(j) + stiff(j)*delta2(j)
c
c      determine if a reversal has occured in the most recent time step.
c
c      if no reversal, then the current backbone curve remains unchanged:
c      determine where on this curve we are, and then calculate the
c      corresponding stiffness (and be quick about it)
c
       if(delta1(j)*delta2(j).ge. -1.0d-100 )then
```

```
      mdum=1
 14    continue
      if(ydel(2,j).ge.ycur(j,mdum).and.ydel(2,j).lt.ycur(j,mdum+1))
    &  then
       mm=mdum
       go to 15
      else
       mdum=mdum+1
       go to 14
      endif
 15    continue
c
c      compute the tangent stiffness
c
      stiff(j) = (pcur(j,mm+1) - pcur(j,mm)) /
    &           (ycur(j,mm+1) - ycur(j,mm))
c
      if  ( dabs(p(j)/pbb(j,2*npt-2)) .gt. 1.d0
    &        .and. dir*p(j)          .gt. 0.d0)
    &  stiff(j) = (pcur(j,2*npt-1) - pcur(j,2*npt-2)) /
    &           (ycur(j,2*npt-1) - ycur(j,2*npt-2))
c
      stiff(j)  = dmax1(stiff(j),1.d0)
c
c     otherwise, a reversal has occured: determine the reversal point,
c     scale and update the current backbone curve, and then calculate the
c     corresponding stiffness (in three nano-seconds or less)
c
     else
      yrev(j) = ydel(1,j)
      mdum=1
 16    continue
      if(yrev(j).ge.ycur(j,mdum).and.yrev(j).lt.ycur(j,mdum+1))
    &  then
       mm=mdum
       go to 17
      else
       mdum=mdum+1
       go to 16
      endif
 17    continue
      prev(j) = pcur(j,mm) + (yrev(j) - ycur(j,mm)) *
    &  (pcur(j,mm+1) - pcur(j,mm)) / (ycur(j,mm+1) - ycur(j,mm))
c
```

```
      c = dabs( dir - prev(j) / dabs( pbb(j,2*npt-2) ) )
c
      do 18 m=1,2*npt-1
       ycur(j,m) = yrev(j) + c * ybb(j,m)
       pcur(j,m) = prev(j) + c * pbb(j,m)
 18    continue
c
      mdum=1
 19    continue
      if(ydel(2,j).ge.ycur(j,mdum).and.ydel(2,j).lt.ycur(j,mdum+1))
     &  then
       mm=mdum
       go to 21
      else
       mdum=mdum+1
       go to 19
      endif
 21    continue
c
c      compute the tangent stiffness
c
      stiff(j) = (pcur(j,mm+1) - pcur(j,mm)) /
     &          (ycur(j,mm+1) - ycur(j,mm))
c
      if  ( dabs(p(j)/pbb(j,2*npt-2)) .gt. 1.d0
     &   .and. dir*p(j)              .gt. 0.d0)
     &  stiff(j) = (pcur(j,2*npt-1) - pcur(j,2*npt-2)) /
     &          (ycur(j,2*npt-1) - ycur(j,2*npt-2))
c
      stiff(j) = dmax1(stiff(j),1.d0)
c
     endif
c
c     update delta1 for the next time step
c
     delta1(j) = delta2(j)
 22  continue
    stiff(3) = stiff(3)/2.d0
    stiff(jtot-2) = stiff(jtot-2)/2.d0
    return
    end
ccccccccccccccccccccccccccccccccccccccccccccccccccccccccccccccccccccc
c This subroutine implements the far-field soil model of Nogami, Otani,
c Konogai, and Chen (1992), "Nonlinear Soil-Pile Interaction Model for
```

```
c Dynamic Lateral Motion," Jrnl of Gtch Eng, ASCE, v118, n1, pp 89-106
cccccccccccccccccccccccccccccccccccccccccccccccccccccccccccccccc
      subroutine nogami(jtot,kt,dt,r0,dr,mp,mn11,cn,kn,dup,dvp,dap,
     &         duff,dvff,gmod,rho,unf,ppile,vnf)
      implicit double precision (a-h,o-z)
      parameter (jmax=50)
c
c   arrays for internal d.o.f.'s
c
      dimension  unf(2,jmax), ua(2,jmax), ub(2,jmax)    !# displacement
      dimension  vnf(2,jmax), va(2,jmax), vb(2,jmax)    !# velocity
      dimension  anf(2,jmax), aa(2,jmax), ab(2,jmax)    !# acceleration
      dimension  fsnf(2,jmax), fsa(2,jmax), fsb(2,jmax) !# spring force
      dimension  fanf(2,jmax), fab(2,jmax)              !# applied force
      dimension  finf(2,jmax)                           !# inertial force
c
c   scalers for internal d.o.f.'s
c
      real     dunf,    dua,    dub    !# incr. displ.
      real     dvnf,    dva,    dvb    !# incr. velc.
      real     danf,    daa,    dab    !# incr. accn.
      real     dpnf,    dpa,    dpb    !# incr. load
      real     dubarnf, dubara, dubarb !# extended incr. displ.
      real     sumnf,   suma,   sumb   !# force summation
c
c   specified increments of motion @ pile and free field
c
      dimension dup(jmax),  duff(jmax)         !# incr. displ.
      dimension dvp(jmax),  dvff(jmax)         !# incr. velc.
      dimension dap(jmax)                      !# incr. accn.
c
c   material properties and other variables
c
      real*8 cn(jmax),kn(jmax)
      real*8 mn11(jmax),mn12(jmax),mn22(jmax)
      dimension gmod(jmax),rho(jmax),ppile(jmax)
      real k1,k2,k3,c1,c2,c3,coef,pi,dr
      real k11,k12,   k22,k23,k33,kdet
      real f11,f12,f13,f22,f23,f33
      real cinv11,cinv22,cinv33,cinv12,cinv13,cinv23
      real cdet
      real dt,tau,theta,r0,r1,kfac,mfac,vs,mf,mp,pr
c
      integer jtot,kt
```

```
c
c    initialization of values
c
     if(kt.eq.1) then
      write(*,*)'begin sr NOGAMI - initialization'
      pi = 4.d0*datan(1.d0)
      pr = 0.5d0                   !# Poisson's Ratio
      theta = 1.4d0                !# Wilson's theta
      tau  = dt*theta              !# extended time step
      kfac = 2.d0                  !# implies poisson's ratio = 0.5
      mfac = 1.d0                  !# implies poisson's ratio = 0.5
      r1 = 2.d0*r0                 !# near field outer radius
      do 12 j=3,jtot-2
c
c       near field consistent mass matrix
c
        coef  = pi * r0**2.d0 * (r1/r0 - 1.d0) * rho(j)/6.d0
        mn11(j) = coef * (     r1/r0 + 3.d0)
        mn12(j) = coef * (     r1/r0 + 1.d0)
        mn22(j) = coef * (3.d0*r1/r0 + 1.d0)
c
c       near field damping
c
        cn(j)=dr*2.d0*dsqrt(kn(j)*(mp+mn11(j)))
        do 11 i=1,2
          anf(i,j) = 0.d0
          ua(i,j)  = 0.d0
          va(i,j)  = 0.d0
          aa(i,j)  = 0.d0
          ub(i,j)  = 0.d0
          vb(i,j)  = 0.d0
          ab(i,j)  = 0.d0
          finf(i,j)= 0.d0
          fanf(i,j)= 0.d0
          fab(i,j) = 0.d0
          fsnf(i,j)= 0.d0
          fsa(i,j) = 0.d0
          fsb(i,j) = 0.d0
 11       continue
 12     continue
      write(*,*)'end sr NOGAMI - initialization'
     else
     endif
 13  continue
```

```
c
c   COMPUTATION OF THE PILE-SOIL INTERACTION FORCE, ppile(j)
c
c   (Wilson's theta method is used here for determining the
c    response of the internal d.o.f.'s in the Nogami model)
c
      do 14 j=3,jtot-2
        vs = dmax1(1.d-1,dsqrt(dmax1(0.d0,gmod(j)/rho(j))))  !# shear wave velocity
        k1 = kfac*gmod(j)*3.518d0          !# far field stiffness
        k2 = kfac*gmod(j)*3.581d0          !# far field stiffness
        k3 = kfac*gmod(j)*5.529d0          !# far field stiffness
        c1 = kfac*r1*gmod(j)/vs*113.097d0  !# far field damping
        c2 = kfac*r1*gmod(j)/vs*25.133d0   !# far field damping
        c3 = kfac*r1*gmod(j)/vs*9.362d0          !# far field damping
        mf = mfac*pi*r1**2.d0*rho(j)       !# far field mass
c
c    effective stiffness matrix
c
        k11 =  kn(j) + k1 + 6.d0/tau**2.d0 * (mn22(j) + mf)
     &                    + 3.d0/tau     * (cn(j) + c1)
        k22 =  k1 + k2 + 3.d0/tau*(c1+c2)
        k33 =  k2 + k3 + 3.d0/tau*(c2+c3)
        k12 = -k1     - 3.d0/tau*c1
        k23 = -k2     - 3.d0/tau*c2
c
c    inverse of the effective stiffness matrix
c
        kdet = k11*k22*k33 - k11*k23**2.d0 - k33*k12**2.d0
        f11  = (k22*k33 - k23**2.d0) / kdet
        f22  =           k11 * k33 / kdet
        f33  = (k11*k22 - k12**2.d0) / kdet
        f12  =         - k12 * k33 / kdet
        f13  =           k12 * k23 / kdet
        f23  =         - k11 * k23 / kdet
c
c    effective load increment
c
        dpnf = theta*(kn(j)*dup(j) + cn(j)*dvp(j) - mn12(j)*dap(j))
     &       + (mn22(j) + mf)*(6.d0/tau*vnf(1,j) + 3.d0*anf(1,j))
     &       + (cn(j)+c1)*(3.d0*vnf(1,j) + tau/2.d0*anf(1,j))
     &       -    c1*(3.d0* va(1,j) + tau/2.d0* aa(1,j))         !# near field
c
        dpa = -    c1*(3.d0*vnf(1,j) + tau/2.d0*anf(1,j))
     &       + (c1+c2)*(3.d0* va(1,j) + tau/2.d0* aa(1,j))
```

```
   &     -    c2*(3.d0* vb(1,j) + tau/2.d0* ab(1,j))          !# point "a"
c
      dpb = theta*(k3*duff(j) + c3*dvff(j))
   &     -    c2*(3.d0*va(1,j) + tau/2.d0*aa(1,j))
   &     + (c2+c3)*(3.d0*vb(1,j) + tau/2.d0*ab(1,j))          !# point "b"
c
c     displacement increment over the extended time step
c
      dubarnf = f11*dpnf + f12*dpa + f13*dpb        !# near field
      dubara  = f12*dpnf + f22*dpa + f23*dpb        !# point "a"
      dubarb  = f13*dpnf + f23*dpa + f33*dpb        !# point "b"
c
c     acceleratation increment over the normal time step
c
      danf = (6.d0/tau**2.d0*dubarnf-6.d0/tau*vnf(1,j)-3.d0*anf(1,j))
   &       /theta                                              !# near field
      daa  = (6.d0/tau**2.d0* dubara-6.d0/tau* va(1,j)-3.d0* aa(1,j))
   &       /theta                                              !# point "a"
      dab  = (6.d0/tau**2.d0* dubarb-6.d0/tau* vb(1,j)-3.d0* ab(1,j))
   &       /theta                                              !# point "b"
c
c     velocity increment over the normal time step
c
      dvnf = anf(1,j)*dt + danf*dt/2.d0            !# near field
      dva  =  aa(1,j)*dt +  daa*dt/2.d0            !# point "a"
      dvb  =  ab(1,j)*dt +  dab*dt/2.d0            !# point "b"
c
c     displacement increment over the normal time step
c
      dunf = vnf(1,j)*dt + anf(1,j)*dt**2.d0/2.d0 + danf*dt**2.d0/6.d0     !# near field
      dua  =  va(1,j)*dt +  aa(1,j)*dt**2.d0/2.d0 +  daa*dt**2.d0/6.d0     !# point "a"
      dub  =  vb(1,j)*dt +  ab(1,j)*dt**2.d0/2.d0 +  dab*dt**2.d0/6.d0     !# point "b"
c
c     updated velocity based on dynamic equillibrium
c
      cdet    = 1.d0/(1.d0/cn(j) + 1.d0/c1 + 1.d0/c2 + 1.d0/c3)
      cinv11  = cdet/cn(j)*(1.d0/c1 + 1.d0/c2 + 1.d0/c3)
      cinv22  = cdet*(1.d0/cn(j) + 1.d0/c1)*(1.d0/c2 + 1.d0/c3)
      cinv33  = cdet/c3*(1.d0/cn(j) + 1.d0/c1 + 1.d0/c2)
      cinv12  = cdet/cn(j)*(1.d0/c2 + 1.d0/c3)
      cinv13  = cdet/cn(j)/c3
      cinv23  = cdet/c3*(1.d0/cn(j) + 1.d0/c1)
c
      fanf(2,j) = fanf(1,j)-mn12(j)*dap(j)+cn(j)*dvp(j)+kn(j)*dup(j)
```

```
      fab(2,j)  = fab(1,j) + c3*dvff(j) + k3*duff(j)
c
      finf(2,j) = finf(1,j) + (mn22(j) + mf)*danf
c
      fsnf(2,j) = fsnf(1,j) + (kn(j)+k1)*dunf - k1*dua
      fsa(2,j)  = fsa(1,j)  - k1*dunf + (k1+k2)*dua - k2*dub
      fsb(2,j)  = fsb(1,j)  - k2*dua  + (k2+k3)*dub
c
      sumnf = fanf(2,j) - fsnf(2,j) - finf(2,j)
      suma  =           - fsa(2,j)
      sumb  = fab(2,j)  - fsb(2,j)
c
      vnf(2,j) = cinv11*sumnf + cinv12*suma + cinv13*sumb
      va(2,j)  = cinv12*sumnf + cinv22*suma + cinv23*sumb
      vb(2,j)  = cinv13*sumnf + cinv23*suma + cinv33*sumb
c
      dvnf = vnf(2,j) - vnf(1,j)
      dva  = va(2,j) -  va(1,j)
      dvb  = vb(2,j) -  vb(1,j)
c
c     updated displacement and acceleration
c
      unf(2,j) = unf(1,j) + dunf          !# near field
      anf(2,j) = anf(1,j) + danf
c
      ua(2,j) = ua(1,j) + dua             !# point "a"
      aa(2,j) = aa(1,j) + daa
c
      ub(2,j) = ub(1,j) + dub             !# point "b"
      ab(2,j) = ab(1,j) + dab
c
c     pile force
c
      ppile(j) = ppile(j) - kn(j)*(dup(j)-dunf) - mn12(j)*danf
c
c     update vectors for next time step - internal d.o.f.'s only!
c
      unf(1,j)  =  unf(2,j)   !# near field
      vnf(1,j)  =  vnf(2,j)
      anf(1,j)  =  anf(2,j)
c
      ua(1,j)   =  ua(2,j)    !# point a
      va(1,j)   =  va(2,j)
      aa(1,j)   =  aa(2,j)
```

```
c
     ub(1,j)  =  ub(2,j)  !# point b
     vb(1,j)  =  vb(2,j)
     ab(1,j)  =  ab(2,j)
c
     fanf(1,j) = fanf(2,j)  !# applied force at the near field
     fab(1,j)  =  fab(2,j)  !# applied force at b
c
     finf(1,j) = finf(2,j)        !# inertial force at the near field
c
     fsnf(1,j) = fsnf(2,j)  !# spring force at the near field
     fsa(1,j)  =  fsa(2,j)  !# spring force at point a
     fsb(1,j)  =  fsb(2,j)  !# spring force at point b
c
 14  continue
     return
     end
cccccccccccccccccccccccccccccccccccccccccccccccccccccccccccccccccccc
c This subroutine computes the soil-pile force based on the stiffness
c computed from the most recent time step, and the difference between
c the free field and pile displacements for the present time step
cccccccccccccccccccccccccccccccccccccccccccccccccccccccccccccccccccc
     subroutine nofar(jtot,stiff,ddp,ddff,ppile)
     implicit double precision (a-h,o-z)
     parameter (jmax=50)
c
     dimension stiff(jmax),ppile(jmax)
     dimension ddp(jmax),ddff(jmax)
     integer jtot
c
     do 11 j=3,jtot-2
      ppile(j) = ppile(j) + stiff(j) * (ddff(j) - ddp(j))
 11  continue
     return
     end
cccccccccccccccccccccccccccccccccccccccccccccccccccccccccccccccccccc
c  For each time step, this routine updates the displacements of the
c  pile along its length based on the governing differential equation.
c
c  v(i,j), ffd(i,j) and ffu(i,j) are the pile displacements, free field
c  displacements, and free field pore water pressures, respectively,
c  at time step i and depth j.
c
c  Note the following index definitions for v(i,j) and ffd(i,j),
```

```
c  and ffu(i,j):    i=1 is the past time step
c                   i=2 is the current time step
c                   i=3 is the next time step
c
c  jtot is the total number of pile elements + 4 (virtual)
c  dx is the incremental pile length i.e. "delta-x"
c  dt is the time increment i.e. "delta-t"
c
c  stiff(j) is the stiffness of the pile/soil interface per unit length
c  cn(j) is the damping of the pile/soil interface per unit length.
c  mpile is the mass of the pile per unit length.
cccccccccccccccccccccccccccccccccccccccccccccccccccccccccccccccccccc
      subroutine tstep(jtot,kt,ppile,mn11,cn,v,ffv,ddp,dvp,dap)
      implicit double precision (a-h,o-z)
      parameter (jmax=50)
      dimension v(3,jmax),s(3,jmax),a(3,jmax),ppile(jmax),ffv(2,jmax)
      dimension ddp(jmax),dvp(jmax),dap(jmax)
      dimension cn(jmax)
      real*8 mn11(jmax)
      integer jtot,kt
      real emod,inert,length,diam,area,axload,wpile,rhopile,dz,dt
      real mpile,kv,amax
c       real c1,c2,tfact
      real eid4v,qd2v,dnum,enum,fnum
      common /piledat/ emod,inert,length,diam,area,axload,
     &              wpile,rhopile,mpile,dz,dt
c
c     zero resident array for first time step
c
      if(kt.eq.1)then
        amax = 0.d0
        do 12 j=3,jtot-2
          do 11 i=1,3
            a(i,j) = 0.d0
            s(i,j) = 0.d0
 11       continue
 12     continue
      else
      endif
c
c     MAIN LOOP OF THE SUBROUTINE
c
      do 13 j=3,jtot-2
c
```

```
c      calculate components of the finite difference equation
c
       eid4v = emod*inert/dz**4.d0*
     & (v(2,j+2)-4.d0*v(2,j+1)+6.d0*v(2,j)-4.d0*v(2,j-1)+v(2,j-2))
c
       qd2v = axload*(v(2,j+1)-2.d0*v(2,j)+v(2,j-1)) / dz**2.d0
c
       kv = -ppile(j)
c
       dnum = (mpile+mn11(j)) /dt**2.d0*(v(1,j)-2.d0*v(2,j))
c
       enum = -cn(j) * ( v(1,j)/2.d0/dt + ffv(2,j) )  !# we know ffv explicitly here
c
       fnum = -((mpile+mn11(j))/dt**2.d0 + cn(j)/2.d0/dt)
c
c  updated displacement, velocity, and acceleration
c
       v(3,j) = (eid4v + qd2v + kv + dnum + enum) / fnum
       s(3,j) = (v(3,j) - v(2,j))/dt
       a(3,j) = 1.d0/(mpile+mn11(j)) * (eid4v + qd2v + kv +
     &        cn(j)*((v(3,j)-v(1,j))/2.0d0/dt - ffv(2,j)))
c
c  incremental displacement, velocity, and acceleration
c
       ddp(j) = v(3,j) - v(2,j)
       dvp(j) = s(3,j) - s(2,j)
       dap(j) = a(3,j) - a(2,j)
 13    continue
c
c     update vectors for the next time step
c
      do 14 j=3,jtot-2
       v(1,j)   = v(2,j)
       v(2,j)   = v(3,j)
       s(1,j)   = s(2,j)
       s(2,j)   = s(3,j)
       a(1,j)   = a(2,j)
       a(2,j)   = a(3,j)
 14    continue
      return
      end
cccccccccccccccccccccccccccccccccccccccccccccccccccccccccccccccccccc
c  At the end of each time step, this routine extends the newly-computed
c  data from the computational region (j = 3, 4,..jtot-2) to the
```

```
c virtual cells outside the region (j = 1, 2,..jtot-1, jtot)
c depending on the boundary conditions (fixed or pinned).
c
c Note the following index definitions for v(i,j) and ffd(i,j),
c and ffu(i,j):   i=1 is the past time step
c                 i=2 is the current time step
c                 i=3 is the next time step
c
c jtot is the number of pile elements plus 4 virtual elements.
c bchead is the boundary condition of the pile head.
c bctoe is the boundary condition of the pile toe.
cccccccccccccccccccccccccccccccccccccccccccccccccccccccccccc
      subroutine bc(v,jtot,bchead,bctoe)
      implicit double precision (a-h,o-z)
      parameter (jmax=50)
      dimension v(3,jmax)
      character bchead*3,bctoe*3
c
      if(bchead.eq.'pin')then              !# zero shear & moment
        v(2,1)=4.d0*(v(2,3)-v(2,4))+v(2,5)
        v(2,2)=2.d0*v(2,3)-v(2,4)
      elseif(bchead.eq.'fix')then          !# zero shear & rotation
        v(2,1)=v(2,5)
        v(2,2)=v(2,4)
      elseif(bchead.ne.'pin'.and.bchead.ne.'fix')then
        write(*,*)'WRONG BOUNDARY CONDITION SPEC FOR PILE HEAD'
      endif
c
      if(bctoe.eq.'pin')then
        v(2,jtot)   = 4.d0*(v(2,jtot-2)-v(2,jtot-3))+v(2,jtot-4)      !# zero shear & moment
        v(2,jtot-1) = 2.d0*v(2,jtot-2)-v(2,jtot-3)
      elseif(bctoe.eq.'fix')then                         !# zero shear & rotation
        v(2,jtot)=v(2,jtot-4)
        v(2,jtot-1)=v(2,jtot-3)
      elseif(bctoe.ne.'pin'.and.bctoe.ne.'fix')then
        write(*,*)'WRONG BOUNDARY CONDITION SPEC FOR PILE TOE'
      endif
c
      return
      end
cccccccccccccccccccccccccccccccccccccccccccccccccccccccccccccccccccc
c This routine calculates and returns the bending moments and shear
c forces in the pile based on the displacement vector passed to it.
c Centered difference approximations are used for the second and third
```

```
c derivatives.
ccccccccccccccccccccccccccccccccccccccccccccccccccccccccccccccccc
      subroutine forces(jtot,v,bend,shear)
      implicit double precision (a-h,o-z)
      parameter (jmax=50)
      dimension v(3,jmax),bend(jmax),shear(jmax)
      real emod,inert,length,diam,area,axload,wpile,rhopile,mpile,dz,dt
      real amp,omega
      integer jtot
      common /piledat/ emod,inert,length,diam,area,axload,
     &            wpile,rhopile,mpile,dz,dt
      common /cmplxdat/ amp,omega
      common /gravity/ grav
      do 11 j=3,jtot-2
       bend(j) = emod*inert*(v(2,j+1)-2.d0*v(2,j)+v(2,j-1))/dz**2.d0
c
       shear(j)  = emod*inert*(v(2,j+2)-2.d0*v(2,j+1)+2.d0*v(2,j-1)
     &          -v(2,j-2))/2.d0/dz**3.d0
11    continue
      return
      end
ccccccccccccccccccccccccccccccccccccccccccccccccccccccccccccccccc
c This routine outputs the newly calculated pile displacement
c vector, free field displacement vector, and the shear/bending moment
c vector for selected time steps.
c
c v(2,j) is the newly calculated displacement vector (due to updating)
c jtot is the total number of pile elements + 4 (virtual)
c z(j) is the depth of the jth pile element
ccccccccccccccccccccccccccccccccccccccccccccccccccccccccccccccccc
      subroutine output(jtot,v,bend,shear)
      implicit double precision (a-h,o-z)
      parameter (jmax=50)
      dimension v(3,jmax),bend(jmax),shear(jmax)
      integer jtot
      write(25,1000) (v(2,j),     j=3,jtot-2)      !# displacements
      write(26,1000) (bend(j),  j=3,jtot-2)      !# bending moments
      write(27,1000) (shear(j), j=3,jtot-2)      !# shear forces
 1000 format(100e15.8)
      return
      end
```

□

# VITA

John Charles Horne obtained bachelors degrees in civil and mechanical engineering from Oregon State University in 1986. From 1986 to 1991, he worked for the Boeing Company in Seattle, Washington as a structural engineer on the B2 Bomber program. During this time, he began graduate studies at the University of Washington, and obtained a masters degree in civil engineering in 1990. In 1991, he joined the Seattle office of Dames & Moore as a project geotechnical engineer. In 1993, he left Dames & Moore to begin his doctoral studies at the University of Washington.